# INNOVATIVE APPLICATIONS AND RESEARCH METHODS IN SCIENCE AND MATHEMATICS

***EDITOR***
***PROF. MUSTAFA DEDE, PH.D.***

9 786258 513363

DOI: 10.5281/zenodo.18100824

# Innovative Applications and Research Methods in Science and Mathematics

Editor

Prof. Mustafa Dede, Ph.D.

**Publisher**
Platanus Publishing®

**Editors in Chief**
Prof. Mustafa Dede, Ph.D.

**Cover & Interior Design**
Platanus Publishing®

**The First Edition**
December, 2025

**ISBN**
978-625-8513-36-3



**Platanus Publishing®**
**Address:** Natoyolu Cad. Fahri Korutürk Mah. 157/B, 06480, Mamak, Ankara, Turkey.

**Phone:** +90 312 390 1 118
**web:** www.platanuspublishing.com
**e-mail:** platanuskitap@gmail.com

Platanus Publishing®

# CONTENTS

# CHAPTER 1

## The Most Realistic Models for Alpha Decay

**F. Aysun Uğur[1] & Mehmet Akif Kara[2]**

[1] Prof. Dr., Osmaniye Korkut Ata University, ORCID:0000-0003-4134-6799
[2] Osmaniye Korkut Ata University

## 1. Introduction and Historical Background

By 1908, Rutherford and Geiger had determined that alpha particles are helium nuclei $^4_2He$, consisting of two protons and two neutrons. This identification marked a turning point in understanding the structure of matter, confirming that atoms contain smaller constituents governed by forces much stronger than those in chemical interactions. However, the mechanism by which alpha particles escape from the nucleus remained a mystery for nearly two decades (U, 2010).

Early classical models could not explain how an alpha particle, trapped inside a nuclear potential well surrounded by a large Coulomb barrier, could possess sufficient energy to escape. The typical Coulomb barrier height for heavy nuclei such as uranium or thorium is on the order of 25–30 MeV, whereas the observed alpha-particle kinetic energies are only 4–8 MeV. Thus, classically, the particle should be confined indefinitely (Krane, 1988).

The resolution came with the advent of quantum mechanics. In 1928, George Gamow and independently Condon and Gurney proposed that alpha emission is a quantum tunneling process: the alpha particle, pre-formed inside the nucleus, has a finite probability of penetrating the potential barrier even when its total energy is less than the barrier height. This model not only explained the existence of alpha decay but also accurately reproduced the observed exponential relationship between half-life and alpha energy, now known as the Geiger–Nuttall law (Wong, 2004) .

The success of Gamow's theory demonstrated the physical reality of quantum tunneling, influencing nearly all subsequent developments in nuclear and quantum physics. Over the following decades, theoretical models evolved from simple one-dimensional barrier penetration approximations to microscopic cluster models, double-folding potentials, and density-functional frameworks (DFT and RMF) that incorporate realistic nucleon-nucleon interactions and density-dependent effects (Heyde, 2004).

In modern nuclear theory, alpha decay is understood as a delicate balance between nuclear structure, pairing correlations, and quantum tunneling dynamics. The half-life of an alpha emitter depends sensitively on the preformation probability, the height and width of the potential barrier, and the energy of the emitted alpha particle. This relationship not only provides insights into nuclear stability but also serves as a probe of the underlying nuclear potential, particularly in heavy and superheavy nuclei (G, 1928).

## 2. Quantum Mechanical Foundations of Alpha Decay

The theoretical explanation of alpha decay lies at the intersection of quantum mechanics and nuclear structure physics. Within the quantum framework, the nucleus is modeled as a many- body system of strongly interacting nucleons, bound by the nuclear potential and opposed by the Coulomb repulsion between

protons. For heavy nuclei, the potential landscape governing an alpha particle is characterized by three distinct

### 2.1 The Nuclear Potential Well

Inside the nucleus, nucleons experience an attractive force arising from the strong nuclear interaction, which is short-ranged and saturating. A simplified description of this potential for an alpha particle interacting with the residual daughter nucleus can be expressed as: (Eq.1)

$$V(r) = \begin{cases} -V_0, & r < R \\ \frac{Z_d Z_a e^2}{4\pi\varepsilon_0 r}, & r \geq R \end{cases} \quad (1)$$

where $V_0$ is the depth of the nuclear potential well (typically 30-40 MeV), $Z_d$ is the charge of the daughter nucleus, and $R$ represents the nuclear radius, often parameterized as $R = r_0 A^{1/3},\ r_0 \cong 1.2\ fm$.

Within this potential well, the alpha particle behaves as a bound state of the nucleus. However, at $r \cong R$, it encounters a steep Coulomb barrier that classically confines it. The alpha decay process therefore requires a mechanism beyond classical physics - namely, uantum tunneling (Fig.1, Fig. 2) (Landau, 1977) .

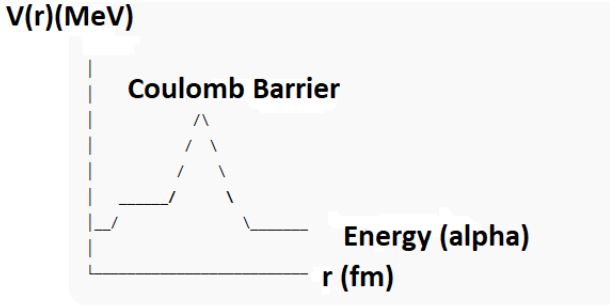


Figure 1. Coulomb barrier and radius relationship

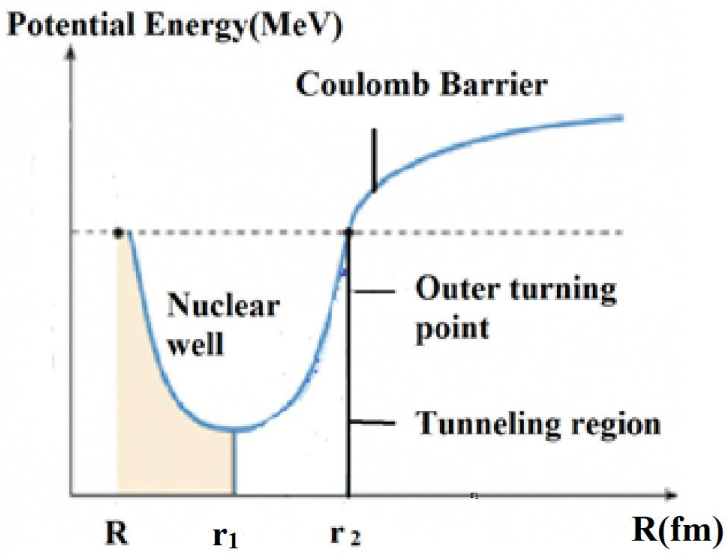


Figure 2. Well model diagram

### 2.2 The Schrödinger Equation for Alpha Emission

The time-independent Schrödinger equation governing the radial motion of the alpha particle is:

$$\left[-\frac{\hbar^2}{2\mu}\frac{d^2}{dr^2} + V(r)\right]\Psi(r) = E\,\Psi\,(r) \qquad (2)$$

where μ is the reduced mass of the alpha-daughter system and E is the total energy of the alpha particle. The boundary conditions are such that.

- Inside the well (r< $R$): the wavefunction oscillates (bound state behavior)
- Under the barrier (R< $r$ < $R_b$): the wavefunction decays exponentially.
- Outside the barrier (r> $R_b$): the wavefunction describes a free, outgoing alpha particles.

The existence of a non-zero wavefunction beyond the barrier implies a finite probability that the alpha particle escapes from the nucleus per unit time (Merzbacher, 1998).

### 2.3 Quantum Tunneling and Barrier Penetration

In classical mechanics, a particle cannot cross a region where its energy E is less than the potential V(r). However, quantum mechanics allows for a non-zero transmission probability, derived from the continuity and

differentiability of the wavefunction. The amplitude of the wavefunction in the forbidden region decreases exponentially according to:

$$\Psi(r) \propto \exp\left[-\frac{1}{\hbar}\int_{R}^{R_0}\sqrt{2\mu(V(r)-E)}\,dr\right] \qquad (3)$$

This integral quantifies the degree of tunneling suppression, the larger the barrier or the smaller the alpha energy, the lower the probability of transmission.

Thus, even though the alpha particle lacks sufficient energy to overcome the Coulomb barrier, it can quantum mechanically penetrate it with a small but finite probability (Geiger H, 1911). Geiger, H., & Nuttall, J. M. (1911).

### 2.4 Physical Interpretation

The tunneling probability is the central quantity linking microscopic nuclear properties to macroscopic observables such as half-life $T_{1/2}$. A highly bound alpha particle (with lower kinetic energy) must penetrate a thicker barrier, resulting in an exponentially longer half-life. Conversely, higher-energy alphas correspond to shorter-lived nuclei.

This physical insight explains why the half-lives of alpha emitters span a vast range—from microseconds for superheavy nuclei to billions of years for isotopes likeuranium-238 despite only modest variations in the emitted alpha energy . (Buck, 1992).

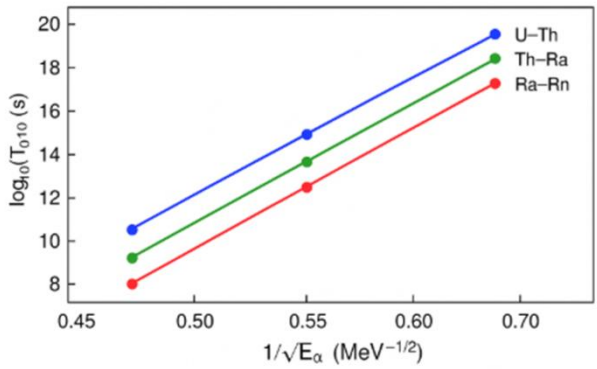


**Figure 3.** Linear relationship between $\log_{10}(T_{1/2})$ and $1/\sqrt{E_\alpha}$

## 3. Gamow Model and WKB Approximation

### 3.1 Conceptual Framework of the Gamow Model

In 1928, George Gamow proposed a revolutionary quantum explanation of alpha decay, introducing the concept of barrier penetration. He suggested that

alpha particles are preformed inside the nucleus and move within a potential well created by the nuclear and Coulomb interactions. Even though the total energy of the alpha particle Eα is below the Coulomb barrier height $V_b$, there exists a finite probability for the particle to tunnel through the barrier and escape.

The decay constant (λ), representing the probability per unit time that an alpha particle escapes, can be expressed as:

$$\lambda = f\ x\ P \tag{4}$$

where

- f is the frequency of collisions of the alpha particle with the nuclear barrier (the attempt frequency), and

P is the tunneling probability, derived from the WKB approximation (Horiuchi, 1977) .

### 3.2 The WKB Approximation

The **Wentzel–Kramers–Brillouin (WKB)** method provides a semi-classical solution to the Schrödinger equation when the potential varies slowly compared to the wavelength of the particle. In a one-dimensional potential barrier problem, the WKB approximation gives the transmission probability as:

$$P = -exp\left[-2\ \int_R^{R^b} k(r)dr\right] \tag{5}$$

where

$$k(r) = \sqrt{\sqrt{\frac{2\mu}{\hbar^2}}[v(r) - E_\alpha]} \tag{6}$$

and$R$ and$R_b$are the classical turning points defined by

$$V(R) - V(R_b) - E_\alpha, \tag{7}$$

for the alpha decay problem, the potential $V(R)$ is composed of two main terms;

$$V(r) - V_N(r) + V_C(r), \tag{8}$$

where $V_N(r)$is the short-range attractive nuclear potential, and $V_C(r)$ is the repulsive Coulomb potential,

$$V_C(r) = \frac{Z_d Z_\alpha e^2}{4\pi\varepsilon_0 r} \quad (9)$$

Inside the nucleus ($r < R$), $V_N$ dominates, while beyond the nuclear surface, the Coulomb potential defines the barrier (Lovas, 1998).

### 3.3 Decay Constant and Half-Life

The attempt frequency fff can be approximated as the number of times per second the alpha particle "hits" the barrier while oscillating inside the potential well. Using simple quantum mechanical arguments:

$$f = \frac{v}{2R} = \frac{1}{2R}\sqrt{\frac{2E_\alpha}{\mu}}, \quad (10)$$

where $v$ is the velocity of the alpha particle inside the nucleus.

The decay constant is then given by;

$$\lambda = fP = \frac{1}{2R}\sqrt{\frac{2E_\alpha}{\mu}} \exp\left[\frac{2}{\hbar}\int_R^{R_b}\sqrt{2\mu(V(r) - E_\alpha)}\,dr\right] \quad (11)$$

The half-life ($T_{1/2}$) is related to the decay constant by:

$$T_{1/2} = \frac{ln2}{\lambda} \quad (12)$$

Taking the logarithm of both sides and simplifying, we obtain an expression of the form;

$$log_{10}T_{1/2} = a\ \frac{Z_d}{\sqrt{E_\alpha}} + \ b, \quad (13)$$

which corresponds to the Geiger- Nuttall law, where *a*and *b* are empirical constants dependent on the nuclear structure and barrier properties (R.K, 2000).

### 3.4 Physical Significance

Gamow's model captures the essence of quantum tunneling in nuclear decay and provides a direct connection between measurable quantities (half-life and alpha energy)

The model's accuracy demonstrates that the probability of barrier penetration — an intrinsically quantum phenomenon — dictates the stability of heavy nuclei (Satchler G R, 1979).

### 3.5. Physical Significance

Gamow's model captures the essence of quantum tunneling in nuclear decay and provides a direct connection between measurable quantities (half-life and alpha energy).

The model's accuracy demostrates that the probability of barrier penetration- an intrinsically quantum phenomenon- dictates the stability of heavy nuclei.

Moreover, the exponential sensitivity of $T_{1/2}$ to $E_\alpha$explains why small variations in alpha energy (on the order of 1 MeV) can produce changes in half-life spanning many orders of magnitude.

Gamow's formulation thus remains a cornerstone of modern nuclear theory, forming the bridge between microscopic quantum mechanics and macroscopic decay laws observed experimentally (Kobos, 1982).

## 4. Geiger–Nuttall Law and Empirical Relations

### 4.1 Historical Background

The Geiger–Nuttall Law, first formulated by Hans Geiger and John Mitchell Nuttall in 1911, describes an empirical relationship between the alpha-particle energy ($E_\alpha$) and the decay constant ($\lambda$) or equivalently, the half-life ($T_{1/2}$) of alpha-emitting nuclei.

Before the advent of quantum mechanics, this relationship was purely experimental. However, Gamow's quantum tunneling model (1928) later provided a theoretical foundation for this empirical law.

Geiger and Nuttall observed that nuclei emitting alpha particles with higher energies decay faster, following a simple logarithmic correlation:

$$log_{10} T_{1/2} = \alpha \frac{Z_d}{\sqrt{E}\alpha} + b, \qquad (14)$$

where

- $T_{1/2}$ is the half-life,
- $E_\alpha$ is the alpha-particle kinetic energy,
- $Z_d$ is the atomic number of the daughter nucleus, and
- a and b are constants determined from experimental data.

This relationship implies that even a small change in $E_\alpha$ leads to a large variation in half-life, spanning from microseconds to billions of years (T, 2001).

### 4.2 Theoretical Derivation from the Gamow Model

Starting from the WKB approximation (Section 3), the tunneling probability for alpha decay is:

$$P = exp\left[-2\int_{R}^{R_b}\sqrt{\frac{2\mu}{\hbar^2}\left(V_{(r)} - E_\alpha\right)}\right] \quad (15)$$

Assuming a pure Coulomb potential beyond the nuclear radius (r>R):

$$V_{(r)} = \frac{Z_d Z_\alpha e^2}{4\pi\varepsilon_0 r}, \quad (16)$$

the integral can be solved approximately as:

$$\int_{R}^{R_b} k_{(r)}\, dr \approx \frac{2Z_d Z_\alpha e^2}{\hbar v_\alpha}\left[arccos\left(\sqrt{\frac{R}{R_b}}\right) - \sqrt{\frac{R}{R_b}\left(1 - \frac{R}{R_b}\right)}\right] \quad (17)$$

where $$v_\alpha = \sqrt{\frac{2E_\alpha}{\mu}} \quad (18)$$

is the alpha-particle velocity.

For heavy nuclei $R_b \gg R$, so the expression simplifies, and the logarithm of the half-life becomes approximately linear in

$z_d \,/\, \sqrt{E_\alpha}$: (19)

$$log_{10} T_{1/2} = A\frac{Z_d}{\sqrt{E}\alpha} + B, \quad (20)$$

Thus, the Geiger–Nuttall law emerges naturally from quantum tunneling theory (Khoa D T, 1996).

### 4.3 Empirical Verification

Extensive experimental data confirm the linear dependence predicted by the law. For each isotopic chain, a specific pair of constants A and B provides an accurate description of decay rates.

Table 1. Example of experimental values for α-decay in isotopic chains

| Parent Nucleus | Daughter ($Z_a$) | $E_a$ (MeV) | $T_{1/2}$ (s) | $\log_{10} T_{1/2}$ | $Z_d / \sqrt{E_a}$ |
|---|---|---|---|---|---|
| $^{210}$Po | $^{206}$Pb (82) | 5.41 | $1.2 \times 10^{7}$ | 7.08 | 35.3 |
| $^{214}$Po | $^{210}$Pb (82) | 7.69 | $1.6 \times 10^{-4}$ | -3.80 | 29.6 |
| $^{226}$Ra | $^{222}$Rn(86) | 4.78 | $5.0 \times 10^{10}$ | 10.7 | 39.3 |
| $^{238}$U | $^{234}$Th (90) | 4.27 | $1.4 \times 10^{17}$ | 17.15 | 43.6 |

It is evident that as $E\alpha$ increases, $T_{1/2}$ decreases dramatically, confirming the inverse correlation predicted by the tunneling model.

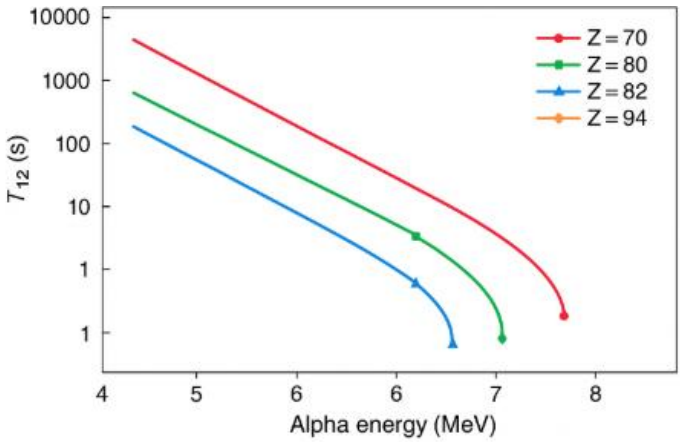


Figure 4. Isotonic chain: half-life alpha energy

### 4.5 Physical Interpretation

The Geiger–Nuttall law demonstrates that:

- Alpha decay is governed not by classical energetics but by quantum tunneling probabilities.
- The exponential dependence of tunneling probability on the barrier width and height causes extreme sensitivity to energy.

Different isotopic (or isotonic) chains exhibit nearly parallel lines on a Geiger–Nuttall plot, indicating similar nuclear potential structures but varying barrier penetrabilities (Khoa, 1994) .

### 4.6 Modified Geiger – Nuttall Laws

Later refinements introduced additional parameters, including angular momentum ($l$) and preformation probability ($P_\alpha$), leading to generalized forms such as:

$$log_{10} T_{1/2} = a\frac{Z_d\sqrt{\mu}}{\sqrt{E\alpha}} + bl(l+1) + c \qquad (21)$$

and density-dependent or cluster - model - based relations used in microscopic nuclear theories (discussed in Section 5) (P, 1996) .

## 5. Microscopic and Density-Based Models of Alpha Decay

### 5.1 Introduction

While the Gamow model and the Geiger–Nuttall law provide an elegant phenomenological description of alpha decay, they rely on macroscopic approximations such as the smooth Coulomb and nuclear potentials. In modern nuclear theory, microscopic models derived from many-body quantum mechanics and density functional theory (DFT) offer a more fundamental description. These approaches explicitly account for the nucleon-nucleon (NN) interaction, the structure of the parent and daughter nuclei, and the cluster preformation probability of the alpha particle (Vretenar, 2005).

### 5.2 Resonating Group Model (RGM)

The Resonating Group Model (RGM), developed by Wheeler and others in the 1930s, treats the alpha particle and the daughter nucleus as two interacting clusters of nucleons. The total wavefunction of the decaying nucleus is expressed as an antisymmetrized product of the internal wavefunctions of each cluster and a relative-motion function $x(r)$:

$$\Psi = A[\Phi_\alpha(\xi_\alpha)\Phi_d(\xi_d)x(r)] \qquad (22)$$

where $A$ ensures the Pauli exclusion principle between nucleons in different clusters.

The corresponding integro-differential equation obtained from the Schrödinger equation is:

$$\int [H(r,r') - EN(r)]x(r')dr' = 0 \qquad (23)$$

where H and N represent the Hamiltonian and normalization kernels, respectively (Bender, 2003).

The RGM provides:

- A **microscopic foundation** for cluster formation,
- The ability to compute **preformation probabilities**, and
- A consistent framework to derive the **effective alpha–daughter interaction potential**

### 5.3 The Dynamical Cluster Model (DCM)

The Dynamical Cluster Model (DCM) extends the RGM by incorporating collective motion and temperature-dependent dynamics of the parent nucleus.

In this model, the total decay constant is expressed as:

$$\lambda = P_0 v_0 P \qquad (24)$$

where:

$P_0$ = preformation probability of the alpha cluster inside the parent nucleus,

$v_0$ = assault frequency (number of barrier attempts per second), and

$P$ = barrier penetrability obtained via the WKB approximation.

The DCM provides a quantitative link between nuclear structure and decay properties. It predicts half-lives with higher accuracy than purely phenomenological models, especially for super heavy nuclei and deformed isotopes (Meng, 2006).

### 5.4 The Double-Folding Model

The Double-Folding Model (DFM) constructs the potential between the alpha particle and the daughter nucleus from the nucleon densities and the effective NN interaction:

$$V(R) = \iint \rho_\alpha(r_1)\rho_d(r_2) vNN(|R + r_2 - r_1|)\, d^3r_1\, d^3r_2 \qquad (25)$$

This microscopic folding potential naturally includes effects from both the nuclear interior and the surface. The advantage of the DFM is that it eliminates empirical parameters like potential depths and radii, making it fully derived from nuclear densities obtained via Hartree – Fock or RMF calculations (Poenaru, 1996).

### 5.5 The Density-Dependent M3Y (DDM3Y) Interaction

The DDM3Y model refines the double-folding approach by using the M3Y nucleon-nucleon effective interaction with a density-dependent factor that accounts for medium effects:

$$vNN\ (\ r,\rho) = \mathrm{t}^{\mathrm{M3Y}}(r)\mathrm{g}(\rho) \qquad (26)$$

where

$\mathrm{t}^{\mathrm{M3Y}}(r)$ represents the original M3Y Yukawa-type interaction, $\mathrm{g}(\rho) = c\left(1 - \beta\rho^{2/3}\right)$ introduces a reduction at higher densities.

The resulting potential, when combined with WKB barrier penetration, yields highly accurate predictions for alpha-decay half-lives across isotopic and isotonic chains. In modern research, the DDM3Y + WKB framing is considered one of the most reliable semi-microscopic methods for heavy nuclei . (Qi, 2009).

### 5.6 Density Functional Theory (DFT) and Relativistic Mean Field (RMF) Approaches

The DFT and RMF models provide a self-consistent mean-field description of the nucleus from first principles.

In RMF theory, nucleons are treated as Dirac particles interacting via meson fields (σ, ω, and ρ ).

The Lagrangian density is:

$$\mathscr{L} = \bar{\psi}\left[i\gamma^{\mu}\partial\mu - M - g_{a}\sigma - g_{\omega}\gamma^{\mu}\omega_{\mu} - g_{\rho}\gamma^{\mu}\vec{T} - \overrightarrow{\rho_{\mu}}\right]\psi\cdots \qquad (27)$$

Solving the coupled field equations yields self-consistent nuclear densities, which can be used as input for folding calculations or to extract alpha preformation probabilities (Xu, 2006).

These models successfully reproduce:

- Binding energies and charge radii;
- Shell effects near closed proton/neutron numbers; and
- Isotopic and isotonic trends in alpha-decay half-lives.

### 5.7 Summary of Model Comparison

| Model | Main Concept | Key Quantities | Level of Microscopic Detail | Predictive Power |
|---|---|---|---|---|
| Gamow (1928) | Quantum tunneling through Coulomb barrier | P,λ, $T_{1/2}$ | Phenomenological | Moderate |
| RGM | Cluster wavefunction + antisymmetry | $P_0$,$V_{(r)}$ | Microscopic | High |
| DCM | Dynamical preformation and tunneling | $P_0$, P,$v_0$ | Semi-microscopic | Very High |
| DDM3Y | Density-dependent folding potential | $V_{DDM3Y}$ (R) | Semi-microscopic | Excellent |
| RMF / DFT | Self-consistent nuclear structure | $\rho$ (r), $E_{bind}$ | Fundamental | Excellent |

### 5.8 Concluding Remarks

The progression from Gamow's simple quantum model to density-based and relativistic frameworks demonstrates the **evolution of nuclear theory** from empirical observation to first-principles prediction. Modern microscopic models not only reproduce experimental half-lives with remarkable accuracy but also offer insight into **cluster preformation, shell effects**, and **isotonic trends** in alpha decay.

## References


Bender, M. H.-G. (2003). Self-consistent mean-field models. *Reviews of Modern Physics* , 121-180.

Buck, B. M. (1992). New look at alpha decay. *Physical Review Letters* , 2975-2978.

Condon, E. G. (1928). Wave mechanics and radioactive disintegration . *Nature* , 122, 439.

G, G. (1928). Zur Quantentheorie des Atomzerfalls. Zeitschrift für Physik. *Zeitschrift für Physik* , 204-212.

Geiger H, N. J. (1911). The ranges of the alfa particles. *Philosophical Magazine* , 613-622.

Heyde, K. (2004). *Basic ideas and concepts in nuclear physics(3rd ed.).* CRC Press.

Horiuchi, H. (1977). The resonating group method. *Progress of Theoretical Physics Supplement 62* , 1-80.

Khoa D T, V. O. (1996). Nuclear mean-field potentials. *Physics Letters B (342)* , 6-12.

Khoa, D. T. (1994). Complex density dependent M3Y interaction. *Physical Review C 49(4)* , 1652- 1664.

Kobos, A. M. (1982). Realistic nuclear potentials. *Nuclear Physics A 384(1)* , 65-78.

Krane, K. (1988). *Nuclear Physics.* Wiley.

Landau. (1977). Pergamon Press.

Landau, L. (1977). *Quantum mechanics: Non-relativistic theory.* Pergamon Press.

Lovas, R. G. (1998). Microscopic theory of cluster radioactivity. *Physics Reports 294(5)* , 265-362.

Meng, J. T.-G.-Q.-H.-S. (2006). RCHB theory. *Progress in Particle and Nuclear Physics 57(2)* , 470-563.

Merzbacher, E. (1998). *Quantum Mechanics (3 rd ed).* Wiley.

P, R. (1996). Relativistic mean-field theory in finite nuclei. *Progress in Particle and Nuclear Physics (37)* , 193-263.

Poenaru, D. N. (1996). *Nuclear decay modes.* Institute of physics publishing.

Qi, C. Z. (2009). Microscopic mechanism. *Physical review letters (103)7* , 072501.

R.K, G. (2000). Cluster radioactivity and the preformed cluster model. *Journal of Physics G 26(5)* , 23-30.

Satchler G R, L. W. (1979). Folding model potentials. *Physics Reports 55(3)* , 183-254.

T, K. D. (2001). Folding Model Study. *Nuclear Physics A 693(1-2)* , 113-138.

U, A. (2010). Nuclear Physics.

Vretenar, D. A. (2005). Relativistic H-B theory. *Physics Reports 409(3)* , 101-259.

Wong, S. S. (2004). *Introductory nuclear physics (2nd ed.).* Wiley-VHC.

Xu, C. R. (2006). Systematics of alfa decay half lives. *Physical Review C (74)* , 014304.

# CHAPTER 2

# Nuclear Waste Disposal and Management

F. Aysun Uğur[1] & Elif Gören[2]

[1] Prof. Dr., Osmaniye Korkut Ata University, ORCID:0000-0003-4134-6799
[2] Osmaniye Korkut Ata University

## 1. Introduction

The generation of radioactive waste is an inherent aspect of nuclear technology, including nuclear power production, medical and industrial applications, research activities, and military programs. As the use of nuclear energy and radioactive materials continues to expand worldwide, the safe and sustainable management of radioactive waste has become a critical environmental, technical, and societal concern (IAEA, 2016; NEA, 2016).

Radioactive waste is distinguished by its long-term radiotoxicity, persistence, and potential environmental and health risks, necessitating specialized treatment, storage, and disposal strategies. The complexity of nuclear waste management arises not only from the diversity of waste types—ranging from low-level waste (LLW) to high-level waste (HLW)—but also from the long timescales over which radioactive materials remain hazardous, sometimes extending thousands of years (IAEA, 2018).

This chapter provides a comprehensive overview of nuclear waste management, exploring the classification, sources, treatment, storage, transportation, and disposal of radioactive waste. It also examines international regulations, safety standards, ethical and environmental considerations, as well as emerging technologies and future trends in the field. Special attention is given to Turkey's nuclear waste management program, highlighting regulatory frameworks, interim storage strategies, and plans for long-term disposal (Jianquan Liu, 2019).

By integrating technical, regulatory, environmental, and ethical perspectives, this chapter aims to provide a holistic understanding of nuclear waste management, emphasizing the importance of long-term safety, public trust, and intergenerational responsibility. The insights presented here are intended to support policymakers, engineers, researchers, and students in developing and implementing safe, sustainable, and socially responsible nuclear waste management practices (Hyatt, 2018).

## 2. Classification of Nuclear Wastes

The classification of nuclear waste is a fundamental component of radioactive waste management because it determines the appropriate handling, treatment, storage, and disposal strategies for each type of waste. Classification systems vary slightly among international organizations and national regulatory bodies, but most are based on three key parameters: radioactivity level, half-life of radionuclides, and thermal output (NEA, 2017).

### 2.1 Low-Level Waste (LLW)

Low-Level Waste includes materials that have relatively small amounts of radioactivity and usually require minimal shielding during handling and transportation. LLW typically originates from the routine operations of nuclear power plants, hospitals, research laboratories, and industrial facilities. Examples include contaminated clothing, paper, cleaning materials, filters, and tools. The disposal of LLW is commonly performed in near-surface engineered facilities, such as concrete-lined trenches or vaults. These wastes generally decay to background radiation levels within a few hundred years, making long-term geological isolation unnecessary (Nikunj Khelurkar, 2015).

### 2.2 Intermediate-Level Waste (ILW)

Intermediate-Level Waste contains higher concentrations of radionuclides than LLW and often requires shielding, but not active cooling. It may include resins, sludges, reactor components, and metal cladding from fuel assemblies. Because of its intermediate activity, ILW is typically solidified in concrete or bitumen before being placed in engineered storage facilities, sometimes several tens of meters below the surface. The long-lived radionuclides present in ILW demand controlled disposal conditions that prevent environmental contamination for thousands of years (Freiesleben, 2013).

### 2.3 High-Level Waste (HLW)

High-Level Waste is the most hazardous category due to its extremely high radioactivity and heat generation. It mainly arises from the spent nuclear fuel (SNF) removed from reactors and the waste products of fuel reprocessing. HLW emits intense radiation and must be cooled and shielded during handling and storage.

The management of HLW involves multiple stages, including interim storage in water-filled pools or dry casks, followed by final disposal in deep geological repositories (DGRs). HLW remains radioactive for tens of thousands of years, necessitating isolation in stable geological formations such as granite, clay, or salt beds (Droste, 2015).

### 2.4 Very Low-Level Waste (VLLW) and Exempt Waste

Some national frameworks, including those of the European Union and IAEA, also recognize Very Low-Level Waste (VLLW) and Exempt Waste (EW) categories. VLLW includes materials with negligible levels of radioactivity, such as lightly contaminated soils or construction debris. Such wastes can often be disposed of in conventional landfills with minimal restrictions (M K Sneve, 2020).

Exempt Waste refers to materials whose radioactivity is so low that they are exempt from regulatory control under specific conditions. Their disposal poses no significant radiological risk to the public or the environment (Lits, 2020).

### 2.5 Classification Criteria

The International Atomic Energy Agency (IAEA) defines radioactive waste classes using measurable quantities, such as:

- Activity concentration (Bq/g)
- Total activity per package or volume
- Heat generation rate ($W/m^3$)
- Half-life and radionuclide inventory

These parameters help determine whether a waste stream should be managed as LLW, ILW, or HLW, ensuring that each is treated according to its potential hazard and longevity (IAEA, 2016).

## 3. Sources of Nuclear Waste

Radioactive waste originates from a variety of human activities involving the use of radioactive materials and nuclear technology. Understanding the sources of nuclear waste is essential for developing appropriate management and disposal strategies. The principal contributors include nuclear power generation, fuel cycle processes, medical and industrial applications, research and education, and military and defense programs (Hosan, 2017).

### 3.1 Nuclear Power Generation

The largest and most significant source of radioactive waste is commercial nuclear power production. During the operation of nuclear reactors, uranium or plutonium fuel undergoes fission, producing highly radioactive fission products and transuranic elements (Nikunj Khelurkar, A Review of Radioactive Waste Management, 2015).

After several years of use in a reactor core, fuel assemblies lose their efficiency and are removed as spent nuclear fuel (SNF), which constitutes high-level waste (HLW). In addition, reactor operation generates low-level waste (LLW) and intermediate-level waste (ILW) from contaminated equipment, filters, resins, and structural components exposed to neutron radiation (Katarzyna Kiegiel, 2025).

### 3.2 Nuclear Fuel Cycle Activities

Nuclear waste is produced throughout the entire nuclear fuel cycle, from uranium mining to reprocessing and decommissioning:

- Uranium Mining and Milling: Generates large quantities of tailings containing residual radioactivity and heavy metals.
- Fuel Fabrication: Produces contaminated scrap materials, filters, and chemical waste from enrichment and fuel pellet production.
- Fuel Reprocessing: Results in significant quantities of liquid and solid high-level waste containing fission products and actinides.
- Decommissioning of Facilities: When nuclear reactors or fuel cycle facilities reach the end of their operational life, dismantling and decontamination produce large amounts of LLW and ILW, such as concrete, steel, and piping materials (Cochran, 2013).

### 3.3 Medical and Industrial Applications

The use of radionuclides in medicine for diagnosis and therapy also generates low- and intermediate-level radioactive waste. Hospitals, clinics, and research institutions employ isotopes such as technetium-99m, iodine-131, and cobalt-60 for imaging and cancer treatment (Filipe Boccato Payolla, 2019).

Similarly, industrial applications, including radiography, food irradiation, and instrument calibration, yield small but widespread quantities of LLW. These wastes often consist of contaminated syringes, gloves, vials, and sealed sources requiring secure disposal (Hossein Ahari Mostafavi, 2012).

### 3.4 Research and Educational Institutions

Research reactors, universities, and laboratories that handle radioactive isotopes contribute a smaller but important fraction of the overall waste inventory.

Materials such as used experimental targets, irradiated samples, and contaminated lab equipment are categorized as LLW or ILW. Although volumes are typically modest, the diversity of isotopes and variable activity levels demand strict handling and regulatory oversight (J. G. Marques, 2012).

### 3.5 Military and Defense Activities

Historically, nuclear weapons production and military research programs have produced substantial amounts of radioactive waste. Activities such as plutonium and uranium enrichment, nuclear testing, and weapons dismantlement have generated both high-level and transuranic wastes.

In several countries, these legacy wastes remain a major environmental challenge, requiring long-term remediation of contaminated sites (Dean Kyne, 2016).

### 3.6 Consumer Products and Miscellaneous Sources

Small quantities of radioactive waste can also originate from consumer products containing minute amounts of radioactive material—such as smoke detectors (americium-241), luminous watches (tritium), and certain industrial gauges. Although individually low in activity, the cumulative effect of such products necessitates controlled disposal pathways to prevent environmental contamination (Nikunj Khelurkar, A Review of Radioactive Waste Management, 2015).

The generation of radioactive waste from such diverse sources underscores the complexity of establishing comprehensive management systems. Effective regulation must therefore consider not only the volume and activity of waste but also its chemical composition, form, and potential for environmental release (IAEA, Predisposal management of radioactive waste , 2018) .

## 4. Principles of Nuclear Waste Management

The management of nuclear waste is guided by a set of fundamental principles designed to ensure the protection of human health, the environment, and future generations. These principles are articulated in international frameworks such as those of the International Atomic Energy Agency (IAEA), the OECD Nuclear Energy Agency (NEA), and the European Commission (Cochran, 2013)

Effective waste management requires integrating scientific, technical, regulatory, and ethical considerations into a coherent system that governs all stages of waste generation, treatment, storage, transportation, and disposal.

### 4.1 The Principle of Safety and Protection

The foremost objective of nuclear waste management is to protect human beings and the environment from harmful effects of ionizing radiation.

This includes limiting exposure levels during all phases of waste handling and ensuring that releases of radionuclides remain below internationally accepted limits. The IAEA (2018) defines safety as the achievement of proper operating conditions and the prevention of accidents or mitigation of their consequences, thereby reducing risks to people and the environment (IAEA, Deep geological disposal of radioactive waste, 2009).

### 4.2 The ALARA Principle (As Low As Reasonably Achievable)

The ALARA principle is a cornerstone of radiation protection. It requires that all radiation exposures be kept *as low as reasonably achievable*, taking into account economic and social factors.

This principle is applied to the design and operation of facilities, emphasizing optimization of shielding, containment, and waste minimization. For instance, during the treatment and conditioning of radioactive materials, process efficiency is balanced against safety and cost to maintain low radiation doses for workers and the public (IAEA, Deep geological disposal of radioactive waste, 2009).

### 4.3 The Principle of Long-Term Sustainability

Since radioactive waste can remain hazardous for thousands of years, management strategies must ensure long-term containment and isolation.

The multi-barrier concept, combining engineered and natural barriers (e.g., waste form, container, backfill, and geological formations), is implemented to prevent the migration of radionuclides into the biosphere. Long-term safety assessments evaluate the performance of these barriers under diverse geological and climatic conditions to guarantee sustainability over geological timescales (IAEA, Predisposal management of radioactive waste , 2018).

### 4.4 The Polluter Pays Principle

An important economic and ethical guideline is the polluter pays principle, which asserts that the entities responsible for generating radioactive waste must also bear the financial burden of its management and disposal.

This principle ensures accountability and prevents the transfer of financial responsibility to future generations or the public sector. Many national nuclear regulatory frameworks require that nuclear facility operators maintain dedicated financial reserves or funds to cover decommissioning and waste disposal costs (IAEA, Management of radioactive waste, 2016).

### 4.5 The Principle of Transparency and Public Involvement

Public confidence is crucial for the success of nuclear waste management programs.

Transparency involves providing accurate, accessible, and timely information regarding waste management activities, risks, and safety measures. Engaging local communities, stakeholders, and non-governmental organizations (NGOs) in decision-making fosters trust and social acceptance—especially for projects such as geological repositories, which often face public resistance (IAEA, The safety of nuclear fuel cycle facilities, 2019).

### 4.6 The Principle of Stepwise Decision-Making

The stepwise or adaptive approach to decision-making allows for gradual progress in nuclear waste management while incorporating new scientific data and technological developments.

Rather than pursuing irreversible solutions prematurely, decisions are made incrementally—each stage informed by safety assessments, public input, and regulatory review. This adaptive strategy enhances flexibility and resilience in long-term planning (Hyatt, 2018).

### 4.7 Intergenerational Responsibility

A defining ethical dimension of radioactive waste management is intergenerational equity—the obligation to prevent undue burdens on future generations.

Because high-level wastes remain hazardous over geological timeframes, current societies must ensure that disposal systems are safe without requiring continuous human intervention.

The IAEA (2019) emphasizes that responsibility for nuclear waste does not end with its emplacement but extends to maintaining institutional control and preserving knowledge for future oversight (IAEA, Deep geological disposal of radioactive waste, 2009).

### 4.8 Regulatory and Institutional Control

Finally, effective nuclear waste management depends on robust regulatory and institutional frameworks.

Governments must establish independent authorities to oversee compliance with safety standards, licensing, and inspection procedures. Clear delineation of responsibilities between operators, regulators, and policymakers helps avoid conflicts of interest and enhances accountability throughout the waste management lifecycle (Gabriele Mraz, 2019).

In summary, the principles of nuclear waste management provide the ethical, technical, and legal foundation upon which all practical activities are built. Adherence to these principles ensures that radioactive waste is handled in a manner that safeguards people, preserves the environment, and upholds public trust in the long-term sustainability of nuclear energy.

## 5. Treatment and Conditioning of Radioactive Waste

The treatment and conditioning of radioactive waste represent essential stages in the nuclear waste management process, aiming to reduce waste volume,

stabilize radionuclides, and prepare waste for safe storage and final disposal. These operations ensure that the waste is transformed into a form suitable for handling, transport, and long-term isolation from the biosphere. According to the International Atomic Energy Agency (IAEA, 2018), treatment and conditioning are guided by the fundamental objectives of safety, minimization of environmental impact, and optimization of cost-effectiveness (IAEA, The safety of nuclear fuel cycle facilities, 2019).

### 5.1 Objectives of Waste Treatment and Conditioning

The overarching goal of treatment and conditioning is to minimize the potential hazards associated with radioactive waste. Specific objectives include:

- Reducing the volume of waste to lower storage and disposal requirements.
- Concentrating radionuclides into smaller volumes for easier containment.
- Stabilizing waste physically and chemically to prevent the release of radioactive materials.
- Ensuring that the conditioned waste form meets regulatory acceptance criteria for transport and disposal.

Treatment focuses on modifying waste characteristics, while conditioning provides the waste with a final, stable physical form (V. Valdovinos, 2014).

### 5.2 Waste Treatment Techniques

Radioactive waste treatment processes depend on the waste's physical state (solid, liquid, or gaseous) and radiological characteristics. The main treatment methods include volume reduction, decontamination, and separation of radionuclides.

#### 5.2.1 Mechanical and Physical Processes

Mechanical techniques are primarily used for solid waste. These include compaction, shredding, and incineration, which significantly reduce waste volume.

- Compaction is effective for compressible materials such as paper, plastics, and clothing, often reducing volume by up to 90%.
- Incineration is used for combustible materials, converting them into ash and gases; the ash is later solidified for disposal.

- Melting and pressing may also be used for metallic waste to homogenize materials and reduce surface contamination.

### 5.2.2 Chemical and Ion-Exchange Processes

Chemical methods are often applied to liquid wastes. Precipitation, flocculation, and ion exchange are used to remove radionuclides from solutions.

- Ion exchange resins selectively capture radioactive ions, which are later solidified.
- Evaporation concentrates liquid waste by removing water, leaving behind a smaller, highly radioactive residue.
- Chemical oxidation and reduction processes can change the chemical state of radionuclides, facilitating separation or immobilization.

### 5.2.3 Biological and Advanced Processes

In recent years, biotechnological methods have gained attention for treating low-level radioactive effluents. Certain microorganisms can absorb or precipitate radionuclides, contributing to eco-friendly waste management.

Additionally, membrane filtration, plasma treatment, and supercritical fluid extraction are emerging technologies offering higher efficiency in waste minimization.

## 5.3 Waste Conditioning Techniques

After treatment, radioactive waste must be conditioned to produce a stable, solid form suitable for storage or disposal. Conditioning involves immobilizing radioactive materials within a durable matrix and placing them into containers that meet long-term safety requirements.

### 5.3.1 Solidification

Solidification converts liquid or slurry waste into a stable solid form. Common solidification agents include:

- Cementation, where waste is mixed with cement and additives to produce a monolithic block resistant to leaching.
- Bituminization, which embeds waste in bitumen, providing waterproofing and flexibility.
- Vitrification, the most advanced method for high-level waste, melts waste with glass-forming materials at high temperatures to create a durable, glass-like matrix that immobilizes radionuclides for thousands of years.

### 5.3.2 Encapsulation

Encapsulation involves enclosing conditioned waste in robust containers, typically made of steel, lead, or reinforced concrete. This provides mechanical strength, radiation shielding, and containment integrity.

Encapsulated waste packages are labeled and stored in engineered facilities pending final disposal.

### 5.3.3 Packaging and Quality Assurance

Conditioned waste must comply with strict quality assurance and regulatory standards. Packaging ensures compatibility with handling systems, transport requirements, and repository acceptance criteria. The IAEA (2016) emphasizes that traceability and record-keeping are critical for long-term safety verification.

### 5.4 Integrated Waste Processing Systems

Modern nuclear facilities employ integrated waste management systems that combine multiple treatment and conditioning steps in a continuous or semi-continuous process. Such systems reduce manual handling, optimize radiation protection, and allow real-time monitoring of waste parameters. Automation, remote handling, and robotics are increasingly applied in high-radiation environments to minimize worker exposure.

### 5.5 Environmental and Safety Considerations

All treatment and conditioning processes must comply with international safety standards and environmental regulations. Secondary wastes (such as off-gases, residues, and contaminated tools) generated during processing must also be properly collected and treated.

Life-cycle assessments help identify the most sustainable options by evaluating the total environmental footprint of each method.

In summary, the treatment and conditioning of radioactive waste are vital to achieving safe and sustainable nuclear waste management. Through a combination of physical, chemical, and technological approaches, radioactive materials can be stabilized, immobilized, and prepared for long-term containment, ensuring that their risks to humans and the environment remain acceptably low for future generations ( Radioactive waste management, 2023).

## 6. Interim Storage and Transportation

Interim storage and transportation are critical stages in the nuclear waste management process, bridging the gap between waste generation and final disposal. Proper management at these stages ensures radiation protection,

environmental safety, and structural integrity of waste packages while providing flexibility for the development of long-term disposal solutions.

### 6.1 Interim Storage of Radioactive Waste

Interim storage provides a temporary, controlled environment for radioactive waste until it can be safely moved to a final disposal facility. It is particularly important for high-level waste (HLW) and spent nuclear fuel (SNF), which require cooling and shielding due to their intense radioactivity and heat generation.

#### 6.1.1 Wet Storage

The most common method for storing spent nuclear fuel in the short term is wet storage, typically in water-filled pools. Water acts as both a coolant and a radiation shield, absorbing heat and gamma radiation. Pools are designed with multiple safety barriers, including corrosion-resistant liners, cooling systems, and continuous radiation monitoring.

Wet storage is generally used for 5–10 years, allowing the decay of short-lived radionuclides and reducing heat and radiation before moving to dry storage or final disposal.

#### 6.1.2 Dry Storage

After sufficient cooling in wet storage, SNF or conditioned high-level waste can be transferred to dry cask storage systems. These systems involve placing the waste in sealed, robust containers, often made of steel or concrete, which provide structural integrity, radiation shielding, and passive heat dissipation. Dry storage is advantageous for its modularity, passive safety, and long-term stability, typically allowing safe storage for several decades.

#### 6.1.3 Storage of Low- and Intermediate-Level Waste

Low-level waste (LLW) and intermediate-level waste (ILW) may be stored in engineered surface or near-surface facilities, depending on their activity levels. These facilities are designed to prevent leakage, allow monitoring, and facilitate eventual transfer to disposal sites. Vaults, silos, and bunkers are commonly employed to isolate ILW, while LLW may be stored in trenches or modular concrete structures.

### 6.2 Transportation of Radioactive Waste

Transportation is a vital component of nuclear waste management, connecting generation sites, interim storage, and final disposal locations. It must ensure the protection of workers, the public, and the environment, adhering to stringent international and national regulations.

### 6.2.1 Packaging and Containment

Radioactive materials are transported in certified casks or containers designed to withstand accidents, mechanical stress, and environmental extremes. Key design features include:

- Structural strength to resist impact, puncture, and compression.
- Radiation shielding to protect handlers and the public.
- Thermal management to dissipate heat from HLW or SNF.
- Leak-tight seals to prevent the release of radioactive materials.

The IAEA classifies transportation packages according to the activity level and heat generation of the waste, ranging from Type A (for low-activity materials) to Type B (for high-activity, high-heat materials).

### 6.2.2 Transportation Modes

Radioactive waste may be transported via road, rail, sea, or air, depending on distance, infrastructure, and regulatory approval.

- Road transport uses specialized trucks and trailers, often accompanied by escort vehicles and security measures.
- Rail transport is suitable for bulk or heavy casks, offering stability and reduced accident risk.
- Sea transport is used for international shipments, requiring reinforced containers and compliance with maritime regulations.
- Air transport is rare and typically reserved for small quantities of high-value isotopes or emergency transfers.

### 6.2.3 Safety and Regulatory Compliance

Transportation is strictly governed by international conventions (e.g., IAEA Safety Standards, ADR, IMDG Code) and national laws. Requirements include package certification, route planning, emergency preparedness, personnel training, and real-time monitoring of radioactive shipments. Regular inspections, maintenance, and quality assurance ensure that containers remain safe throughout transit.

## 6.3 Security Considerations

In addition to radiological protection, the transportation and storage of radioactive waste must consider security threats, including theft, sabotage, or terrorist attacks. Measures include:

- Physical barriers and surveillance systems at storage and transport points.
- Tracking and real-time monitoring of shipments.
- Coordination with local and national security agencies.

In conclusion, interim storage and transportation are not merely logistical steps but integral parts of the nuclear waste management system. Proper design, operation, and regulatory compliance ensure that radioactive materials remain safely contained and isolated until their final disposal, protecting human health and the environment while maintaining public confidence in nuclear programs.

## 7. Final Disposal Methods

Final disposal represents the ultimate stage in nuclear waste management, aiming to isolate radioactive materials permanently from humans and the environment. While interim storage provides temporary containment, final disposal must ensure long-term safety, accounting for the hazardous nature of high-level waste (HLW) and long-lived intermediate-level waste (ILW). The choice of disposal method depends on waste type, radiological characteristics, heat generation, and local geological conditions.

### 7.1 Near-Surface Disposal

Near-surface disposal is generally used for low-level waste (LLW) and some short-lived intermediate-level waste (ILW). This approach involves placing waste in engineered facilities close to the Earth's surface, typically in trenches, vaults, or concrete bunkers.

Key features of near-surface disposal include:

- Multiple containment barriers (waste form, container, engineered backfill).
- Monitoring systems for radiation, groundwater, and environmental conditions.
- Controlled access to prevent inadvertent exposure.

Near-surface disposal is suitable for wastes whose radioactivity decays to safe levels within a few hundred years, eliminating the need for deep geological isolation.

### 7.2 Deep Geological Repositories (DGRs)

For high-level waste (HLW) and long-lived ILW, deep geological repositories are considered the most reliable method of final disposal. DGRs isolate waste

hundreds of meters below the surface in stable rock formations such as granite, clay, or salt.

The deep geological approach relies on a multi-barrier system:

1. Waste form barrier (vitrified HLW or immobilized ILW).
2. Canister or container barrier (corrosion-resistant steel or copper).
3. Buffer and backfill materials (bentonite clay or cement).
4. Geological barrier (natural rock formation providing long-term isolation).

Extensive safety assessments, including modeling of radionuclide migration, groundwater flow, and seismic activity, ensure repository stability for tens of thousands of years. Countries such as Finland, Sweden, and France are developing operational or near-operational DGRs as part of their long-term waste management strategies ((NRC), 2015) .

### 7.3 Transmutation and Advanced Disposal Concepts

Transmutation involves converting long-lived radionuclides into shorter-lived or stable isotopes using nuclear reactions, typically in fast reactors or accelerator-driven systems. While still largely experimental, transmutation can reduce the radiotoxicity and heat load of high-level waste, potentially simplifying disposal requirements.

Other emerging disposal concepts include deep borehole disposal, where waste is placed in boreholes several kilometers deep, and sub-seabed disposal, although these approaches face technical, environmental, and regulatory challenges.

### 7.4 Reprocessing and Recycling

Although not a disposal method per se, reprocessing and recycling of spent nuclear fuel can reduce the volume of HLW. In reprocessing, uranium and plutonium are chemically separated for reuse as reactor fuel, while the remaining high-level fission products are conditioned for final disposal. Recycling strategies must balance economic feasibility, proliferation risk, and long-term safety considerations.

### 7.5 Criteria for Disposal Site Selection

The selection of a final disposal site is governed by geological, environmental, technical, and social criteria:

- Geological stability: low seismicity, impermeable rock, absence of groundwater flow pathways.

- Isolation capability: natural barriers that prevent radionuclide migration.
- Engineering feasibility: ability to construct and maintain disposal facilities safely.
- Societal acceptance: stakeholder engagement and public confidence in safety measures.

Regulatory agencies conduct extensive site characterization, risk assessments, and environmental impact studies to ensure that repositories meet long-term safety objectives (IAEA, Deep geological disposal of radioactive waste, 2009).

### 7.6 Monitoring and Institutional Control

Even after emplacement, final disposal sites require monitoring and institutional control. This includes:

- Radiation and environmental monitoring.
- Maintenance of access restrictions.
- Record-keeping to ensure that future generations can locate and understand the repository.

Long-term stewardship ensures that the disposal system remains effective, even if human institutions or knowledge change over centuries or millennia.

In summary, final disposal methods represent the cornerstone of a safe and sustainable nuclear waste management strategy. While near-surface disposal suffices for low-activity materials, high-level and long-lived wastes demand deep geological isolation, supported by engineered barriers, advanced treatment, and ongoing monitoring. Emerging technologies such as transmutation and deep boreholes may further enhance safety and reduce radiotoxicity in the future.

## 8. International Regulations and Safety Standards

The management of radioactive waste is governed not only by national legislation but also by a robust framework of international regulations and safety standards. These standards aim to ensure the protection of human health, the environment, and future generations, while promoting consistency and best practices across countries. Adherence to international regulations is essential for transport, storage, and disposal of nuclear waste, particularly in the context of cross-border shipments and multinational projects.

### 8.1 Role of the International Atomic Energy Agency (IAEA)

The International Atomic Energy Agency (IAEA) serves as the primary global authority for nuclear safety and waste management. Its Safety Standards Series

provides comprehensive guidance on all aspects of radioactive waste handling, including:

- Classification of waste types
- Treatment, conditioning, and storage requirements
- Design and operation of disposal facilities
- Transport regulations
- Environmental protection and monitoring

IAEA standards are considered recommendatory but influential, forming the basis for national regulations and guiding the development of legal frameworks. Member states are encouraged to adopt these standards to achieve international harmonization.

### 8.2 Key International Safety Guidelines

Several key documents and recommendations govern the safe management of nuclear waste:

- IAEA Safety Fundamentals: Establish the fundamental safety principles for protecting people and the environment.
- IAEA Safety Requirements (e.g., SSR-5): Provide mandatory requirements for the predisposal management of radioactive waste, storage, and disposal.
- IAEA Safety Guides: Offer detailed technical guidance on specific practices, such as facility design, radiological monitoring, and waste characterization.

Other organizations also contribute to international safety standards, including:

- OECD Nuclear Energy Agency (NEA): Develops best practices, facilitates collaboration among member states, and promotes research on repository safety.
- World Nuclear Association (WNA): Provides guidance for industry stakeholders on operational and regulatory compliance.

### 8.3 International Transport Regulations

The transportation of radioactive materials across borders is subject to rigorous international standards:

- IAEA Transport Regulations (SSR-6): Define packaging, labeling, handling, and documentation requirements for all categories of radioactive material.
- ADR (European Agreement on the Transport of Dangerous Goods by Road) and IMDG Code (International Maritime Dangerous Goods Code): Adopt IAEA principles and provide legally binding requirements for road and sea transport, respectively.
- Air Transport: ICAO (International Civil Aviation Organization) regulates air shipment of radioactive materials based on IAEA recommendations.

These regulations ensure that radioactive materials are transported safely, minimizing the risk of accidents or environmental contamination.

### 8.4 National Implementation and Compliance

While international standards provide guidance, individual countries implement national regulatory frameworks tailored to local conditions, geological settings, and social considerations. Key national agencies include:

- United States Nuclear Regulatory Commission (NRC)
- UK Office for Nuclear Regulation (ONR)
- French Nuclear Safety Authority (ASN)
- Turkish Atomic Energy Authority (TAEK)

National authorities are responsible for licensing, inspections, compliance monitoring, and enforcement of waste management practices in alignment with international guidance.

### 8.5 Safety Assessment and Performance Evaluation

A central principle of international regulation is the requirement for safety assessment and performance evaluation. Waste management facilities, particularly final disposal sites, must demonstrate long-term safety through:

- Predictive modeling of radionuclide migration
- Assessment of engineered and natural barrier performance
- Scenario analysis for natural events (earthquakes, floods) and human intrusion
- Environmental impact assessment

These assessments are reviewed by regulatory bodies to ensure that the facility design and operational plan meet or exceed safety requirements.

### 8.6 Harmonization and Global Cooperation

International collaboration is crucial for sharing knowledge, technology, and best practices. Multilateral initiatives include:

- IAEA Technical Cooperation Programs: Support developing countries in establishing safe waste management practices.
- NEA Working Groups: Facilitate exchange of safety data, repository design experiences, and research outcomes.
- Joint Projects: Collaborative ventures, such as multinational deep geological repository research, advance scientific understanding and harmonization of standards.

In summary, international regulations and safety standards provide the backbone for safe, consistent, and sustainable nuclear waste management. By adhering to IAEA principles, complying with transport regulations, and implementing rigorous safety assessments, countries can ensure the protection of public health, the environment, and future generations while fostering global cooperation and public confidence in nuclear energy programs (Cochran, 2013).

## 9. Nuclear Waste Management in Turkey

Turkey's nuclear energy program has been expanding in recent years, particularly with the construction of the Akkuyu Nuclear Power Plant (NPP) and the operation of research reactors. Effective nuclear waste management is essential to ensure that radioactive materials generated in the country are handled safely, in compliance with national regulations and international standards.

### 9.1 Regulatory Framework

The regulatory authority responsible for nuclear safety and radioactive waste management in Turkey is the Turkish Atomic Energy Authority (TAEK). TAEK oversees licensing, inspection, and enforcement of safety regulations across all nuclear facilities, including research reactors, industrial applications, and the newly established commercial nuclear power plants.

Turkey has also ratified several international treaties and conventions, including the IAEA Joint Convention on the Safety of Spent Fuel Management and on the Safety of Radioactive Waste Management, ensuring alignment with global standards.

### 9.2 Sources of Radioactive Waste in Turkey

The main sources of radioactive waste in Turkey include:

1. Research reactors: Turkey operates research reactors, which generate low- and intermediate-level waste from fuel, experimental targets, and decommissioning activities.

2. Medical and industrial facilities: Hospitals and laboratories generate low-level radioactive waste from the use of isotopes such as technetium-99m, iodine-131, and cobalt-60.

3. Nuclear power plants: With the commissioning of the Akkuyu NPP, Turkey will produce high-level waste (HLW), primarily spent fuel, and intermediate-level waste from operational and maintenance activities.

### 9.3 Current Waste Management Practices

Turkey has developed a centralized approach to collect, treat, and store radioactive waste:

- Low- and intermediate-level waste: Managed through on-site storage facilities at reactors and industrial sites, followed by transfer to centralized storage facilities.
- High-level waste and spent fuel: Interim storage plans are being developed, including wet and dry storage systems, in line with IAEA recommendations.
- Waste treatment techniques, such as cementation and solidification, are employed to condition LLW and ILW prior to storage.

### 9.4 Interim Storage Facilities

Turkey currently operates centralized interim storage facilities designed to accommodate waste from research reactors and medical applications. These facilities implement:

- Radiation shielding and containment for safe handling
- Monitoring systems to track radiation levels and environmental parameters
- Segregation of waste types based on activity and half-life

For high-level waste generated by commercial reactors, dedicated interim storage solutions will be implemented as part of Akkuyu NPP's nuclear waste management plan, consistent with international safety standards.

### 9.5 National Plans for Final Disposal

Although Turkey does not yet have an operational deep geological repository, long-term planning includes:

- Site selection studies for geological disposal of high-level and long-lived intermediate-level waste
- Assessment of geological, hydrological, and seismic conditions for repository safety
- Development of a national radioactive waste management strategy that integrates treatment, interim storage, and eventual disposal

Turkey's plans follow the principle of intergenerational responsibility, ensuring that radioactive waste is isolated and managed safely for future generations (TENMAK, 2020).

### 9.6 International Cooperation

Turkey actively engages in international collaborations to strengthen its nuclear waste management capabilities:

- Participation in IAEA technical cooperation programs for facility design, safety assessment, and regulatory capacity building
- Collaboration with countries experienced in deep geological repositories, such as Finland and France, to exchange expertise on long-term disposal strategies
- Compliance with international transport regulations to ensure safe movement of radioactive materials

In summary, Turkey's nuclear waste management framework is developing in line with international best practices. Centralized interim storage, regulatory oversight by TAEK, and planning for long-term disposal ensure that radioactive waste is managed safely, protecting both the environment and public health while supporting the growth of the country's nuclear energy program.

## 10. Environmental and Ethical Considerations

The management of nuclear waste extends beyond technical and regulatory measures to encompass environmental protection and ethical responsibility. Given the long-lived nature of high-level waste (HLW) and intermediate-level waste (ILW), decisions made today have implications for future generations, the ecosystem, and societal trust. Understanding these dimensions is essential for sustainable nuclear waste management (Chapman, 2017) .

### 10.1 Environmental Impact

Radioactive waste has the potential to impact ecosystems if not properly managed. Key environmental concerns include:

- Groundwater contamination: Improper storage or disposal can allow radionuclides to leach into soil and water, affecting human and ecological health.
- Surface contamination: Spills, accidents, or facility breaches can contaminate surrounding land, plants, and animals.
- Atmospheric releases: Although controlled, gaseous radioactive emissions from treatment or storage processes may pose environmental risks if containment fails.

To mitigate these risks, waste management facilities implement multiple engineered barriers, including sealed containers, concrete vaults, and backfill materials, complemented by long-term monitoring. Additionally, environmental impact assessments (EIAs) are conducted before construction or expansion of disposal facilities, ensuring that ecological effects are minimized and regulatory standards are met.

### 10.2 Ethical Considerations

Ethical considerations in nuclear waste management revolve around intergenerational justice, societal responsibility, and informed consent:

- Intergenerational responsibility: Radioactive waste remains hazardous for thousands of years. Current generations have a moral obligation to prevent undue burden on future generations by providing secure disposal and maintaining records of waste locations.
- Equity and justice: Waste disposal sites are often located in less-populated areas, raising questions of environmental justice. Ethical management requires fair distribution of risks and benefits across communities.
- Transparency and public engagement: Societal acceptance is critical. Ethical principles demand open communication, public consultation, and inclusion of stakeholders in decision-making processes.

### 10.3 Long-Term Stewardship

Long-term stewardship involves maintaining institutional control, records, and monitoring to ensure that radioactive waste remains contained and that future societies are aware of its location and hazards. This includes:

- Clear marking and documentation of disposal sites
- Establishment of regulatory frameworks for ongoing oversight
- Research into durable warning systems for deep geological repositories to communicate risk over millennia

### 10.4 Risk Perception and Social Acceptance

Public perception of nuclear waste risk significantly influences policy and management. Misinformation or lack of trust can lead to community resistance, delaying or preventing repository development. Ethical management therefore requires:

- Educational programs to explain waste characteristics, safety measures, and monitoring
- Engagement with local communities, respecting cultural, social, and environmental values
- Transparent reporting of incidents, safety assessments, and research findings

### 10.5 Sustainability and Ethical Decision-Making

Sustainability in nuclear waste management integrates environmental, social, and economic dimensions. Decisions about waste treatment, storage, and disposal must balance technical feasibility, long-term safety, and ethical responsibility, ensuring that the energy benefits of nuclear power do not compromise human health or environmental integrity for future generations.

In summary, environmental and ethical considerations are central to responsible nuclear waste management. Protecting ecosystems, ensuring intergenerational equity, maintaining public trust, and implementing long-term stewardship measures are as crucial as technical containment strategies in achieving a safe and sustainable nuclear energy program.

## 11. Future Trends and Emerging Technologies

The field of nuclear waste management continues to evolve as technological innovations, scientific research, and societal needs drive improvements in safety, efficiency, and sustainability. Future trends focus on reducing waste volume and toxicity, enhancing long-term containment, and developing advanced monitoring and treatment systems.

### 11.1 Advanced Reprocessing and Recycling

One of the most promising trends in nuclear waste management is the reprocessing and recycling of spent nuclear fuel. Modern reprocessing techniques aim to:

- Recover uranium and plutonium for reuse as fuel
- Separate long-lived actinides from fission products to reduce overall radiotoxicity

- Minimize the volume of high-level waste requiring final disposal

Technologies such as aqueous reprocessing (PUREX) and emerging pyroprocessing methods allow for more efficient recycling of nuclear fuel. By reducing the quantity and hazard of waste, these methods can significantly enhance the sustainability of nuclear energy programs.

### 11.2 Partitioning and Transmutation

Partitioning and transmutation (P&T) is an advanced technology designed to transform long-lived radionuclides into shorter-lived or stable isotopes.

- Partitioning separates specific actinides and fission products from the waste stream.
- Transmutation uses fast reactors or accelerator-driven systems to convert these radionuclides through nuclear reactions.

P&T has the potential to reduce the radiotoxicity and heat load of high-level waste, decreasing the demands on geological repositories and enhancing long-term safety.

### 11.3 Deep Borehole Disposal

Deep borehole disposal is an emerging concept for the long-term isolation of high-level waste. This method involves:

- Drilling boreholes 3–5 kilometers deep into stable crystalline rock formations
- Emplacing waste canisters in the lower sections of the borehole
- Sealing the borehole to prevent radionuclide migration

Deep boreholes offer significant advantages, including enhanced geological isolation and a smaller surface footprint compared to conventional deep geological repositories. Research and pilot studies are ongoing to assess technical feasibility and safety.

### 11.4 Enhanced Monitoring and Remote Technologies

Future nuclear waste management systems will increasingly rely on advanced monitoring, automation, and robotics:

- Remote handling and robotic systems reduce human exposure to radiation during treatment, transport, and repository operations
- Sensor networks and real-time monitoring enable continuous assessment of temperature, radiation levels, and structural integrity

- Data analytics and predictive modeling improve decision-making for long-term safety and operational efficiency

Such technologies enhance both the safety and reliability of waste management facilities, particularly in high-radiation environments.

### 11.5 Low- and Intermediate-Level Waste Innovations

Emerging methods for LLW and ILW focus on volume reduction, immobilization, and environmentally friendly treatment:

- Plasma arc treatment to reduce waste volume
- Supercritical fluid extraction to separate contaminants
- Bioremediation and microbial techniques to treat liquid effluents

These innovations aim to minimize environmental impact while maintaining cost-effectiveness and compliance with regulatory standards.

### 11.6 International Collaboration and Research

Global cooperation remains critical in advancing nuclear waste management technologies. Collaborative initiatives include:

- IAEA technical programs for knowledge transfer and capacity building
- OECD NEA research networks on repository design and waste transmutation
- Multinational projects exploring shared repositories and innovative disposal methods

Sharing scientific data, best practices, and technological breakthroughs helps countries optimize waste management strategies and accelerate safe adoption of emerging technologies.

In summary, the future of nuclear waste management is shaped by recycling, transmutation, advanced disposal methods, and digital monitoring technologies. These innovations aim to reduce hazards, extend repository life, enhance safety, and support sustainable nuclear energy production while addressing environmental and societal concerns (UNSCEAR, 2016).

## 12. Conclusion

Nuclear waste management is a complex, multi-faceted challenge that requires the integration of scientific, technical, regulatory, environmental, and ethical considerations. From generation to final disposal, radioactive waste poses risks that extend across temporal and spatial scales, necessitating meticulous planning and rigorous adherence to safety standards.

Throughout this chapter, the classification, sources, treatment, storage, transportation, and disposal of nuclear waste have been explored. Low-level and intermediate-level wastes are typically managed through near-surface storage and engineered containment, while high-level waste and spent nuclear fuel demand deep geological isolation supported by multi-barrier systems and long-term monitoring. Emerging technologies, including reprocessing, partitioning and transmutation, deep borehole disposal, and advanced monitoring systems, offer promising avenues for enhancing safety, reducing radiotoxicity, and promoting sustainability.

Ethical considerations, such as intergenerational responsibility, environmental justice, and public engagement, underscore the importance of societal participation and transparency in decision-making. International regulations and standards, particularly those of the IAEA and OECD NEA, provide a framework for harmonizing safety practices, guiding national policies, and ensuring that nuclear waste management adheres to the highest global standards.

In the context of Turkey, the development of nuclear power plants and research reactors highlights the growing need for robust national strategies, centralized interim storage, and plans for long-term disposal. By aligning with international best practices and integrating advanced technologies, Turkey is positioned to manage its radioactive waste safely, responsibly, and sustainably.

In conclusion, the safe management of nuclear waste is not solely a technical challenge but a long-term societal commitment. It requires continuous innovation, vigilant oversight, and responsible stewardship to protect human health, preserve the environment, and maintain public confidence in the benefits of nuclear energy. By adopting a comprehensive and forward-looking approach, nations can ensure that the risks associated with radioactive waste are minimized for present and future generations.

## References


Radioactive waste management. (2023, October 1). October 21, 2025 tarihinde World Nuclear Association: www.world- nuclear.org/information-library/nuclear-fuel-cycle/nuclear-wastes-management.aspx adresinden alındı

(NRC), N. R. (2015). Low-level radioactive waste management. Washington, D.C. USA: NRC.

Chapman, N. &. (2017). Geological disposal of radioactive waste. A guide to international practice , 29-48.

Cochran, J. e. (2013). Nuclear waste: Management, treatment and disposal. Nuclear waste , 65-89.

Dean Kyne, B. B. (2016). Emerging Environmental Justice Issues in Nuclear Power and Radioactive Contamination. International Journal of Environmental Research and Public Health , 2-19.

Droste, B. (2015). Packaging, transport, and storage. K. B. Sorenson içinde, Woodhead Publishing Series in Energy: Safe and Secure Transport (s. 231-270). Berlin, Germany: ELSEVIER.

Filipe Boccato Payolla, A. C. (2019). Radiopharmaceuticals for diagnosis in nuclear medicine: a short review . Ecletica Quımica Journal , 11-20.

Freiesleben, H. (2013). Final disposal of radioactive waste. Dresden, Germany: EDP Sciences.

Gabriele Mraz, P. L. (2019). Implementation of Directive 2011/70/EURATOM . Austrian: Nuclear waste management in the EU.

Hosan, M. I. (2017). Radioactive Waste Classification, Management . Engineering International, Volume 5, No 2 , 53-63.

Hossein Ahari Mostafavi, S. M. (2012). The Potential of Food Irradiation: Benefits and Limitations. A. H. Eissa içinde, Trends in Vital Food and Control Engineering (s. 43-68). Egypt: InTech Open.

Hyatt, C. C. (2018). Nuclear Waste Management. Bristol, UK: IOP Publishing.

IAEA. (2009). Deep geological disposal of radioactive waste. Vienna: IAEA.

IAEA. (2016). Management of radioactive waste. Vienna: IAEA.

IAEA. (2018). Predisposal management of radioactive waste . Vienna: IAEA.

IAEA. (2019). The safety of nuclear fuel cycle facilities. Vienna: IAEA.

J. G. Marques, A. K. (2012). Radıoactıve waste from research reactor operatıon and decommıssıonıng . W. H. Satoshi Yuan içinde, Radioactive Waste: Sources, Types and Management (s. 41-77). Lisboa, Portugal : Nova Science Publishers, Inc.

Jianquan Liu, W. D. (2019). Overview of nuclear waste treatment and management. Shanghai : E3S Web of Conferences 118.

Katarzyna Kiegiel, T. S.-K. (2025). Advanced Nuclear Reactors—Challenges Related to the Reprocessing of Spent Nuclear Fuel. Energies , 1-23.

Lits, G. (2020). The European Governance of Radioactive Waste: A Story of Stakeholder's Involvement. EU Environmental Governance: Current and , 79-99.

M K Sneve, O. A. (2020). Management of waste containing very low activity levels under conditions. Moscow, Russia: Norwegian Radiation Protection Authority.

NEA, O. (2017). Advances in partitioning and transmutation of nuclear waste. Paris: OECD Publishing.

Nikunj Khelurkar, S. S. (2015). A Review of Radioactive Waste Management . Mumbai, India: International Conference on Technologies for Sustainable Development (ICTSD-2015).

Nikunj Khelurkar, S. S. (2015). A Review of Radioactive Waste Management. International Conference on Technologies for Sustainable Development (s. 1-6). Mumbai, India : IEEE .

Nikunj Khelurkar, S. S. (2015). A Review of Radioactive Waste Management. Mumbai, India : (ICTSD-2015).

TENMAK. (2020). National strategy for radioactive waste management. ANKARA: TENMAK.

UNSCEAR. (2016). Sources, effects and risks of ionizing radiation. New York: UNSCEAR.

V. Valdovinos, F. M.-G. (2014). Treatment Methods for Radioactive Wastes and Its Electrochemical Applicactions. Intech.

# CHAPTER 3

# Leveraging Drosophila Melanogaster for Modelling Human Cancers and Advancing Personalised Treatment Strategies

**Arif Ayar**[1]

[1] Prof. Dr., Amasya University, Sabuncuoglu Serefeddin Health Services Vocational School, Amasya, Türkiye, ORCID: 0000-0003-0473-4653

## 1. Introduction

Cancer encompasses a broad spectrum of disorders that may originate in virtually any tissue of the human body and progress through exceptionally intricate cellular and molecular mechanisms. These mechanisms involve the cumulative effects of genetic mutations, epigenetic modifications, dysregulated cell-signalling networks, metabolic reprogramming, and dynamic interactions within the tumour microenvironment. Such complexity underpins the profound clinical heterogeneity observed across and within tumour types. Consequently, therapeutic responses vary widely among patients, and conventional monotherapies frequently fail to produce durable outcomes, largely due to the rapid emergence of drug resistance and the evolutionary adaptability of cancer cells.

In this context, model organisms have become indispensable tools for dissecting the multilayered mechanisms of oncogenesis and for developing more effective therapeutic strategies. Among the various experimental systems used in cancer biology, *Drosophila melanogaster*, commonly known as the fruit fly, has gained exceptional prominence over the past two decades (Figure 1). Despite its morphological simplicity, Drosophila exhibits a remarkable degree of conservation with humans at the genetic, cellular, and pathway levels. Approximately 75% of human disease-related genes have identifiable orthologues in Drosophila, and many signalling pathways central to tumourigenesis such as RAS/MAPK, PI3K/AKT/mTOR, JAK/STAT, NOTCH, WNT, and HIPPO are evolutionarily preserved (Prober & Edgar, 2000; Hariharan & Bilder, 2006; Zhao et al., 2008).

Beyond genetic similarity, Drosophila offers numerous methodological advantages that make it a powerful system for modelling human cancers. Its short life cycle, high fertility, and minimal maintenance requirements enable rapid generation of large cohorts for reproducible experiments. More importantly, the species possesses one of the most sophisticated genetic toolkits available in any model organism. Techniques such as GAL4/UAS system, FLP/FRT-mediated clonal analysis, RNA interference, CRISPR/Cas9 genome editing, and transgenic overexpression systems allow researchers to manipulate gene function with exquisite temporal and spatial precision. These tools facilitate the creation of tumour models that accurately recapitulate human cancer phenotypes, from neoplastic overgrowth and invasion to metastasis-like cell dissemination.

A major strength of Drosophila lies in its capacity to bridge the gap between reductionist in vitro systems and more complex vertebrate models. While cell cultures provide mechanistic insights at the single-cell level, they fail to capture organism-wide interactions such as immune responses, hormonal influences,

systemic metabolic changes, and inter-organ communication all of which play critical roles in determining tumour behaviour and therapy outcomes. Drosophila, as a whole-body organism, allows these integrative processes to be observed in real time, thereby providing a more holistic understanding of cancer progression. Furthermore, its suitability for high-throughput drug screening has positioned it as a valuable platform for identifying novel antitumour compounds, testing drug combinations, and predicting toxicity profiles (Woodard et al., 2021).

In recent years, Drosophila models have also been increasingly utilised in the context of precision oncology. By introducing patient-specific oncogenic mutations or tumour genotypes into the fly, researchers can generate "personalised fly avatars" that mimic an individual's cancer biology. These avatars enable rapid, cost-effective testing of tailored drug regimens and combinatorial therapies, offering a promising avenue for guiding clinical decision-making. As such, Drosophila is no longer merely a model for studying fundamental cancer mechanisms; it has evolved into a translationally relevant organism that supports the development of personalised treatment strategies and next-generation therapeutics.

This chapter provides a comprehensive overview of the expanding role of *Drosophila melanogaster* in contemporary cancer research. We examine the genetic and biological foundations that make the fly a robust system for modelling tumourigenesis, review established and emerging Drosophila cancer models, discuss its strategic advantages in drug discovery and toxicology, and highlight its potential applications in personalised medicine.

**Figure 1.** *Drosophila melanogaster* (Photo provided by the authors)

## 2. The Role of the Drosophila Model Organism in Cancer Research

### 2.1. Advantages of the Model Organism

*Drosophila melanogaster* has emerged as one of the most influential experimental systems in contemporary cancer biology. Its unique combination of

genetic, practical, and translational advantages places it at the intersection of fundamental research and clinically oriented investigations. The key advantages that make Drosophila an indispensable cancer model are detailed below (Figure 2).

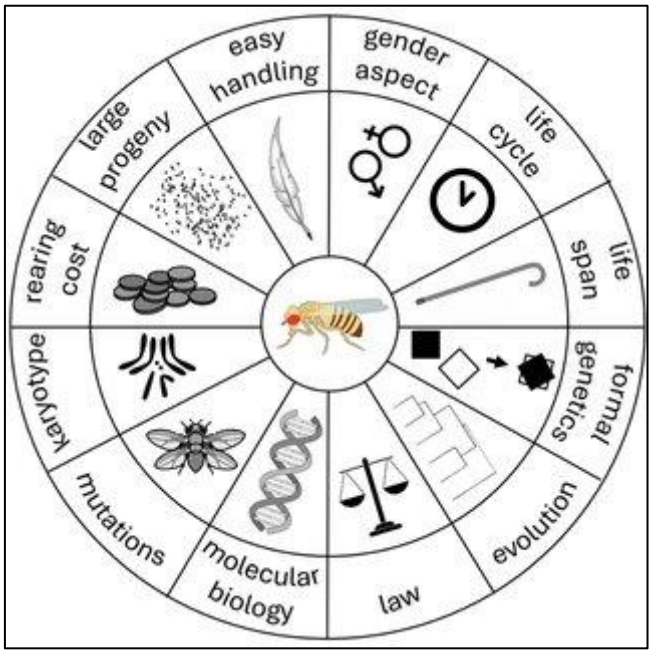


**Figure 2.** Advantages of Drosophila

**• Advanced Genetic Tools and Exceptional Manipulability**

One of the foremost strengths of *Drosophila* lies in its remarkably sophisticated genetic toolkit, which allows precise, reproducible, and targeted manipulation of gene function. Systems such as GAL4/UAS, LexA/LexAop, and QF/QUAS provide powerful binary expression platforms enabling tissue-specific and temporal regulation of oncogenes, tumour suppressor genes, or signalling pathway components. Furthermore, FLP/FRT-mediated mitotic recombination enables clonal analysis allowing genetically distinct cell populations to be generated within the same tissue for studying tumour initiation, cell competition, invasion, and metastasis-like behaviour.

The recent integration of CRISPR/Cas9 gene editing, transgenic RNA interference libraries, and mosaic analysis tools has substantially expanded the capacity for modelling patient-specific mutations. These technologies together allow for high-resolution investigation of the genetic drivers of tumourigenesis and the functional dissection of complex signalling networks that underpin cancer development and progression.

- **Short Life Cycle and High Reproductive Rate:** The rapid generation time of *Drosophila* approximately 10 to 12 days from egg to adult facilitates the analysis of multiple generations within a short experimental timeframe. This accelerated life cycle is particularly advantageous for:

- assessing long-term phenotypic consequences of oncogenic mutations,
- conducting genetic crosses to create complex multi-mutant models,
- evaluating tumour progression across developmental stages, and
- performing large-scale drug screening assays with statistically robust sample sizes (Woodard et al., 2021).

The high fecundity of females, which lay hundreds of eggs, enables efficient replication of experiments and ensures reproducibility at the population level. This scalability is crucial for cancer research, where multiple replicates and variable genetic backgrounds are often required.

- **Low Cost and Easy Maintenance:** Compared to vertebrate models such as mice or zebrafish, *Drosophila* offers an exceptionally low-cost platform for cancer research. Housing requirements are minimal, and large colonies can be maintained in compact incubators without specialised facility infrastructure. These logistical advantages allow researchers to:

- perform high-throughput genetic screens,
- test extensive pharmacological libraries,
- analyse combinatorial therapies, and
- evaluate toxicological profiles of new compounds with minimal resource investment.

This economic efficiency has transformed *Drosophila* into a central tool for early-phase drug discovery and pathway-oriented therapeutic analysis.

- High Degree of Genetic and Pathway Homology with Humans: Despite its evolutionary distance from humans, Drosophila retains a surprisingly high degree of genetic conservation. Approximately 75% of human disease-related genes have identifiable homologues in the fly genome. Moreover, nearly all major signalling cascades that play central roles in tumour development including RAS/MAPK, PI3K/AKT/mTOR, HIPPO, JAK/STAT, WNT, NOTCH, and TGF-β pathway are deeply conserved in structure and function (Prober & Edgar, 2000; Hariharan & Bilder, 2006; Zhao et al., 2008).

This evolutionary conservation enables researchers to model human cancer genotypes with high biological relevance. Many hallmark processes of cancer such as uncontrolled proliferation, evasion of apoptosis, epithelial–mesenchymal transition (EMT)-like changes, metabolic reprogramming, and abnormal cell–cell communication can be phenocopied in *Drosophila* tissues. As a result, it provides an invaluable system for decoding core mechanisms underlying tumourigenesis and for validating human genomic data in a whole-organism context.

### 2.2. Historical Background and Role in Cancer Research

The use of *Drosophila melanogaster* as a model organism in cancer research has its origins in the early twentieth century, during a period when genetics was rapidly emerging as a foundational discipline in the biological sciences. The earliest pivotal discoveries can be traced back to the 1930s, when the identification of mutations in the lethal giant larvae (lgl) gene revealed that loss of this tumour suppressor function led to dramatic neoplastic overgrowth in larval tissues. This was one of the first demonstrations in any organism that disruption of specific genes could induce tumour-like phenotypes, establishing *Drosophila* as a tractable and genetically informative system for studying the fundamental principles of malignancy.

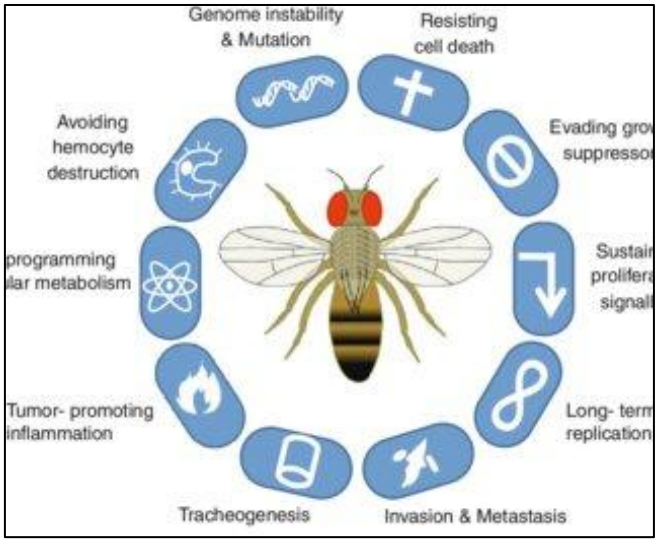


**Figure 3.** Drosophila and Hallmarks of Cancer

Subsequent investigations throughout the mid-20th century uncovered additional tumour suppressor genes including scribble (scrib) and discs large (dlg) which together formed the canonical “neoplastic tumour suppressor gene” (nTSG) group. These discoveries provided early insight into how the loss of cell polarity, impairment of epithelial integrity, and dysregulation of tissue

architecture contribute to cancer initiation. Indeed, many of the conceptual advances regarding cell–cell junctions, apico-basal polarity, and epithelial homeostasis first emerged from studies conducted in *Drosophila*. These findings proved profoundly influential, as homologous genes and pathways were later identified in humans and found to play major roles in tumour formation and metastasis.

By the 1970s and 1980s, the genetic revolution in *Drosophila* driven by mutagenesis screens, enhancer trap lines, and mosaic analysis techniques—enabled researchers to model tumours with increasingly sophisticated precision. The introduction of the FLP/FRT system in the 1990s further advanced the field by allowing clonal patches of mutant cells to be generated within otherwise wild-type tissue, facilitating detailed examination of tumour initiation, cell competition, and invasive behaviour. These studies laid the groundwork for modern cancer genetics by demonstrating how oncogenic mutations interact with their surrounding microenvironment and how competitive cell interactions can influence tumour progression.

The advent of binary expression systems, most notably the GAL4/UAS system, transformed Drosophila into a versatile platform for targeted manipulation of cancer-associated genes. This innovation allowed researchers to activate oncogenic RAS, inhibit tumour suppressors, overexpress components of the PI3K pathway, or introduce human cancer gene orthologues in precisely defined tissues. As a result, Drosophila became indispensable for modelling solid-tumour growth, metastatic behaviour, and systemic effects such as cachexia, insulin dysregulation, and altered organ crosstalk (Prober & Edgar, 2000; Hariharan & Bilder, 2006).

In the 21st century, the role of Drosophila in cancer research expanded further with the incorporation of CRISPR/Cas9 genome editing, genome-wide RNAi libraries, and high-throughput drug screening capabilities. These advances aligned the model organism closely with the goals of translational oncology. Drosophila is now widely used to: (Woodard et al., 2021).

- identify and validate oncogenic drivers;
- explore conserved signalling pathways such as RAS/MAPK, PI3K/AKT/mTOR, JAK/STAT, HIPPO and NOTCH; (Prober & Edgar, 2000; Hariharan & Bilder, 2006; Zhao et al., 2008).
- model patient-specific cancer genotypes using “fly avatars”;
- rapidly screen pharmacological libraries for therapeutic efficacy; and

- investigate mechanisms of drug resistance and tumour-host metabolic interactions.

Today, *Drosophila melanogaster* has become an essential component of both fundamental cancer biology and preclinical therapeutic research. Its contribution spans mechanistic exploration, experimental genetics, comparative oncology, and personalised medicine. The historical trajectory from the discovery of early tumour suppressor mutants to the use of fly-based drug screens highlights how this organism has shaped and continues to shape our understanding of cancer at genetic, cellular, and systemic levels.

## 3. Cancer Types Modelled in *Drosophila*

*Drosophila melanogaster* provides a versatile and genetically tractable platform for modelling multiple human cancer types that share conserved signalling pathways and cellular behaviours. Despite anatomical differences between flies and humans, the evolutionary conservation of oncogenic and tumour-suppressive pathways enables the construction of robust in vivo tumour models that recapitulate key features of colon, lung, thyroid, and brain cancers. This section provides an expanded overview of how these malignancies are modelled in Drosophila and how such models contribute to drug discovery and mechanistic understanding.

### 3.1. Colon Cancer (Colorectal Cancer)

Colorectal cancer (CRC) is a major global health burden, accounting for high levels of morbidity and mortality. In Drosophila, colon cancer models primarily focus on the hindgut and midgut epithelia, which share conserved cellular organisation, proliferative dynamics, and signalling mechanisms with the human gastrointestinal tract (Miles et al., 2015).

**Genetic Basis of Drosophila Colon Cancer Models**

CRC models are constructed by manipulating core tumour suppressors and oncogenes commonly mutated in human patients, including:

- APC (loss resulting in WNT pathway activation)
- p53 (loss of DNA damage response)
- RAS^G12V (constitutive MAPK pathway activation) (Wu et al., 2010).
- PTEN (suppression increases PI3K signalling) (Hariharan & Bilder, 2006).

**Modelling Approaches:**

•GAL4/UAS-directed tumour induction

RNAi-mediated depletion or transgenic activation of target genes facilitates the construction of multi-hit tumour models. Typical combinations include:

- RAS^G12V + p53^RNAi (Wu et al., 2010)
- *APC^RNAi + PTEN^RNAi*
- Pathway-activated clusters such as RAS^G12V; PTEN^RNAi (Prober & Edgar, 2000)

These combinations produce intestinal hyperplasia, disrupted epithelial architecture, impaired cell differentiation, and tumour-like overgrowth.

**Physiological parallels**

The *Drosophila* hindgut exhibits striking conservation in cell polarity, junctional complexes, and stem cell regulation. Consequently, this system enables fine-scale analysis of:

- tumour initiation,
- cell competition,
- microenvironmental crosstalk, and
- invasion-like behaviours.

**Drug Screening and Therapeutic Investigations**

CRC models driven by RAS or PI3K pathway activation are particularly suitable for testing targeted therapies (Woodard et al., 2021)

•PI3K/mTOR inhibitors (e.g., BEZ235)

These inhibitors reduce pathway hyperactivation but often show limited efficacy as monotherapies in both flies and human tumour models.

•Synergistic drug combinations

Studies have demonstrated enhanced therapeutic effects with:

- SC79, an AKT activator that paradoxically sensitises cells to PI3K/mTOR blockade (Hariharan & Bilder, 2006)
- Bortezomib, a proteasome inhibitor that potentiates apoptosis

Combination therapies reduce tumour overgrowth, restore epithelial integrity to some extent, and improve survival in fly models.

**Table 1.** Key Features of Drosophila Colon Cancer Models

| Cancer Type | Genetic Mutations | System Used | Drug Responses / Approaches |
|---|---|---|---|
| Colon Cancer | RASG12V, p53RNAi, APCRNAi, PTENRNAi | GAL4/UAS | BEZ235, SC79, bortezomib combinations |

Table 1 summarises the major genetic configurations and targeted drug combinations tested in *Drosophila* CRC systems.

### 3.2. Lung Cancer

Lung cancer remains the leading cause of cancer-related deaths worldwide. Although *Drosophila* does not possess lungs, its branched tracheal network and conserved RTK/MAPK signalling pathways allow effective modelling of non-small-cell lung cancer (NSCLC) mechanisms.

**Modelling Approaches**

Key oncogenic drivers used in fly models include:

- EGFR hyperactivation (mirroring human EGFR-mutant NSCLC) (Read, 2011).
- KIF5B–RET fusion constructs, modelling RET-rearranged tumours (Saal et al., 2017).
- RAS activation combined with PTEN suppression, producing aggressive tissue overgrowth and early lethality (Prober & Edgar, 2000).

The tracheal epithelium provides an accessible platform for imaging and quantifying tumour-like dysplasia.

**Therapeutic Screening**

A landmark discovery in fly-based NSCLC models is the synergy between:

- Trametinib (MEK inhibitor)
- Fluvastatin (HMG-CoA reductase inhibitor)

**This combination:**

- suppresses RAS-driven hyperproliferation in Drosophila, and (Prober & Edgar, 2000).
- significantly reduces viability in human NSCLC cell lines such as A549, thereby confirming cross-species translational relevance.

**Table 2.** Drosophila Lung Cancer Models

| Cancer Type | Genetic Alterations | Model Organ | Drug Combinations |
|---|---|---|---|
| Lung Cancer | EGFR mutations, KIF5B–RET fusions, RAS activation, PTEN suppression | Tracheal system | Trametinib + Fluvastatin |

### 3.3. Thyroid Cancer

Medullary thyroid carcinoma (MTC) and other RET-driven cancers can be modelled effectively in Drosophila using ectopic expression systems (Saal et al., 2017).

**Modelling Approaches**

Because flies lack a thyroid gland, alternative epithelial tissues particularly the compound eye act as surrogate organs.

Using GMR-GAL4 in the developing eye:

- RET mutations such as C695R or M918T (human RET-M918T) (Saal et al., 2017).
- induce cell overproliferation, polarity defects, and tumour-like disorganisation

These phenotypes closely mirror aberrant signalling observed in human RET-associated cancers.

**Drug Screening**

• Vandetanib (ZD6474), a RET kinase inhibitor, partially rescues eye overgrowth. (Saal et al., 2017)

Excessively high doses cause developmental toxicity, demonstrating the utility of *Drosophila* for dose–response optimisation.

### 3.4. Brain Cancer (Glioma Models)

Glioblastoma and other malignant gliomas are characterised by aggressive infiltration and treatment resistance. *Drosophila* offers a powerful system for modelling glial neoplasia due to the conservation of glial biology and neural architecture.

**Modelling Approaches**

Using repo-GAL4 for glia-specific expression:

- dEGFR activation
- dp110 (PI3K) activation (Hariharan & Bilder, 2006)
- dPTEN suppression

drives robust glial overproliferation, loss of neural organisation, organ compression, and lethality closely resembling hallmark features of human gliomas.

**Drug Screening**

Natural compounds with anticancer activity have been tested:

- Artemisinin: induces caspase-mediated apoptosis
- Curcumin: reduces glial cell division, restores structural organisation

**Table 3.** Drosophila Glioma Models

| Cancer Type | Genetic Modifications | Driver / System | Drugs and Effects |
|---|---|---|---|
| Brain Cancer | dEGFR activation, dp110 activation, dPTEN suppression | repo-GAL4 | Artemisinin, Curcumin (apoptosis induction, neoplasia inhibition) |

## 4. Drug Discovery and Personalised Therapies

### 4.1. Drug Screening Strategies Using Drosophila

Conventional in vitro cancer models cannot replicate whole-body physiology, inter-organ communication, or systemic toxicities. *Drosophila*, however, provides an integrated organismal context ideally suited for preclinical drug discovery.

**High-Throughput Screening (HTS)**

Larvae or adults can be placed in 96-well assay formats, enabling rapid testing of extensive drug libraries, including:

- FDA-approved collections
- natural product panels
- pathway-specific compound sets

**Polypharmacology and Multi-Target Assessment**

Because cancer progression often involves simultaneous dysregulation of multiple pathways, Drosophila is uniquely suited for identifying drugs that:

- modulate intersecting signalling networks

- overcome redundancy or compensation in tumour cells
- synergise with existing therapies

**Host–Tumour Interaction Studies**

The model allows direct observation of systemic therapy responses, including:

- metabolic disruption,
- immune activation,
- tissue wasting, and
- developmental or behavioural toxicity.

**Table 4.** Drug Discovery Strategies in Drosophila

| Strategy | Description |
|---|---|
| High-Throughput Screening | Large drug libraries screened using 96-well platforms |
| Polypharmacology | Agents targeting multiple pathways assessed |
| Toxicity and Efficacy Evaluation | Whole-organism responses measured |

### 4.2. Personalised Treatment Approaches and "Avatar" Models

Personalised medicine seeks to tailor therapeutic strategies to individual tumour genotypes. *Drosophila* has become a pioneering organism in this arena through the development of patient-specific "fly avatars."

**How Fly Avatar Models Are Generated** (Cagan & Grunwald, 2021)

Tumour DNA from a patient is sequenced and the corresponding oncogenic mutations are introduced into *Drosophila* using:

- CRISPR-mediated knock-in approaches
- GAL4/UAS-driven expression of mutant human genes
- combinatorial RNAi strategies to match patient mutation profiles

These avatars recapitulate essential features of the patient's tumour, including:

- growth behaviour,
- drug sensitivity,
- pathway dependence, and
- resistance mechanisms.

**Clinical Applications**

Fly avatars enable the rapid in vivo testing of:

- approved anticancer drugs
- experimental compounds
- drug combinations aimed at pathway synergy
- dose optimisation strategies

In several clinical case reports, Drosophila avatar-guided therapy has led to improved patient outcomes, validating the translational potential of the model.

## 5. Technical Considerations, Limitations and Practical Challenges

Although *Drosophila melanogaster* provides a powerful and cost-effective platform for modelling tumourigenesis and screening potential anticancer compounds, several biological, methodological and translational limitations must be acknowledged. Understanding these limitations is crucial for designing rigorous experiments and interpreting findings appropriately, particularly when aiming to translate results into mammalian systems or clinical settings.

### 5.1. Anatomical and Physiological Differences

While *Drosophila* exhibits substantial conservation of core signalling pathways, significant anatomical and physiological differences limit the modelling of certain human cancer types.

- Lack of direct anatomical counterparts: Several key human organs including the thyroid gland, lungs, liver, and kidneys do not have precise structural equivalents in *Drosophila*. As a result, tumour models in flies rely on surrogate tissues (e.g., the eye, tracheal system, or midgut), which, although genetically informative, cannot fully replicate the microenvironmental complexity of human tissues.

- Immune system differences: Flies possess only an innate immune system that operates through Toll, Imd, and JAK/STAT pathways. They do not have an adaptive immune system, meaning that T-cell–mediated immunity, antigen presentation, and tumour–immune co-evolution cannot be modelled directly. This limits the study of immunotherapies, immune checkpoint inhibitors, and tumour-immune escape mechanisms.

- Metabolic distinctions: Systemic metabolism and endocrine regulation differ considerably between insects and mammals, affecting the modelling of cancers that depend on metabolic rewiring.

These constraints require researchers to complement Drosophila studies with assays in mammalian models to validate organ-specific and immunologically driven phenomena.

### 5.2. Challenges in Drug Administration and Dosage

Drug delivery in Drosophila offers convenience but also introduces variability that must be accounted for in experimental design.

- Food-based administration variability: Drugs are typically mixed into fly food or applied to the surface of culture media. The actual ingested dose varies among individual flies, depending on developmental stage, health status, and feeding behaviour.

- Taste and feeding preference: Certain compounds alter the palatability of food, reducing intake and resulting in inconsistent drug exposure. Bitter or strongly aromatic compounds may be avoided by larvae or adults, confounding dose–response relationships.

- Pharmacokinetics and distribution: The absorption, distribution, metabolism, and excretion of drugs differ in flies, making it challenging to correlate fly dosage directly with human therapeutic concentrations.

Despite these challenges, careful optimisation of food conditions, use of dye-based feeding assays, and verification of internal drug levels can mitigate variability.

### 5.3. Tumour Heterogeneity and Evolution

Cancer is fundamentally an evolutionary disease characterised by genomic instability, clonal diversity, and dynamic tumour progression. Modelling this complexity in *Drosophila* presents several limitations.

- Reduced intratumoural heterogeneity: Fly models often rely on engineered mutations that create relatively uniform tumour cell populations. They do not fully recapitulate the genetic and phenotypic mosaicism observed in human cancers.

- Limited capacity for long-term tumour evolution studies: The short lifespan of *Drosophila* limits the observation of tumour progression over extended periods. While this is advantageous for rapid screens, it constrains the study of late-stage tumour evolution, mesenchymal transitions, metastatic dissemination, or therapy-induced resistance.

- Microenvironmental constraints: Although flies provide whole-organism contexts, their smaller scale limits detailed analysis of vascularisation, hypoxic

niches, and stromal epithelial interactions that are central to human tumour biology.

Nevertheless, mosaic clonal systems (e.g., MARCM, twin-spot analysis) offer partial solutions by allowing multiclonal tumour formation at a finer resolution.

### 5.4. Economic and Application Limitations

While cost effectiveness is a major advantage of the Drosophila model, certain translational limitations remain.

- Requirement for mammalian validation: Findings from *Drosophila* must be validated in mouse models or human cell systems before they can inform clinical research. This is particularly necessary for therapies targeting organ-specific physiology or adaptive immunity.
- Restrictions in modelling certain therapeutic modalities:
    - Immunotherapies such as CAR-T cells, PD-1/PD-L1 inhibitors, or tumour vaccines cannot be meaningfully replicated.
    - Organ-specific therapies, including those involving liver detoxification pathways or kidney clearance mechanisms, require mammalian physiology.
- Pharmaceutical scalability: Although *Drosophila* is ideal for early-stage drug discovery, late-stage pharmacokinetic and toxicity testing require vertebrate models.

Overall, *Drosophila* excels as a discovery platform but must be integrated within a broader translational pipeline.

## 6. Conclusion and Future Perspectives

*Drosophila melanogaster* has emerged as a cornerstone model organism in contemporary cancer research, offering a unique combination of genetic precision, whole-organism context and suitability for high-throughput experimentation. Advances in binary expression systems, particularly the GAL4/UAS platform, along with modern genome-editing tools such as CRISPR/Cas9, have enabled the modelling of multiple human cancer types with remarkable molecular and phenotypic fidelity. These innovations have also facilitated drug discovery, polypharmacological analyses, and the development of patient-specific avatar models, bridging fundamental research with translational and personalised oncology (Cagan & Grunwald, 2021).

Despite these achievements, several limitations including anatomical differences, lack of adaptive immunity, dosage variability and reduced capacity

for modelling tumour heterogeneity necessitate complementary studies in mammalian systems. Fly-based findings should therefore be positioned as an integral but early stage of the translational research pipeline rather than a standalone substitute for vertebrate models.

This chapter has explored the diverse applications of *Drosophila melanogaster* in cancer biology, detailing its genetic tools, tumour modelling strategies, drug screening methodologies, and contributions to personalised medicine. As technological innovations continue to expand the model's capabilities through improved genome-editing tools, enhanced imaging platforms, and increasingly sophisticated computational genetics Drosophila is poised to open new avenues in cancer research. Its ability to integrate genetic tractability with organism-wide physiology will ensure its continuing role in decoding tumour biology and guiding the development of next-generation therapies (Woodard et al., 2021).

## References


Bailey, A. M., & Posakony, J. W. (1995). Suppressor of hairless directly activates transcription of enhancer of split complex genes in response to Notch receptor activity. Genes & Development, 9(21), 2609–2622.

Bangi, E., Ang, C., Smibert, P., Uzilov, A. V., Teague, A. G., Antipin, Y., ... & Cagan, R. L. (2016). A personalized platform identifies trametinib plus statin as a candidate therapy for a genetically defined cancer. Scientific Reports, 6, 31664.

Bangi, E., & Cagan, R. (2019). Fast-track drug discovery in Drosophila. Disease Models & Mechanisms, 12(4), dmm039636.

Bilder, D. (2004). Epithelial polarity and proliferation control: links from the Drosophila neoplastic tumor suppressors. Genes & Development, 18(16), 1909–1925.

Brand, A. H., & Perrimon, N. (1993). Targeted gene expression as a means of altering cell fates and generating dominant phenotypes. Development, 118(2), 401–415.

Cagan, R. L., & Grunwald, D. J. (2021). Drosophila as a tool for personalized oncology: progress and prospects. Nature Reviews Cancer, 21(8), 522–537.

Gateff, E. (1978). Malignant neoplasms of genetic origin in *Drosophila melanogaster*. Science, 200(4346), 1448–1459.

Hanahan, D., & Weinberg, R. A. (2011). Hallmarks of cancer: The next generation. Cell, 144(5), 646–674.

Hariharan, I. K., & Bilder, D. (2006). Regulation of imaginal disc growth by tumor-suppressor pathways. Cell Growth & Differentiation, 17(5), 373–379.

Miles, W. O., Dyson, N. J., & Walker, J. A. (2015). Modeling cancer in Drosophila: From basic principles to translational applications. Disease Models & Mechanisms, 8(8), 853–864.

Potter, C. J., Huang, H., & Xu, T. (2001). Drosophila Tsc1 functions with Tsc2 to antagonize insulin signaling in regulating cell growth. Cell, 105(3), 357–388.

Prober, D. A., & Edgar, B. A. (2000). Ras1 promotes cellular growth in the Drosophila wing. Cell, 100(4), 435–446.

Read, R. D. (2011). A Drosophila model for EGFR-dependent glioma. PLoS Genetics, 7(2), e1001251.

Woodard, C. R., Baena, V., Pandey, U. B., & Nichols, C. D. (2021). Drug screening in Drosophila. Current Protocols, 1(8), e238.

Wu, M., Pastor-Pareja, J. C., & Xu, T. (2010). Interaction between Ras(V12) and scribbled clones induces tumor growth and invasion. Nature, 463(7280), 545–548.

# CHAPTER 4

# In Silico Genotoxicological Evaluation of Benzobicyclon Herbicide and Adequacy of In Silico Toxicity Prediction Programs

**Ahmet Ali Berber[1] & Sinem Öztürk[2]**

[1] Çanakkale Onsekiz Mart University, Vocational School of Health Services, Orcid: 0000-0002-2036-6929

[2] Çanakkale Onsekiz Mart University, School of Graduate Studies, Department of Biology, Orcid: 0009-0007-3458-4912

## 1. INTRODUCTION

Rice (Oryza sativa) is a staple food crop globally, playing a crucial role in the diet of a significant portion of the world's population. According to data from the Republic of Türkiye Ministry of Agriculture and Forestry, global rice production during the 2014-2015 period was 715.794 million tons, with consumption at 471.780 million tons. Projections for the 2023-2024 period estimate production at 772.801 million tons and consumption at 518.845 million tons (Arslan, 2024).

Rice cultivation faces significant challenges, such as weed infestations, which can severely reduce yield and quality. The increasing global population and the corresponding rise in food demand have underscored the need to enhance the sustainability and productivity of rice farming. This has elevated the critical role of pesticides in managing pests in rice cultivation.

Pesticides are chemical plant protection products used to control harmful organisms. They reduce plant diseases, protect crops from insects, bacteria, viruses, fungi, and other organisms, and improve yield. (Bondareva & Fedorova, 2021) Among these, herbicides are defined as effective chemical agents against unwanted and harmful plants.

While herbicides are effective in weed control, concerns have been raised about their environmental persistence, potential toxicity, and impacts on human health.(Handford, Elliott, & Campbell, 2015) Pesticides including herbicides can be transported from agricultural fields to groundwater and aquatic ecosystems through rain or irrigation, posing threats to non-target organisms such as humans, fish, and other aquatic species (Aktar, Sengupta, & Chowdhury, 2009). Some herbicides have been classified as carcinogenic and linked to various health problems in humans(Morrison, Wilkins, Semenciw, Mao, & Wigle, 1992).

chromosomes, potentially leading to mutations and Therefore, comprehensive toxicity assessments of all developed herbicides are critical for ensuring sustainable and safe agricultural practices.

Weed infestations are a major issue that negatively impacts the yield and quality of rice farming. To address this problem, various herbicides are widely used. Since the 1980s, benzoyl cyclohexanedione herbicides have been commonly applied in rice fields. However, despite their high herbicidal activity, these herbicides exhibited low tolerance for rice plants, highlighting the need for more effective and environmentally safer alternatives(Komatsubara, Sekino, Yamada, Koyanagi, & Nakahara, 2009) .

In 2009, Komatsubara and colleagues developed benzobicyclon ([3-(2-chloro-4-methylbenzoyl)-2-phenylthiobicyclo[3.2.1]oct-2-en-4-one]), specifically

targeting problematic weeds such as *Scirpus juncoides*, which had developed resistance to sulfonylurea herbicides. This 4-hydroxyphenylpyruvate dioxygenase (HPPD) inhibitor herbicide acts by blocking plastoquinone biosynthesis, causing bleaching in plant organs, inhibiting photosynthesis, and leading to plant death (Komatsubara et al., 2009).

During its development, toxicity tests on rats and mice indicated low acute toxicity, with no skin or eye irritation observed in rabbits, and no carcinogenic, teratogenic, or reproductive toxicity reported. However, detailed data from these toxicity studies were not provided. Post-market studies have mainly focused on soil and plant effects, with no research conducted on the genotoxic and cytotoxic effects on human and animal health reported in the literature.

In this context, investigating the genotoxic properties of pesticides such as benzobicyclon is of great importance to protect human and environmental health. Genotoxicity is defined as a substance's ability to cause damage to DNA or chromosomes, potentially leading to mutations and cancer(Phillips & Arlt, 2009).

Therefore, evaluating the genotoxic potential of pesticides is a critical step in their safety analysis.

Today, in addition to in vivo and in vitro methods, in silico tools provide a valuable alternative for genotoxicity studies. In silico toxicity assessments involve computational modeling and simulation to analyze or predict the toxicity potential of chemical substances(Parthasarathi & Dhawan, 2018).

In silico testing methods offer several advantages, including reducing the use of financial resources, providing alternatives to animal testing, minimizing the number of animals used in experiments, reducing workload, and serving as preliminary studies for subsequent in vivo and in vitro research (Myatt et al., 2018). In silico methods align with the ethical principles of the 3Rs (Replacement, Reduction, Refinement), which aim to replace, reduce, or refine animal use in research, thus supporting efforts to minimize animal testing.

Numerous in silico prediction programs have been developed to investigate and predict genetic toxicity, such as VEGA, Toxtree, and TEST programs. These software tools predict various toxicity endpoints and create a toxicity profile based on the chemical structures of substances. VEGA-QSAR uses over 100 QSAR models and in silico tools to predict and assess toxicological properties, such as acute toxicity, mutagenicity, and carcinogenicity(Danieli et al., 2023). T.E.S.T (Toxicity Estimation Software Tool) utilizes molecular descriptors and QSAR methodologies to estimate potential toxic effects, such as mutagenicity, carcinogenicity, and developmental toxicity (Martin & Todd, 2020). Toxtree applies decision-tree approaches to identify relationships between the structural

features of chemical compounds and toxicity classes, thereby predicting the Cramer classification and potential toxicity of a substance (Patlewicz, Jeliazkova, Safford, Worth, & Aleksiev, 2008).

In this study, the toxicological potentials of benzobicyclon, including genotoxicity, mutagenicity, and carcinogenicity, were predicted using in silico tools such as VEGA, TEST, and Toxtree. The study aims to predict the Cramer classification, carcinogenicity, and mutagenicity endpoints of benzobicyclon, contributing to the assessment of potential risks to human health. Furthermore, this research seeks to highlight the potential of in silico toxicity tools in genotoxicity studies, providing a significant contribution to the literature in this field.

## 2. METHODOLOGY

Three different programs were used for in silico toxicity prediction of benzobicyclon: VEGA-QSAR, TEST and Toxtree. These programs were preferred because they are free of charge, easy to use and provide toxicity prediction based on chemical structure.

### 2.1. Chemical structure of Benzobicyclon

The SMILES (Simplified Molecular Input Line Entry Specification) code for benzobicyclon was obtained from CAS Common Chemistry. CAS Common Chemistry is an open access web-based database providing a variety of information about chemicals. The CAS number of benzobicyclon is 156963-66-5 and the SMILES code is S(C1=C(C(=O)C2=C(Cl)C= C(S(C)(=O)=O)C= C2)C(=O)C3CC1CC3)C4=CC=CC=CC=C4 (CAS Common Chemistry). The information obtained was entered into the programs one by one and the desired genotoxicological endpoints were determined.

### 2.2. VEGA-QSAR

VEGA is an open-source artificial intelligence platform for predictive toxicological assessments, offering dozens of models for the prediction of various properties. By evaluating molecular attributes, the platform generates predictions about various endpoints based on similarities with known toxic compounds. In particular, it includes a large set of models for the prediction of persistence, logP, bioconcentration factor (BCF), carcinogenicity, mutagenicity, and dermal sensitization (Benfenati et al., 2013). In this study, VEGA software version 1.2.3 was used.

Using VEGA software version 1.2.3, mutagenicity (Mutagenicity (Ames test) CONSENSUS model 1.0.4, Mutagenicity (Ames test) model (CAESAR) 2.1.14, Mutagenicity (Ames test) model (ISS) 1.0.3, Mutagenicity (Ames test) model

(SarPy-IRFMN) 1.0.8, and Mutagenicity (Ames test) model (KNN-Read-Across) 1.0.1), Carcinogenicity (Carcinogenicity model (CAESAR) 2.1.10, Carcinogenicity model (ISS) 1.0.3, Carcinogenicity model (IRFMN-ISSCAN-CGX) 1.0.2, and Carcinogenicity model (IRFMN-Antares) 1.0.2) and micronucleus activity (in vitro IRFMN-VERMEER 1.0.1 and in vivo IRFMN 1.0.2 models) were evaluated. The predicted toxicity value, applicability domain index (AD index), accuracy index and related reliability metrics were evaluated as outputs of each model.

### 2.3. Toxtree

Toxtree is an easy to use and open-source software that uses decision tree approaches to classify chemicals and predict different toxic effects. One of the highlights of the program is its ability to transparently report the rationale underlying each prediction.

Toxtree classifies substances into three different categories, Class I, Class II, and Class III, in line with the Cramer classification scheme. This classification is based on the structural properties of the substances and known toxicity data. The program uses a decision tree consisting of 33 questions for each substance. The answers to these questions enable the classification of the substance and the assessment of its potential toxic threat.

Class I substances show a low level of oral toxicity given their structural characteristics and available data. Class II substances carry a higher risk of toxicity than Class I but are not as dangerous as Class III. Class III substances indicate high toxicity.

Toxtree classifies substances by combining chemical structure characteristics with metabolism or toxicity data. Using decision tree approaches, it determines the Cramer class, and the potential toxicity of a chemical based on its similarity to structural alerts associated with specific toxicity classes (Patlewicz et al., 2008). At the same time, the program includes a module based on the Benigni and Bossa rules. This module allows for a more comprehensive toxicological assessment by predicting properties such as carcinogenicity and mutagenicity.

### 2.4. T.E.S.T

T.E.S.T. (Toxicity Estimation Software Tool) is a Java-based software developed by the US Environmental Protection Agency (EPA) that enables toxicity and physical property predictions based on molecular structures. This open-source software allows users to evaluate the toxic properties of chemicals using different QSAR (Quantitative Structure-Activity Relationships) methodologies. T.E.S.T. offers reliability in toxicity prediction and can be easily

used by non-experts due to its user-friendly structure. The program can be downloaded free of charge from EPA's website. The program can estimate parameters such as oral LD50 for rats, LC50 for freshwater fish, effects on Daphnia magna and growth inhibitor concentration for microorganisms, together with various endpoints such as bioaccumulation factor, developmental toxicity, Ames mutagenicity test and acute toxicity (Martin & Todd, 2020). The Ames mutagenicity test allows to assess the mutagenic, carcinogenic potential of a compound through effects on Salmonella typhimurium (Jain et al., 2018).

TEST software was used to evaluate the in vitro mutagenic potential of benzobicyclon.

## 3. RESULTS

### 3.1. Vega-QSAR

VEGA-QSAR results showed inconsistency between models in terms of mutagenicity, carcinogenicity, and micronucleus activity. In many models, benzobicyclon was found to be outside the applicability domain (low AD index). Similarity coefficients and compatibility indices were also low in most models. This reduces the reliability of the predictions.

#### 3.1.1. Mutagenicity Prediction

The consensus model predicts that Benzobicyclon is **non-mutagenic** with a consensus score of 0.5 based on four models. The Caesar model provides a moderately reliable prediction that the compound is **non-mutagenic**, while the ISS model suggests this with low reliability. Similarly, the SarPy-IRFMN and KNN models also predicted the compound as **non-mutagenic** with moderate reliability. Despite the different Applicability Domain scores and reliability issues, all models considered this compound as **non-mutagenic**.

#### 3.1.2. Carcinogenicity Prediction

The carcinogenicity potential of Benzobicyclon was evaluated with four different models (CAESAR, ISS, IRFMN-ISSCAN-CGX and IRFMN-Antares) in VEGA QSAR software.

The CAESAR model predicted the compound as **non-carcinogenic**, but it was noted that the results may not be reliable. The model was found to be **out of applicability domain**, and fragment analysis revealed that many atom-centered fragments were absent or rare in the model's training set. The global AD index was determined as 0.312.

The ISS model predicted the compound as a **carcinogen** and detected a structural alarm. However, this model also showed low prediction reliability,

limited similarities with the training set and fragments were rare. The global AD index is 0.367.

The IRFMN-ISSCAN-CGX model predicted the compound as a **carcinogen** and identified a structural alarm. The accuracy of similar molecules was found to be high, but the model was reported to be at the limit of its applicability domain. The global AD index is 0.737.

The IRFMN-Antares model predicted the compound as a **carcinogen** and identified three different structural alarms. The prediction reliability was also found to be low in this model and the model was stated to be outside the applicability domain. The global AD index was calculated as 0.355.

The results revealed that the predicted carcinogenicity status was inconsistent between the models and the reliability levels were generally low.

### 3.1.3. Micronucleus Prediction

The in vitro micronucleus activity of the compound was predicted using the IRFMN-VERMEER 1.0.1 model. The model predicted that the compound is active in terms of **micronucleus**; however, this prediction is considered unreliable due to several factors indicating that the compound lies outside the applicability domain (AD) of the model. The similarity index of 0.741 indicates that only moderately similar compounds with known experimental values were present in the training set. Furthermore, the agreement index of 0.507 reveals that similar molecules in the training set exhibit experimental values that contradict the predicted activity. A significant number of atom-centered fragments (ACF) in the compound are rare in the training set (ACF index = 0.34), two unknown fragments and one rare fragment were identified by the program. The global AD index was calculated to be 0.247, further supporting the position of the compound outside the applicability domain of the model. Although there are some structural caveats associated with micronucleus activity, their presence is not sufficient to overcome the limitations imposed by the low similarity and high dissimilarity within the training set.

The in vivo micronucleus activity of the compound was evaluated using the IRFMN 1.0.2 model. The model predicted that the compound is not genotoxic. This prediction was supported by both the Sarpy and KNN models and a consensus situation emerged. However, several factors warrant caution in interpreting this result. The similarity index of 0.784 indicates that only moderately similar compounds with known empirical values are present in the training set. The consistency index of 0.646 indicates that there is some mismatch between the predicted activity and the experimental values of similar molecules in the training set. Although all atom-centered fragments were present in the

training set (ACF index = 1), the global AD index of 0.794 indicates that the compound may be outside the applicability domain of the model. Both the Sarpy and KNN models showed moderate reliability.

### 3.2. Toxtree

According to the decision tree approach of the Toxtree software, it was determined that elements other than C, H, O, N, or divalent S were present in the structure of the compound. In line with this situation, it was directed to question 4 of the decision tree.

Within the scope of question 4, it was evaluated whether the other elements contained in the compound existed only as sodium (Na), potassium (K), calcium (Ca), magnesium (Mg) or nitrogen (N) salt; carboxylic acid, sulfamate, sulfate, sulfonate, or hydrochloride. If these elements meet the above definitions, the compound is considered as a free acid, amine, non-sulfonated or non-sulfated compound; however, a different evaluation is required for questions 24 and 33 of the decision tree.

As a result of the analysis, it was determined that these criteria were not met, and the compound was assigned to the Class III category with a high risk of toxicity. It is also noted by the program that this assessment considers the fact that sulfamate salts are not hydrolysable.

### 3.3. T.E.S.T

The T.E.S.T software consensus method classified the compound as non-mutagenic, predicting a mutagenicity value of 0.28. Predictions from hierarchical clustering and nearest neighbor methods supported this classification. However, confidence in this prediction is limited by several factors.

Analysis of similar chemicals in the external test set yielded only 0.60 agreement, 0.50 sensitivity and 0.67 specificity. The similarity coefficients (SC) for the most similar chemicals in this set ranged from 0.52 to 0.70. Examination of similar chemicals in the training set showed improved prediction statistics with 0.80 consistency, 0.67 sensitivity and 0.86 specificity. Similarity coefficients for the training set ranged from 0.56 to 0.71.

The low similarity coefficients and inconsistent results (low consistency, sensitivity, and specificity) in both the training and test sets reduce the reliability of this prediction. The low similarity coefficients in both training and test sets, despite the higher agreement rate in the training set, suggest that benzobicyclon may be outside the model's optimal prediction range.

## 4. DISCUSSION

The results of the three different in silico programs for benzobicyclon were inconsistent. This inconsistency can be explained by the different algorithms of the programs, differences in the training sets and the low similarity of benzobicyclon to the molecules in the training sets. In silico methods are fast, cost-effective and ethically advantageous, but the reliability of the results depends on the extent of the training sets and the similarity of the tested compound to these sets. Low similarity coefficients and low concordance indices emphasize the limitations of in silico predictions and the need for experimental validation.

### VEGA-QSAR

The reliability levels of different models in predicting benzobicyclon as non-mutagenic are notable. The Caesar model classified this compound as non-mutagenic with moderate reliability, while the ISS model made a similar prediction with low reliability. Although the Caesar model is reported to be in the domain of applicability (AD index = 0.741), the limited number of compounds very similar to this compound in the training set and the presence of rare atom-centered fragments (e.g. CC(=C)S, CS(c)(=O)=O) is an important limitation.

For the ISS model, the compound was reported to be outside the applicability domain of the model (AD index = 0.245) and the low accuracy for molecules similar to the predicted results (Accuracy index = 0.5) reduces the prediction reliability of this model. Furthermore, fragments that were absent or rare in the training set of the model made the predictions of the ISS model less reliable.

The SarPy-IRFMN model classified the compound as non-mutagenic, similar to the Caesar model, but indicated the presence of rare fragments in the training set. The model's overall AD score (0.741) and high accuracy for similar molecules (Accuracy index = 1) support this prediction.

The KNN model, on the other hand, predicted the compound as non-mutagenic, but the accuracy was low (Accuracy index = 0.744) for similar compounds in the training set. Furthermore, a rare atom-centered fragment (e.g., CS(c)(=O)=O) was also observed in the KNN model.

In conclusion, all models used in VEGA-QSAR software, despite their limitations, suggest that benzobicyclon is non-mutagenic. However, the low similarity, rare fragments, and low levels of reliability in some models, common to model evaluations, emphasize the need to validate predictions with experimental data.

As a result of the evaluation of the carcinogenicity potential of benzobicyclon, it was found that the predicted results differed among the four models. While the CAESAR model predicted the compound as non-carcinogenic, the other three models (ISS, IRFMN-ISSCAN-CGX, IRFMN-Antares) evaluated the compound as carcinogenic. Limited similarities between the training sets of these models and the analyzed compound, fragment deficiencies and low global Applicability Domain Index values led to reliability issues.

Structural alarms (such as halogenated benzene, aliphatic carbon chains) identified by the ISS and IRFMN-Antares models suggest that the compound may be associated with potentially toxic mechanisms. However, the lack of a sufficient number of molecules with similar structures in the training set and low model accuracy indices reduce the precision of these predictions.

In conclusion, in vitro and in vivo experimental studies are necessary to confirm the carcinogenicity potential of benzobicyclon. Although computer predictions are useful for preliminary evaluation, it is not possible to make definitive judgments due to low reliability rates.

The prediction of in vitro micronucleus activity by the IRFMN-VERMEER 1.0.1 model for this compound is not reliable as it lies outside the applicability domain of the model. The low similarity to compounds in the training set (Similarity index = 0.741), coupled with conflicting experimental values between similar molecules (Concordance index = 0.507), significantly undermines confidence in the prediction. The presence of novel or rare atom-centered fragments (ACF index = 0.34) further highlights the limitations of the model in extrapolating to this chemical structure. Although some structural caveats indicating micronucleus activity were detected, their presence is insufficient to offset the negative indicators resulting from the limitations of the model. The low AD index (0.247) confirms this assessment.

Experimental validation is important to determine the true in vitro micronucleus activity of this compound. The limitations of the model emphasize the importance of considering the applicability space and relying on structural caveats and relevant ACFs in a model's training set. The presence of new fragments emphasizes the need for continuous refinement of the model and expansion of the training dataset to cover a wider range of chemical structures, thus increasing the predictive power of the model and reducing the occurrence of unreliable predictions outside the applicability domain. Future work should focus on expanding the chemical domain represented in the training set to increase the robustness and accuracy of the model in predicting micronucleus activity for a wider range of compounds.

The IRFMN 1.0.2 model predicts that the compound is not genotoxic based on the presence of several structural caveats associated with inactive compounds. However, the moderate similarity to compounds in the training set (Similarity index = 0.784) and the partial mismatch between the prediction and experimental values of similar molecules (Consistency index = 0.646) raise concerns regarding the reliability of the prediction. The AD index (0.794) also reveals the possibility that the compound lies outside the domain of applicability of the model, which limits confidence in the prediction.

The observed limitations emphasize the importance of assessing the applicability domain of the model and considering the overall context of the prediction, including agreement with similar compounds and the reliability of the prediction algorithms. By expanding the training dataset to include a wider variety of chemical structures similar to the test compound, better model accuracy can be achieved, potentially reducing the uncertainty associated with predictions of compounds moderately similar to those in the current dataset.

The T.E.S.T. program predicts that Benzobicyclon is not mutagenic, but reliability in this prediction is significantly reduced due to the low similarity of the compound to those in both the training and test sets, and discrepancies between predicted and experimental values in the test set. The relatively low consistency in the external test set highlights the potential limitations of the model when dealing with compounds that are structurally dissimilar to those in the training data. While the training set shows improved prediction performance, the low similarity coefficients for the most similar compounds even within the training set raise concerns about the generalizability of the model's prediction.

Although there is consistency between the mutagenicity predictions of VEGA and T.E.S.T software, further experimental testing is needed to confirm the mutagenicity of Benzobicyclon. Improvements in the prediction model could be achieved by expanding the training dataset to include a wider range of chemical structures, especially those with structural properties more similar to Benzobicyclon. This would likely increase the accuracy of the model and reduce uncertainty in predictions for new compounds. The present results emphasize that it is crucial to consider both the similarity of the test compound to the training set and reliability metrics (consistency, sensitivity, specificity) when evaluating results from QSAR models.

## 5. CONCLUSION

In this study, the results obtained in the process of predicting the genotoxic and carcinogenic potential of benzobicyclon with different in silico models showed significant inconsistencies. Three different in silico models used in the

study predicted the genotoxic effects and carcinogenic potential of benzobicyclon to different degrees. These discrepancies can be attributed to the different algorithms of the programs, the diversity of the training sets and the low similarity of the compound to the molecules in the training sets. In silico models provide fast, cost-effective, and ethically advantageous solutions, but have limitations that affect the reliability of predictions. In particular, low similarity coefficients, rare atom-centered fragments and low compatibility indices suggest that the accuracy of predictions should be supported by experimental validation.

In the evaluation of the genotoxic and carcinogenic potential of benzobicyclon, most of the models yielded non-mutagenic results, but the low reliability levels and limited training sets of some models call into question the precision of these results. In terms of carcinogenic potential, only the CAESAR model predicted the compound as non-carcinogenic, while the other models classified it as carcinogenic. This can be explained especially by the deficiencies in the training set of the models and the insufficient similarity of the compound to the molecules in these sets.

Evaluations based on micronucleus activity predictions produced similarly inconsistent results. In particular, the out-of-applicability of the IRFMN-VERMEER 1.0.1 model and the lack of similar compounds in the training set reduce the reliability of this prediction. Although the structural caveats observed in other models when predicting micronucleus activity suggest that the compound may be associated with genotoxic effects, the accuracy of these results should be confirmed by experimental data.

In conclusion, in vitro and in vivo experimental validation studies are still needed to more reliably assess the genotoxic and carcinogenic potential of benzobicyclon. The predictions of in silico models, although useful at the initial stage, are not conclusive due to low reliability rates and limited data sets. Improving such models to cover larger training sets and more diverse chemical structures would improve the accuracy of predictions. Future studies should be extended with larger data sets and molecules representing different chemical domains to improve the reliability of these models.

## REFERENCES


Arslan, S. (2024). *Tarım Ürünleri Piyasa Raporları.* T.C. Tarım ve Orman Bakanlığı Tarımsal Ekonomi ve Politika Geliştirme Enstitüsü. Retrieved December 4, 2024, from https://arastirma.tarimorman.gov.tr/tepge/Belgeler/PDF%20Tar%C4%B1m%20%C3%9Cr%C3%BCnleri%20Piyasalar%C4%B1/Birle%C5%9Ftirilmi%C5%9F%20T%C3%9CP%20Raporlar%C4%B1/2024-Tar%C4%B1m%20%C3%9Cr%C3%BCnleri%20Piyasa%20Raporlar%C4%B1%20TEPGE%20Tamsay%C4%B1.pdf

Aktar, W., Sengupta, D., & Chowdhury, A. (2009). Impact of pesticides use in agriculture: Their benefits and hazards. *Interdisciplinary Toxicology*, *2*(1), 1–12. https://doi.org/10.2478/v10102-009-0001-7

Benfenati, E., Carla, G., Politecnico, G., Milano, D., Manganaro, A., & Gini, G. (2013). *VEGA-QSAR: AI inside a platform for predictive toxicology*. Retrieved from https://www.researchgate.net/publication/287320856

Bondareva, L., & Fedorova, N. (2021, September 1). Pesticides: Behavior in agricultural soil and plants. *Molecules*, Vol. 26. MDPI. https://doi.org/10.3390/molecules26175370

CAS Common Chemistry. Retrieved December 4, 2024, from https://commonchemistry.cas.org/detail?cas_rn=156963-66-5

Danieli, A., Colombo, E., Raitano, G., Lombardo, A., Roncaglioni, A., Manganaro, A., … Benfenati, E. (2023). The VEGA Tool to Check the Applicability Domain Gives Greater Confidence in the Prediction of In Silico Models. *International Journal of Molecular Sciences*, *24*(12). https://doi.org/10.3390/ijms24129894

Handford, C. E., Elliott, C. T., & Campbell, K. (2015). A review of the global pesticide legislation and the scale of challenge in reaching the global harmonization of food safety standards. *Integrated Environmental Assessment and Management*, *11*(4), 525–536. https://doi.org/10.1002/ieam.1635

Jain, A. K., Singh, D., Dubey, K., Maurya, R., Mittal, S., & Pandey, A. K. (2018). Models and Methods for In Vitro Toxicity. *In Vitro Toxicology*, 45–65. https://doi.org/10.1016/B978-0-12-804667-8.00003-1

Komatsubara, K. ichi, Sekino, K., Yamada, Y., Koyanagi, H., & Nakahara, S. (2009). Discovery and development of a new herbicide, benzobicyclon. *Journal of Pesticide Science*, Vol. 34, pp. 113–114. https://doi.org/10.1584/jpestics.J09-01

Martin, & Todd. (2020). *User's Guide for T. E. S. T. (Toxicity Estimation Software Tool) Version 5.1 A Java Application to Estimate Toxicities and Physical Properties from Molecular Structure*. Retrieved from

https://www.epa.gov/chemical-research/toxicity-estimation-software-tool-test

Morrison, H. I., Wilkins, K., Semenciw, R., Mao, Y., & Wigle, D. (1992). REVIEW Herbicides and Cancer. In *J Natl Cancer Inst* (Vol. 84). Retrieved from http://jnci.oxfordjournals.org/

Myatt, G. J., Ahlberg, E., Akahori, Y., Allen, D., Amberg, A., Anger, L. T., … Hasselgren, C. (2018). In silico toxicology protocols. *Regulatory Toxicology and Pharmacology*, *96*, 1–17. https://doi.org/10.1016/J.YRTPH.2018.04.014

Parthasarathi, R., & Dhawan, A. (2018). In Silico Approaches for Predictive Toxicology. *In Vitro Toxicology*, 91–109. https://doi.org/10.1016/B978-0-12-804667-8.00005-5

Patlewicz, G., Jeliazkova, N., Safford, R. J., Worth, A. P., & Aleksiev, B. (2008). An evaluation of the implementation of the Cramer classification scheme in the Toxtree software. *SAR and QSAR in Environmental Research*, *19*(5–6), 495–524. https://doi.org/10.1080/10629360802083871

Phillips, D. H., & Arlt, V. M. (2009). Genotoxicity: damage to DNA and its consequences. In *Clinical and Environmental Toxicology* (Vol. 1).

# CHAPTER 5

# Silver Nanoparticle-Based Antioxidant Capacity Assays: Principles, Mechanisms, and Analytical Approaches

**Mustafa Özyürek**[1]

[1] Istanbul University-Cerrahpaşa, Engineering Faculty, Department of Chemistry, Division of Analytical Chemistry, Avcilar, 34320 Istanbul, Turkey
ORCID: 0000-0001-5426-9775

## 1. INTRODUCTION

Reliable assessment of antioxidant capacity has become essential in food science, pharmaceutical chemistry, biochemistry, toxicology and natural products research. Reactive oxygen species (ROS) are known to damage lipids, proteins and nucleic acids, and oxidative stress has been linked to ageing, cardiovascular and neurodegenerative diseases, inflammation and carcinogenesis (Halliwell & Gutteridge, 2015). Accordingly, there is a strong demand for analytical methods that can quantify antioxidant behaviour rapidly, selectively and with mechanistic insight. Classical total antioxidant capacity (TAC) assays such as DPPH• scavenging, $ABTS^{\bullet+}$ decolorization, FRAP, and the CUPRAC method are widely used in laboratories and industry (Brand-Williams et al., 1995; Re et al., 1999; Benzie & Strain, 1996; Apak et al., 2004). However, these assays differ in radical type, redox potential, solvent composition and reaction time, and they are variably affected by pH, surfactants, proteins and metal ions. Their kinetic and mechanistic biases, matrix interferences and limited comparability have been critically discussed in comprehensive reviews of antioxidant activity/capacity measurements (Apak et al., 2016).

In search of more sensitive and versatile readouts, attention has turned to the localized surface plasmon resonance (SPR) of noble metal nanoparticles as an optical transducer of redox events. Silver nanoparticles (AgNPs), in particular, display intense and narrow SPR bands in the visible region whose position and intensity are exquisitely dependent on particle size, shape, aggregation and the surrounding dielectric medium (Kelly et al., 2003). When $Ag^{+}$ is reduced to $Ag^{0}$ by antioxidants, or when pre-formed seeds grow in the presence of reductants, the resulting changes in the AgNP population can be monitored as well-defined absorbance increases or spectral shifts. This provides a direct, electron-transfer-based optical signal that can be quantified in terms of TAC. A dedicated review by Bedlovičová et al. (2020) has summarized the rapidly expanding literature on antioxidant activity determination of AgNPs and highlighted their potential as colorimetric sensing platforms.

A major milestone in this field was the development of the seed-mediated silver nanoparticle antioxidant capacity (SNPAC) method by Özyürek et al. (2012). In this electron-transfer assay, pre-formed AgNP seeds catalyse the reduction of $Ag^{+}$ by antioxidants, leading to controlled particle growth and a reproducible increase in the SPR band, which can be calibrated against Trolox equivalents. This approach afforded broad linear ranges, good precision and moderate sensitivity, and was successfully applied to commercial fruit juices and herbal teas without extensive sample pre-treatment (Özyürek et al., 2012). Building on this concept, Szydłowska-Czerniak et al. adapted AgNP-based assays to determine the antioxidant capacity of rapeseed and its products, and compared their performance with modified DPPH and FRAP methods

(Szydłowska-Czerniak et al., 2012; Szydłowska-Czerniak & Tułodziecka, 2013). The influence of nanoparticle growth on plasmonic signal evolution under different reaction environments is summarized in Table 1.

More recently, green synthetic routes and hybrid sensing formats have broadened the scope of AgNP-based antioxidant assays. Beğiç et al. (2021) reported a green synthesized silver nanoparticle-based antioxidant capacity (GSNP-AC) method using carob extract both as a reducing and capping agent, emphasizing environmental friendliness and sustainability (Beğiç et al., 2021). Martínez-Cabañas et al. (2021) evaluated plant extracts for their ability to both act as antioxidants and drive green synthesis of metal nanoparticles, directly comparing SNPAC with DPPH and Folin–Ciocalteu assays and demonstrating the suitability of SNPAC for screening bio-based reducing agents (Martínez-Cabañas et al., 2021). In parallel, Zor et al. (2024) developed a silver nanoparticle–chitosan composite film for determining the total antioxidant capacity of fruit juices and plant extracts, illustrating how AgNP chemistry can be embedded into solid-state sensor architectures for portable applications (Zor et al., 2024).

**Table 1.** Reaction-environment coupled SPR signal behavior in $Ag^+$ reservoir electron-transfer antioxidant assays

| **Approximate Diameter / Morphology** | **Observed SPR $\lambda_{max}$ (nm)** | **Extinction / Scattering Behavior** | **Reference(s)** |
|---|---|---|---|
| ~ 10–20 nm (small quasi-spherical) | ~ 380–410 nm (blue-violet region) | Absorption-dominated, narrow-ish peak | Kelly et al., 2003 |
| ~ 20–40 nm (quasi-spherical) | ~ 400–430 nm (blue-green) | Increasing extinction, mix absorption + scattering | Gonzalez et al., 2014 |
| ~ 40–60 nm (spherical / slightly faceted) | ~ 420–460 nm (green-yellow) | Strong extinction, significant scattering, peak broadening | Car & Krstulović, 2022 |
| ~ 60–80 nm (larger spheres / faceted shapes) | ~ 440–500 nm, sometimes > 500 nm depending on medium | Scattering-dominated, broad absorption + scattering band, red-shift | Sharma et al., 2020 |
| Polydisperse / aggregated / non-spherical / anisotropic shapes | Broad, often red-shifted and damped SPR; secondary peaks or broad tailing | Strong scattering, possible multiple plasmon modes, low reproducibility | Sharma et al., 2020 |

Despite these advantages—high molar absorptivity, straightforward visual detection, compatibility with miniaturized formats and flexible assay design—AgNP-based systems also have important limitations. The colloidal stability of AgNPs is strongly influenced by pH, ionic strength, complexing anions (especially chloride), proteins and surfactants; uncontrolled aggregation or precipitation can compromise both linearity and sensitivity (Szydłowska-Czerniak & Tułodziecka, 2013; Bedlovičová et al., 2020). Moreover, as primarily electron-transfer-based systems, AgNP assays respond preferentially to reductants with suitable redox potentials and may under-represent lipophilic or hydrogen-atom-transfer (HAT)-dominated antioxidants, a general issue for ET-type TAC methods (Apak et al., 2016; Bedlovičová et al., 2020). These features underline the need for careful control of experimental parameters, mechanistic understanding of competing processes (seed growth vs. nucleation, dissolution, aggregation) and critical interpretation of results in comparison with conventional TAC assays.

Taken together, silver nanoparticle-based antioxidant assays now constitute a distinct and rapidly developing branch of antioxidant methodology, characterized by plasmonic optical sensitivity, tunable reaction kinetics and compatibility with green synthesis and sensor technologies. The present chapter aims to provide a comprehensive account of the chemical principles, mechanistic foundations, methodological variants, kinetic and thermodynamic aspects, analytical performance characteristics, and application potential of AgNP-based antioxidant capacity measurements, while also highlighting current limitations and directions for future development.

## 2. THEORETICAL FOUNDATIONS AND REACTION MECHANISMS

Silver nanoparticle (AgNP)–based total antioxidant capacity assays translate the electron-transfer capability of antioxidants into an amplified SPR optical signal through chemical growth dynamics of a finite $Ag^+$ reservoir. The $Ag^+/Ag^0$ pair possesses a high standard reduction potential of +0.80 V, positioning $Ag^+$ as a strong and thermodynamically favourable electron acceptor for phenolic reductants in aqueous environments. Especially o-diphenols, with adjacent hydroxyl motifs that stabilize transient semiquinone/phenoxyl states, are predisposed to transfer two-electron fluxes into inorganic redox pools, a principle mechanistically unified for CUPRAC and metal-ion sinks in electron-transfer antioxidant assays by earlier classifications (Apak et al., 2016). The oxidative conversion of phenolic antioxidants into phenoxyl radicals and subsequently quinone structures is therefore not a side reaction but the signal-forming oxidation half-cell itself, liberating electrons that are harvested by $Ag^+$, progressively increasing $Ag^0$ atom population within the reaction medium (Apak et al., 2016).

Metal nanoparticles offer signal-escalation advantages over homogeneous ion-sinks because their optical extinction is not a 1:1 stoichiometric readout but a size-dependent plasmonic amplification. Kelly and coworkers demonstrated that the centroid wavelength of the SPR band and its extinction coefficient scale strongly with diameter, morphology and dielectric coupling to the ligand shell and medium (Kelly et al., 2003). Optical studies supported by Mie theory—and those examining morphology and dielectric environment effects—have established a quantitative correlation between the AgNP SPR/LSPR band characteristics and both nanoparticle size and surrounding dielectric properties (Sosa et al., 2003; Chhatre et al., 2012; Alzoubi et al., 2023)

In classical bottom-up AgNP assays without seeds, nanoparticle formation initiates from randomly emerged critical nuclei, generating an unavoidable stochastic dispersion of cluster size, which in turn broadens signal uncertainty when used analytically (Kelly et al., 2003). Özyürek and coworkers advanced the $Ag^{+}$ pool sensing logic by demonstrating that pre-formed AgNP seeds impose kinetic directionality onto atom deposition: $Ag^{+}$ reduction is driven preferentially to surface-mediated growth rather than de novo nucleation, suppressing nucleus-count–driven signal variance and converting bulk $Ag^{0}$ deposition into a controlled enlargement of seeds (Özyürek et al., 2012). Because seed-growth is energetically downhill relative to spontaneous nucleus-formation, the free-energy landscape of the colloidal population is homogenized across replicates, giving rise to wider analytical linearity and improved inter-run precision (Özyürek et al., 2012).

In such seed-enlargement directed systems, each antioxidant molecule contributes to the consumption of an $Ag^{+}$ reservoir that feeds atom deposition on seeds; the analytical signal is therefore a kinetic integral of $Ag^{+}$ depletion rate and seed-surface enlargement efficiency rather than an instantaneous equilibrium absorbance response. $Ag^{0}$ atom deposition onto seeds increases diameter gradually, enabling a near-linear coupling region in which incremental $Ag^{0}$ flux shifts SPR band amplitude and produces slight red-shifts before damping by broadening or scattering becomes dominant at larger diameters, an optical behaviour providing quantitative leverage for $Ag^{+}$ pool titration by antioxidants (Kelly et al., 2003; Özyürek et al., 2012). By adapting this framework, Szydłowska-Czerniak and coworkers demonstrated AgNP enlargement assays for rapeseed oils and products, showing that $Ag^{+}$ redox pools could be monitored in lipid-rich complex matrices when nucleation variance is constrained, while also emphasizing that $Ag^{+}$ reservoir diversion into halide-driven precipitation, notably AgCl, kinetically intercepts SPR emergence under high ionic/chloride content (Szydłowska-Czerniak et al., 2012; Szydłowska-Czerniak & Tułodziecka, 2013). Bedlovičová and coworkers later summarized that silver colloids, although powerful ET-driven optical antioxidant transducers, are chemically fragile to ionic strength, pH and complexing anions, necessitating

ligand-shell stabilization to preserve plasmonic TAC signal linearity (Bedlovičová et al., 2020). Because AgNP assays are ET-weighted, they fundamentally under-report lipophilic or hydrogen-atom-transfer–dominant antioxidants such as carotenoids, a mechanism-classification bias critically discussed in broad matrix reviews comparing ET and HAT families (Apak et al., 2016; Bedlovičová et al., 2020). Polymer and biopolymer caps (e.g. citrate, PVA, chitosan) have been shown to modulate atom-deposition kinetics and short-time TAC readouts, not by altering thermodynamic driving forces but by steering reaction rate constants and surface accessibility constraints (Teerasong et al., 2017; Özyürek et al., 2012; Szydłowska-Czerniak & Tułodziecka, 2013).

Collectively, this methodology represents a departure from persistent-radical or homogeneous ion-sink optics toward a finite-reservoir redox–growth competition model where plasmonic response is kinetically sculpted through $Ag^+$ pool consumption, ligand competition and seed-surface atom deposition. The analytical signal strength is therefore dictated by redox potential compatibility of antioxidants to $Ag^+$, kinetic preference of surface growth on seeds, and stabilization chemistry that protects the $Ag^+$ reservoir from precipitation or aggregation diversion pathways. This framework, free from slow radical-generation steps or forced organic-solvent environments, provides a mechanistically transparent, kinetically directed, optically amplified and analytically tractable platform for redox-driven antioxidant quantification (Özyürek et al., 2012; Teerasong et al., 2017; Martínez-Cabañas et al., 2021; Zor et al., 2024; Bedlovičová et al., 2020).

## 3. METHODOLOGICAL CLASSIFICATION

Silver nanoparticle-based antioxidant assays are best understood as a modular methodology family rather than a single uniform protocol. The assays can be grouped into three main analytical design architectures: solution-phase seed-mediated methods, green-chemistry-driven biogenic reduction systems, and solid-supported AgNP composite sensor platforms. This classification follows the degree of kinetic steering imposed on $Ag^+$ reduction chemistry, the nature of stabilizing ligand shells, and the physical phase in which SPR extinction emerges as the analytical signal. Earlier mechanistic reviews in nanoparticle plasmonics established that size-dependent optical extinction, dielectric coupling, and ligand competition determine both SPR $\lambda_{max}$ position and signal precision in metal colloids (Kelly et al., 2003; Bedlovičová et al., 2020).

### 3.1. Solution-Phase Seed-Mediated AgNP Methods

Solution-phase seed-mediated assays represent the most kinetically directed subclass of $Ag^+$ reservoir consumption methods (Figure 1). Instead of allowing $Ag^0$ atoms to self-assemble into randomly spawning critical nuclei, the system is intentionally initiated using monodisperse or quasi-uniform AgNP seeds. This allows antioxidants to reduce the $Ag^+$ pool exclusively through surface-mediated

atom deposition on seeds, suppressing spontaneous nucleation dispersion and converting $Ag^0$ atom output into controlled particle enlargement kinetics. Özyürek et al. (2012) showed that this kinetic steering dramatically improves inter-run precision, provides extended linearity windows for Trolox-equivalent calibration, and avoids slow pre-generated persistent radical reporters typical of classical TAC methods (Özyürek et al., 2012).

In such systems, surface charge and growth rate constants are not dictated purely by the intrinsic redox potential of antioxidants but are modulated by the selected stabilizers and ligand competitiveness of the medium. Citrate-capped systems maintain electrostatic stabilization at early growth, while polymeric caps such as PVA influence redox-site accessibility and short-time kinetic integrals without disrupting the thermodynamic favorability of the $Ag^+/Ag^0$ couple. By translating $Ag^+$ depletion kinetics into monotonic absorbance increases of the amplification surface, the seed-mediated assays offer highly discriminative optical kinetics that can be interpreted both as quantitative capacity and as growth-sculpted kinetic profiles of purified antioxidants. Szydłowska-Czerniak et al. (2012) further confirmed the oil-matrix applicability of $Ag^+$ reservoir assays, demonstrating that antioxidant heterogeneity in rapeseed oils could be optically discriminated when nucleation variance is properly constrained (Szydłowska-Czerniak et al., 2012).

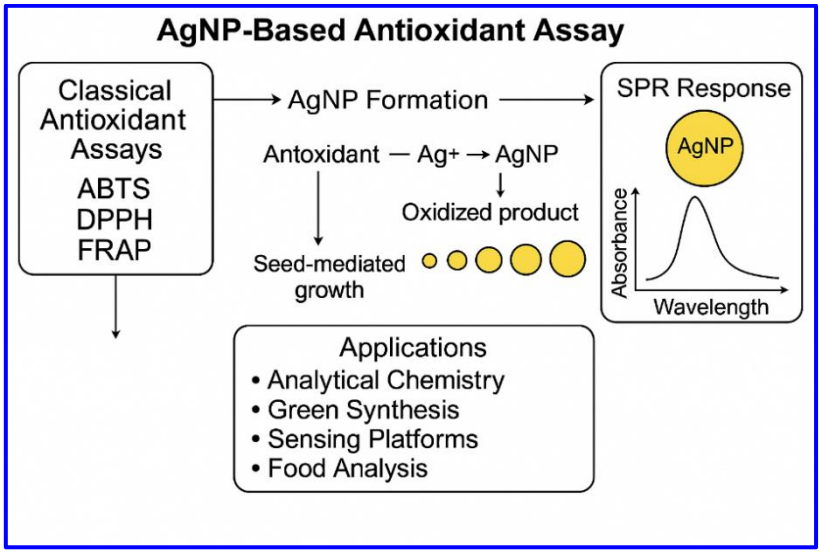


**Figure 1.** Mechanistic illustration of $Ag^+$ reduction by antioxidants, seed-mediated AgNP growth, and SPR signal generation.

### 3.2. Green Synthesis-Based AgNP Systems

Green synthesis-based AgNP platforms form a second methodology family where $Ag^{+}$ reduction is driven by biogenic reductants provided inherently by plant and food extracts (Table 2). In these systems, polyphenols, carbohydrates, or extract-borne reducing metabolites perform the $Ag^{+}$ to $Ag^{0}$ reduction step while tannins, polysaccharides, flavonoids, or phenolic ligand-sinks simultaneously act as the stabilizing shell. Martínez-Cabañas et al. (2021) demonstrated that SPR signal evolution in green-reduction AgNP synthesis strongly correlates with phenolic electron-donation density, extract dielectric milieu, and ligand-mediated aggregation suppression competitiveness of the capping layer (Martínez-Cabañas et al., 2021). Beğiç et al. (2021) further emphasized that sustainable $Ag^{+}$ reduction-capping systems using carob-extract produce measurable antioxidant signals while minimizing harsh synthetic ligand or solvent footprints (Beğiç et al., 2021; Özyürek et al., 2012).

However, even when $Ag^{0}$ colloids form reliably through ET-rich extracts, the analytical precision of the SPR signal can be limited by compositional flexibility and batch variabilites of extract ligand pools. Because the identity and concentration of bio-based reductants fluctuate seasonally or between extraction batches, these systems require careful calibration strategies to ensure $Ag^{+}$ reservoir accessibility and scattering-artifact suppression do not broaden statistical uncertainty beyond analytically useful thresholds. Sharma et al. (2019) showed that dispersing medium, extract ligand competitiveness, and surfactant-equivalent capping pools influence SPR intensities in ways that are orthogonal to intrinsic electron transfer thermodynamics (Sharma et al., 2019). Bedlovičová et al. (2020) highlighted that AgNP antioxidant assays, although plasmon-amplified and environment friendly, remain chemically susceptible to ionic strength diversion and ligand-exchange phase instability unless ligand-shell design or composition is tightly controlled (Bedlovičová et al., 2020).

**Table 2.** Phytochemicals contributing to green synthesis of AgNPs.

| Plant source | Phytochemicals | Reduction role | Stabilization | AgNP features | Ref. |
|---|---|---|---|---|---|
| Green tea | Catechins | Strong | Strong | Uniform, small | Asghar et al., 2018 |
| Pomegranate | Ellagitannins | Strong | Medium | Mostly spherical | Devanesan et al., 2018 |
| Clove | Eugenol | Moderate | Weak | Polydisperse | Tekin et al., 2019 |
| Rosemary | Rosmarinic acid | High | Strong | Small, fairly uniform | Farghaly & Nafady, 2015 |
| Coffee | Chlorogenic acids | Medium | Moderate | Medium-sized | Sulistyarti et al., 2023 |

### 3.3. Solid-Phase Composite Film-Embedded AgNP Sensors

Solid-phase composite AgNP sensors form the third analytical architecture family by translating solution diffusion uncertainty into immobilized atom-deposition-surfaces supported by polymers. Instead of quantifying antioxidant capacity from purely colloidal $Ag^0$ SPR emergence, these systems embed AgNP populations or growth surfaces into biopolymeric or synthetic sensor films where $Ag^+$ reduction and atom deposition occur within a structurally stabilizable solid extinction pool. These architectures emerged from the signal-steering logic of $Ag^+/Ag^0$ kinetics while resolving aggregation variance using solid dielectric constraints.

Zor et al. (2024) demonstrated that chitosan-AgNP composite films retain plasmon-responsive ET reporters inside biopolymers, enabling rapid visual TAC screening without dedicated spectrophotometric collection, a property not attainable through persistent radical TAC assays alone (Zor et al., 2024; Beğiç et al., 2021). By defining a fixed ion reservoir depletion–growth surface pair supported by dielectric polymer pools, solid-phase AgNP films serve as truly portable electron-sink reporters that harvest extract electron donation on a finite $Ag^+$ depletion surface rather than secondary radical decay alone (Özyürek et al., 2012; Zor et al., 2024).

In these SPR-film platforms, analytical signal precision is regulated by both diffusion timelines of $Ag^+$ reduction feeders and the dielectric anchoring effect of the polymer medium. The peak intensity and shape of the SPR band emerging on sensors is constrained by particle growth surfaces and mass transfer restrictions, reducing cluster-level stochastic broadening seen in classical AgNP nucleation chemistry. However, because reduction occurs within a solid matrix rather than

freely diffusing colloids, kinetic integrals may be slower than seed-solution systems, and signal extinction may broaden asymmetrically depending on polymer dielectric coupling, illustrating that portability often trades inversely with mass-transfer kinetic speed (Kelly et al., 2003; Sharma et al., 2019; Bedlovičová et al., 2020). These limitations must be interpreted as ligand–medium dielectric convolution effects rather than thermodynamic incompatibility of antioxidants.

## 4. KINETIC AND THERMODYNAMIC EVALUATIONS

The analytical behavior of silver nanoparticle (AgNP) — based antioxidant assays stems from a balance between the thermodynamic favorability of the $Ag^+/Ag^0$ redox couple and the kinetic control over nanoparticle nucleation and growth. The $Ag^+/Ag^0$ standard reduction potential (≈ +0.80 V) renders $Ag^+$ a strong electron acceptor under aqueous conditions, making reduction thermodynamically feasible for many phenolic antioxidants, ascorbate, and similar reductants (Bard & Faulkner, 2001; Kelly et al., 2003). However, whether this theoretical feasibility translates into a measurable plasmonic response depends largely on kinetic factors: electron-transfer rates, ligand shell composition, ionic strength, pH, and stabilizer interactions.

In uncontrolled bottom-up synthesis, $Ag^0$ atoms may spontaneously nucleate into a population of small clusters whose size, shape, and distribution are largely stochastic. Such polydispersity undermines spectrophotometric readout precision because each cluster contributes variably to surface plasmon resonance (SPR) extinction. By contrast, seed-mediated approaches—where pre-formed, monodisperse AgNP seeds are introduced before antioxidant-driven reduction—steer $Ag^0$ deposition preferentially onto existing seeds rather than triggering new nuclei. This yields more uniform size growth, improved linear response with antioxidant concentration, and reduced inter-run variability (Özyürek et al., 2012; Teerasong et al., 2017).

During the growth phase, incremental deposition of $Ag^0$ onto seed surfaces increases nanoparticle diameter. Classical plasmonic theory predicts that even modest size increases enhance extinction coefficients significantly and may shift SPR $\lambda_{max}$ slightly toward longer wavelengths (bathochromic shift), thereby boosting measured absorbance (Kelly et al., 2003). In optimally stabilized and kinetically controlled systems, this size-growth driven SPR signal can act as a sensitive readout of the cumulative electron transfer from antioxidant reductants. Because the readout reflects a dynamic process of $Ag^+$ consumption and $Ag^0$ accumulation, the time evolution of absorbance often approximates a first-order kinetics model under certain conditions:

$$A(t) = A_\infty(1 - e^{-k_{\text{app}}t})$$

Here, $A(t)$ is the absorbance at time $t$, $A_{(\infty)}$ is the asymptotic absorbance after complete growth, and $k_{(app)}$ is the apparent rate constant, which correlates with

the reducing strength and reaction kinetics of the antioxidant. Indeed, studies employing well-controlled seed-mediated or green-synthesis AgNP assays report that strong electron-donating antioxidants (e.g. polyphenols) produce large $k_{(app)}$ values and rapid SPR signal development, whereas weaker or sterically hindered reductants yield slower kinetics and smaller SPR changes (Teerasong et al., 2017). Importantly, the microenvironment plays a decisive role: stabilizers such as citrate, poly(vinyl alcohol) (PVA), or biopolymers (e.g. chitosan) affect collision frequencies, steric accessibility, surface adsorption dynamics, and colloidal stability. Meanwhile, ionic strength, pH, and the presence of competing ligands or anions (e.g. halides) may suppress or divert $Ag^+$ into non-plasmonic precipitates (e.g. AgCl), undermining the optical readout even when redox potentials are favorable (Szydłowska-Czerniak & Tułodziecka, 2013; Bedlovičová et al., 2020; Chambers et al., 2014).

Thus, AgNP-based antioxidant assays function within a thermodynamically allowed but kinetically gated regime. The interplay between redox chemistry, nanoparticle surface energetics, ligand competition, and growth dynamics governs analytical sensitivity, selectivity, and reproducibility. When these parameters are optimized, AgNP assays can yield rapid, sensitive and mechanistically interpretable antioxidant capacity measurements; but careful optimization and critical interpretation remain necessary due to potential side-reactions, precipitation, or matrix interference.

## 5. ADVANTAGES AND LIMITATIONS

The appeal of silver nanoparticle (AgNP)-based antioxidant capacity assays originates from the intrinsic signal magnification offered by surface plasmon resonance (SPR), a property fundamentally distinct from homogeneous ion-sink or persistent-radical reporters. In classical radical assays, the analytical signal corresponds to consumption of a pre-generated radical pool, coupling absorbance change directly to radical decay rather than electron-flux amplification; this results in solvent-biased reaction kinetics and limited cross-matrix robustness (Brand-Williams et al., 1995; Re et al., 1999). In contrast, AgNP plasmonic response is a redox-triggered optical amplification that intensifies with the number of reduced $Ag^+$ ions feeding particle expansion, making reductants with strong electron-donating ability—predominantly o-diphenols and ascorbate-like systems—highly compatible with $Ag^+$ reduction thermodynamics in water (Apak et al., 2016; Kelly et al., 2003).

The introduction of seed-mediated designs in AgNP assays narrowed the uncertainty landscape by kinetically steering $Ag^0$ atom deposition onto pre-formed nuclei rather than permitting de novo nucleation. This created analytically advantageous linear windows in which plasmon extinction increased reproducibly with $Ag^+$ depletion rate and incremental diameter growth, enabling precise calibration schemes in antioxidant scoring (Ozyurek et al., 2012). The

method's pronounced SPR absorbance evolution and visible color emergence enabled the technology to be used beyond conventional cuvette spectrophotometry, catalysing translation into solid films and micro-platform formats capable of uninstrumented visual antioxidant screening (Zor et al., 2024). Parallel efforts in green synthesis demonstrated that plant-derived polyphenols and saccharidic reductants can simultaneously reduce and stabilize colloidal silver, generating sustainable TAC reporters in water without relying on classical chemical reductants such as hydrides or borohydrides (Begic et al., 2021; Martinez-Cabanas et al., 2021), further broadening matrix scope in AgNP sensing logic.

However, even for systems that are thermodynamically feasible ($\Delta G = -nF\Delta E < 0$ for $Ag^+$ reduction), signal emergence is kinetically vulnerable to the chemical fate of the $Ag^+$ pool. Halide complexation and chloride-mediated AgCl precipitation directly collapse the feed-reservoir required for plasmonic signal growth, particularly in salt-rich or protein-crowded aqueous matrices (Szydlowska-Czerniak & Tulodziecka, 2013; Kelly et al., 2003). Comprehensive evaluations have continued to emphasize that ionic strength, pH, and anion competition destabilize the double-layer environment surrounding nanoparticles, inducing aggregation or precipitation pathways that suppress SPR amplitude even when strong antioxidants are present (Bedlovicova et al., 2020). Moreover, as ET-weighted optics, AgNP plasmonic TAC systems do not symmetrically report lipophilic or hydrogen-atom-transfer-dominant antioxidants, a mechanism bias acknowledged across large inter-method antioxidant surveys discussing ET/HAT reporter orthogonality gaps (Apak et al., 2016; Bedlovicova et al., 2020). Polymeric capping systems such as PVA or chitosan, although beneficial for colloidal persistence, sterically gate $Ag^0$ deposition on seed surfaces and modulate collision probability by viscosity or interfacial confinement, frequently slowing colorimetric TAC signal kinetics or narrowing plasmonic leverage windows in diffusion-constrained films (Teerasong et al., 2017; Zor et al., 2024).

Therefore, AgNP antioxidant assays should be interpreted not as instantaneous equilibrium absorbance methods but as plasmon-amplified $Ag^+$ reservoir consumption reporters whose analytical utility depends on kinetically steered growth, ligand-shell choice, and matrix-compatible stabilization strategies. This mechanistic framework explains why the method provides high sensitivity and kinetic discriminative power under well-stabilized, halide-protected, aqueous seed-growth conditions (Ozyurek et al., 2012; Teerasong et al., 2017), while also clarifying why matrix fragility and mechanism bias remain key experimental constraints in complex biological or food environments.

## 6. COMPARATIVE ANALYSIS WITH CLASSICAL ANTIOXIDANT METHODS

Spectrophotometric total antioxidant capacity assays were historically built on either stable synthetic radicals or homogeneous metal-ion redox reporters, each offering a one-dimensional view of antioxidant behaviour. The DPPH radical assay, one of the earliest radical sinks for antioxidant measurement, depends on organic solvent environments to maintain radical solubility and remains kinetically slow due to diffusion-limited hydrogen atom transfer steps (Brand-Williams et al., 1995). The ABTS method improved aqueous compatibility, yet the radical cation's strong reactivity increases the probability of non-specific electron or hydrogen transfer interception in complex sample matrices, which can inflate antioxidant scores if kinetic quenching competes with redox thermodynamics (Re et al., 1999; Apak et al., 2016). The FRAP method formalized ferric-to-ferrous redox pool monitoring, but its strongly acidic Fe-based reduction environment limits its ability to report hydrogen atom transfer–dominant antioxidants, shifting apparent antioxidant capacity toward species compatible with the $Fe^{3+}$ pool rather than the complete antioxidant mixture (Benzie et al., 1996; Rice-Evans et al., 1996). The cupric ion reduction logic employed by the CUPRAC method provides mechanistic alignment with electron transfer thermodynamics, yet ligand competition and matrix-born chelators can kinetically gate surface accessibility or collapse the redox feed pool, constraining signal development even when $\Delta G$ is favorable (Apak et al., 2004; Apak et al., 2016).

Silver nanoparticle–based antioxidant methods depart from the 1:1 stoichiometric absorbance change of classical reporters by converting redox feasibility into size-dependent plasmonic amplification. When $Ag^{+}$ ions are reduced to $Ag^{0}$, the resulting SPR extinction is magnified by nanoparticle diameter increases, enabling optical signal escalation that reflects kinetic integrals of electron flux feeding particle growth. In unseeded bottom-up systems, signal noise is dominated by nucleus-count variance arising from the stochastic nature of critical $Ag^{0}$ cluster formation, broadening inter-run uncertainty despite favourable redox potentials (Kelly et al., 2003). Seed-mediated formats, as formalized in Analytical Chemistry by Ozyurek et al. (2012), constrain this variance by steering $Ag^{0}$ atom deposition toward controlled seed enlargement, yielding more predictable SPR amplitude windows and improved reproducibility compared with radical-decay sinks. The ability to embed AgNP chemistry into solid films expanded the method's analytical reach, enabling uninstrumented visual TAC screening in plant and beverage matrices (Zor et al., 2024), a capability absent from persistent radical cuvette tests. However, the same plasmonic amplification that increases optical sensitivity also inherits matrix fragility. Anions such as chloride divert $Ag^{+}$ into AgCl precipitation, collapsing the aqueous feed pool required for SPR signal emergence and suppressing

apparent TAC scoring, an issue repeatedly emphasized in Food Chemistry (Szydlowska-Czerniak et al., 2013, et al.) and later limitation surveys overviewing ionic fragility of silver colloids (Bedlovicova et al., 2020, et al.). Additionally, ET-weighted $Ag^{+}/Ag^{0}$ reporter platforms respond preferentially to strong electron donors and under-amplify lipophilic or hydrogen atom transfer–dominant antioxidants, a mechanism bias recognized across inter-method TAC classification literature (Apak et al., 2016; Bedlovicova et al., 2020).

AgNP-based assays (Table 3&4), therefore, are not replacements for classical methods but complementary analytical redox amplifiers whose strengths emerge in kinetically controlled, ligand-stabilized, halide-protected, neutral aqueous environments, while their limitations surface when $Ag^{+}$ feed pools are chemically diverted or interfacial growth is sterically gated. Comparative interpretation across conventional TAC and plasmon-amplified AgNP TAC platforms requires an understanding of which oxidation half-cells liberate electrons into compatible $Ag^{+}$ pools and which environmental variables collapse or preserve plasmon emergence leverage windows.

**Table 3.** Colloidal (solution-phase) AgNP TAC assay frameworks

| AgNP TAC | Typical LOD / Sensitivity | Practical Linear Working Range | Typical Reaction Time | Ref |
|---|---|---|---|---|
| In situ AgNP enlargement | µM-level, moderate sensitivity | 2–100 µM to 10–200 µM (matrix-dependent) | 1–10 min | Kelly et al. 2003; Teerasong et al. 2017; Apak et al. 2016 |
| Seed-mediated growth TAC | 0.05–0.2 µM, tunable high sensitivity | 0.1–200 µM (purified → crude extracts) | ≤1 min to few min | Özyürek et al. 2012; Szydłowska-Czerniak et al. 2012 |

**Table 4.** Solid-state and green-matrix AgNP TAC sensor frameworks

| Embedded AgNP TAC Platform | Practical LOD / Sensitivity | Typical Portable Linear Working Range | Typical Signal Time Frame | Ref |
|---|---|---|---|---|
| Biopolymer-film TAC sensors | µM-equiv., diffusion-limited sensitivity | 5–200 µM (solid matrix dependent) | 5–20 min | Zor et al. 2014; Teerasong et al. 2017 |
| Green-extract-driven TAC | 2–50 µg/mL, batch-sensitive | Wide, batch-dependent | 5–30 min | Martínez-Cabañas et al. 2021; Beğiç et al.2021 |

## 7. FUTURE PERSPECTIVES AND APPLICATION AREAS

Silver nanoparticle-based antioxidant assays are positioned not only to address current analytical needs but also to shape the next generation of sensing technologies. Advances in nanotechnology have enabled the integration of AgNP-based optical systems into microfluidic platforms, paper-based devices, biopolymer films, and smartphone-assisted readout modules. Owing to the strong chromatic response of surface plasmon resonance, these methods support the development of low-cost, portable, and user-friendly analytical tools (Zor et al., 2024).

Microfluidic systems offer precise control over AgNP nucleation and growth under laminar-flow conditions, enabling exceptionally rapid reaction times, reduced reagent consumption, and enhanced kinetic resolution. Multichannel microfluidic chips facilitate simultaneous screening of multiple antioxidant types, providing high-throughput analysis capabilities. Recent studies indicate that AgNP-based microfluidic sensors can be extended beyond antioxidant detection to include metal-ion sensing and biomolecular interaction analysis (Martínez-Cabañas et al., 2021).

Smartphone-based analytical systems represent another promising direction. Through high-resolution imaging and RGB-based quantification, the intense color transitions associated with AgNP formation can be transformed into objective analytical signals. Coupled with machine-learning–enhanced mobile applications, these platforms can deliver laboratory-grade accuracy in field settings. This approach is particularly attractive for food quality monitoring, herbal product authentication, and consumer-oriented rapid testing devices.

In biomedical analysis, AgNPs offer dual optical–redox functionality that can be leveraged to monitor oxidative stress biomarkers, evaluate antioxidant therapies, and quantify reactive oxygen species–related biochemical changes in serum or plasma. However, nanoparticle stability in biological matrices remains a challenge due to protein corona formation, which can alter particle growth behavior and SPR response (Szydłowska-Czerniak & Tułodziecka, 2013). In food analytics, AgNP-based assays show strong potential for rapid quality assessment, spoilage tracking, and evaluation of processing effects in polyphenol-rich products such as olive oil, tea, wine, honey, and fruit juices. Their portability and fast response time offer significant advantages for on-site quality control.

A key emerging direction involves coupling AgNP-based antioxidant assays with nanotoxicological assessments. Understanding nanoparticle–cell interactions, intracellular redox perturbations, and biological compatibility will allow these methods to evolve from purely chemical assays into biologically informed diagnostic tools. Overall, the future of AgNP-based antioxidant assays is defined by their versatility, optical sensitivity, miniaturization capacity, and

compatibility with modern sensor technologies. These characteristics position them as powerful tools in next-generation analytical chemistry.

## 8. OVERALL ASSESSMENT AND CONCLUSION

Silver nanoparticle-based antioxidant assays represent a significant advancement in analytical chemistry by overcoming several inherent limitations of classical TAC methods. The high optical sensitivity of surface plasmon resonance, the controlled growth enabled by seed-mediated strategies, and the electron-transfer-based reaction mechanism make these assays not only sensitive but also mechanistically informative (Özyürek et al., 2012). Their ability to selectively evaluate electron-transfer–dominant antioxidants distinguishes them clearly from radical scavenging assays, whose analytical performance is often influenced by radical stability and solvent effects (Apak et al., 2016).

The controlled manipulation of nucleation and growth processes improves reproducibility, establishing AgNP-based assays as robust and reliable analytical platforms. The responsiveness of the SPR band to antioxidant redox kinetics allows the technique to deliver more than endpoint measurements; it also enables the extraction of kinetic profiles valuable for mechanistic interpretation. Nonetheless, nanoparticle stability issues—particularly sensitivity to chloride ions, proteins, ionic strength, and pH—highlight the need for careful optimization when analyzing complex matrices (Szydłowska-Czerniak & Tułodziecka, 2013).

Green synthesis approaches make AgNP assays more environmentally sustainable while enabling direct assessment of plant extract phenolic content. The development of polymer-based films, paper microfluidic devices, and portable colorimetric sensors further expands the applicability of the technique beyond laboratory settings (Martínez-Cabañas et al., 2021; Zor et al., 2024). These advancements open opportunities for rapid on-site screening, food quality testing, and portable diagnostic applications. Looking ahead, integration with microfluidic platforms, AI-assisted image analysis, smartphone-based color quantification, and biomedical monitoring tools will likely shape the next phase of AgNP assay development. In particular, portable tracking of oxidative stress biomarkers may position AgNP-based sensors as valuable tools in clinical and point-of-care diagnostics.

In summary, silver nanoparticle-based antioxidant assays combine optical sensitivity, mechanistic selectivity, miniaturization capability, and application versatility, making them a compelling alternative in modern analytical chemistry. When their limitations are adequately managed, they serve as a powerful complement to existing TAC methods in both research and industry.

## REFERENCES


Apak, R., Güçlü, K., Özyürek, M., & Karademir, S. E. (2004). Novel total antioxidant capacity index for dietary polyphenols and vitamins C and E using their cupric ion reducing capability in the presence of neocuproine: The CUPRAC method. *Journal of Agricultural and Food Chemistry, 52*(32), 7970–7981.

Apak, R., Özyürek, M., Güçlü, K., & Çapanoğlu, E. (2016). Antioxidant activity/capacity measurement. I. Classification, physicochemical principles, mechanisms, and electron transfer (ET)-based assays. *Journal of Agricultural and Food Chemistry, 64*(5), 997–1027.

Asghar, M. A., Zahir, E., Shahid, S. M., Khan, M. N., Iqbal, J., & Walker, G. (2018). Iron, copper and silver nanoparticles: Green synthesis using green and black tea leaf extracts and evaluation of antibacterial, antifungal and aflatoxin B1 adsorption activity. *LWT – Food Science and Technology, 90*, 98–107.

Car, J., & Krstulović, V. (2022). Analytical model for determination of size-distribution of colloidal silver nanoparticles from their surface plasmon resonance wavelength and dielectric functions. *Nanomaterials, 12*(19), 3474.

Chambers, B. A., Afrooz, A. R. M. N., Bae, S., Aich, N., Katz, L., Saleh, N. B., & Kirisits, M. J. (2014). Effects of chloride and ionic strength on physical morphology, dissolution, and bacterial toxicity of silver nanoparticles. *Environmental Science & Technology, 48*(1), 761–769.

Chhatre, A., Solasa, P., Sakle, S., Thaokar, R., & Mehra, A. (2012). Color and surface plasmon effects in nanoparticle systems: The case of silver nanoparticles prepared by the microemulsion route. *Colloids and Surfaces A: Physicochemical and Engineering Aspects, 404*, 83–92.

Devanesan, S., AlSalhi, M. S., Balaji, R. V., Ranjitsingh, A. J. A., Ahamed, A., Alfuraydi, A. A., AlQahtani, F. Y., Aleanizy, F. S., & Othman, A. H. (2018). Antimicrobial and cytotoxicity effects of silver nanoparticles synthesized from Punica granatum peel extract. Nanoscale Research Letters, 13, 315.

Farghaly, A. A., & Nafady, N. A. (2015). Green synthesis of silver nanoparticles using *Rosmarinus officinalis* leaf extract and their antibacterial activity. *Journal of Agricultural Science, 7*(3), 277–287.

Gonzalez, A. L., Noguez, C., Beránek, J., & Barnard, A. S. (2014). Size, shape, stability, and color of plasmonic silver nanoparticles. *The Journal of Physical Chemistry C, 118*(17), 9128–9136.

Kelly, K. L., Coronado, E., Zhao, L. L., & Schatz, G. C. (2003). The optical properties of metal nanoparticles: The influence of size, shape, and dielectric environment. *The Journal of Physical Chemistry B, 107*(26), 668–677.

Martínez-Cabañas, M., López-García, M., Rodríguez-Barro, P., Vilariño, T., Lodeiro, P., Herrero, R., Barriada, J. L., & Sastre de Vicente, M. E. (2021).

Antioxidant capacity assessment of plant extracts for green synthesis of nanoparticles. *Nanomaterials, 11*(7), 1679.

Sosa, I. O., Noguez, C., & Barrera, R. G. (2003). Optical properties of metal nanoparticles with arbitrary shapes. *The Journal of Physical Chemistry B, 107*(26), 6269–6275.

Sulistyarti, H., Utama, M. M., Fadhila, A. M., Cahyaningrum, A., Murti, R. J., & Febriyanti, A. (2023). Green synthesis of silver nanoparticles using *Coffea canephora* fruit-skin extract and application for mercury detection in cosmetic matrices. *Analytical Sciences, 39*(3), 335–346.

Szydłowska-Czerniak, A., Tułodziecka, A., & Szłyk, E. (2012). A silver nanoparticle-based method for determination of antioxidant capacity of rapeseed and products. *Analyst, 137*(16), 3750–3759.

Szydłowska-Czerniak, A., & Tułodziecka, A. (2013). Comparison of a silver nanoparticle-based method with modified spectrophotometric TAC approaches in rapeseed varieties. *Food Chemistry, 141*(3), 1865–1873.

Teerasong, S., Jinnarak, A., Chaneam, S., Wilairat, P., & Nacapricha, D. (2017). Poly(vinyl alcohol) capped silver nanoparticles for antioxidant assay based on seed-mediated nanoparticle growth. Talanta, 170, 193–198.

Tekin, V., Kozgus Guldu, O., Dervis, E., Yurt Kilcar, A., Uygur, E., & Muftuler, F. Z. (2019). Green synthesis of silver nanoparticles using eugenol and evaluation of antimicrobial potential. *Applied Organometallic Chemistry, 33*(6), e4969.

Zor, M., Güçlü, K., Özyürek, M., & Apak, R. (2024). Development of a silver nanoparticle-chitosan composite film for determination of total antioxidant capacity of fruit juices and botanical extracts. *Journal of Taibah University for Science, 18*, 2331436.

# CHAPTER 6

# Synthesis and Characterization of Mixed N-Heterocyclic Carbene/Bidentate N-Donor Ligand Copper(I) Complexes

**Deniz Demir Atlı**[1]

[1] Doç. Dr., Manisa Celal Bayar University, ORCID: 0000-0001-8442-4916

## 1. INTRODUCTION

The stable complexes formed by the strong σ-donor N-heterocyclic carbenes (NHCs) with transition metals have been of interest to scientists for many years. These compounds have a broad spectrum of applications, particularly in the field of homogeneous catalysis. Among them, the copper(I) NHC compounds have been widely studied since their first synthesis in 1993 because they are relatively cheap and less toxic (Arduengo et al., 1993). The synthesis methods can be listed as follows: Deprotonation of NHC precursors (in situ) with a base (Beig et al., 2023; Sk et al., 2024), transmetallation (Garcés et al., 2015 Chen et al., 2025) and ligand displacement (Bour et al., 2017; Hashim et al., 2022).

Many significant transformations, such as hydrosilylation (Cheng and Mankad, 2020; Cheng and Mankad, 2021; Lin et al., 2025), [3+2] cyloaddition reactions (Hall et al., 2021; González-Lainez et al. 2022), A3 reactions (Rokade et al., 2019; Beig et al., 2023), boration and hydroboration (DiBenedettoet al., 2019; English et al., 2023; Rutz and Kleeberg, 2024) are efficiently catalysed by NHC-Cu(I) complexes. These compounds have antibacterial activity and also act as anticancer agents (Jakob et al., 2021; Nayak and Gaonkar, 2021; Alsalhi, 2023; Chen et al. 2025). NHC copper (I) complexes exhibit photophysical properties (Wang et al. 2020; Cheng et al. 2023; Dou et al., 2024). Photoluminescent LEDs and anti-counterfeiting applications have been successfully manufactured (Wu et al., 2024).

In this work, a novel neutral NHC-copper(I) chloride complex and its two cationic derivatives containing bidentate N-donor ligands are prepared. The structures of the complexes are determined by $^{1}$H NMR, $^{13}$C NMR, $^{31}$P NMR, LC-MS/MS and elemental analysis methods.

## 2. EXPERIMENTAL

### 2.1. General Remarks

The synthesis procedures were executed under argon atmosphere and dried solvents were used. **1** was prepared in accordance with the literature (Demir Atlı, 2021).

### 2.2. Synthesis of [CuCl(NHC)] (2)

The mixture of **1** (0.28 g, 0.71 mmol), $Cu_2O$ (74.5 mg, 0.52 mmol) and some molecular sieve in 1,2-dichloroethane (20 mL) was stirred at 90 °C for 24 hours. 1,2-dichloroethane was removed at reduced pressure. THF was added and filtration was performed. The filtrate was concentrated. White solids were precipitated by adding n-hexane. Yield: 0.26 g, 81%. $^{1}$H NMR (400 MHz, $CDCl_3$): δ = 7.23 (d, *J* = 8.3 Hz, 4H, Ar-H), 7.09 (d, *J* = 7.7 Hz, 2H, Ar-H), 7.03

(d, *J* = 7.8 Hz, 2H, Ar-H), 6.68 (s, 2H, Ar-H), 5.60 (s, 4H, $NCH_2$), 2.32 (s, 6H, $CH_3$), 2.20 (s, 6H, $CH_3$) ppm. $^{13}C$ NMR (101 MHz, $CDCl_3$): δ = 136.2, 133.9, 132.5, 132.4, 130.9, 129.1, 127.8, 124.2, 112.0, 51.1, 21.1, 19.2 ppm. Anal. Calcd. for $C_{25}H_{26}N_2ClCu$ (%): C, 66.20; H, 5.79; N, 6.18. Found: C, 66.43; H, 5.62; N, 6.28.

### 2.3. Synthesis of [Cu(NHC)(phen)]$PF_6$ (3)

The mixture of **2** (65.4 mg, 0.14 mmol), phen (33.7 mg, 0.19 mmol) ve $KPF_6$ (34.4 mg, 0.19 mmol) in acetone (15 mL) was stirred at 25 °C for 48 hours. The solvent was removed at reduced pressure. After $CH_2Cl_2$ (15 mL) addition, the filtration was carried out through celite. The solvent was removed from the filtrate at reduced pressure. Recrystallization using methanol/$Et_2O$ (1/4) solvent system gave yellow product. Yield: 86 mg, 83%. $^1H$ NMR (400 MHz, dmso-$d_6$): δ = 8.78 (s, 2H, Ar-H), 8.44 (s, 2H, Ar-H), 8.21 (s, 2H, Ar-H), 7.96 (s, 4H, Ar-H), 7.50 (dd, J = 6.0, 3.2 Hz, 2H, Ar-H), 6.86 (s, 2H, Ar-H), 6.60 (d, J = 7.6 Hz, 2H, Ar-H), 6.04 (d, J = 7.6 Hz, 2H, Ar-H), 5.44 (s, 4H, $NCH_2$), 2.01 (s, 6H, Me), 1.02 (s, 6H, Me) ppm. $^{13}C$ NMR (101 MHz, dmso-$d_6$): δ = 134.2, 134.2, 133.8, 133.6, 130.4, 129.9, 127.8, 123.5, 111.2, 50.8, 19.8, 17.8 ppm. $^{31}P$ NMR (162 MHz, dmso-$d_6$): δ = -144.16 (septet, $PF_6^-$) ppm. LC-MS/MS ($CH_2Cl_2$): $[M\text{-}PF_6\text{-}H]^-$ at m/z 597.2. Anal. Calcd. for $C_{37}H_{34}N_4CuPF_6$ (%): C, 59.79; H, 4.62; N, 7.54. Found: C, 59.17; H, 5.39; N, 7.43.

### 2.4. Synthesis of [Cu(NHC)(bipy)]$PF_6$ (4)

Compound **4** was obtained by the reaction of **2** (26.7 mg, 0.059 mmol) with bipy (11.9 mg, 0.076 mmol) and $KPF_6$ (14.1 mg, 0.076 mmol) with the same method as that used for the compound **3**. Yellow solid. Yield: 32.6 mg, 77%. $^1H$ NMR (400 MHz, dmso-$d_6$): δ = 8.48 (s, 2H, Ar-H), 8.14 (s, 4H, Ar-H), 7.92 (dd, *J* = 6.1, 3.1 Hz, 2H, Ar-H), 7.62 (s, 2H, Ar-H), 7.48 (dd, *J* = 6.0, 3.1 Hz, 2H, Ar-H), 6.86 (s, 2H, Ar-H), 6.65 (d, *J* = 7.6 Hz, 2H, Ar-H), 6.35 (d, *J* = 8.7 Hz, 2H, Ar-H), 5.41 (s, 4H, $NCH_2$), 1.99 (s, 6H, Me), 1.49 (s, 6H, Me) ppm. $^{13}C$ NMR (101 MHz, dmso-$d_6$): δ = 134.4, 134.1, 133.7, 133.4, 130.6, 130.0, 128.1, 123.4, 111.2, 49.2, 19.7, 18.2 ppm. $^{31}P$ NMR (162 MHz, dmso-$d_6$): δ = -144.16 (septet, $PF_6^-$) ppm. LC-MS/MS ($CH_2Cl_2$): $[M\text{-}PF_6\text{-}H]^-$ at m/z 573.2. Anal. Calcd. for $C_{35}H_{34}N_4CuPF_6$ (%): C, 58.44; H, 4.77; N, 7.79. Found: C, 57.61; H, 5.16; N, 7.33.

## 3. RESULTS AND DISCUSSION

The synthetic scheme for the NHC copper(I) complexes is shown in Figure 1. Neutral [CuCl(NHC)] complex (**2**) was synthesized by deprotonation of **1** with $Cu_2O$ in 1,2-dichloroethane at 90 °C. White product which was recrystallized

from THF/n-hexane mixture in 81% yield. It is soluble in $CH_2Cl_2$, THF, acetonitrile and insoluble in n-hexane and $Et_2O$.

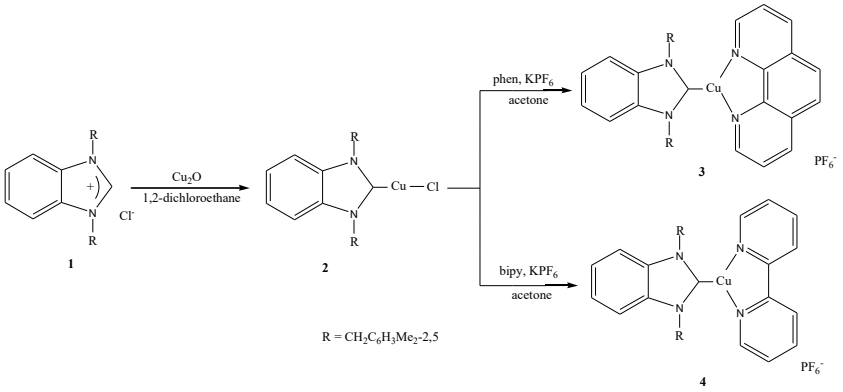


**Figure 1**. Synthesis of the NHC-Cu(I) complexes

Cationic NHC-Cu(I) complexes (**3** and **4**) were synthesized using the procedure outlined in the literature (Guo et al., 2013). The reaction of [CuCl(NHC)] with bidentate ligand (phen or bipy) and $KPF_6$ in acetone afforded the products in high yields. The solubilities of these are similar to those of the **2**.

The copper(I) complexes were characterized by $^{1}H$ NMR, $^{13}C$ NMR, $^{31}P$ NMR, LC-MS/MS and elemental analysis methods. The elemental analysis results are close to theoretical values. The NMR data indicates that the desired compounds have been formed. In the $^{1}H$ NMR spectrum of **2**, the disappearance of the downfield signal of the salt compound indicates that deprotonation occurred and the copper(I) complex was formed (Figure 2) (Demir Atlı, 2021). No $C_{carbene}$ signal was detected in the $^{13}C$ NMR spectrum of compound **2**. Observation of the This situation is thought to stem from the lability of the Cu-$C_{carbene}$ bond. The $^{1}H$ NMR spectra of **3** and **4** show signals from aromatic protons in the range 6.04-8.78 ppm and 6.35-8.48 ppm, respectively (Figures 3 and 4). Their integrations are consistent with the proposed structures. As in the case of compound **2**, no signal was observed for the carbene carbon in these compounds. (Demir Atlı and Sözerli, 2019). The $^{31}P$ NMR spectra of these two complexes, which are hexafluorophosphate salts, show a septet signal at -144.16 ppm in accordance with the literature (Perera, 2021). The $[M\text{-}PF_6\text{-}H]^+$ peaks observed at 597.2 and 573.2 in the LC-MS/MS spectra for **3** and **4**, respectively, also confirm the formation of these cationic compounds (Figures 5 and 6).

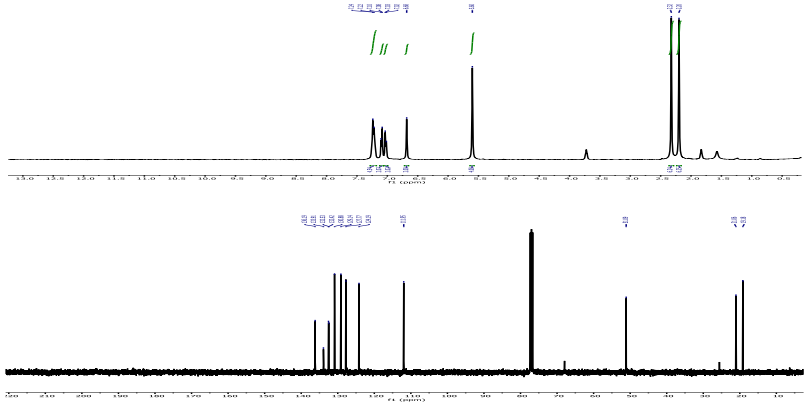

**Figure 2.** $^{1}$H NMR and $^{13}$C NMR spectra of **2**

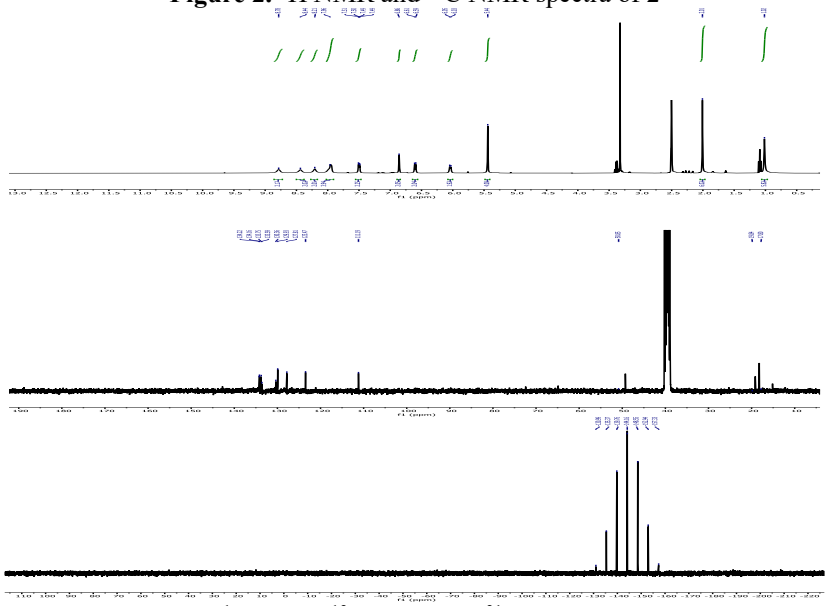

**Figure 3.** $^{1}$H NMR, $^{13}$C NMR and $^{31}$P NMR spectra of **3**

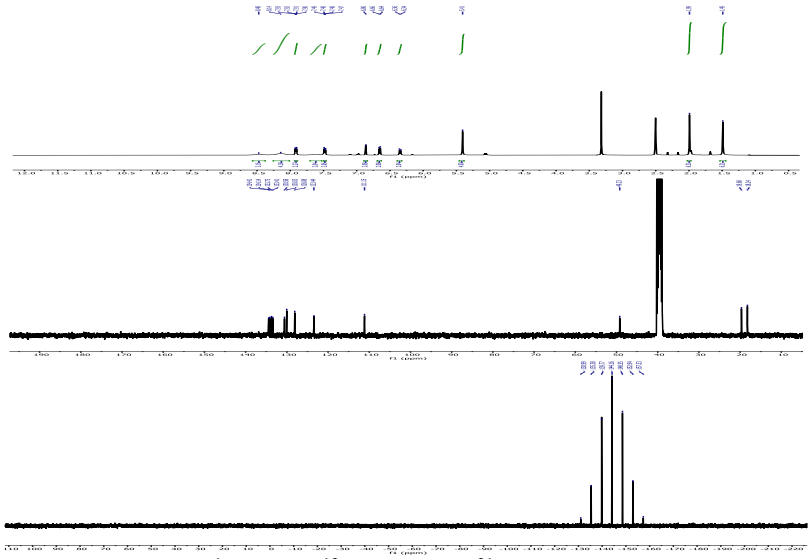

**Figure 4.** $^{1}$H NMR, $^{13}$C NMR and $^{31}$P NMR spectra of **4**

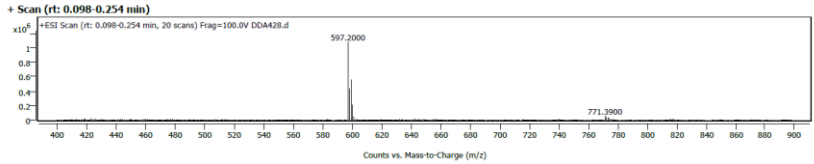


**Figure 5.** LC-MS/MS spectrum of **3**

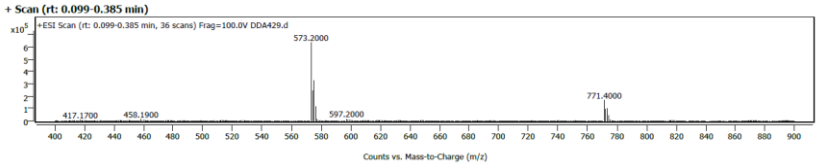


**Figure 6.** LC-MS/MS spectrum of **4**

## 4. CONCLUSIONS

In this study, three new NHC-copper(I) complexes were synthesized. The compounds were characterized by NMR spectroscopy, LC-MS/MS and elemental analysis methods. Research into the various applications of these complexes is ongoing.


## ACKNOWLEDGEMENTS

This work was supported by the Manisa Celal Bayar University Scientific Research Projects Coordination Unit. Project Number: 2022-001.

## REFERENCES


Alsalhi, A. (2023), N-heterocyclic carbene complexes of Au(I), Ag(I), and Cu(I) as potential anticancer agents: a review, *Journal of Coordination Chemistry*, 76 (7-8), 847-861

Arduengo III, A.J., Dias, H.V.R., Calabrese, J.C., Davidson, F. (1993) Homoleptic carbene-silver(I) and carbene-copper(I) complexes, *Organometallics*, 12 (9), 3405-3409

Beig, N., Goyal, V., Bansal, R.K. (2023), N-heterocyclic carbene: thiazolylidene–Cu(I) complexes: microwave-assisted synthesis and use as catalyst in A3 reaction, *Phosphorus, Sulfur and Silicon and the Related Elements*, 198 (8), 682–692

Bour, J.R., Kariofillis, S.K., Sanford, M.S. (2017), Synthesis, reactivity, and catalytic applications of isolable (NHC)Cu(CHF2) complexes, *Organometallics*; 36 (7), 1220–1223

Cheng, L.J., Mankad, N.P. (2020) Cu-catalyzed carbonylative silylation of alkyl halides: Efficient access to acylsilanes, *Journal of the American Chemical Society,* 142 (1), 80–84

Cheng, L.J., Mankad, N.P. (2021), Copper-catalyzed carbonylative coupling of alkyl halides, *Accounts of Chemical Research,* 54 (9), 2261–2274

Cheng, Y., Gontard, G., Khatyr, A., Knorr, M., Amouri, H. (2023), N-heterocyclic carbene copper (I) complexes incorporating pyrene chromophore: Synthesis, crystal structure, and luminescent properties, *Molecules*, 28 (10), 4025

Demir Atlı, D., Sözerli, Ş.E. (2019), Synthesis, characterization and catalytic properties of cationic N-heterocyclic carbene copper(I) complex, *Celal Bayar University Journal of Science,* 15 (1), 95-98

Demir Atlı, D. (2021), A mixed N-heterocyclic carbene/triphenylphosphine palladium(II) complex for Suzuki-Miyaura cross-coupling reactions, *Celal Bayar University Journal of Science,* 17 (4), 405-415

DiBenedetto, T.A., Parsons, A.M., Jones, W.D. (2019), Markovnikov-selective hydroboration of olefins catalyzed by a copper N-heterocyclic carbene complex, *Organometallics,* 38 (17), 3322–3326

English, L.E., Downie, T.M.H., Lyall, C.L., Mahon, M.F., McMullin, C.L., Neale, S.E., Saunders, C.M., Liptrot, D.J. (2023), Selective hydroboration of electron-rich isocyanates by an NHC-copper(I) alkoxide, *Chemical Communications*, 59, 1074-1077

Garcés, K., Fernández-Alvarez, F.J., García-Orduña, P., Lahoz, F.J., Pérez-Torrente, J.J., Oro, L.A. (2015), Grafting of copper(I)–NHC species on MCM-41: Homogeneous versus heterogeneous catalysis, *ChemCatChem*, 7 (16), 2501–2507

González-Lainez, M., Gallegos, M., Munarriz, J., Azpiroz, R., Passarelli, V., Jiménez, M.V., Pérez-Torrente, J.J. (2022), Copper-catalyzed azide–alkyne cycloaddition (CuAAC) by functionalized NHC-based polynuclear catalysts: Scope and mechanistic insights, *Organometallics*, 41 (15), 2154–2169

Guo, S., Lim, M.H., Huynh, H.V. (2013), Copper(I) heteroleptic bis(NHC) and mixed NHC/phosphine complexes: Syntheses and catalytic activities in the one-pot sequential CuAAC reaction of aromatic amines, *Organometallics*, 32 (23), 7225-7233

Hall, J.W., Bouchet, D., Mahon, M.F., Whittlesey, M.K., Cazin, C.S.J. (2021), Synthetic access to ring-expanded N-heterocyclic carbene (RE-NHC) copper complexes and their performance in click chemistry, *Organometallics*, 40 (9), 1252-1261

Hashim, I.I., Scattolin, T., Tzouras, N.V., Bourda, L., Hecke, K.V., Ritacco, I., Caporaso, L., Nolan, S.P., Cazin, C.S.J. (2022), Straightforward synthesis of [Cu(NHC)(alkynyl)] and [Cu(NHC)(thiolato)] complexes (NHC = N-heterocyclic carbene, *Dalton Transactions*, 51 (1), 231-240

Jakob, C.H.G., Munoz, A.W., Schlagintweit, J.F., Weiß, V., Reich, R.M., Sieber, S.A., Correia, J.D.G., Kühn, F.E. (2021), Anticancer and antibacterial properties of trinuclear Cu(I), Ag(I) and Au(I) macrocyclic NHC/urea complexes, *Journal of Organometallic Chem*istry, 932, 121643

Lin, C.F., Tseng, Y.H., Hsieh, H.Y., Hung, P.J., Huang, Y.W., Lee, D.S., Lu, T.J. (2025), Development of new indole-based N-heterocyclic carbene copper complexes and their applications in catalysis, *The Journal of Organic Chemistry*, 90 (22), 7236-7245

Nayak, S., Gaonkar, S.L. (2021), Coinage metal N-heterocyclic carbene complexes: Recent synthetic strategies and medicinal applications, *ChemMedChem*, 16 (9), 1360-1390

Perera, S.D. (2021), Synthesis of platinum(II) complexes of a pyridyl azafluoranthene ligand, *Rajarata University Journal*, 6 (1), 29-36

Rokade, B.V., Barker, J., Guiry, P.J. (2019), Development of and recent advances in asymmetric A3 coupling, *Chemical Society Rev*iews, 48 (18), 4766–4790

Rutz, P.M., Kleeberg, C. (2024), Copper catalyzed borylation of alkynes: An experimental mechanistic study, *Chemistry An Asian Journal*, 19 (14), e202400286

Sk, A.I., Ghosh, A., Kundu, K., Murugan, I., Kundu, P.K. (2024), Azobenzene-attached (NHC)gold(I) and (NHC)copper(I) complexes as photoswitchable catalysts, *Chemistry-A European Journal*, 30 (64), e202402381

Wang, J., Chen, H., Xu, S., Su, Q., Zhao, F., He, H. (2020), Highly effective luminescence stemmed from thermally activated delayed fluorescence

(TADF) and phosphorescence for the new four-coordinate copper(I) complexes containing N-heterocyclic carbene (NHC) ligands, *Journal of Photochemistry and Photobiology A: Chemistry,* 387, 112104

Wu, X., Liu, S., Chen, H., Ding, H., Xu, S., Wu, Y., Wang, Y., Zhao, F. (2024), Synthesis and photophysical properties of dinuclear N-heterocyclic carbene (NHC) copper(I) complexes and their application to photoluminescent light-emitting diodes and anti-counterfeiting, *Spectrochimica Acta Part A: Molecular and Biomolecular Spectroscopy,* 308, 123758

# CHAPTER 7

# A Compact Low-Cost Ball Milling System: Design, Fabrication and Preliminary Mg–Al Powder Processing

**Tuna Aydoğmuş**[1]

[1] Assoc. Prof. Dr., Hitit University, ORCID: 0000-0002-8736-2949

## 1. Introduction

Ball milling is a versatile process widely utilized in powder metallurgy, mechanical alloying, composite fabrication, and particle-size refinement. Its fundamental mechanism is based on repeated deformation, cold welding, fracturing, and re-welding cycles driven by the kinetic energy of colliding balls within a confined milling chamber (Khoa, Bae, Bae, Kim, & Kim, 2014). In particular, high-energy ball milling can alter powder morphology within minutes, making it an essential tool for materials scientists working on alloy development, surface modification, and solid-state reactions (Gupta, Murty, & Birbilis, 2017; Nagesha, Rajanish, & Shivappa, 2013; C Suryanarayana, 2022).

Despite its usefulness, commercial ball milling systems are often associated with several limitations. High-energy planetary mills and attrition mills are expensive, heavy, and require specialized laboratory infrastructure. Their rigid design restricts researchers from tailoring the milling environment, cell geometry, or ball–powder configuration to specific experimental conditions. Furthermore, their large batch capacities make them unsuitable for preliminary micro-scale alloying trials where only a few grams of powder are available (Gilleland, Hornbuckle, Darling, & Thompson, 2025; Khoa et al., 2014; Challapalli Suryanarayana, 2019).

To overcome these constraints, a compact and cost-effective ball milling system was designed and fabricated in-house. The aim was to develop a device that is easy to operate, cost-efficient, and flexible enough to support rapid small-scale experiments. The milling cell was fabricated from AISI 2379 tool steel—a material known for its high wear resistance—ensuring durability even at high impact intensities (Mottaghi, Rahman, Kulkarni, & Pearce, 2023; Sharma, Raj, & Jangra, 2016; C Suryanarayana, 2022).

Mg and Al powders were intentionally selected as the first test materials due to their high plastic deformability, strong affinity during cold welding, and relevance in lightweight alloy development. Early-stage morphological changes in Mg–Al mixtures provide valuable insights into the effectiveness of milling energy transfer. Short milling durations (5–15 min) are particularly suitable to demonstrate the capacity of the newly designed system.

This paper documents:

1. The design and fabrication concept of the milling system,
2. The characteristics of the custom-built milling cell,
3. The preliminary milling experiments on Mg–Al powders,
4. The morphological evolution of particles and the WC ball surface.

## 2. Materials and Methods

### 2.1. Design and Structural Features of the Milling System

The milling system was engineered to provide high-frequency impact forces within a small-volume environment. The core structure consists of a compact steel frame supporting a 3000 rpm electric motor. The motor drives the milling cell via a belt–pulley transmission, enabling smooth and stable rotation while filtering sudden torque fluctuations. This configuration also reduces vibration, which is essential for consistent milling energy.

The milling cell is the most critical component of the device. It was manufactured from AISI 2379 tool steel, heat-treated under vacuum and quenched to produce a final hardness near 70 HRC. The high hardness ensures resistance against abrasive wear, micro-chipping, and dimensional distortion during repetitive impacts with the WC ball.

The effective internal volume of the cell is approximately 8 $cm^3$, making it suitable for micro-scale milling trials. All inner surfaces were sandblasted to slightly roughen the texture, improving powder–wall interaction and preventing excessive powder slippage during motion.

The overall design philosophy emphasizes:

- Low material cost,
- High durability,
- Ease of maintenance,
- Simple and safe operation,
- Compatibility with single-ball and small-powder experiments.

The external view of the system and the milling cell is provided in Figure 1.

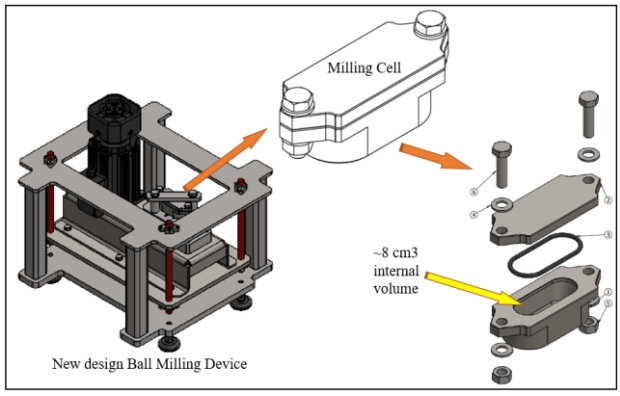


**Figure 1.** General view of the compact ball milling device, including the 3000-rpm motor, belt–pulley assembly, and the custom AISI 2379 milling cell (≈8 $cm^3$ internal volume).

### 2.2. Raw Materials and Initial Characterization

Commercial Mg and Al powders supplied by Nanografi were used. Both powders exhibit 10–40 μm spherical morphology, which ensures stable flowability and reproducible packing behavior.

For each experiment:

- 1 g Mg + 1 g Al powder mixture was used,
- A single 5 mm WC ball served as the milling medium,
- No process control agent was added.

Initial images of powders and the unused ball are presented in Figure 2.

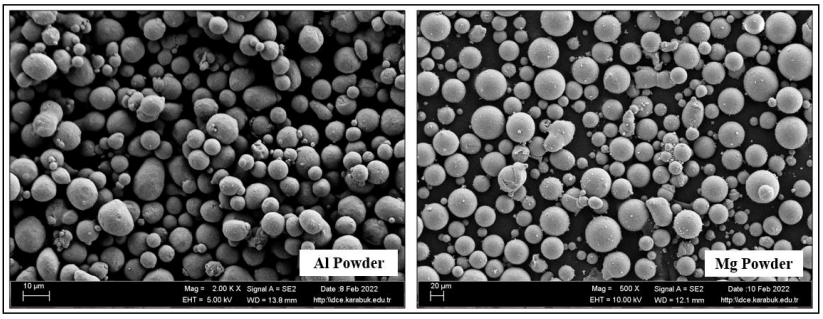


**Figure 2.** Initial morphology of Mg–Al powders (10–40 μm spherical) and the 5 mm WC ball before milling.

### 2.3. Milling Procedure

Experiments were carried out at ambient atmosphere without lubrication. Milling durations were selected as:

- 5 minutes,
- 10 minutes,
- 15 minutes.

These short durations were chosen deliberately to highlight early morphological transitions. After milling, the powders and WC ball were collected, cleaned, and examined under SEM to observe deformation, welding, fragmentation, and adhesion mechanisms.

## 3. Results and Discussion

### 3.1. Operational Performance of the Designed System

The system demonstrated stable rotational behavior throughout the tests. The belt–pulley assembly effectively dampened excessive vibration, allowing a

consistent impact pattern within the compact cell. No overheating, abnormal noise, or structural displacement was observed during operation.

The 8 $cm^3$ volume of the milling cell facilitated intense collision between the ball and powders, generating sufficient mechanical energy even with a single 5 mm WC ball. This confirms that the design is appropriate for high-energy interactions within limited powder quantities.

### 3.2. Initial Powder and Ball Morphology

Figure 2 shows that the starting Mg–Al powders possess smooth, spherical surfaces characteristic of gas-atomized powders. The WC ball also exhibits a clean, polished surface with no visible scratches or adhered debris.

Such a well-defined initial morphology provides a clear baseline for evaluating mechanical deformation after milling.

### 3.3. Microstructural Evolution After Milling

**After 5 minutes**

- Mg and Al particles begin to deform under impact, losing their spherical shape.
- Localized cold welding occurs at particle–particle contact points, forming initial necks.
- Few small particle clusters appear, indicating the onset of agglomeration.

**After 10 minutes**

- Cold welding becomes more pronounced.
- Flattened, plate-like particles are observed due to repeated compressive impacts.
- Several welded particles form larger agglomerates with visible neck regions.
- Surface abrasion produces fine debris adhered to the larger particles.

**After 15 minutes**

- The highest deformation level is recorded.
- Extensive agglomeration results in large, interconnected clusters.
- Particles exhibit severe flattening, elongation, and fracture–rewelding cycles.
- The WC ball surface shows metallic flakes, smeared layers, and adhered fragments, demonstrating strong ball–powder interaction.

- These adhered layers confirm that the system provides enough kinetic energy to initiate mechanical alloying-like behavior.

The post-milling results (Figure 3) clearly validate the capability of the newly designed mill to produce measurable morphological changes in very short durations.

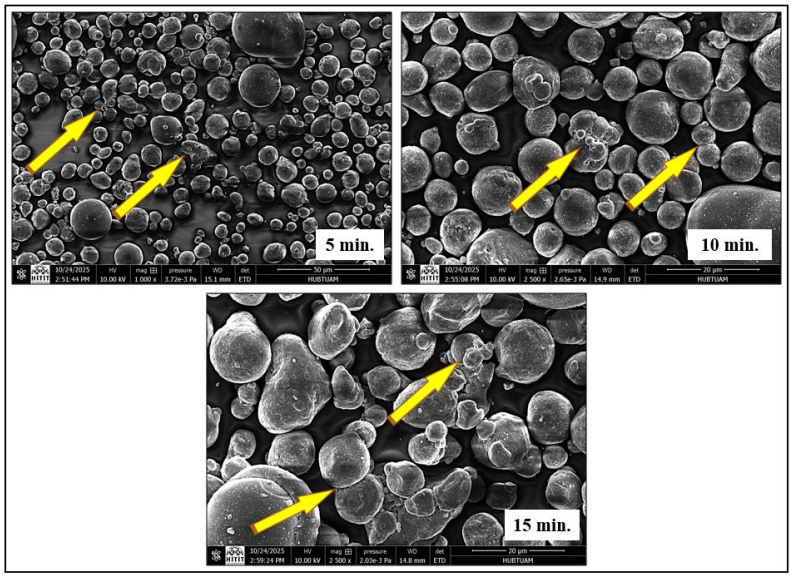


**Figure 3.** SEM images of Mg–Al powders after 5, 10, and 15 minutes of milling.

The condition of the WC ball also reflects the intensity of the milling process. Before milling, the ball surface is clean and smooth with no visible defects. After 15 minutes of operation, metallic flakes, smeared layers, and localized deformation marks appear on the surface due to repeated high-energy impacts with Mg–Al powders. In addition, distinct agglomerated regions and strongly adhered material clusters are visible, indicating significant buildup on the ball surface. These adhered fragments confirm strong ball–powder interaction and demonstrate the onset of mechanical alloying behavior even within short milling durations.

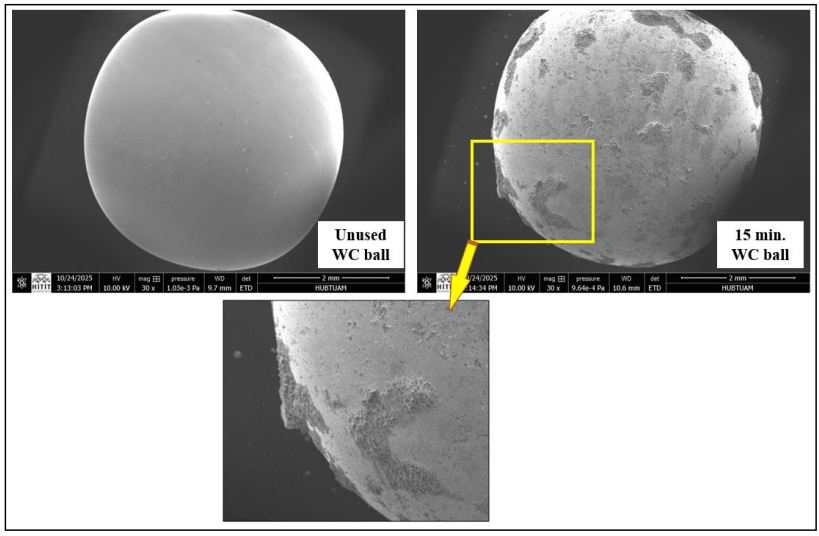


**Figure 4.** Surface condition of the WC ball before milling and after 15 minutes, showing adhered metallic flakes and deformation marks.

Short-duration milling experiments revealed a clear and time-dependent morphological evolution in the Mg–Al powder mixture. After 5 minutes, the powders exhibited early signs of plastic deformation, partial flattening, and the formation of initial necks between contacting particles, indicating the onset of cold-welding behavior. Extending the milling duration to 10 minutes intensified this effect, producing larger welded clusters, more pronounced flake-like structures, and visible fracture–rewelding cycles. By 15 minutes, deformation became severe, with extensive agglomeration, elongated platelets, and interconnected particle networks, demonstrating that the custom system can generate sufficient impact energy for rapid microstructural modification even in very small powder batches (Kim et al., 2015; Song, Kim, Kim, Kim, & Hong, 2010; Tousi, Rad, Salahi, & Razavi, 2009).

The condition of the WC ball further supports these observations. The unused ball initially presents a smooth, defect-free surface, but after 15 minutes of milling, clear metallic adhesion, smeared layers, and localized deformation marks become evident. Strongly adhered agglomerated regions and compacted material patches indicate that repeated high-energy impacts transfer enough kinetic energy to cause both powder adhesion and surface modification of the ball itself (Ajaal, Smith, & Yen, 2002; Gilleland et al., 2025; Johansson, 2012). Overall, the combined powder and ball responses confirm that the developed system provides efficient energy delivery and reliable milling performance, marking it as a practical and effective tool for small-scale mechanical alloying studies.

## 4. Conclusion

This study successfully demonstrated the design, fabrication, and application of a compact, low-cost ball milling system suitable for preliminary powder metallurgy research. Key outcomes include:

1. A durable milling cell made from AISI 2379 tool steel (70 HRC) was developed for long-term impact resistance.
2. The device operates reliably using a 3000-rpm motor and belt–pulley setup.
3. Mg–Al powders showed significant morphological evolution even within 5–15 minutes.
4. Cold welding, neck formation, and particle flattening increased with milling duration.
5. Metallic layers adhered to the WC ball surface confirmed strong energy transfer.
6. The system is well-suited for rapid, low-quantity alloy development studies.

**Acknowledgment:** We would like to thank 4D Machine and Technology for their technical support.

## References


Ajaal, T., Smith, R., & Yen, W. (2002). The development and characterization of a ball mill for mechanical alloying. *Canadian Metallurgical Quarterly, 41*(1), 7-14.

Gilleland, C. A., Hornbuckle, B. C., Darling, K. A., & Thompson, G. B. (2025). Understanding the impact of high-energy ball mill tooling on powder refinement and alloy formation: Microstructural evolution in immiscible W-Cr alloys. *Powder Metallurgy*, 00325899251372204.

Gupta, R. K., Murty, B., & Birbilis, N. (2017). High-energy ball milling parameters in production of nanocrystalline Al alloys *An overview of high-energy Ball Milled nanocrystalline aluminum alloys* (pp. 7-28): Springer.

Johansson, A. (2012). Correlation between process parameters and milling efficiency.

Khoa, H. X., Bae, S., Bae, S., Kim, B.-W., & Kim, J. S. (2014). Planetary ball mill process in aspect of milling energy. *Journal of Powder Materials, 21*(2), 155-164.

Kim, H.-S., Madavali, B., Eom, T.-J., Kim, C.-M., Koo, J.-M., Lee, T., & Hong, S.-J. (2015). Effect of different mechanical milling processes on morphology and microstructural changes of nano and micron Al-powders. *Archives of Metallurgy and Materials, 60*.

Mottaghi, M., Rahman, M., Kulkarni, A., & Pearce, J. M. (2023). AC/off-grid photovoltaic powered open-source ball mill. *HardwareX, 14*, e00423.

Nagesha, K., Rajanish, M., & Shivappa, D. (2013). A review on mechanical alloying. *International Journal of Engineering Research and Applications, 3*(3), 921-924.

Sharma, N., Raj, T., & Jangra, K. K. (2016). Microstructural evaluation of NiTi-powder, steatite, and steel balls after different milling conditions. *Materials and Manufacturing Processes, 31*(5), 628-632.

Song, J.-W., Kim, H.-S., Kim, H.-M., Kim, T.-S., & Hong, S.-J. (2010). Refinement behavior of coarse magnesium powder by high energy ball milling (HEBM). *Journal of Powder Materials, 17*(4), 302-311.

Suryanarayana, C. (2019). Mechanical alloying: a novel technique to synthesize advanced materials. *Research, 2019*, 4219812.

Suryanarayana, C. (2022). Mechanical alloying: a critical review. *Materials Research Letters, 10*(10), 619-647.

Tousi, S. R., Rad, R. Y., Salahi, E., & Razavi, M. (2009). Effect of milling time and addition of alumina powder on the structural properties and fracture surface of nanocrystalline Al. *Materials Science-Poland, 27*(3).

# CHAPTER 8

## The Effects of Olive Leaves on Health

**Hülya Yıldız**[1]

1

## Introduction

Olives have been considered a source of healing among the people; olive fruit, olive oil, leaves and shoots, and extracts obtained from them have been used since ancient times for pain relief, lowering blood pressure, lowering blood sugar, and treating many diseases, including cancer (Pieroni et al., 1996). A study on determining the antioxidant capacity of olive leaves showed that the dried extract of olive leaves has a higher antioxidant potential than the fresh leaf extract (Kamran et al., 2015). The olive tree, belonging to the Oleaceae family, is a long-lived, woody tree that always has green leaves. Olive leaves contain many biologically rich chemical components. Among these compounds, we can mention oleuropein, hydroxytyrosol, flavonoids, phenolic acids, and triterpeneids (Guerreiro et al., 2023, Pongrac et al 2022).

## Chemical Composition of Olive Leaves

The ratio of chemical components in olive leaves varies depending on the geographical region, olive variety, leaf maturity, harvest time, and extraction method. Young leaves are generally richer in oleuropein, while the proportion of flavonoids and triterpenoids may increase in mature leaves (Lockyer et al., 2017, Pongrac et al 2022).

### 1. Polyphenol Compounds

Olive leaves contain the highest proportion of oleuropein, a phenolic glycoside. Oleuropein ($C_{25}H_{32}O_{13}$; ma: 540.51 g/mol) is a secoiridoid found in the fruit and especially the leaves of the olive tree (Duke, 1992). Oleuropein, which gives olives and olive oil their bitter-astringent taste, is a glycosidic ester of hydroxytyrosol and elenolic acid (Panizzi et al., 1960; Andrewes et al., 2003). Oleuropein's antioxidant, anti-inflammatory, antimicrobial, and cardioprotective properties are quite important for human health (Somova et al., 2003; de Bock et al., 2013). While the oleuropein content in olive oil ranges from 0.005-0.12%, in olive leaves it ranges from 1-14%. Oleuropein can be obtained in various proportions through leaf extraction (Yıldız & Uylaşer, 2011). Studies have investigated the effects of oleuropein, obtained from olive leaves, on oxidative damage, enzymatic and non-enzymatic antioxidant compounds in diabetic rabbits given alloxan. It was reported that oleuropein has the ability to inhibit hyperglycemia and oxidative damage associated with diabetes and is beneficial in preventing complications related to oxidative stress (Al-Azzawie et al., 2006).

### 2. Flavonoids

Olive leaves are known to contain flavonoid compounds such as luteolin, apigenin, and diosmetin. Although the flavonoid concentration in the leaf varies, these flavonoids increase the plant's antioxidant capacity. Along with antioxidant activity, these flavonoids play a role in eliminating free radicals and modulating cellular inflammatory responses (Visioli et al., 2002).

**3. Hydroxytyrosol and Tyrosol**

Hydroxytyrosol and tyrosol are powerful antioxidants. These antioxidant compounds are released during the hydrolysis of the flavonoid oleuropein. These released antioxidants are effective in protecting cellular DNA from oxidative damage by inhibiting ROS production, and also in supporting cardiovascular health by preventing lipid peroxidation (Corona et al., 2006).

**4. Phenolic Acids**

Olive leaves are also rich in phenolic acids. The main phenolic acids are caffeic acid, chlorogenic acid, and ferulic acid. These compounds have also been reported to be quite effective in antioxidant activity and in protecting health against metabolic diseases (Benavente-García et al., 2000).

**5. Triterpenoids, Vitamins and Minerals**

Olive leaves also contain triterpenoids such as maslinic acid and oleanolic acid. These terpenoid compounds have anti-inflammatory and hepatoprotective properties (Giner et al., 2007). Olive leaves also contain vitamin C, calcium, magnesium, and potassium, offering additional health benefits (Pongrac et al. 2022).

**Biological Effects of Olive Leaves**

It has been determined that phenolic compounds in olive fruit and leaves have inhibitory and delaying effects on the growth of microorganisms, that olive leaf extract has antioxidant properties (31), and that it is a potential source of antifungal substances and can be used as an additive in the food industry and in the pharmaceutical industry (Korukluoğlu et al. 2008).

**1. Antioxidant Effect**

Polyphenols, flavonoids, hydroxytyrosol and tyrosol, phenolic acids, and triterpenoids found in olive leaves exhibit antioxidant properties. These chemical components are effective in eliminating free radicals, known as reactive oxygen species. Thus, DNA damage caused by free radicals is prevented. Furthermore, lipid peroxidation and protein oxidation are also reduced through antioxidant activity (Visioli et al., 2002; Corona et al., 2006). For example, one study determined that oleuropein and hydroxytyrosol, active ingredients in olive leaves, prevent lipid peroxidation. It was also observed that this prevention was more effective than trolox, a vitamin E analogue (Umeno et al. 2015). Another study indicated that hydroxytyrosol and oleuropein showed a greater antioxidant effect on DNA and lipid oxidation than natural and synthetic antioxidants. Studies have shown that olive leaves contain flavonoid structures with more free hydroxyl groups, in addition to the most effective phenolic compound antioxidants for radical cations (Benavente-Garcia et al., 2000). Another study examining the effect of olive leaves on pancreatic beta cells found a reduction in hydrogen

peroxide (H2O2) toxicity in beta cells. Furthermore, this study compared the effect of olive leaf extract with only oleuropein and found that olive leaf extract had a greater antioxidant effect (Cumaoğlu et al. 2011). In addition to oleuropein, olive leaves also contain various compounds exhibiting antioxidant effects, such as vanillin, vanillic acid, apigenin, diosmetin, rutin, luteolin, and caffeic acid. Based on this information, the antioxidant effect of olive leaves has gained undeniable importance (Ryan et al., 2002; Skerget et al., 2005; Ok-Hwan et al., 2010).

**2. Antimicrobial and Antiviral Effects**

Oleuropein and hydroxytyrosol are effective against gram-positive and gram-negative bacteria. They have also shown in vitro activity against viral infections such as influenza and herpes simplex (Bisignano et al., 1999; Romani et al., 2017). In preclinical studies, their activity against Staphylococcus aureus, Escherichia coli, and some influenza and herpes viruses has been observed (Bisignano et al., 1999; Romani et al., 2017). It has been determined that the phenolic compounds in olive leaves, oleuropein and its degradation product hydroxytyrosol, exhibit anti-HIV properties, and that their use, separately and together, prevents the entry and integration of the virus into the cell, both intracellularly and extracellularly (Bao et al., 2007; Lee-Huang et al., 2007; Şekeroğlu & Gezici, 2020). Therefore, the use of olive leaf is recommended as an alternative approach to support immunity and reduce the risk of infection (Şekeroğlu & Gezici, 2020).

**3. Cardiovascular Effect**

Olive leaf supports cardiovascular health, especially thanks to its oleuropein and polyphenol content. It is suggested that the extract obtained from the fruit and leaves of the olive tree has vasodilatory, hypotensive, anti-rheumatic, diuretic, hypoglycemic, cholesterol-lowering, and cardioprotective effects (Pieroni et al. 1996). Oleuropein has been reported to prevent lipid peroxidation and cardiotoxicity induced by anthracyclines (Gürbüz & Öğüt, 2018). Clinical studies have shown that olive leaf extract lowers systolic and diastolic blood pressure in hypertensive patients (Susalit et al., 2011). Furthermore, it can reduce LDL cholesterol while increasing HDL cholesterol, which lowers the risk of atherosclerosis (de Bock et al., 2013). These mechanisms are also known to be supported by antioxidant and anti-inflammatory effects. Literature indicates that the phenolic compounds found in olive leaves minimize the harmful effects of free radicals in the body through their antioxidant properties. This effect has also been observed to be significant in protecting against cardiovascular diseases. Polyphenol-rich olive leaf extracts have been shown to reduce lipogenesis and lipid accumulation. In animal models and preclinical studies, olive leaf supplementation reduced fatty liver and serum triglyceride levels (de Bock et al., 2013). In another study by Eidi et al., serum cholesterol, triglyceride, urea, uric

acid, creatinine, aspartate aminotransferase, and alanine aminotransferase levels were significantly reduced in diabetic rats given 0.5 g/kg of olive leaf (2009). Andreadou et al. In a study conducted by Susalit et al. (2009), hypercholesterolemic rabbits that received 10-20 mg/kg of oleuropein for 6 weeks showed a significant decrease in total cholesterol and triglyceride levels at the end of the study. In a study by Susalit et al. (2011), it was determined that patients with stage 1 hypertension who received 500 mg/day of olive leaf extract twice a day for 8 weeks had lower systolic and diastolic blood pressure. Similarly, in another study of 60 prehypertensive male individuals with an average age of 45, a significant decrease in systolic and diastolic blood pressure was observed in patients given olive leaf extract. Furthermore, both studies indicated a positive effect on lipid profiles in the patients. In a study conducted on hypertensive volunteers, it was observed that 1,600 mg of oleuropein intake also reduced systolic and diastolic blood pressure (Lockyer et al. 2017; Cabrera et al. 2015). In a study investigating the cardioprotective effect of oleuropein in rats, it was stated that oleuropein treatment was both protective against myocardial infarction and protective against heart failure developing due to myocardial infarction (Janahmadi et al., 2015).

**4. Effect on Type 2 Diabetes and Metabolic Syndrome**

Studies have shown that polyphenols in olive leaves exhibit a hypoglycemic effect, and this effect is mainly due to the oleuropein component. In a study conducted with diabetic rats, blood glucose levels were found to be significantly lower in groups receiving 16 mg/kg and 8 mg/kg of oleuropein and hydroxytyrosol. Furthermore, the hypoglycemic effect was found to be more effective in the group receiving oleuropein and hydroxytyrosol at a level of 16 mg/kg compared to the group receiving it at a level of 8 mg/kg. Moreover, this study also showed that the group given oleuropein and hydroxytyrosol had higher hepatic glucose concentrations compared to the control group (Jemai et al. 2009). Olive leaf extracts can increase insulin sensitivity and improve glucose metabolism. In clinical trials, significant reductions in HbA1c and fasting blood glucose levels were observed (Katsarou et al., 2015). Polyphenols support insulin secretion by protecting pancreatic β-cells from oxidative stress. In a study comparing diabetic rats given olive leaf extract at doses of 0.1, 0.25, and 0.5 g/kg respectively for 14 days via intragastric gavage with healthy rats given the same doses, serum glucose levels decreased significantly in the diabetic rat group receiving 0.5 mg/kg of olive leaf extract daily, while glucose levels remained unchanged in healthy rats (Eidi et al. 2009). In a 12-week study of 46 overweight middle-aged participants, olive leaf extract increased insulin sensitivity by 15% and pancreatic β-cell response by 28% (de Bock et al., 2013).

**5. Neurodegenerative Diseases**

Olive leaf polyphenols show protective potential in Alzheimer's and Parkinson's diseases by reducing oxidative stress and neuroinflammation (Rigacci & Stefani, 2016). Cellular studies have shown that they prevent β-amyloid accumulation and synaptic damage.

**6. Anti-inflammatory and Oxidative Stress-Related Diseases**

Olive leaf extracts reduce inflammation by acting on the NF-κB pro-inflammatory signaling pathway and suppressing the expression of pro-inflammatory cytokines TNF-α and IL-6. With these effects, it is shown to be a potential supportive treatment in diseases associated with chronic inflammation (metabolic syndrome, obesity, cardiovascular diseases) (Hadrich et al., 2015).

It has been determined that hydroxytyrosol, released by the hydrolysis of oleuropein found in olive leaves, suppresses the expression of pro-inflammatory cytokines, cyclooxygenase-2 (COX-2) and inducible nitric oxide synthase (iNOS) in a dose-dependent manner, thus reporting that hydroxytyrosol has a strong anti-inflammatory property (Zhang et al., 2009).

## 7. Cancer

Olive leaf extract and polyphenols derived from olive leaves have been shown to exhibit antiproliferative and apoptosis-inducing effects in various cancer types, including breast, bladder, mesothelioma, and leukemia (Goulas et al., 2009; Fares et al., 2011; Samet et al., 2014). In a study by Goulas et al. (2009) using olive leaf extract, an antiproliferative effect was observed in MCF-7 and T-24 bladder cancer cells. Furthermore, another study found that olive leaf extract induced apoptosis in K562 cells and initiated the differentiation process of the cells into monocytes/macrophages (Samet et al., 2014). Oleuropein has been found to cause cell cycle arrest in cancer cells by downregulating cyclin D1, cyclin D2, cyclin D3, CDK4, and CDK6, and upregulating p53, CDKN2A, CDKN2B, and CDKN1A. It has also been reported that oleuropein induces apoptosis by inhibiting Bcl-2 and activating Bax, caspase-9, and caspase-3 gene expression (Seçme et al., 2016; Sirianni et al., 2010). Furthermore, oleuropein has been shown to induce estrogen and inhibit proliferation in MCF-7 cells (Sirianni et al., 2010).

## Conclusion

The health benefits of olives, known for centuries, are increasingly supported by scientific studies, including the benefits of their leaves. Data obtained from studies show that olive leaf has antioxidant, antihypertensive, hypocholesterolemic, hypolipidemic, hypoglycemic, antimicrobial, anti-inflammatory, antithrombotic, and cardioprotective effects. These effects are currently observed primarily due to the strong antioxidant properties of olive leaf, particularly the compounds oleuropein and hydroxytyrosol. The increasing number of studies on olive leaf is crucial for research into its effects in treating new diseases, achieving optimal benefits, and determining the appropriate dosage and method of use. More detailed research on olive leaf will shed light on this subject for current and future researchers.

## References


Kamran M, Hamlin AS, Scott CJ, Obied HK. Drying at high temperature for a short time maximizes the recovery of olive leaf biophenols. Ind Crops Prod 2015;78:29-38.

Lockyer S, Rowland I, Spencer JPE, Yaqoob P, Stonehouse W. Impact of phenolic-rich olive leaf extract on blood pressure, plasma lipids and inflammatory markers: a randomised controlled trial. Eur J Nutr 2017;56(4):1421-32.

Panizzi L, Scarpati ML, Oriente EG. Structure of oleuropein, bitter glycoside with hypotensive action of olive oil. Note II. Gazz Chim Ital 1960;90:1449-85.

Somova LI, Shode FO, Ramnanan P, Nadar A. Antihypertensive, antiatherosclerotic and antioxidant activity of triterpenoids isolated from Olea europea, subspecies Africana leaves. J Ethnopharmacol 2003;84(2-3):299- 305.

de Bock M, Derraik JG, Brennan CM, Biggs JB, Morgan PE, Hodgkinson SC, et al. Olive (olea europaea L.) leaf polyphenols improve insulin sensitivity in middle-aged overweight men: a randomized, placebo-controlled, crossover trial. PloS One 2013;8(3):e57622

Al-Azzawie HF, Alhamdani MS. Hypoglycemic and antioxidant effect of oleuropein in alloxan-diabetic rabbits. Life Sci 2006;78(12):1371-7.

Benavente-García O, Castillo J, Lorente J, Ortuño A, Del Rio JA. Antioxidant activity of phenolics extracted from Olea europea L. leaves. Food Chem 2000;68(4):457-62.

Giner E, Recio MC, Ríos JL, Giner RM. Oleuropein protects against dextran sodium sulfate-induced chronic colitis in mice. J Nat Prod 2013;76(6):1113-20.

Umeno A, Takashima M, Murotomi K, Nakajima Y, Koike T, Matsuo T, et al. Radical-scavening activity and antioxidative effects of olive leaf components oleuropein and hydroxytyrosol in comparison with homovanillic alcohol. J Oleo Sci 2015;64(7):793-800.

Cumaoğlu A, Rackova L, Stefek M, Kartal M, Maechler P, Karasu C. Effects of olive leaf polyphenols against H2O2 toxicity in insulin secreting ß-cells. Acta Biochim Pol 2011;58(1):45-50.

Bisignano G, Tomaino A, Lo Cascio R, Crisafi G, Uccella N, Saija A. On the in-vitro antimicrobial activity of oleuropein and hydroxytyrosol. J Pharm Pharmacol 1999;51(8):971-4.

Lee-Huang S, Zhang L, Huang PL, Chang YT, Huang PL. Anti-HIV activity of olive leaf extract (OLE) and modulation of host cell gene expression by HIV-1 infection and OLE treatment. Biochem Biophys Res Commun 2003;307(4):1029-37.

Gürbüz M, Öğüt S. Zeytin Yaprağının Potansiyel Sağlık Yararları Turkiye Klinikleri J Health Sci 2018;3(3):242-53.

Yıldız G, Uylaşer V. A natural antimicrobial: oleuropein. U.Ü. Ziraat Fakültesi Dergisi 2011;25(1):131-4

Susalit E, Agus N, Effendi I, Tjandrawinata RR, Nofiarny D, Perrinjaquet-Moccetti T, et al. Olive (Olea europaea) leaf extract effective in patients with stage-1 hypertension: comparison with captopril. Phytomedicine 2011;18(4):251-8.

Eidi A, Eidi M, Darzi R. Antidiabetic effect of olea europaea L. in normal and diabetic rats. Phytother Res 2009;23(3):347-50.

Andreadou I, Iliodromitis EK, Mikros E, Constantinou M, Agalias A, Magiatis P, et al. The olive constituent oleuropein exhibits anti-ischemic, antioxidative, and hypolipidemic effects in anesthetized rabbits. J Nutr 2006;136(8):2213-9.

Lockyer S, Rowland I, Spencer JPE, Yaqoob P, Stonehouse W. Impact of phenolic-rich olive leaf extract on blood pressure, plasma lipids and inflammatory markers: a randomised controlled trial. Eur J Nutr 2017;56(4):1421-32.

Cabrera-Vique C, Navarro-Alarcón M, Rodríguez Martínez C, Fonollá-Joya J. [Hypotensive effect of an extract of bioactive compounds of olive leaves: preliminary clinical study]. Nutr Hosp 2015;32(1):242-9.

Janahmadi Z, Nekooeian AA, Moaref AR, Emamghoreishi M. Oleuropein offers cardioprotection in rats with acute myocardial infarction. Cardiovasc Toxicol 2015;15(1):61-8.

Jemai H, El Feki A, Sayadi S. Antidiabetic and antioxidant effects of hydroxytyrosol and oleuropein from olive leaves in alloxan-diabetic rats. J Agric Food Chem 2009;57(19):8798- 804.

Zhang X, Cao J, Zhong L. Hydroxytyrosol inhibits pro-inflammatory cytokines, iNOS, and COX-2 expression in human monocytic cells. Naunyn Schmiedebergs Arch Pharmacol 2009;379(6):581-6.

Romani, A.., 2017, Polyphenols and secoiridoids in raw material (Olea europaea L. leaves) and commercial food supplements, European Food Research and Technology , 243, pages429–435.

Korukluoğlu M, Şahan Y, Yiğit A. 2008. Antifungal Properties of Olive Leaf Extracts and Their Phenolic Compounds. Journal of Food Safety, 28 (2008) 76–87.

Pieroni A, Heimler D, Piethers L, Van Poel B, Vlietinck AJ. 1996. In vitro anti-complemantary activity of flavonoids from olive leaves. Pharmazie; 51(10): 765-768.

Hadrich, F., et al. (2015). Anti-inflammatory activity of olive leaf extracts. Journal of Functional Foods, 19, 1–9.

Ok-Hwan L., Boo-Yong L. Antioxidant and antimicrobial activities of individual and combined phenolics in *Olea europaea* leaf extract Bioresource Technology Volume 101, Issue 10, May 2010, Pages 3751-3754

Corona, G., et al. (2006). Phenolic compounds in olive leaves: Hydroxytyrosol and tyrosol. Journal of Agricultural and Food Chemistry, 54(2), 454–461.

Guerreiro, Í.; Ferreira-Pêgo, C.; Carregosa, D.; Santos, C.N.; Menezes, R.; Fernandes, A.S.; Costa, J.G. Polyphenols and their metabolites in renal diseases: An overview. Foods, 2022,11, 1060-63.

Pongrac Barlovic, D.; Harjutsalo, V.; Groop, P.H. Exercise and nutrition in type 1 diabetes: Insights from the FinnDiane cohort.Front Endocrinol. 2022,13, 1064185.

Duke, J. A., 1992. Handbook of phytochemical constituents of GRAS herbs and other economic plants. Boca Raton, FL. CRC Press.

Goulas, V., Exarchou, V., Troganis, A. N., Psomiadou, E., Fotsis, T., Briasoulıs, E., and Gerothanassis, I. P., 2009. Phytochemicals in olive-leaf extracts and their antiproliferative activity against cancer and endothelial cells. Mol. Nutr. Food Res. 53: 600 – 608

Fares, R., Bazzi, S., Baydoun, S. E. and Abdel-Massih, R. M., 2011. The Antioxidant and Anti-proliferative Activity of the Lebanese Olea europaea Extract. Plant Foods Hum Nutr, 66: 58–63.

Samet, I., Han, J., Jlaie, L., Sayadi S. and Isoda, H., 2014. Olive (Olea europaea) Leaf Extract Induces Apoptosis and Monocyte/Macrophage Differentiation in Human Chronic Myelogenous Leukemia K562 Cells: Insight into the Underlying Mechanism.

Visioli, F., et al. (2002). Olive oil phenolics and cardiovascular disease. Nature, 423(6943), 502–505.

Seçme, M., Eroğlu, C., Dodurga, Y. and Bağcı G., 2016. Investigation of anticancer mechanism of oleuropein via cell cycle and apoptotic pathways in SH-SY5Y neuroblastoma cells. Gene, 585; 93–99.

Sirianni, R.; Chimento, A.; De Luca, A.; Casaburi, I.; Rizza, P.; Onofrio, A.; Iacopetta, D.; Puoci, F.; Andò, S.; Maggiolini, M.; et al. Oleuropein and hydroxytyrosol inhibit MCF-7 breast cancer cell proliferation interfering with ERK1/2 activation. *Mol Nutr. Food Res*. 2010, 54,833-840.

Ryan, D., Antolovich, M. Prenzler, P. Robards, K. Lavee S. Biotransformations of phenolic compounds in Olea europaea L. Sci. Hortic. (Amsterdam), 92 (2002), pp. 147-176,

Katsarou, A., et al. (2015). Olive leaf extract in type 2 diabetes. Phytotherapy Research, 29(4), 523–529.

Rigacci, S., & Stefani, M. (2016). Nutraceuticals and neurodegeneration: Olive polyphenols as neuroprotective agents. Current Pharmaceutical Design, 22(1), 92–99.

Şekeroğlu N., Gezici S. 2020. Koronavirüs Pandemisi ve Türkiye'nin Bazı Şifalı Bitkileri Anadolu Kliniği Tıp Bilimleri Dergisi Special Issue on COVID 19, 163 – 182.

Bao, J.; Zhang, D.W.; Zhang, J.Z.H.; Lee Huang, P.; Lin Huang, P.; Lee-Huang, S. Computational study of bindings of olive leaf extract (OLE) to HIV-1 fusion protein gp41. FEBS Lett. 2007, 581, 2737-42.

Lee-Huang, S., Zhang, H., Young-Tae, C., & Paul, L. (2003). Anti-HIV activity of olive leaf extracts (OLE) and modulation of host cell gene expression by HIV-1infection and OLE treatment. *Biochemical and Biophysical Research Communications*, **307**, 1029–1037.

Skerget, M.; Kotnik, P.; Hadolin, M.; Hraš, A.R.; Simonič, M.; Knez, Ž. Phenols, proanthocyanidins, flavones and flavonols in some plant materials and their antioxidant activities. Food Chem. 2005, 89, 191-98

# CHAPTER 9

# Metal–Semiconductor Junctions for Next-Generation Electronics and Optoelectronics

**İlhan Candan[1] & Sezai Asubay[2]**

[1] Dr. Öğr. Üyesi, Dicle University, ORCID: 0000-0001-9489-5324
[2] Prof. Dr., Dicle University, ORCID: 0000-0003-2171-8479

## 1. Introduction

The interface between a metal and a semiconductor has been one of the most extensively studied junctions in solid-state physics. Since the pioneering work of Walter Schottky in the late 1930s (Ahsan et al., 2025; Ezhilmaran et al., 2021; Schottky, 1938), MS junctions have been recognized as fundamental building blocks in electronics. They enable rectification, photodetection, and hot-carrier generation, making them indispensable in devices ranging from Schottky diodes and transistors to solar cells and biosensors.

In contrast to p–n junctions, MS junctions rely on majority-carrier transport, which eliminates charge storage effects and allows faster switching. This makes them particularly attractive for radio frequency (RF) electronics, high-speed rectifiers, and plasmonic devices (Gregor et al., 2023; Sze et al., 2021).

Recent advances in nanotechnology have expanded the scope of MS junctions. The incorporation of wide-bandgap semiconductors (SiC, GaN), 2D materials (graphene, $MoS_2$), and plasmonic nanostructures has enabled unprecedented control over charge transport, barrier tuning, and light–matter interactions (Dasgupta et al., 2025; Novoselov et al., 2005; Singh, 2007). These advances open the door for applications in energy-efficient power electronics, flexible optoelectronics, quantum devices, and neuromorphic computing.

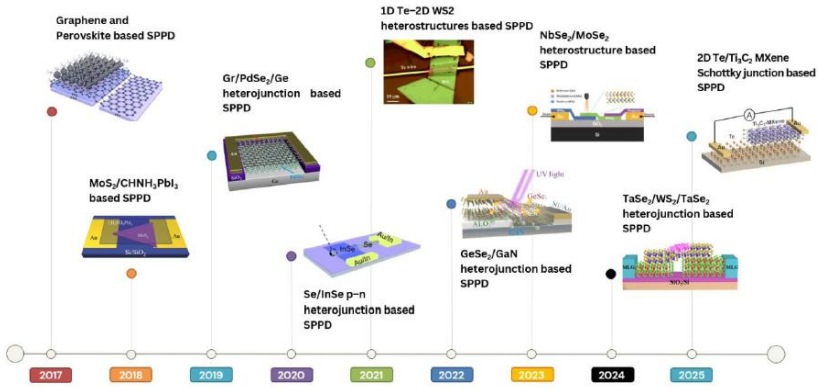


Figure 1. Self-powered photodetectors' evolution (Ahsan et al., 2025).

Metal–semiconductor (MS) junctions are among the most fundamental building blocks in modern electronic and optoelectronic devices. From Schottky diodes and field-effect transistors to photodetectors, solar cells, and light-emitting devices, the interface between a metal and a semiconductor governs charge transport, energy conversion, and signal modulation as seen in figure 1 (Ouyang et al., 2019). As device dimensions continue to shrink and performance demands escalate, the role of MS junctions has become even more critical in enabling next-

generation technologies that extend beyond the limits of conventional silicon-based electronics (Dasgupta et al., 2025).

At its core, an MS junction is defined by the alignment of the metal work function and the semiconductor electron affinity, leading to the formation of a Schottky barrier or an ohmic contact depending on the interface energetics and doping conditions. This barrier controls carrier injection, recombination, and transport, determining key device parameters such as turn-on voltage, leakage current, switching speed, and noise characteristics. Despite their conceptual simplicity, real MS interfaces exhibit complex behavior due to interface states, Fermi-level pinning, interfacial oxides, strain, and atomic-scale inhomogeneities, which can dramatically influence practical device performance (Supplie et al., 2017).

The emergence of new semiconductor platforms has revitalized interest in MS junction physics. Wide-bandgap materials such as gallium nitride (GaN), silicon carbide (SiC), and gallium oxide ($Ga_2O_3$) have enabled high-power, high-frequency, and high-temperature applications that were previously unattainable with traditional silicon devices (Yeboah et al., 2025). Meanwhile, low-dimensional materials, including two-dimensional crystals (such as graphene and transition metal dichalcogenides), nanowires, and quantum dots, have introduced unprecedented control over electronic and optical properties at the nanoscale. In these systems, the metal–semiconductor interface is often the dominant factor governing carrier dynamics, contact resistance, and overall device efficiency.

In parallel, optoelectronic technologies are rapidly evolving to meet the needs of high-speed communication, sensing, imaging, and energy harvesting. MS junctions play a pivotal role in photodetectors, light modulators, plasmonic devices, and hybrid metal–semiconductor nanostructures that concentrate and manipulate light beyond the diffraction limit. The interaction of electromagnetic fields with free carriers at metal surfaces, combined with the tunable band structures of semiconductors, has opened new pathways for enhancing light–matter interaction, enabling ultrafast and highly sensitive optoelectronic systems (Tao et al., 2021; Yu et al., 2019).

This chapter focuses on the physics, materials, and device implications of metal–semiconductor junctions in the context of next-generation electronics and optoelectronics. It will examine fundamental mechanisms such as Schottky barrier formation, carrier transport models, and interface engineering strategies, as well as recent advances in material systems and fabrication techniques. By bridging foundational theory with emerging applications, this chapter aims to provide a comprehensive perspective on how MS junctions are shaping the future of high-performance, scalable, and energy-efficient electronic and optoelectronic technologies.

## 2. Fundamentals of Metal–Semiconductor Junctions

### *2.1 Energy Band Alignment*

When a metal comes into contact with a semiconductor, Fermi-level alignment leads to charge transfer at the interface, forming a Schottky barrier or an Ohmic contact (Mönch, 1994).

For an n-type semiconductor, the barrier height is given by:

$$\Phi_B = \Phi_M - \chi$$

where $\Phi_M$ is the metal work function and $\chi$\chi is the semiconductor electron affinity (Li, 2006).

For p-type semiconductors:

$$\Phi_{Bp} = E_g - (\Phi_M - \chi)$$

where $E_g$ is the bandgap.

### *2.2 Transport Mechanisms*

Carrier transport depends on barrier height, doping level, and temperature:

- Thermionic emission: Carriers surmount the barrier at moderate doping levels.
- Field emission (tunneling): Important for heavily doped semiconductors with thin depletion widths.
- Thermionic field emission: Combination of both mechanisms.

The current–voltage (I–V) characteristics can be described as (Tsu & Esaki, 1973)[6]:

$$I = I_o \left( e^{\frac{qV}{nkT}} - 1 \right)$$

where $I_0$ is reverse saturation current, n is the ideality factor, and T is temperature.

### *2.3 Fermi-Level Pinning*

In practice, the Schottky–Mott rule often fails due to interface states, metal-induced gap states (MIGS), and defects, which "pin" the Fermi level and reduce tunability of barrier height (Robertson, 2000). Overcoming Fermi-level pinning is a major focus of modern MS junction engineering.

*2.4 Ohmic vs. Schottky Contacts*

- Ohmic contacts: Provide negligible resistance and allow current to flow bidirectionally.
- Schottky contacts: Exhibit rectifying behavior, making them suitable for diodes and detectors.

A single device often requires both contacts for optimal performance.

## 3. Fabrication of Metal Semiconductor Junctions

*3.1 Material Selection*

- Metals: Au, Pt, Ni, Ti, and Al are widely used due to stable work functions. Emerging plasmonic metals like Ag and Al also enable optical applications (Atwater & Polman, 2010).
- Semiconductors: Si remains dominant, but GaAs, GaN, SiC, and 2D semiconductors (graphene, $MoS_2$, $WSe_2$) are increasingly important as seen in figure 2 (Taur & Ning, 2021).

*3.2 Deposition Techniques*

- Thermal and electron-beam evaporation: Simple and widely used.
- Sputtering: Provides better adhesion and uniformity.
- Pulsed laser deposition (PLD): Allows stoichiometric transfer and high-purity films (Chrisey & Hubler, 1994).
- Atomic layer deposition (ALD): Enables sub-nanometer control for interfacial layers.

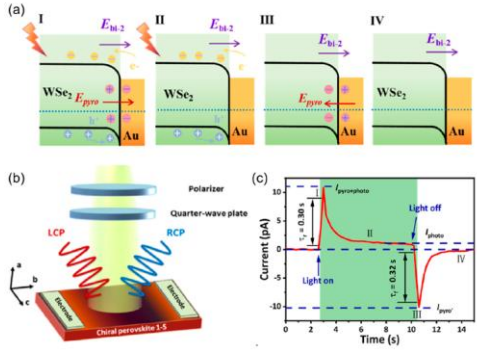


Figure 2. (a) Schematic illustrating the working mechanism of the $WSe_2$/Au Schottky junction (Li et al., 2023), (b) structural configuration of the chiral perovskite device, and (c) pyro-phototronic current–time (I–t) response of the chiral perovskite (Dong et al., 2019).

*3.3 Interface Engineering*

To improve junction performance, several strategies are employed:

- *Insertion layers*: Thin oxides (e.g., $Al_2O_3$, $TiO_2$) reduce Fermi-level pinning.
- *Surface functionalization:* Passivation of dangling bonds minimizes interface traps.
- *Nanostructuring:* Plasmonic nanoparticles or nanorods enhance light absorption and hot-carrier injection (Brongersma et al., 2015).

**4. Emerging Architectures**

*4.1 Wide-Bandgap Schottky Junctions*

SiC and GaN Schottky diodes are widely used in high-power and high-temperature electronics, such as electric vehicles and renewable energy systems (Millan et al., 2013). Their wide bandgap provides higher breakdown voltage and reduced leakage current compared to Si.

*4.2 2D Metal–Semiconductor Junctions*

Van der Waals materials like graphene and transition metal dichalcogenides (TMDs) have enabled ultrathin Schottky junctions. Graphene's tunable Fermi level allows control of barrier height through electrostatic gating, while TMDs provide direct bandgaps for optoelectronics (Koppens et al., 2014).

*4.3 Plasmonic MS Junctions*

Plasmonic nanostructures integrated at the metal–semiconductor interface enhance light absorption and generate hot carriers. These carriers can cross the Schottky barrier, improving photodetector responsivity and solar energy harvesting (Polman & Atwater, 2012).

*4.4 Hybrid MS Heterojunctions*

Combinations of MS junctions with p–n junctions, heterostructures, and quantum dots offer hybrid functionalities such as multiband photodetection, improved efficiency, and neuromorphic switching (Khanna, 2016).

**5. Applications**

*5.1 High-Frequency Electronics*

Schottky diodes are widely used in RF mixers, detectors, and millimeter-wave circuits due to their majority-carrier conduction and ultrafast response times.

*5.2 Power Electronics*

SiC and GaN Schottky devices exhibit low losses and high efficiency in power converters, electric vehicles, and grid systems.

*5.3 Photodetectors and Solar Cells*

MS junctions form the basis of metal–semiconductor–metal (MSM) photodetectors, which offer high-speed and broadband operation. Schottky solar cells, although less efficient than p–n junction cells, benefit from plasmonic enhancements and hybrid designs (Green, 2006).

*5.4 Sensors*

MS junctions are highly sensitive to surface adsorption of gases or biomolecules, which modifies barrier height and current. Applications include gas sensors, biosensors, and chemical detectors (Cui et al., 2001).

*5.5 Neuromorphic and Quantum Devices*

Emerging research shows that MS junctions can function as memristive elements in neuromorphic circuits, as well as hot-carrier generators for quantum optoelectronics (Kuzum et al., 2013).

**6. Challenges**

Despite extensive progress, several challenges remain:

- *Barrier height inhomogeneity:* Nanoscale variations degrade reproducibility.
- *Fermi-level pinning:* Limits barrier tunability and performance optimization.
- *Leakage current:* Especially problematic in small-bandgap semiconductors.
- *Thermal stability:* High-temperature diffusion of metals into semiconductors can degrade junctions.
- *Scalability:* Integrating advanced MS junctions into CMOS-compatible processes remains difficult.

**7. Future Outlook**

The next generation of MS junctions will be driven by new materials, interface engineering, and hybrid architectures:

- *2D materials and van der Waals junctions:* Enable atomically sharp, tunable barriers.

- *Plasmonic Schottky devices:* Enhance hot-carrier collection for ultrafast photodetection and photocatalysis.
- *Flexible and transparent electronics:* MS junctions fabricated on polymers and glass expand into wearable applications.
- *Quantum and neuromorphic systems:* MS junctions coupled with quantum dots and memristors enable unconventional computing paradigms (Kuzum et al., 2013).

The convergence of *nanophotonics, plasmonics, and semiconductor device physics* positions MS junctions as key enablers of future electronic and optoelectronic technologies.

## 8. Conclusion

Metal–semiconductor junctions remain one of the most fundamental and versatile interfaces in solid-state physics. Their rectification, photodetection, and hot-carrier generation capabilities underpin technologies ranging from RF electronics and power devices to biosensors and solar cells. Emerging materials such as wide-bandgap semiconductors, graphene, and TMDs, coupled with plasmonic and quantum enhancements, are redefining the scope of MS junctions. By overcoming challenges such as Fermi-level pinning and interface instability, MS junctions will continue to play a central role in the evolution of next-generation electronics and optoelectronics.

Metal–semiconductor junctions remain a foundational building block in modern electronics and optoelectronics, and their role is becoming increasingly critical as device architectures evolve toward lower dimensions, higher integration densities, and multifunctional operation. Throughout this chapter, we have highlighted the fundamental physics governing Schottky and Ohmic contacts, emphasizing how interfacial band alignment, carrier transport mechanisms, and interface states dictate device performance across a wide range of material systems.

Recent advances in low-dimensional semiconductors, including two-dimensional materials, perovskites, and organic–inorganic hybrids, have expanded the design space of metal–semiconductor junctions beyond conventional bulk systems. These emerging materials enable unprecedented tunability of barrier height, contact resistance, and carrier selectivity through interface engineering, surface functionalization, and electrostatic control. As a result, metal–semiconductor junctions are no longer passive contacts but active elements that can enhance rectification, photodetection, energy harvesting, and sensing functionalities.

The chapter also underscored the growing importance of non-equilibrium and coupled phenomena—such as photonic, thermal, ferroelectric, and chiral effects—in redefining charge transport at metal–semiconductor interfaces. Concepts including hot-carrier injection, pyro-phototronic coupling, and spin-selective transport illustrate how junctions can be leveraged to achieve novel device responses that transcend traditional operation limits. These developments are particularly promising for next-generation applications in neuromorphic computing, broadband photodetectors, and low-power optoelectronic systems.

Despite these advances, significant challenges remain. Achieving reproducible, scalable, and defect-controlled junctions continues to be a major bottleneck, especially for emerging materials and heterogeneous integration. Addressing these issues will require synergistic progress in materials synthesis, interface characterization, and multiscale modeling.

In conclusion, metal–semiconductor junctions will continue to serve as a central platform for innovation in next-generation electronics and optoelectronics. A deeper understanding of interfacial physics combined with advanced fabrication strategies will be essential to fully unlock their potential in future technologies.

## References


Ahsan, U., Elahi, E., Sattar, A., Sarkar, K. J., Asad, M., Mustafa, H.,…Sofer, Z. (2025). Advances in Self-Powered Photodetectors: Unveiling the Potential of 2D Materials and Janus Heterostructures for a Promising Future in Next-Generation Optoelectronics. *Nanoscale*.

Atwater, H. A., & Polman, A. (2010). Plasmonics for improved photovoltaic devices. *Nature materials*, *9*(3), 205-213.

Brongersma, M. L., Halas, N. J., & Nordlander, P. (2015). Plasmon-induced hot carrier science and technology. *Nature nanotechnology*, *10*(1), 25-34.

Chrisey, D. B., & Hubler, G. (1994). *Pulsed laser deposition*.

Cui, Y., Wei, Q., Park, H., & Lieber, C. M. (2001). Nanowire nanosensors for highly sensitive and selective detection of biological and chemical species. *science*, *293*(5533), 1289-1292.

Dasgupta, A., Sen, S., Singh, P., & Raman, A. (2025). A Comprehensive Overview of the Foundations of Semiconductor Materials. *Semiconductor Nanoscale Devices: Materials and Design Challenges*, 80-109.

Dong, J., Wang, Z., Wang, X., & Wang, Z. L. (2019). Temperature dependence of the pyro-phototronic effect in self-powered p-Si/n-ZnO nanowires heterojuncted ultraviolet sensors. *Nano Today*, *29*, 100798.

Ezhilmaran, B., Patra, A., Benny, S., MR, S., VV, A., Bhat, S. V., & Rout, C. S. (2021). Recent developments in the photodetector applications of Schottky diodes based on 2D materials. *Journal of Materials Chemistry C*, *9*(19), 6122-6150.

Green, M. A. (2006). *Third generation photovoltaics: advanced solar energy conversion*. Springer.

Gregor, R., Yeap, K. H., & Nwajana, A. O. (2023). *Power Electronics, Radio Frequency and Microwave Engineering*. BoD–Books on Demand.

Khanna, V. K. (2016). Integrated nanoelectronics. *NanoSci. Technol*.

Koppens, F., Mueller, T., Avouris, P., Ferrari, A., Vitiello, M. S., & Polini, M. (2014). Photodetectors based on graphene, other two-dimensional materials and hybrid systems. *Nature nanotechnology*, *9*(10), 780-793.

Kuzum, D., Yu, S., & Wong, H. P. (2013). Synaptic electronics: materials, devices and applications. *Nanotechnology*, *24*(38), 382001.

Li, S. S. (2006). Metal–semiconductor contacts. In *Semiconductor Physical Electronics* (pp. 284-333). Springer.

Li, Z., Ji, C., Fan, Y., Zhu, T., You, S., Wu, J.,…Kuang, X. (2023). Circularly polarized light-dependent pyro-phototronic effect from 2D chiral–polar

double perovskites. *Journal of the American Chemical Society*, *145*(46), 25134-25142.

Millan, J., Godignon, P., Perpiñà, X., Pérez-Tomás, A., & Rebollo, J. (2013). A survey of wide bandgap power semiconductor devices. *IEEE transactions on Power Electronics*, *29*(5), 2155-2163.

Mönch, W. (1994). Metal-semiconductor contacts: electronic properties. *Surface science*, *299*, 928-944.

Novoselov, K. S., Jiang, D., Schedin, F., Booth, T., Khotkevich, V., Morozov, S., & Geim, A. K. (2005). Two-dimensional atomic crystals. *Proceedings of the National Academy of Sciences*, *102*(30), 10451-10453.

Ouyang, W., Teng, F., He, J. H., & Fang, X. (2019). Enhancing the photoelectric performance of photodetectors based on metal oxide semiconductors by charge-carrier engineering. *Advanced Functional Materials*, *29*(9), 1807672.

Polman, A., & Atwater, H. A. (2012). Photonic design principles for ultrahigh-efficiency photovoltaics. *Nature materials*, *11*(3), 174-177.

Robertson, J. (2000). Band offsets of wide-band-gap oxides and implications for future electronic devices. *Journal of Vacuum Science & Technology B: Microelectronics and Nanometer Structures Processing, Measurement, and Phenomena*, *18*(3), 1785-1791.

Schottky, W. (1938). Halbleitertheorie der sperrschicht. *Naturwissenschaften*, *26*(52), 843-843.

Singh, J. (2007). *Semiconductor devices: basic principles*. John Wiley & Sons.

Supplie, O., May, M. M., Brückner, S., Brezhneva, N., Hannappel, T., & Skorb, E. V. (2017). In situ characterization of interfaces relevant for efficient photoinduced reactions. *Advanced Materials Interfaces*, *4*(21), 1601118.

Sze, S. M., Li, Y., & Ng, K. K. (2021). *Physics of semiconductor devices*. John wiley & sons.

Tao, L., Chen, Z., Li, Z., Wang, J., Xu, X., & Xu, J. B. (2021). Enhancing light-matter interaction in 2D materials by optical micro/nano architectures for high-performance optoelectronic devices. *InfoMat*, *3*(1), 36-60.

Taur, Y., & Ning, T. H. (2021). *Fundamentals of modern VLSI devices*. Cambridge university press.

Tsu, R., & Esaki, L. (1973). Tunneling in a finite superlattice. *Applied Physics Letters*, *22*(11), 562-564.

Yeboah, L. A., Abdul Malik, A., Oppong, P. A., Acheampong, P. S., Morgan, J. A., Addo, R. A. A.,…Osei-Amponsah, S. (2025). Wide-Bandgap Semiconductors: A Critical Analysis of GaN, SiC, AlGaN, Diamond, and

Ga2O3 Synthesis Methods, Challenges, and Prospective Technological Innovations. *Intelligent and Sustainable Manufacturing*, *2*(1), 10011.

Yu, H., Peng, Y., Yang, Y., & Li, Z.-Y. (2019). Plasmon-enhanced light–matter interactions and applications. *npj Computational Materials*, *5*(1), 45.

# CHAPTER 10

# Determination of Chlorophyll Amounts of *Zea Mays and Helianthus annuus* Grown in Different Localities of Osmaniye Province By the Remote Sensing Method

**Zeynep Sevim Geyik[1] & Pınar Bacaksız[2] & Kağan Veryer[3] & Fuat Bozok[1,4]**

[1] Department of Biology, Institute of Postgraduate Education, Osmaniye Korkut Ata University, 80000, Osmaniye, Türkiye
[2] Department of Geomatic Engineering, Faculty of Engineering and Natural Sciences, Osmaniye Korkut Ata University, 80000 Osmaniye, Türkiye
[3] Department of Biology, Faculty of Engineering and Natural Sciences, Osmaniye Korkut Ata University, 80000 Osmaniye, Türkiye
[4] Department of Biology, Faculty of Engineering and Natural Sciences, Osmaniye Korkut Ata University, 80000 Osmaniye, Türkiye

## Introduction

One biophysical measure of the vegetation's ability to maintain photosynthetic processes is its chlorophyll content (Ciganda et al., 2012). Nitrogen content is associated with biophysical parameters of vegetation such as aboveground biomass, green and total leaf area, net ecosystem CO2 exchange, and absorbed photosynthetically active radiation (Evans, 1989; Gitelson et al., 2006). In order to ascertain the vitality and stress of vegetation, numerous researchers have focused on estimating the chlorophyll content of plants (Barton, 2000; Gitelson et al., 2005; Le Maire et al., 2008; Ustin et al., 2009).

A model was improved by Gitelson et al. (2003) to estimate the pigment content of leaves and used to estimate canopy-level chlorophyll content in plants (Gitelson et al., 2005). In these studies, the relationship between canopy chlorophyll content and the red edge chlorophyll index (CIred edge) was established and used to estimate chlorophyll contents in corn and soybean canopies. According to Ciganda et al. (2009), the chlorophyll content in the middle of the corn canopy was directly correlated with the chlorophyll contents in the collar and the ear leaves. CIred edge was also utilized to measure the amount of chlorophyll in corn. This study examined the depth to which the CIred edge can detect within the maize canopy and how correctly it calculates the canopy chlorophyll concentration. It was discovered that the number of leaf layers in a corn canopy affected how much chlorophyll content the CIred edge detected and, consequently, how much chlorophyll content was remotely estimated in the canopy. It was also established how much chlorophyll content in each leaf layer contributed to the CIred edge.

Classifying each pixel in an image is known as image classification. Because image classification techniques may be applied to wider areas and synoptic viewpoints, they are frequently employed to determine land cover. The two main techniques for classifying generic images are pixel-based classification (PBC) and object-based classification (OBC). Despite the general opinion that OBC gives better results, studies have been conducted to obtain high accuracy from PBC methods (Myint et al., 2011; Whiteside et al., 2011; Meneguzzo et al., 2013; Michez et al., 2016). It has been discovered that support vector machines (SVM) and artificial neural networks (ANN) produce more accurate results than the maximum likelihood (ML) technique (Oommen et al., 2008; Naguib et al., 2009; Sakieh et al., 2016). SVM produced the highest accuracy when compared to ANN and decision tree approaches for the ML method (Huang et al., 2002). According to a comparison between the Conditional Random Fields (CRF) approach and the SVM, the latter yielded more accurate findings (Hoberg and Müller, 2011). It was discovered that the ML approach and SVM outperformed supervised classification techniques (Yang et al., 2011). In the study conducted by Kumar et

al. (2015), more accurate results were obtained from SVM and ANN methods in product classification compared to pixel-based classification.

In the present study, leaf samples of *Z. mays* and *H. annuus* plants in different localities of Osmaniye province (East Mediterranean of Türkiye) were collected, and their chlorophyll contents were investigated by spectrophotometric and remote sensing methods.

## Materials and Methods

### Plant Sample

Leaves of *Zea mays* (corn) and *Helianthus annuus* (sunflower) were collected from different localities of Osmaniye province in June and July 2024 (Table 3.1).

Table 3.1 Localities of collected plant samples

| No | Coordinates | Plants | Localities | Collection date |
|---|---|---|---|---|
| 1 | 37,08267 36,213548 | *Zea mays* | Yeşilyurt, Divlimoğlu | 29.06.2024 |
| 2 | 37,082798 36,213675 | *Zea mays* | Yeşilyurt | 29.06.2024 |
| 3 | 37,08332 36,213688 | *Zea mays* | Yeşilyurt | 29.06.2024 |
| 4 | 37,08491 36,213431 | *Zea mays* | Yeşilyurt | 29.06.2024 |
| 5 | 37,086239 36,213167 | *Zea mays* | Yeşilyurt | 29.06.2024 |
| 6 | 37,087862 36,21235 | *Zea mays* | Yeşilyurt | 29.06.2024 |
| 7 | 37,088387 36,21298 | *Zea mays* | Yeşilyurt | 29.06.2024 |
| 8 | 37,088863 36,213504 | *Zea mays* | Yeşilyurt | 29.06.2024 |
| 9 | 37,089548 36,211359 | *Zea mays* | Alahanlı | 29.06.2024 |
| 10 | 37,089824 36,211415 | *Zea mays* | Alahanlı | 29.06.2024 |
| 11 | 37,090098 36,211386 | *Zea mays* | Nohuttepe Dr.İhsan Göknal | 29.06.2024 |
| 12 | 37,090358 36,211481 | *Zea mays* | Nohuttepe Dr.İhsan Göknal | 29.06.2024 |

| | | | | |
|---|---|---|---|---|
| 13 | 37,091201<br>36,210133 | *Zea mays* | Alahanlı | 29.06.2024 |
| 14 | 37,082035<br>36,212031 | *Helianthus annuus* | Yeşilyurt | 29.06.2024 |
| 15 | 37,081719<br>36,2112 | *Helianthus annuus* | Yeşilyurt | 29.06.2024 |
| 16 | 37,081563<br>36,210439 | *Helianthus annuus* | Yeşilyurt | 29.06.2024 |
| 17 | 37,081078<br>36,21005 | *Helianthus annuus* | Vatan | 29.06.2024 |
| 18 | 37,0894<br>36,226805 | *Zea mays* | Dr.İhsan Göknal Kemal Satır Cd. Nohuttepe | 29.06.2024 |
| 19 | 37,090018<br>36,226171 | *Zea mays* | Dr.İhsan Göknal Kemal Satır St. Nohuttepe | 29.06.2024 |
| 20 | 37,092373<br>36,222288 | *Zea mays* | Dr.İhsan Göknal Kemal Satır St. Nohuttepe | 29.06.2024 |
| 21 | 37,092102<br>36,222295 | *Zea mays* | Dr.İhsan Göknal | 29.06.2024 |
| 22 | 37,091828<br>36,222315 | *Zea mays* | Dr. İhsan Göknal | 29.06.2024 |
| 23 | 37,091562<br>36,216248 | *Zea mays* | Dr.İhsan Göknal | 29.06.2024 |
| 24 | 37,091562<br>36,216248 | *Zea mays* | Dr.İhsan Göknal | 29.06.2024 |
| 25 | 37,091562<br>36,216248 | *Zea mays* | Dr.İhsan Göknal | 29.06.2024 |
| 26 | 37,097372<br>36,214877 | *Zea mays* | Nohuttepe | 29.06.2024 |
| 27 | 37,097759<br>36,213943 | *Zea mays* | Nohuttepe | 29.06.2024 |

| | | | | |
|---|---|---|---|---|
| 28 | 37,098142<br>36,213335 | *Zea mays* | Nohuttepe | 29.06.2024 |
| 29 | 37,098472<br>36,212651 | *Zea mays* | Nohuttepe | 29.06.2024 |
| 30 | 37,098617<br>36,212269 | *Zea mays* | Nohuttepe | 29.06.2024 |
| 31 | 37,098876<br>36,211586 | *Zea mays* | Nohuttepe | 29.06.2024 |
| 32 | 37,083587<br>36,230084 | *Zea mays* | Dr.İhsan Göknal | 29.06.2024 |
| 33 | 37,083393<br>36,229841 | *Zea mays* | Dr.İhsan Göknal | 29.06.2024 |
| 34 | 37,083134<br>36,229735 | *Zea mays* | Dr.İhsan Göknal Nohuttepe | 29.06.2024 |
| 35 | 37,078775<br>36,228735 | *Helianthus annuus* | Yeşilyurt | 29.06.2024 |
| 36 | 37,078452<br>36,228174 | *Helianthus annuus* | Yeşilyurt | 29.06.2024 |
| 37 | 37,078278<br>36,227825 | *Helianthus annuus* | Yeşilyurt | 29.06.2024 |
| 38 | 37,077919<br>36,226958 | *Helianthus annuus* | Yeşilyurt | 29.06.2024 |
| 39 | 37,077689<br>36,226214 | *Helianthus annuus* | Yeşilyurt | 29.06.2024 |
| 40 | 37,108327<br>36,235338 | *Zea mays* | Yunus Emre | 1.07.2024 |
| 41 | 37,108711<br>36,234882 | *Zea mays* | Yunus Emre | 1.07.2024 |
| 42 | 37,109085<br>36,234487 | *Zea mays* | Yunus Emre | 1.07.2024 |
| 43 | 37,109163<br>36,23468 | *Helianthus annuus* | Yunus Emre İskender Türkmen St. | 1.07.2024 |
| 44 | 37,109138<br>36,234193 | *Helianthus annuus* | Yunus Emre İskender Türkmen St. | 1.07.2024 |

| | | | | |
|---|---|---|---|---|
| 45 | 37,109395<br>36,234452 | *Helianthus annuus* | Yunus Emre İskender Türkmen St. | 1.07.2024 |
| 46 | 37,109963<br>36,234385 | *Zea mays* | Yunus Emre İskender Türkmen St. | 1.07.2024 |
| 47 | 37,109873<br>36,234038 | *Zea mays* | Yunus Emre | 1.07.2024 |
| 48 | 37,110073<br>36,234193 | *Zea mays* | Yunus Emre | 1.07.2024 |
| 49 | 37,110167<br>36,233409 | *Zea mays* | Yunus Emre | 1.07.2024 |
| 50 | 37,111797<br>36,231393 | *Zea mays* | Yunus Emre | 1.07.2024 |
| 51 | 37,116745<br>36,220358 | *Zea mays* | Cevdetiye | 1.07.2024 |
| 52 | 37,116687<br>36,220328 | *Zea mays* | Cevdetiye | 1.07.2024 |
| 53 | 37,115088<br>36,217867 | *Helianthus annuus* | Karataş Cevdetiye | 1.07.2024 |
| 54 | 37,115038<br>36,217758 | *Helianthus annuus* | Karataş Cevdetiye | 1.07.2024 |
| 55 | 37,114755<br>36,217717 | *Helianthus annuus* | Karataş Cevdetiye | 1.07.2024 |
| 56 | 37,114481<br>36,217673 | *Helianthus annuus* | Karataş Cevdetiye | 1.07.2024 |
| 57 | 37,115322<br>36,217687 | *Helianthus annuus* | Karataş Cevdetiye | 1.07.2024 |
| 58 | 37,115662<br>36,216987 | *Helianthus annuus* | Karataş Cevdetiye | 1.07.2024 |
| 59 | 37,116232<br>36,216465 | *Helianthus annuus* | Karataş Cevdetiye | 1.07.2024 |
| 60 | 37,116369<br>36,216273 | *Helianthus annuus* | Karataş Cevdetiye | 1.07.2024 |

| | | | | |
|---|---|---|---|---|
| 61 | 37,11663<br>36,216095 | *Helianthus annuus* | Cevdetiye | 1.07.2024 |
| 62 | 37,117043<br>36,215892 | *Helianthus annuus* | Cevdetiye | 1.07.2024 |
| 63 | 37,11378<br>36,219872 | *Helianthus annuus* | Nohuttepe | 1.07.2024 |
| 64 | 37,112547<br>36,220183 | *Helianthus annuus* | Nohuttepe | 1.07.2024 |
| 65 | 37,104648<br>36,218005 | *Zea mays* | Alahanlı | 1.07.2024 |
| 66 | 37,104489<br>36,218105 | *Zea mays* | Alahanlı | 1.07.2024 |
| 67 | 37,104775<br>36,217305 | *Zea mays* | Nohuttepe | 1.07.2024 |
| 68 | 37,104978<br>36,217637 | *Zea mays* | Osmaniye Center | 1.07.2024 |
| 69 | 37,105191<br>36,217391 | *Zea mays* | Osmaniye Center | 1.07.2024 |
| 70 | 37,105398<br>36217131 | *Zea mays* | Osmaniye Center | 1.07.2024 |
| 71 | 37,105635<br>36,216872 | *Zea mays* | Osmaniye Center | 1.07.2024 |
| 72 | 37,105603<br>36,216827 | *Zea mays* | Osmaniye Center | 1.07.2024 |
| 73 | 37,105965<br>36,216474 | *Zea mays* | Osmaniye Center | 1.07.2024 |
| 74 | 37,106088<br>36,216308 | *Zea mays* | Osmaniye Center | 1.07.2024 |
| 75 | 37,106439<br>36,215946 | *Zea mays* | Osmaniye Center | 1.07.2024 |
| 76 | 37,105425<br>36,217754 | *Zea mays* | Nohuttepe Osmaniye Center | 1.07.2024 |
| 77 | 37,105485<br>36,21774 | *Zea mays* | Nohuttepe Osmaniye Center | 1.07.2024 |
| 78 | 37,111868<br>36,220076 | *Zea mays* | Nohuttepe Osmaniye Center | 1.07.2024 |

| | | | | |
|---|---|---|---|---|
| 79 | 37,113651<br>36,22004 | *Zea mays* | Nohuttepe Osmaniye Center | 1.07.2024 |
| 80 | 37,116563<br>36,219855 | *Zea mays* | Kadirli road | 1.07.2024 |
| 81 | 37,116533<br>36,219918 | *Zea mays* | Kadirli road | 1.07.2024 |
| 82 | 37,11677<br>36,219397 | *Zea mays* | On Kadirli road | 1.07.2024 |
| 83 | 37,116791<br>36,219254 | *Zea mays* | Osmaniye Center | 1.07.2024 |
| 84 | 37,11687<br>36,219097 | *Zea mays* | Kadirli road | 1.07.2024 |
| 85 | 37,116922<br>36,21887 | *Zea mays* | Kadirli road Cevdetiye | 1.07.2024 |
| 86 | 37,117202<br>36,218263 | *Zea mays* | Kadirli road Cevdetiye | 1.07.2024 |
| 87 | 37,117349<br>36,217952 | *Zea mays* | Osmaniye Center | 1.07.2024 |

The field appearances of the *Z. mays* and *H. annuus* collected within the scope of the research are shown in the figures below (Figure 3.1 and Figure 3.2)

Figure 3.1 Field appearance of the sunflower plant used in the study

Figure 3.2 Appearance of the corn plant used in the study in the field

**Spectrophotometric Method**

Leaves of plant samples (100 mg) collected from different regions of Osmaniye province were thoroughly crushed using a porcelain mortar in 80% acetone, and the final volume was adjusted to 10 ml with 80% acetone. The samples were kept in the refrigerator at +4 ºC for two days and then centrifuged at 4000 rpm for 10 min. Then, the absorbances of the obtained supernatant (the

upper liquid part) were measured in a spectrophotometer at 645 and 663 nm wavelengths. Chlorophyll contents were calculated according to the method of Arnon (1949).

$$\text{Chlorophyll} - \text{a} = (11{,}75 \text{ x } \text{Abs}663) - (2{,}35 \text{ x } \text{Abs}645) \quad (1)$$

$$\text{Chlorophyll} - \text{b} = (16.61 \text{ x } \text{Abs}645) - (3{,}96 \text{ x } \text{Abs}663) \quad (2)$$

**Remote Sensing Method**

**Sentinel-2**

The Copernicus Land Monitoring effort is supported by Sentinel-2, a large-area, high-resolution, multispectral imaging mission that monitors interior rivers, coastal regions, and vegetation, soil, and water cover. Twin polar-orbiting, 180°-phased, co-orbiting satellites make up the entire Sentinel-2 mission. The mission's broad swath coverage and long revisit time support the monitoring of vegetation changes throughout the growing season, and also variability in land surface conditions. The range of coverage is 56° south to 84° north latitude. The European wide-area, multispectral, high-resolution imaging mission is called Sentinel-2. The full mission capabilities of the twin satellites, which are 180° phased yet co-orbiting, are designed to provide a high revisit frequency of five days at the equator. 13 spectral bands will be sampled by the optical instrument payload carried by Sentinel-2: three bands at 60 m spatial resolution, six bands at 20 m, and four bands at 10 m (Table 3.2). 290 km is the chosen orbit width (URL-1).

Table 3.2 Spectral Band Sampling according to Sentinel-2 satellite

| Name | Identification | Resolution | Wavelength |
|---|---|---|---|
| B1 | Aerosols | 60 m | 443.9 nm / 442.3 nm |
| B2 | Blue | 10 m | 496.6 nm / 492.1 nm |
| B3 | Green | 10 m | 560 nm / 559 nm |
| B4 | Red | 10 m | 664.5 nm / 665 nm |
| B5 | Red Edge 1 | 20 m | 703.9 nm / 703.8 nm |

| | | | |
|---|---|---|---|
| B6 | Red Edge 2 | 20 m | 740.2 nm / 739.1 nm |
| B7 | Red Edge 3 | 20 m | 782.5 nm / 779.7 nm |
| B8 | NIR | 10 m | 835.1 nm / 833 nm |
| B8A | Red Edge 4 | 20 m | 864.8 nm / 864 nm |
| B9 | Water vapor | 60 m | 945 nm / 943.2 nm |
| B11 | SWIR 1 | 20 m | 1613.7 nm / 1610.4 nm |
| B12 | SWIR 2 | 20 m | 2202.4 nm / 2185.7 nm |

**Band Ratio**

The bands that make up the image represent the image in a spectral range. By performing mathematical operations on the bands that represent various spectral ranges, a new image is produced. The generated image can be used to highlight an object's attribute. In the present study, the NDCI band ratio method was used (Mishra and Mishra, 2012; Mutlu et al., 2020).

$$NDCI = (Red\ Edge\ 1 - Red)/(Red\ Edge\ 1 + Red) \quad (1)$$

**Support Vector Machines (SVM)**

Gualtieri and Cromp (1998) were the first to propose image classification in remote sensing. Richards and Jia (2006), Huang et al. (2002), and Burges (1998) all provided more details on this concept. SVM classification is a supervised classification algorithm. The SVM mathematical techniques are later extended to classify multi-class and non-linear data. Estimating the best course of action is the foundation of SVM's operation. The function that can distinguish two classes, in other words, the determination of the sub-platform that can most appropriately separate two classes (Vapnik, 2000). SVMs, which have been successfully used in many fields, have been studied in recent years in remote sensing (Foody et al., 2004; Melgani et al., 2004; Pal et al., 2005).

### Validation Criteria

By comparing the percentage of pixels categorized with the confirmed field data, a confusion matrix is used to assess the method's accuracy and prevent subjective estimation in remote sensing (Congalton, 1991). The percentage of pixels properly categorized is revealed by the confusion matrix's total accuracy. The likelihood that the classified pixel is represented in that class is determined by the omission error and the manufacturer's accuracy. According to Foody (2002), an overall accuracy of 85% is adequate. The accuracy of the user and the omission error indicate how well the training set's pixels are categorized (Rogan et al., 2002). When the kappa coefficient is greater than 0.8, the classification is said to be strong (Landis and Kock 1977). In their investigation, Montserud and Leamans (1992) proposed that the kappa value could not possibly be higher than 0.75.

## Results and Discussion

### Spectrophotometric Analysis Results

The results obtained by spectrophotometer measurements from the leaves of *Z. mays* and *H. annuus* collected from different localities of Osmaniye province are shown in Table 4.1.

Table 4.1 Chlorophyll amounts of corn and sunflower plants collected from different localities of Osmaniye province.

| N | Localities | Plants | Chlo-a (mg/g fw) | Chlo-b (mg/g fw) |
|---|---|---|---|---|
| 1 | Yeşilyurt, Divlimoğlu | *Zea mays* | 3,05 | 0,72 |
| 2 | Yeşilyurt | *Zea mays* | 0,52 | 0,07 |
| 3 | Yeşilyurt | *Zea mays* | 2,19 | 0,67 |
| 4 | Yeşilyurt | *Zea mays* | 1,89 | 0,40 |
| 5 | Yeşilyurt | *Zea mays* | 1,36 | 0,37 |
| 6 | Yeşilyurt | *Zea mays* | 1,47 | 0,34 |
| 7 | Yeşilyurt | *Zea mays* | 1,74 | 0,30 |
| 8 | Yeşilyurt | *Zea mays* | 1,28 | 0,26 |
| 9 | Alahanlı | *Zea mays* | 0,57 | 0,10 |
| 10 | Alahanlı | *Zea mays* | 1,45 | 0,28 |
| 11 | Nohuttepe, | *Zea mays* | 1,95 | 0,36 |

| | | | | |
|---|---|---|---|---|
| | Dr. İhsan Göknal | | | |
| 12 | Nohuttepe, Dr. İhsan Göknal | *Zea mays* | 2,58 | 0,46 |
| 13 | Alahanlı | *Zea mays* | 2,41 | 0,42 |
| 14 | Yeşilyurt | *Helianthus annuus* | 1,39 | 0,22 |
| 15 | Yeşilyurt | *Helianthus annuus* | 2,04 | 0,35 |
| 16 | Yeşilyurt | *Helianthus annuus* | 2,04 | 0,36 |
| 17 | Vatan | *Helianthus annuus* | 1,05 | 0,19 |
| 18 | Dr.İhsan Göknal, Kemal Satır St. Nohuttepe | *Zea mays* | 1,59 | 0,27 |
| 19 | Dr.İhsan Göknal, Kemal Satır St. Nohuttepe | *Zea mays* | 3,07 | 0,67 |
| 20 | Dr.İhsan Göknal, Kemal Satır St. Nohuttepe | *Zea mays* | 2,74 | 0,49 |
| 21 | Dr.İhsan Göknal | *Zea mays* | 2,44 | 0,44 |
| 22 | Dr. İhsan Göknal | *Zea mays* | 3,34 | 0,77 |
| 23 | Dr.İhsan Göknal | *Zea mays* | 2,75 | 0,68 |
| 24 | Dr.İhsan Göknal | *Zea mays* | 3,22 | 0,68 |
| 25 | Dr.İhsan Göknal | *Zea mays* | 2,07 | 0,42 |
| 26 | Nohuttepe | *Zea mays* | 1,47 | 0,53 |
| 27 | Nohuttepe | *Zea mays* | 3,63 | 1,23 |
| 28 | Nohuttepe | *Zea mays* | 2,21 | 0,39 |
| 29 | Nohuttepe | *Zea mays* | 1,85 | 0,31 |
| 30 | Nohuttepe | *Zea mays* | 2,16 | 0,38 |
| 31 | Nohuttepe | *Zea mays* | 1,91 | 0,30 |

| | | | | |
|---|---|---|---|---|
| 32 | Dr. İhsan Göknal | *Zea mays* | 3,08 | 0,71 |
| 33 | Dr. İhsan Göknal | *Zea mays* | 2,00 | 0,31 |
| 34 | Dr. İhsan Göknal, Nohuttepe | *Zea mays* | 1,81 | 0,32 |
| 35 | Yeşilyurt | *Helianthus annuus* | 0,83 | 0,15 |
| 36 | Yeşilyurt | *Helianthus annuus* | 0,50 | 0,03 |
| 37 | Yeşilyurt | *Helianthus annuus* | 1,23 | 0,16 |
| 38 | Yeşilyurt | *Helianthus annuus* | 0,45 | 0,03 |
| 39 | Yeşilyurt | *Helianthus annuus* | 0,74 | 0,08 |
| 40 | Yunus Emre | *Zea mays* | 1,45 | 0,23 |
| 41 | Yunus Emre | *Zea mays* | 1,42 | 0,21 |
| 42 | Yunus Emre | *Zea mays* | 2,13 | 0,43 |
| 43 | Yunus Emre, İskender Türkmen St. | *Helianthus annuus* | 0,72 | 0,06 |
| 44 | Yunus Emre, İskender Türkmen St. | *Helianthus annuus* | 0,44 | 0,01 |
| 45 | Yunus Emre, İskender Türkmen St. | *Helianthus annuus* | 0,58 | 0,03 |
| 46 | Yunus Emre, İskender Türkmen St. | *Zea mays* | 1,38 | 0,20 |
| 47 | Yunus Emre | *Zea mays* | 1,62 | 0,27 |
| 48 | Yunus Emre | *Zea mays* | 2,11 | 0,34 |
| 49 | Yunus Emre | *Zea mays* | 1,99 | 0,35 |
| 50 | Yunus Emre | *Zea mays* | 1,84 | 0,24 |
| 51 | On Kadirli road, Cevdetiye | *Zea mays* | 2,28 | 0,31 |
| 52 | On Kadirli road, Cevdetiye | *Zea mays* | 1,95 | 0,28 |

| | | | | |
|---|---|---|---|---|
| 53 | Karataş, Cevdetiye | *Helianthus annuus* | 1,40 | 0,18 |
| 54 | Karataş, Cevdetiye | *Helianthus annuus* | 0,55 | 0,02 |
| 55 | Karataş, Cevdetiye | *Helianthus annuus* | 1,65 | 0,21 |
| 56 | Karataş, Cevdetiye | *Helianthus annuus* | 1,69 | 0,25 |
| 57 | Karataş, Cevdetiye | *Helianthus annuus* | 0,49 | 0,03 |
| 58 | Karataş, Cevdetiye | *Helianthus annuus* | 1,79 | 0,27 |
| 59 | Karataş, Cevdetiye | *Helianthus annuus* | 0,37 | 0,01 |
| 60 | Karataş, Cevdetiye | *Helianthus annuus* | 1,98 | 0,26 |
| 61 | Cevdetiye | *Helianthus annuus* | 2,19 | 0,32 |
| 62 | Cevdetiye | *Helianthus annuus* | 1,52 | 0,19 |
| 63 | Nohuttepe | *Helianthus annuus* | 0,65 | 0,03 |
| 64 | Nohuttepe | *Helianthus annuus* | 1,30 | 0,18 |
| 65 | Alahanlı | *Zea mays* | 0,69 | 0,06 |
| 66 | Alahanlı | *Zea mays* | 2,33 | 0,31 |
| 67 | Nohuttepe | *Zea mays* | 2,25 | 0,46 |
| 68 | Osmaniye Center | *Zea mays* | 1,85 | 0,27 |
| 69 | Osmaniye Center | *Zea mays* | 1,89 | 0,32 |
| 70 | Osmaniye Center | *Zea mays* | 1,74 | 0,26 |
| 71 | Osmaniye Center | *Zea mays* | 1,44 | 0,77 |
| 72 | Osmaniye Center | *Zea mays* | 1,53 | 0,26 |
| 73 | Osmaniye Center | *Zea mays* | 2,01 | 0,34 |

| | | | | |
|---|---|---|---|---|
| 74 | Osmaniye Center | *Zea mays* | 1,52 | 0,20 |
| 75 | Osmaniye Center | *Zea mays* | 1,11 | 0,13 |
| 76 | Nohuttepe, Osmaniye Center | *Zea mays* | 1,98 | 0,37 |
| 77 | Nohuttepe, Osmaniye Center | *Zea mays* | 2,29 | 0,43 |
| 78 | Nohuttepe, Osmaniye Center | *Zea mays* | 1,77 | 0,28 |
| 79 | Nohuttepe, Osmaniye Center | *Zea mays* | 2,47 | 0,48 |
| 80 | On Kadirli road | *Zea mays* | 2,54 | 0,41 |
| 81 | On Kadirli road | *Zea mays* | 1,44 | 0,23 |
| 82 | On Kadirli road | *Zea mays* | 1,66 | 0,67 |
| 83 | On Kadirli road, Osmaniye Center | *Zea mays* | 2,12 | 0,37 |
| 84 | On Kadirli road | *Zea mays* | 1,00 | 0,65 |
| 85 | On Kadirli road, Cevdetiye | *Zea mays* | 1,32 | 0,41 |
| 86 | On Kadirli road, Cevdetiye | *Zea mays* | 2,40 | 0,33 |
| 87 | On Kadirli road, Osmaniye Center | *Zea mays* | 3,03 | 0,59 |

Chlo-a: Chlorophyll-a, Chlo-b: Chlorophyll-b, fw: fresh weight

When Table 4.1 was examined, it was found that the corn plant collected from Nohuttepe locality had the highest levels of both chlorophyll-a (3.63 mg/g oil) and chlorophyll-b (1.23 mg/g oil) by spectrophotometric method, while the sunflower plant collected from Karataş, Cevdetiye locality had the lowest levels of both chlorophyll-a (0.3 mg/g oil) and chlorophyll-b (0.01 mg/g oil). When the corn plants were compared within themselves, the lowest chlorophyll-a and chlorophyll-b amounts were determined as 0.52 mg/g oil from locality 2 and 0.06

mg/g oil from locality 65, respectively, while the highest amounts of both chlorophyll-a and chlorophyll-b, as mentioned above, were determined as 3.63 mg/g oil and 1.23 mg/g oil from locality 27, respectively. When the chlorophyll-a and chlorophyll-b contents of the sunflower plant were examined, the lowest were determined as 0.37 mg/g oil and 0.01 mg/g oil from locality 59, while the highest were determined as 2.19 mg/g oil from locality 61 and 0.36 mg/g oil from locality 16, respectively.

**Findings Obtained by Remote Sensing**

The results showing the chlorophyll-a values obtained from the NDCI index determined by the ratio of the bands of the Sentinel 2 satellite image are given in Figure 4.1.

Figure 4.1 NDCI image showing chlorophyll-a values determined by scaling the bands of Sentinel 2 satellite imagery

The NDCI values obtained for a year in the study area are shown in Figure 4.2. When the graph is examined, it is seen that the NDCI values do not change throughout the year and take a different value every month. When the results of the study are examined, it is observed that the coordinate value obtained from a single location is not compatible with the band ratio values obtained using remote sensing.

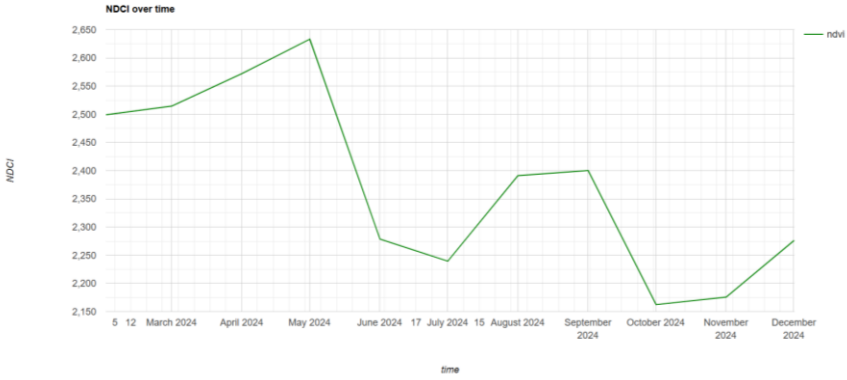


Figure 4.2 *NDCI* values obtained for one year in the study area

Another part of this study is to determine other plant species in the study area according to the samples taken from the fields. While classifying on the GEE platform, 63 corn, 24 sunflower and 427 other classes were marked. In other words, what was planted in the fields that could not be determined within the study area was determined by this method. The other class includes forest areas, mountains, residential areas, roads and water areas. Classification was made with support vector machines according to these three classes. Figure 4.3 shows the classification map obtained according to these three classes.

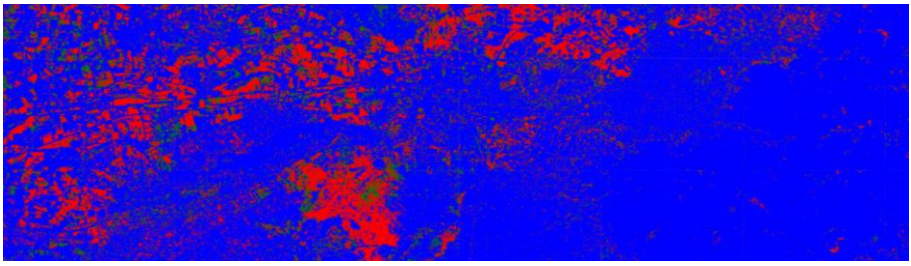

Figure 4.3 Map showing *Z. mays* (red), *H. annuus* (green), and other classes (blue) (living and nonliving things)

## Conclusions

In this study, leaves of *Zea mays* and *Helianthus annuus* were collected from different localities of Osmaniye province, and their chlorophyll contents were investigated by using spectrophotometric and remote sensing methods. At the end of the research, according to the results obtained from spectrophotometric analysis, it was determined that the corn plant collected from Nohuttepe location of Osmaniye province had the highest levels of both chlorophyll-a (3.63 mg/g fw) and chlorophyll-b (1.23 mg/g fw), while the sunflower plant collected from Cevdetiye location of Karataş had the lowest levels of both chlorophyll-a (0.3 mg/g yw) and chlorophyll-b (0.01 mg/g fw).

It was concluded that it would be more accurate to determine the chlorophyll-a value by taking the average of the values obtained from many places in the same field, rather than calculating the chlorophyll-a value by taking a single location from each field.

The amount of chlorophyll affects the photosynthesis ratios in plants. However, the amount of chlorophyll may vary depending on various biotic and abiotic factors, including the place where the plant grows and the type of plant. The amount of chlorophyll in plants affects the photosynthesis rate, and its amount in the plant varies depending on many factors, primarily the conditions of the growing area and the type of plant. As a result of this study, it is suggested that by determining the chlorophyll amounts of the research areas, it will be possible to determine how much fertilizer, water, and other factors the plant needs for growth and development by comparing with previous studies. It is also thought that in future studies, plants (such as hemp) that are illegally cultivated in unauthorized agricultural lands can be detected more easily with the development of remote sensing technology.

## References


Andrianto, H., Suhardi, S., Faizal, A. Performance evaluation of low-cost IoT based chlorophyll meter. Bulletin of Electrical Engineering and Informatics, 9(3), 956-963, 2020.

Anderson, M.C., Stand structure and light penetration. 2. A theoretical analysis. Journal of Applied Ecology, 3(1), 41–54, 1966.

Arnon, D.I. Copper enzymes in isolated chloroplasts, Polyphenoloxidase in *Beta vulgaris.* Plant Physiol. 24(1), 1-15, 1949.

Asner, G. P., Braswell, B. H., Schimel, D. S., Wessman, C.A. Ecological research needs from multi-angle remote sensing data. Remote Sensing of Environment, 63, 155−165, 1998.

Atun, R., Sözmen, E. U., Gürsoy, Ö., Investigation of salt stress in rosemary (Rosmarinus officinalis L.) with the remote sensing technique. Türkiye Tarımsal Araştırmalar Dergisi, 7(2), 120-127, 2020.

Bannari, A., Khurshid, K.S., Staenz, K., Schwarz, J.W.A comparison of hyperspectral chlorophyll indices for wheat crop chlorophyll content estimation using laboratory reflectance measurements. IEEE Transactions on Geoscience and Remote Sensing, 45(10), 3063-3074, 2007.

Barton, C.V.M., A theoretical analysis of the influence of heterogeneity in chlorophyll distribution on leaf reflectance. Tree Physiology, 21, 789–795, 2000.

Bauerle, W.L., Weston, D.J., Bowden, J.D., Dudley, J.B., Toler, J.E., Leaf absorptance of photosynthetically active radiation in relation to chlorophyll meter estimates among woody plant species. Scientia Horticulturae, 101(1-2), 169-178, 2004.

Belanger, M.J., Miller, J.R., Boyer, M.G., Comparative relationships between some red edge parameters and seasonal leaf chlorophyll concentrations. Canadian Journal of Remote Sensing, 21, 16−21, 1995.

Biber, P.D. Evaluating a chlorophyll content meter on three coastal wetland plant species. Journal of Agricultural, Food and Environmental Sciences, 1(2), 1-11, 2007.

Burges, C.J.C., 1998. A tutorial on support vector machines for pattern recognition. Data Mining and Knowledge Discovery, 2,121-167.

Cammarano, D., Fitzgerald, G., Basso, B., Chen, D., Grace, P., O'Leary, G., Remote estimation of chlorophyll on two wheat cultivars in two rainfed environments. Crop and Pasture Science, 62(4), 269-275, 2011.

Carter, G. A. Ratios of leaf reflectances in narrow wavebands as indicators of plant stress. International Journal of Remote Sensing, 15, 697−704, 1994.

Casa, R., Castaldi, F., Pascucci, S., Pignatti, S. Chlorophyll estimation in field crops: an assessment of handheld leaf meters and spectral reflectance measurements. The Journal of Agricultural Science, 153(5), 876-890, 2015.

Ciganda, V., Gitelson, A. A., Schepers, J. Vertical profile and temporal variation of chlorophyll in maize canopy: Quantitative "crop vigor" indicator by means of reflectance-based techniques. Agronomy Journal, 100, 1409–1417, 2008.

Ciganda, V., Gitelson, A.A., Schepers, J., Non-destructive determination of maize leaf and canopy chlorophyll content. Journal of Plant Physiology, 166, 157–167, 2009.

Ciganda, V. S., Gitelson, A. A., Schepers, J., How deep does a remote sensor sense? Expression of chlorophyll content in a maize canopy. Remote Sensing of Environment, *126*, 240-247, 2012.

Congalton, R.G., A review of assessing the accuracy of classification of remotely sensed data. Remote Sens Environ., 37, 35–46, 1991.

Curran, P.J., Imaging spectrometry. Progress in Physical Geography, 18(2), 247−266, 1994.

Datt, B. Remote sensing of chlorophyll a, chlorophyll b, chlorophyll a+ b, and total carotenoid content in eucalyptus leaves. Remote sensing of environment, 66(2), 111-121, 1998.

Datt, B., A new reflectance index for remote sensing of chlorophyll content in higher plants: Tests using Eucalyptus leaves. Journal of Plant Physiology, 154, 30−36, 1999.

Davidson, D., Achal, S., Mah, S., Gauvin, R., Kerr, M., Tam, A., Determination of tree species and tree stem densities in northern Ontario forests using airborne CASI data. Proceedings of the Fourth International Airborne Conference and Exhibition, Ottawa, 178−196, 1999.

De Souza, R., Grasso, R., Peña-Fleitas, M.T., Gallardo, M., Thompson, R.B., Padilla, F.M., Effect of cultivar on chlorophyll meter and canopy reflectance measurements in cucumber. Sensors, 20(2), 509, 2020.

Delegido, J., Vergara, C., Verrelst, J., Gandía, S., Moreno, J., Remote estimation of crop chlorophyll content by means of high-spectral-resolution reflectance techniques. Agronomy Journal, 103(6), 1834-1842, 2011.

Dong, T., Shang, J., Chen, J. M., Liu, J., Qian, B., Ma, B., Zhou, G. Assessment of portable chlorophyll meters for measuring crop leaf chlorophyll concentration. Remote Sensing, 11(22), 2706, 2019.

Dwyer, L.M., Stewart, D.W., Hamilton, R.I., Houwing, L., Ear position and vertical distribution of leaf area in corn. Agronomy Journal, 84, 430–438, 1992.

Evans, J.R., Photosynthesis and nitrogen relationships in leaves of C3 plants. Oecologia, 78, 9–19, 1989.

Fang, Z., Bouwkamp, J., Solomos, T., Chlorophyllase activities and chlorophyll degradation during leaf senescence in nonyellowing mutant and wild type of *Phaseolus vulgaris* L. Journal of Experimental Botany, 49, 503−510, 1998.

Foody, G.M., Mathur, A., A Relative Evaluation of Multiclass Image Classification by Support Vector Machines. IEEE Transactions on Geoscience and Remote Sensing, 42, 1335–1343, 2004.

Foody, G.M., Status of land cover classification accuracy assessment, Remote Sens. Environ., 80, 185–201, 2002.

Gitelson, A.A., Merzlyak, M.N., Signature analysis of leaf reflectance spectra: Algorithm development for remote sensing of chlorophyll. Journal of Plant Physiology, 148, 494−500, 1996.

Gitelson, A.A., Gritz, U., Merzlyak, M.N. Relationships between leaf chlorophyll content and spectral reflectance and algorithms for non-destructive chlorophyll assessment in higher plant leaves. Journal of Plant Physiology, 160, 271–282, 2003.

Gitelson, A.A., Viña, A., Rundquist, D.C., Ciganda, V., Arkebauer, T.J., Remote estimation of canopy chlorophyll content in crops. Geophysical Research Letters, 32, L08403, 2005.

Gitelson, A.A., Viña, A., Verma, S.B., Rundquist, D.C., Arkebauer, T.J., Keydan, G., Relationship between gross primary production and chlorophyll content in crops: Implications for the synoptic monitoring of vegetation productivity. Journal of Geophysical Research, 111, D08S11, 2006.

Gualtieri, J.A., Cromp, R.F, Support Vector Machines for Hyperspectral Remote Sensing Classification. Proc. SPIE, 3584, 221–232, 1998.

Hoberg, T., Müller, S., Multitemporal Crop Type Classification Using Conditional Random Fields and RapidEye Data. ISPRS, XXXVIII-4/W19, 115-121, 2011.

Huang, C., Davis, L.S., Townshend, J.R.G., An Assessment of Support Vector Machines for Land Cover Classification. Int. J. Remote Sensing, 23,725-749, 2002.

Kamarianakis, Z., and Panagiotakis, S., Design and implementation of a low-cost chlorophyll content meter. Sensors, 23(5), 2699, 2023.

Keating, B.A., Wafula, B.M., Modelling the fully expanded area of maize leaves. Field Crops Research, 29, 163–176, 1992.

Kropff, M. J., Goudrian, J., Competition for resource capture in agricultural crops. In J. L. Monteith, R. K. Scott, & M. H. Unsworth (Eds.), Resource Capture by

Crops. Sutton Bonington Campus, Loughborough, Leicestershire: Nottingham University Press 1-897676-21-2, 1994.

Kumar, P., Dileep Gupta, K., Mishra, V. N., Prasad R., Comparison of support vector machine, artificial neural network, and spectral angle mapper algorithms for crop classification using LISS IV Data. International Journal of Remote Sensing, 36(6), 1604–1617, 2015.

Landis, J.R., Kock, G.G., The measurement of observer agreement for categorical data Biometrics, 33,159–174, 1977.

Lawrence, R., Labus, M., Early detection of Douglas-fir beetle infestation with subcanopy resolution hyperspectral imagery. Western Journal of Applied Forestry, 18, 202−206, 2003.

le Maire, G., Francois, C., Soudani, K., Berveiller, D., Pontailler, J.Y., Genet, H., Calibration and validation of hyperspectral indices for the estimation of broadleaved forest leaf chlorophyll content, leaf mass per area, leaf area index and leaf canopy biomass. Remote Sensing of Environment, 112, 3846–3864, 2008.

Luther, J.E., Carroll, A.L., Development of an index of Balsam Fir vigor by foliar spectral reflectance. Remote Sensing of Environment, 69, 241−252, 1999.

Lewis, M., Jooste, V., de Gasparis, A.A., Discrimination of arid vegetation with airborne multispectral scanner hyperspectral imagery. IEEE Transactions on Geoscience and Remote Sensing, 39, 1471−1479, 2001.

Melgani, F., Bruzzone, L., Classification of Hyperspectral Remote Sensing Images with Support Vector Machines, IEEE Transactions on Geoscience and Remote Sensing, 42(8), 1778–1790, 2004.

Meneguzzo, D.M., Liknes, G.C., Nelson, M. D., Mapping trees outside forests using high-resolution aerial imagery: A comparison of pixel- and object-based classification approaches. Environmental Monitoring and Assessment. 185(8), 6261–6275, 2013.

Michez, A., Piégay, H., Lisein, J., Claessens, H., Lejeune, P., Classification of riparian forest species and health condition using multi-temporal and hyperspatial imagery from unmanned aerial system. Environmental Monitoring and Assessment.188:146, 2016.

Mishra, S., & Mishra, D. R., Normalized difference chlorophyll index: A novel model for remote estimation of chlorophyll-a concentration in turbid productive waters. Remote Sensing of Environment, 117, 394-406, 2012.

Montserud R.A., Leamans R., Comparing global vegetation maps with the kappa statistic Ecol. Model., 62, 275–293, 1992.

Mutlu, A., Kazancı, B., Özçetin, A., Sarıyılmaz, F., Akşehir Gölü zamansal değişiminin bant oranlama yöntemleri ile belirlenmesi. Türkiye Uzaktan Algılama Dergisi, 2 (1), 22-28, 2020.

Myint, S.W., Gober, P., Brazel, A., Grossman-Clarke, S., Weng, Q., Per-pixel vs. object-based classification of urban land cover extraction using high spatial resolution imagery. Remote sensing of environment, 115(5),1145-1161, 2011.

Naguib, A.M., Farag, M.A., Yahia, M.A., Ramadan H.H., Abd Elwahab M.S., Comparative study between support vector machines and neural networks for lithological discrimination using hyperspectral data. Egypt Journal of Remote Sensing and Space Science, 12,27–42, 2009.

Noland, T.L., Miller, J.R., Moorthy, I., Panigada, C., Zarco-Tejada, P.J., Mohammed, G.H., Bioindicators of forest sustainability: Using remote sensing to monitor forest condition. In: Meeting emerging ecological, economic, and social challenges in the Great Lakes region: Popular summaries. Compiled by L.J. Buse and A.H. Perera, Ontario Forest Research Institute, Ontario Ministry of Natural Resources, Forest Research Information 155: 75–77, 2003.

Oommen, T., Misra, D., Twarakavi, N.K.C., Prakash A., Sahoo B., Bandopadhyay, S., An objective analysis of support vector machine based classification for remote sensing. Mathematical Geosciences, 40, 409–422, 2008.

Owusu, C. PyGEE-SWToolbox: A Python Jupyter notebook toolbox for interactive surface water mapping and analysis using Google Earth Engine. Sustainability 14, 2557, 2022,

Pal, M., Mather, P.M., Support Vector Machines for Classification in Remote Sensing. International Journal of Remote Sensing, 26,1007-1011, 2005.

Richards, J.A., Jia, X., 2006. Remote Sensing Digital Image Analysis (4. Edition), Germany: Springer.

Rock, B.N., Hoshizaki, T., Miller, J.R., Comparison of in situ and airborne spectral measurements of the blue shift associated with forest decline. Remote Sensing of Environment, 24, 109−127, 1988.

Rogan, J., Franklin, J., Roberts, D.A., A comparison of methods for monitoring multitemporal vegetation change using Thematic Mapper imagery. Remote Sens. Environ., 80,143–156, 2002.

Sakieh, Y., Gholipour, M., Salmanmahiny, A., An integrated spectral-textural approach for environmental change monitoring and assessment: analyzing the dynamics of green covers in a highly developing region. Environmental Monitoring and Assessment.188, 205, 2016

Sampson, P.H., Zarco-Tejada, P.J., Mohammed, G. H., Miller, J.R., Noland, T.L. Hyperspectral remote sensing of forest condition: Estimating chlorophyll content in tolerant hardwoods. Forest Science, 49(3), 381−391, 2003.

Tucker, C.J., Asymptotic nature of grass canopy spectral reflectance. Applied Optics, 16, 1151–1156, 1977.

Ustin, S.L., Gitelson, A.A., Jacquemoud, S., Schaepman, M., Asner, G.P., Gamon, J. A., Retrieval of foliar information about plant pigment systems from high resolution spectroscopy. Remote Sensing of Environment, 113, S67–S77, 2009. URL-1. www.googleearthengine.com.tr, Erişim tarihi: 18.01.2025.

Valentinuz, O.R., Tollenaar, M., Vertical profile of leaf senescence during the grain-filling period in older and newer maize hybrids. Crop Science, 44, 827–834, 2004.

Vapnik, V.N., The Nature Of Statistical Learning Theory (2. Edition) New York: Springer-Verlag, 2000.

Velastegui-Montoya, A., Montalván-Burbano, N., Carrión-Mero, P., Rivera-Torres, H., Sadeck, L., Adami, M. Google Earth Engine: A Global Analysis and Future Trends. Remote Sens. 15, 3675, 2023.

Wang, R.; Pan, L.; Niu, W.; Li, R.; Zhao, X.; Bian, X.; Yu, C.; Xia, H.; Chen, T. Monitoring the spatiotemporal dynamics of surface water body of the Xiaolangdi Reservoir using Landsat-5/7/8 imagery and Google Earth Engine. Open Geosci. 13, 1290–1302, 2021,

Whiteside, T. G., Boggs, G. S., Maier, S. W., Comparing object-based and pixel-based classifications for mapping savannas. International Journal of Applied Earth Observation and Geoinformation, 13, 884-893, 2011.

Wu, Q., Zhang, Y., Zhao, Z., Xie, M., Hou, D., Estimation of relative chlorophyll content in spring wheat based on multi-temporal UAV remote sensing. Agronomy, 13(1), 211, 2023.

Yang, C., Everitt, J. H., Murden, D., Evaluating high resolution SPOT 5 satellite imagery for crop identification. Computers and Electronics in Agriculture 75( 2), 347–354, 2011.

Zarco-Tejada, P.J., Miller, J.R., Harron, J., Hu, B., Noland, T.L., Goel, N., Needle chlorophyll content estimation through model inversion using hyperspectral data from boreal conifer forest canopies. Remote Sensing of Environment, 89, 189−199, 2004a.

Zarco-Tejada, P.J., Miller, J.R., Morales, A., Berjón, A., Agüera, J., Hyperspectral indices and model simulation for chlorophyll estimation in open-canopy tree crops. Remote Sensing of Environment, 90(4), 463−476, 2004b.

Zhang, Y., Chen, J.M., Miller, J.R., Noland, T.L., Retrieving chlorophyll content of conifer needles from hyperspectral measurements. Canadian Journal of Remote Sensing, 34 (3), 296-310, 2008.

Zhang, K., Li, W., Li, H., Luo, Y., Li, Z., Wang, X., Chen, X., A leaf-patchable reflectance meter for in situ continuous monitoring of chlorophyll content. Advanced Science, 10(35), 2305552, 2023.

# CHAPTER 11

# Microwave Power and Temperature Dependence of γ-Irradiation–Induced Radicals in Dicyclomine hydrochloride Studied by EPR Spectroscopy

**Kerem Sütçü**[1]

[1] Prof. Dr., SÜTÇÜ Department of Science, Faculty of Education, Dicle University, Diyarbakır, Turkey, Orcid: 000-0002-5791-1492

## 1 Introduction

Dicyclomine hydrochloride (DC-HCl) is an anticholinergic/antispasmodic medication employed for treating irritable bowel syndrome (IBS), a chronic condition affecting the colon and characterized by abdominal cramps, bloating, diarrhea, and constipation [1]. This study aims to identify the radicals generated by γ-irradiation in a DC-HCl sample and to investigate the power- and temperature-dependent behavior of these radicals through detailed EPR analyses. EPR spectroscopy, widely utilized for scrutinizing both organic and inorganic compounds, distinguishes itself as the preferred spectroscopic technique for comprehensive insights into the structural and motional attributes of free radicals, delivering both qualitative information and quantitative results [2-7]. Due to its popularity in contemporary times, the radiosterilization method, particularly investigated for its contactless sterilization application in drugs, is widely researched [8-12]. Although DC-HCl has been extensively investigated in various studies, there is a notable absence of research providing insights into the structures and sensitivities of the free radicals that could potentially form during the process of radiosterilization [13-15].

Following the recent global pandemic, the need to reduce direct contact with consumable products has become increasingly apparent. Radiation sterilization offers several major advantages, including excellent penetration capacity, minimal residual effects on treated materials, negligible heat generation, fewer variables requiring control, and the ability to sterilize products after packaging [16]. Unlike many conventional methods, cobalt-60 irradiation can eliminate microorganisms in a single step, removing the necessity for a quarantine period [17]. These benefits have contributed to the widespread adoption and success of gamma radiation sterilization in numerous countries [18].

However, when solid pharmaceutical substances are exposed to ionizing radiation, free radicals may form, and some of these radicals can persist within the crystalline matrix for extended durations [19]. Additionally, the appearance of unexpected radiolytic intermediates and differences in national irradiation standards remain challenges associated with radiosterilization practices [20]. To ensure that radiation sterilization is effective and safe, it is essential to evaluate the material's sensitivity to irradiation beforehand. Several analytical techniques—such as thermoluminescence, chemiluminescence, and electron paramagnetic resonance—can be used to detect these intermediates, with EPR being particularly advantageous due to its high sensitivity toward free radicals [21]. Numerous EPR investigations have explored both the structural features and radiation stability of radicals produced after irradiation [22–27].

## 2 Experimental

The dicyclomine hydrochloride (DC-HCl) sample used in this study was obtained from a commercial supplier. The material was irradiated at room temperature with a $^{60}$Co γ-ray source (Isotope, Ob-Servo Sanguis) to a dose of 15 kGy. The chemical characteristics of DC-HCl are summarized in Table 1. Although 25 kGy is generally accepted as the standard sterilization dose, exposure of pharmaceutical substances to such levels may trigger unwanted physical or chemical alterations; therefore, a reduced dose of 15 kGy was selected to minimize potential degradation [28]. All irradiation procedures were performed at the Turkish Energy Nuclear and Mineral Research Agency (TENMAK).

After procurement, the powdered samples were transferred aseptically into plastic tubes to avoid contamination from dust or moisture. Following irradiation, the tubes were sealed tightly to prevent exposure to light. EPR measurements were carried out on a Jeol JES-FA300 X-band spectrometer, and the instrumental parameters used for spectral acquisition are provided in Table 2. The spectrometer is equipped with a closed-loop water-cooling system and a temperature control unit, allowing measurements at temperatures down to liquid-nitrogen levels.

## 3 Results and Discussion

### 3.1 Microwave Power Saturation Studies

In the process of recording spectra for the gamma-irradiated DC-HCl sample, the investigation focused on the variation in signal intensities within the microwave power range of 0.01–20 mW to mitigate the risk of power saturation. Fig. 1 shows the room-temperature EPR spectrum of the γ-irradiated DC-HCl sample, in which several well-resolved resonance lines labeled as $I_1$–$I_{11}$ are observed, indicating the formation of radiation-induced paramagnetic centers. To examine the microwave power dependence of the signal intensities, the peak-to-peak amplitudes of selected lines ($I_4$, $I_6$, and $I_8$) were measured as a function of the square root of the applied microwave power ($P^{1/2}$), as presented in Fig. 2. The variation of signal intensities with increasing microwave power demonstrates an initial linear increase followed by a tendency toward saturation at higher power levels, reflecting differences in relaxation behavior among the selected resonance lines. Evaluation of the microwave power dependence shows that the $I_6$ signal becomes saturated at a microwave power of around 5 mW, while the $I_4$ and $I_8$ signals require a higher power level, reaching saturation near 10 mW. This variation in saturation behavior reflects differences in the relaxation dynamics of the corresponding paramagnetic centers. Accordingly, the observed power-dependent response provides evidence that γ-irradiation induces more than one

radical species in the DC-HCl sample, each characterized by distinct spin–lattice relaxation behavior.

### 3.2. Temperature-Dependent EPR Studies

To evaluate whether variations in temperature lead to the formation of different radical species, the evolution of the EPR spectral line shape and signal intensity of the 15 kGy-irradiated sample was analyzed over the temperature range of 123–373 K. EPR measurements were first carried out at 123 K and subsequently repeated at temperature increments of 50 K up to 373 K.

The EPR spectra of DC-HCl measured at 123 K, 173 K, 223 K, and 373 K are displayed in Figures 3a–3d, respectively. Comparison of the spectra obtained at 123 K and 173 K reveals that the overall line profile remains essentially unchanged. However, a reduction of about 10% is observed in the intensity of the central resonance feature ($I_6$). This temperature-dependent decrease suggests that the paramagnetic species responsible for the $I_6$ signal diminishes in concentration as the temperature increases within this interval.

The EPR spectra recorded at 123 K and 173 K exhibit similar spectral characteristics, with no significant changes observed in the overall signal structure, indicating that the same radical species dominates within this temperature range. In contrast, the spectrum measured at 223 K (Fig. 3c) displays the emergence of additional resonance lines, and all spectral components labeled $I_1$–$I_{11}$ become clearly observable. The appearance of these signals at 223 K suggests that, in addition to the radical species contributing at lower temperatures, a second radical species also participates in the experimental spectrum at this temperature. This temperature-dependent evolution of the spectral features indicates an increased contribution of the second radical type as the temperature rises. Furthermore, increasing the temperature from 123 K to 223 K led to an approximately 10% enhancement in the intensity of the $I_6$ signal. The presence of the $I_6$ resonance line at 123 K, together with its gradual intensity increase as the temperature rises to 223 K, indicates that the $I_6$ signal in Fig. 3c arises from the combined contribution of different radiation-induced radical species. When the temperature was increased to 373 K, the experimental spectrum exhibited a significant simplification, with the disappearance of several resonance features observed at lower temperatures. This behavior indicates that one of the radiation-induced radical species decays at elevated temperatures, while the remaining spectral contribution arises from a more thermally stable radical species. Accordingly, at 373 K, the EPR spectrum of the 15 kGy-irradiated DC-HCl sample is dominated by the contribution of this thermally stable paramagnetic center. In this context, the lack of additional resonance signals observed throughout the temperature range of 123–373 K indicates that the applied temperature variation does not induce the formation of new radical species in the irradiated DC-HCl sample.

## 4. Conclusion

The EPR investigation of γ-irradiated DC-HCl revealed the formation of radiation-induced paramagnetic centers whose behavior strongly depends on both microwave power and temperature. Microwave power saturation studies demonstrated that different resonance lines exhibit distinct saturation thresholds, indicating the presence of radical species with different relaxation characteristics. In particular, the earlier saturation of the $I_6$ signal compared to other resonance lines reflects variations in spin–lattice relaxation behavior, supporting the coexistence of more than one radical species in the irradiated sample.Temperature-dependent EPR measurements carried out between 123 K and 373 K showed that changes in temperature significantly affect the relative contributions of the radiation-induced radicals, while no additional resonance signals were observed within the investigated temperature range. At lower temperatures, the spectral features remain largely unchanged, whereas increasing the temperature leads to variations in signal intensities and the emergence or disappearance of certain resonance lines. At elevated temperatures, the experimental spectrum becomes dominated by a thermally more stable radical species, while less stable species decay. Overall, the combined microwave power and temperature analyses indicate that γ-irradiation of DC-HCl results in the formation of at least two different radical species with distinct relaxation and thermal stability properties. These findings provide important insight into the radiation response and stability of DC-HCl and contribute to a better understanding of the underlying radical processes induced by γ-irradiation. In the pharmaceutical industry, EPR spectroscopy with simulation methods will provide efficient results for determining the free radicals that will arise in the chemical structures of drugs due to the anticipated destructive effect of radiation used in drug sterilization.

### Ethical Approval

This research did not contain any studies involving animal or human participants, nor did it take place on any private or protected areas. No specific permissions were required for corresponding locations.

### Competing Interests

The author has no relevant financial or non-financial interests to disclose

### Authors' Contributions

I, Kerem Sütçü, am solely author of this manuscript.

### Funding

This work was supported by Grant No. ZGEF.22.003 of research Fund of Dicle University (DUBAP).

## References


[1] A.M. Abou Al Alamein, H.A. Hendawy, N.O. Elabd, Voltammetric determination of dicyclomine hydrochloride by carbon paste electrode modified with iron (III) oxide nanoparticles and activated glassy carbon electrode in pharmaceutical dosage form, human plasma and urine. Int. J. Electrochem. Scien. 13, 7989-8005 (2018)

[2] M. Aydın, Z. Kartal, Ş. Osmanoğlu, M.H. Başkan, R. Topkaya, EPR and FT-IR spectroscopic studies of L-lysine monohydrochloride and L-glutamic acid hydrochloride powders. J. Mol. Struct. 994, 150–154 (2011).

[3] M.H. Başkan, Ş. Osmanoğlu, EPR of gamma irradiated Nα-monochloroacetyl-α-aminoisobutyric acid. Z. Naturforsch. A 59, 665–668 (2004).

[4] M. Aydın, M.H. Başkan, S. Yakar, F.Ş. Ulak, M. Aydinol, B. Aydinol, M. Büyüm, EPR studies of gamma-irradiated L-alanine ethyl ester hydrochloride, L-arginine and alanyl-L-glutamine.Radiat. Eff. Defects Solids 163, 41–46 (2008).

[5] M. Aydın, M.H. Başkan, M.Y. Emre Osmanoğlu, EPR study of gamma-induced radicals in amino and iminodiacetic acid derivatives. Braz. J. Phys. 39, 583–586 (2009).

[6] Ş. Osmanoğlu, M.H. Başkan, EPR of gamma irradiated single crystals of N-acetyl- and N-carbamyl-α-aminoisobutyric acid. Z. Naturforsch. A 58, 290–292 (2003).

[7] M.H. Başkan, M. Aydın, Ş. Osmanoğlu, R. Topkaya, Electron paramagnetic resonance characterization of gamma irradiation damage centers in powder of L-(+)-tartaric acid, N-acetyl-L-alanine and 1-methyl-L-histidine. Radiat. Eff. Defects Solids 165, 938–943 (2010).

[8] N. Rosiak, K. Kilińska, R. Skibiński, D. Szymanowska, A. Miklaszewski, K. Lewandowska, P. Zalewski, Radiation sterilization as safe and effective way to obtain sterile biapenem. Radiat. Phys. Chem. 182, 109363 (2021)

[9] M. Farno, C. Lamarche, C. Tenailleau, S. Cavalié, B. Duployer, D. Cussac, S.G. Fullana, Low-energy electron beam sterilization of solid alginate and chitosan, and their polyelectrolyte complexes. Carbohydrate Poly. 261, 117578 (2021)

[10] P. Zalewski, R. Skibiński, D. Szymanowska-Powałowska, H. Piotrowska, W. Bednarski, J. Cielecka-Piontek, Radiolytic studies of cefozopran hydrochloride in the solid state. Electro. J. Biotech. 25, 28-32 (2017)

[11] B.K. Singh, D.V. Parwate, I.B.D. Sarma, S.K. Shukla, Study on gamma and electron beam sterilization of third generation cephalosporins cefdinir and cefixime in solid state. Radiat. Phys. Chem. 79, 1079-1087 (2010)

[12] K. Mäder, A. Domb, H.M. Swartz, Gamma-sterilization-induced radicals in biodegradable drug delivery systems. Appl. Radiat. Isotop. 47, 1669-1674 (1996)

[13] F. Faridbod, B. Larijani, M.R. Ganjali, P. Norouzi, PVC membrane sensor for potentiometric determination of dicyclomine in pharmaceutical formulation. Int. J. Electrochem. Sci, 7, 10404-10413 (2012)

[14] H. Ibrahim, Y.M. Issa, H.M. Abu-Shawish, Potentiometric flow injection analysis of dicyclomine hydrochloride in serum, urine and milk. Anal. Chim. Acta, 532, 79-88 (2005)

[15] J. Singh, M. Singh, S. Sharma, S. Sharma, A.K. Sharma, M. Sharma, Impact of diphenhydramine hydrochloride on an aqueous solution of imidazolium based surface-active ionic liquids at different temperatures: Physicochemical, thermodynamic and transport studies. J. Chem. Thermodyn. 107112 (2023)

[16] J.P. Basly, I. Longy, M. Bernard, Radiosterilization dosimetry by electron-spin resonance spectroscopy: Cefotetan. Anal. Chim. Acta. 359, 107-113 (1998)

[17] J.P. Basly, I. Basly, M. Bernard, Electron spin resonance identification of irradiated ascorbic acid: dosimetry and influence of powder fineness. Anal. Chim. Acta 372, 373-378 (1998)

[18] H.B. Ambrož, E.M. Kornacka, B. Marciniec, M. Ogrodowczyk, G.K. Przybytniak, EPR study of free radicals in some drugs γ-irradiated in the solid state. Radiat. Phys. Chem. 58, 357-366 (2000)

[19] A. Engalytcheff, M. Kolberg, A.L. Barra, K. Kristoffer Andersson, B. Tilquin, The use of multi-frequency EPR techniques to identify the radicals produced in irradiated β-blockers. Free Radical Res. 38, 59-66 (2004)

[20] J.P. Basly, J.L. Duroux, M. Bernard, Radiosterilization dosimetry by ESR spectroscopy: application to terbutaline. Int. J. Pharma. 142, 247-249 (1996)

[21] J.P. Basly, M. Bernard, I. Basly, Electron spin resonance detection of radiosterilization of pharmaceuticals: application to four nitrofurans. Analyst. 123, 1753–1756 (1998)

[22] M. Aydin, Y.E. Osmanoglu, M.H. Başkan, Electron paramagnetic resonance of rγ-irradiated glycyl-L-glutamine monohydrate, iminodiacetic acid and methyliminodiacetic acid. Radiat. Eff. Def. Solids 163, 47-53 (2008)

[23] M.H. Başkan, Y.E. Osmanoğlu, K. Sütçü, M. Aydın, Ş. Osmanoğlu, Radiation effect studies in single crystal of Trifluoroacetyl-α-Aminoisobutyric acid. Radiat. Eff. Def. Solids, 170, 854-861 (2015)

[24] S. Iravani, G.J. Soufi, Electron paramagnetic resonance (EPR) spectroscopy: food, biomedical and pharmaceutical analysis. Biomed. Spectrosc. Imaging 9, 165–182 (2020).

[25] G. Damian, EPR investigation of γ-irradiated anti-emetic drugs. Talanta, 60, 923-927. (2003)

[26] K.I. Aleksieva, N.D. Yordanov, Various approaches in EPR identification of gamma-irradiated plant foodstuffs: A review. Food Res. Int. 105, 1019-1028. (2018)

[27] C.L. Prasuna, R.P.S. Chakradhar, J.L. Rao, N.O. Gopal, EPR as an analytical tool in assessing the mineral nutrients and irradiated food products–vegetables. Spectrochim. Acta Part A: Molec. Biomolec. Spectro. 71, 809-813 (2008)

[28] A.M. Dam, L.G. Gazso, S. Kaewpila, I. Maschek, Radiation sterilization dose calculation for heparin and aprotinin based on ISO Method 1. Int. J. Pharma. 121, 245-248. (1995)

**Figure and Table Captions**

Figure 1. The EPR spectrum of 15 kGy irradiated DC-HCl sample

Figure 2. Variations of the EPR peak intensities of 15 kGy irradiated DC-HCl sample with square root of applied microwave power (P).

Figure 3. a) Experimental spectrum of 15 kGy irradiated DC-HCl sample recorded at 123K

b) Experimental spectrum of 15 kGy irradiated DC-HCl sample recorded at 173K

c) Experimental spectrum of 15 kGy irradiated DC-HCl sample recorded at 223K

d) Experimental spectrum of 15 kGy irradiated DC-HCl sample recorded at 373K

Table 1. Symbol, name, formula, molecular weight and chemical structure of DC-HCl.

Table 2. Spectral parameters used for DC-HCl when recording experimental spectra

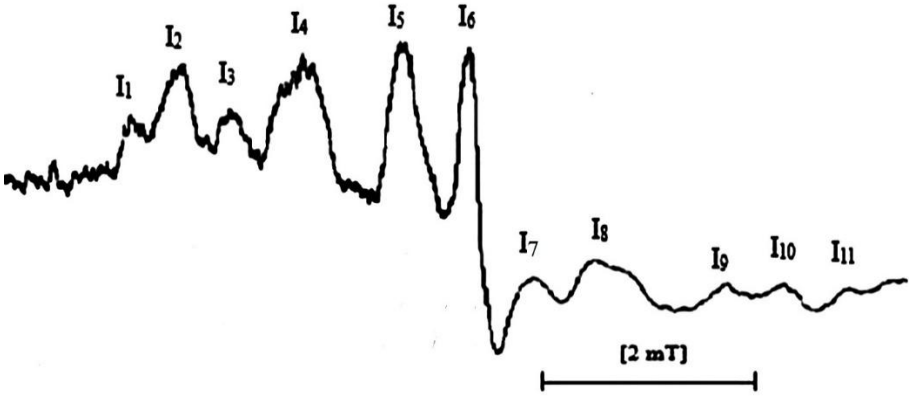
I1
I2
I3
I4
I5
I6
I7
I8
I9
I10
I11
[2 mT]

Fig. 1

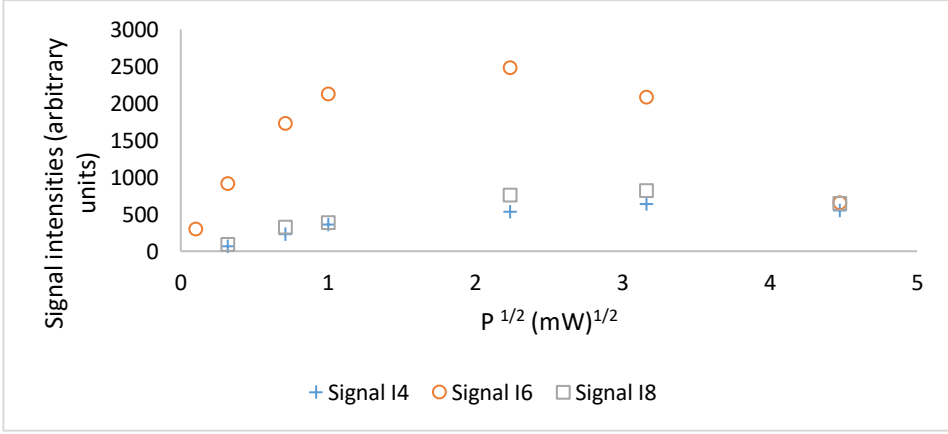
Signal intensities (arbitrary units)
3000
2500
2000
1500
1000
500
0
0
1
2
3
4
5
P 1/2 (mW)1/2
Signal I4
Signal I6
Signal I8

Fig. 2

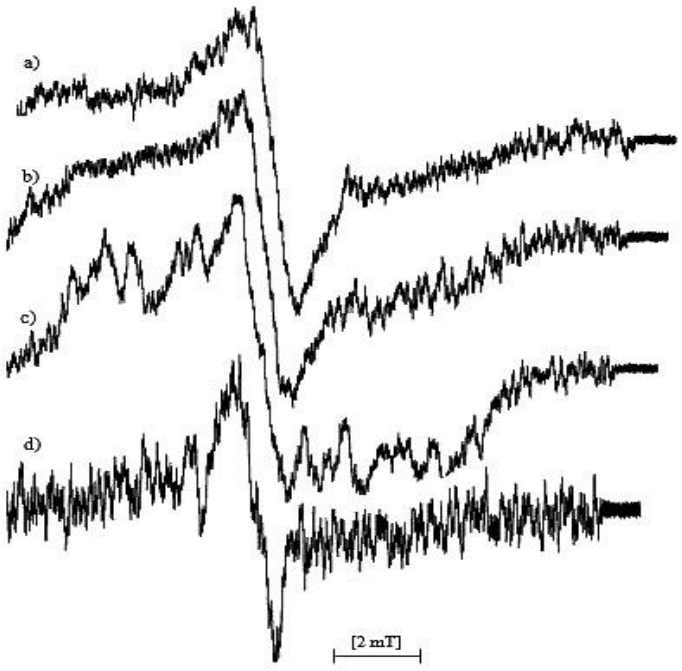


Fig. 3

| Symbol | Name | Chemical Formula | Molecular Weight | Chemical Structure |
|---|---|---|---|---|
| DC-HCl | Dicyclomine hydrochloride | $C_{19}H_{35}NO_2.HCl$ | 345.95 g/mol | 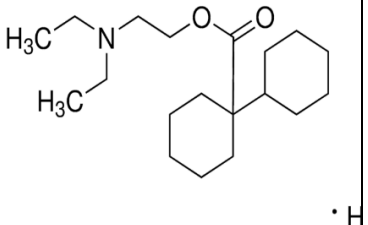 |

Table 1

| | |
|---|---|
| Microwave frequency | 9.2 GHz |
| Microwave power | 0.99 mW |
| Field center | 329 mT |
| Modulation frequency | 100 kHz |

Table 2

# CHAPTER 12

# Feature Selection Problem in Big Data Environments Statistical Tests and Embedded Learning Methods

**Özge Taş**[1]

[1] Öğr.Gör., Kastamonu University, ORCID: /0000-0001-7220-5054

The feature selection problem in big data environ-ments addresses the critical challenge of identifying and selec-ting relevant features from high-dimensional datasets, particu-larly in contexts characterized by massive volumes of data, diverse data types, and the rapid pace of data generation. Effec-tive feature selection is essential for enhancing the performan-ce of machine learning algorithms, as it helps mitigate issues such as overfitting, reduces computational costs, and improves model interpretability and accuracy. As datasets grow in size and complexity, the presence of irrelevant or redundant featu-res can significantly degrade model performance by introdu-cing noise and complicating the learning process. This pheno-menon, often referred to as the "curse of dimensionality," un-derscores the importance of robust feature selection techniques to ensure that models can effectively identify meaningful pat-terns from the data.( Pudjihartono, N., Fadason, T., Kempa-Liehr, A. W., & O'Sullivan, J. M. , 2022).

Various methods exist for feature selection, including filter methods, which assess feature relevance independently of any model; wrapper methods, which evaluate feature subsets based on model performance; and embedded methods, which integra-te feature selection within the model training process itself. Each approach presents unique advantages and challenges that can impact their applicability in big data scenarios.

Notably, recent advancements in feature selection have intro-duced hybrid approaches that combine the strengths of different methods, enabling more effective handling of high-dimensional datasets while addressing issues such as computational effici-ency and correlated features. As the demand for accurate pre-dictive modeling continues to grow across domains such as healthcare, finance, and network security, ongoing research in feature selection remains crucial to developing innovative solu-tions that meet the needs of big data analytics.

Despite the progress made in feature selection methodologies, challenges persist, particularly in the realms of computational complexity and the management of feature interactions. Future directions in research are likely to focus on refining hybrid techniques and enhancing the integration of feature selection within machine learning frameworks, ultimately aiming to improve predictive performance in increasingly complex data environments.

**Feature Selection**

Feature selection is a crucial preprocessing step in the analysis of high-dimensional datasets, particularly in the context of big data environments. It aims to identify and select a subset of relevant features while discarding irrelevant or redundant ones, which can significantly enhance the performance of machine learning algorithms (Cai, J., et. Al. ,2018).The rapid increase in data volume, variety, and velocity characterizes big data, creating challenges for effective feature selection. These challenges include handling large feature sets, which

often contain numerous irrelevant features that contribute little to predictive accuracy and may introduce noise, thereby degrading model performance ( Li, J., & Liu, H. , 2017).

**Importance of Feature Selection**

In high-dimensional spaces, the curse of dimensionality becomes prominent; each training example may become isolated from others, making it difficult for models to identify meaningful patterns. Feature selection helps mitigate this issue by reducing the dimensionality of the dataset, allowing for more efficient learning and improved classification accuracy (Subbiah, S. S., & Chinnappan, J. 2021).

Furthermore, many machine learning algorithms can suffer from overfitting when trained on datasets with excessive features. By selecting a smaller, more relevant subset of features, the likelihood of overfitting can be reduced.

**Methods of Feature Selection**

Feature selection methods can be broadly classified into three categories: filter, wrapper, and embedded methods. Filter methods evaluate the relevance of features independently of any machine learning model, often using statistical tests to rank features based on their significance ( Pudjihartono, N. Et.Al.2022).

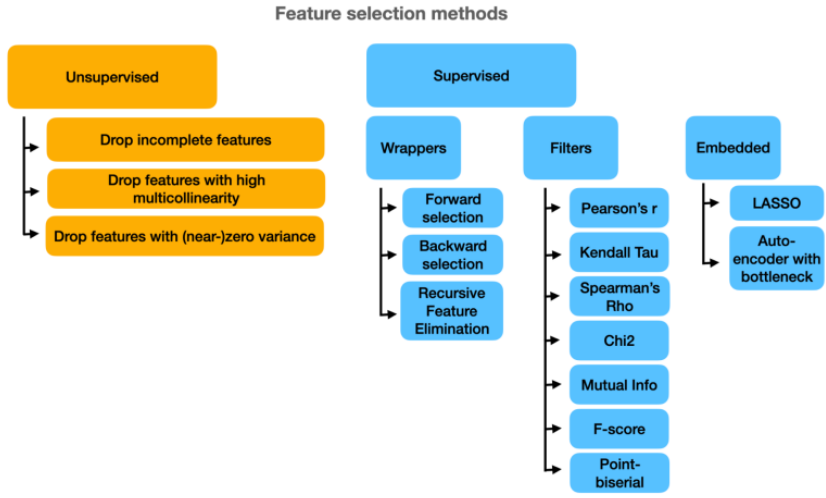


**Figure 1.** feature selection taxonomy.

Wrapper methods, on the other hand, evaluate subsets of features by training a model, which can lead to higher accuracy but also increases the risk of overfitting.

Embedded methods incorporate feature selection as part of the model training process, optimizing both feature selection and model learning simultaneously.

**Challenges in Big Data Context**

The feature selection process in big data environments is further complicated by the presence of numerous features and the need for real-time processing. High-dimensional datasets often contain a mix of ordinal, interval, and ratio features, which can affect the choice of statistical tests and methods employed for feature selection.

Additionally, computational efficiency is critical, as traditional feature selection algorithms may struggle to handle the scale and complexity of big data. Therefore, innovative algorithms, such as those leveraging evolutionary strategies, are being explored to enhance feature selection efficiency without compromising model accuracy ( Li, J., & Liu, H. (2017).

**Feature Selection Techniques**

Feature selection is a critical process in data science and machine learning, aimed at enhancing model performance by selecting a subset of relevant features from a larger dataset. This process not only improves model accuracy and efficiency but also increases interpretability and simplicity of the models, making them easier to maintain and understand

**Overview of Feature Selection**

Feature selection methods can be categorized into three primary types: filter methods, wrapper methods, and embedded methods.

*Filter Methods*

Filter methods evaluate the relevance of features based on their intrinsic properties, such as correlation with the target variable, without involving any machine learning models. Common statistical tests used in filter methods include Chi-squared tests, ANOVA, and correlation coefficients. These methods are computationally efficient but may not account for feature interactions (Khaire, U. M., & Dhanalakshmi, R. (2022).

*Wrapper Methods*

Wrapper methods assess the performance of a machine learning model using different combinations of features. They involve training the model multiple times with different feature subsets, which can be computationally expensive. Recursive Feature Elimination (RFE) is a prominent wrapper method that recursively removes the least important features based on a specific estimator's importance criteria until the desired number of features is reached (Cai, J., Luo, J., Wang, S., & Yang, S. (2018

*Embedded Methods*

Embedded methodologies, which operate within an integrated structure with the model training process, transform feature extraction from an external preprocessing step into an internal algorithmic operation. L1 regularization-based approaches enable this integration while allowing the generation of sparse models through coefficient penalization. The Lasso technique, in particular, optimizes both dimensionality reduction and prediction capabilities simultaneously in complex datasets by reducing the weights of variables with low explanatory power to near zero. ( Cai, J., Luo, J.,et. Al., (2018)

Random Forests, another example of an embedded method, provide feature importance scores based on how much they reduce impurity across decision trees, allowing for effective feature ranking and selection.

**Challenges in Feature Selection**

Despite the advantages of feature selection, challenges persist, especially in high-dimensional datasets where the number of features can become overwhelming. This phenomenon, known as the curse of dimensionality, necessitates robust feature selection techniques to streamline the model-building process ( Khaire, U. M., & Dhanalakshmi, R. 2022).

Moreover, ensuring that the selected features truly contribute to model performance requires careful evaluation and validation to avoid overfitting and maintain generalizability.

**Embedded Learning Methods**

Embedded methods are a class of feature selection techniques that integrate feature selection directly into the model training process. Unlike filter methods, which assess features independently of the learning algorithm, or wrapper methods, which rely on a specific model to evaluate subsets of features, embedded methods perform variable selection during the training phase of the learning algorithm itself. This integration allows for the model to automatically adjust weights and determine the importance of features while optimizing classification accuracy (Guyon, I., & Elisseeff, A. (2003).

**Characteristics of Embedded Methods**

Embedded methods combine the strengths of both filter and wrapper approaches. They are generally more computationally efficient than wrapper methods, yet they still allow for interaction with the classifier, thus improving performance (Hemdanou, A. L., Sefian, M. L., Achtoun, Y., & Tahiri, I. 2024).

For example, decision tree-based algorithms, such as random forests and gradient boosting machines, are commonly used embedded methods that rank

feature importance based on metrics like Mean Decrease Impurity (MDI)( Pudjihartono, N. Et. Al.,2022).

Additionally, regularization techniques like LASSO and elastic net also exemplify embedded methods, as they can shrink coefficients for less relevant features while still being integrated into the model training (Rainio, O., Teuho, J. & Klén, R., 2024).

**Advantages and Disadvantages**

One of the primary advantages of embedded methods is their ability to identify and account for feature interactions, a capability often lacking in simpler filter methods.

This is particularly valuable in high-dimensional datasets where feature interactions can significantly influence the outcome ( Bohrer, J. D. S., & Dorn, M., 2024). However, studies have shown that the effectiveness of algorithms like random forests can diminish as the number of features increases, which may limit their applicability in extremely high-dimensional settings (Rainio, O., Teuho, J. & Klén, R., 2024).

Moreover, while embedded methods generally produce more stable and reproducible results, they may still struggle with redundant features unless specifically designed to address such issues.

**Examples of Embedded Methods**

Common examples of embedded methods include:

*Decision Trees and Random Forests*: These algorithms utilize tree structures to make decisions based on feature importance and can consider higher-order interactions ( Pudjihartono, N., Et. Al., 2022).

Gradient Boosting Machines: Similar to random forests, gradient boosting builds models iteratively, focusing on minimizing errors by combining weak learners (Rainio, O., Teuho, J. & Klén, R. ,2024).

Regularization Models: Techniques like LASSO not only perform feature selection but also regularize models to enhance their predictive performance, particularly in scenarios with multicollinearity ( Tiwari, S. R., & Rana, K. K. (2020).

**Applications in Big Data**

Feature selection (FS) plays a crucial role in the processing and analysis of big data, particularly in improving the performance of machine learning algorithms. As the volume of data generated by modern technologies continues to escalate, organizations are increasingly turning to FS methods to manage high-dimensional datasets efficiently.

**Importance of Feature Selection**

The growing complexity and size of big data often introduce challenges in identifying relevant features that contribute to model accuracy. Irrelevant or redundant features can degrade model performance by introducing noise, increasing computational costs, and leading to poor generalization. Therefore, FS is essential not only for reducing dimensionality but also for enhancing the interpretability of models and ensuring faster processing times.

**FS Methods and Techniques**

Various feature selection methods have been developed and are widely utilized within big data environments. These methods can be broadly categorized into filter, wrapper, and embedded approaches. Filter methods assess features based on statistical measures, while wrapper methods evaluate subsets of features using predictive models. Embedded methods integrate FS within the model training process, effectively combining feature selection with model learning to optimize performance (Pudjihartono, N., Et. Al., 2022).

**Evolutionary Algorithms**

Evolutionary algorithms (EAs), such as the cooperative co-evolutionary algorithm (CCEA), have gained popularity for feature selection due to their ability to explore large search spaces and improve classification accuracy even with numerous features (Subbiah, S. S., & Chinnappan, J. ,2021).

These algorithms can effectively balance the trade-off between the number of features and computational efficiency, achieving optimal feature subsets without prior knowledge of their significance.

**Challenges and Solutions**

Despite advancements in FS, several challenges remain in the context of big data. High dimensionality often leads to computational complexity that can hinder the effectiveness of FS methods. Therefore, hybrid strategies that combine different FS techniques are increasingly being explored to enhance stability and accuracy in model predictions. These strategies aim to reduce search spaces and identify the most relevant features while minimizing resource allocation

**Applications Across Domains**

Feature selection is employed across various fields, including healthcare, finance, and network security, where the analysis of high-dimensional data is critical. For instance, in healthcare analytics, identifying the most relevant features can significantly improve disease risk prediction and patient outcome assessments. Similarly, in network security, effective FS can enhance the classification accuracy of intrusion detection systems by eliminating irrelevant features and focusing on those that provide the most valuable insights

**Comparison of Methods**

Feature selection methods can be broadly categorized into three main types: filter methods, wrapper methods, and embedded methods. Each of these approaches has distinct advantages and limitations, which can significantly impact the performance of machine learning models in big data environments.

**Filter Methods**

Filter methods operate independently of any machine learning algorithm, using statistical techniques to evaluate the importance of features based on their inherent properties. These methods are computationally efficient and easy to implement, making them a popular choice for initial feature selection. However, filter methods may not always yield the optimal subset of features, especially when the dataset is limited and does not adequately capture the statistical correlations between features (Zschaubitz, E., Et. Al. , 2025).

Common examples include statistical tests like Chi-squared tests and ANOVA, which rank features based on their significance.

**Wrapper Methods**

Wrapper methods, in contrast, assess feature subsets by actually training and evaluating a machine learning model with those subsets. While this approach can lead to a more tailored selection of features that enhance model performance, it is computationally intensive and often time-consumin.

Wrapper methods require exhaustive searches through potential feature combinations, making them less feasible for very large datasets. Notably, hybrid approaches that combine filter and wrapper methods can offer a balance, yielding better performance than simple filters while being more efficient than pure wrapper methods.

**Embedded Methods**

Embedded methods provide a middle ground between filter and wrapper techniques. They integrate feature selection as part of the model training process, utilizing statistical calculus to determine the most relevant features while the model is being trained. This dual approach allows for the incorporation of the model's biases into the feature selection process, potentially resulting in better classifier performance with reduced computational costs compared to wrapper methods.

Despite their advantages, embedded methods may require careful tuning of hyperparameters and can be less intuitive to implement than filter methods.

**Challenges and Future Directions**

The feature selection problem in big data environments presents numerous challenges that require ongoing research and innovative solutions. One of the

primary challenges is the "curse of dimensionality," where the number of features significantly exceeds the number of samples, complicating the creation of accurate predictive models (Ali, M. Z., et. Al. , 2024).

As a result, feature selection methods are essential for reducing dimensionality and enhancing model performance by identifying the most informative features while eliminating irrelevant or redundant data ( Fan, J., Han, F., & Liu, H. 2014).

**Key Challenges**

*High Dimensionality and Complexity*

In big data contexts, datasets often contain thousands of features, leading to difficulties in model training and evaluation. Traditional statistical methods frequently fail in these high-dimensional spaces, necessitating the development of new statistical techniques that can effectively handle such challenges.

Moreover, the computational complexity of feature selection methods varies, with hybrid approaches offering a balance between simplicity and performance. These hybrid methods, which combine filter and wrapper techniques, are gaining traction for their ability to improve accuracy without excessive computational costs.

*Correlated Features*

Another significant issue is the presence of correlated features, which can lead to redundancy and overfitting in models. Effective feature selection techniques must be able to manage these correlations to ensure that the selected features contribute meaningfully to the model's predictive capabilities. As noted, a two-stage hybrid approach, where a filter method is used initially to reduce the feature set before applying a more complex wrapper method, can mitigate this problem by addressing feature dependencies more effectively.

**Future Directions**

*Exploration of Hybrid Approaches*

Future research should continue to explore hybrid approaches that combine different feature selection methods to leverage their strengths. For instance, using univariate filter techniques in the initial selection phase can simplify the subsequent wrapper stage, making the overall process more efficient. This strategy not only preserves the accuracy of the model but also reduces computational demands, a critical consideration in big data applications.

*Integration with Machine Learning*

As machine learning becomes increasingly prevalent in precision medicine and other fields, integrating feature selection methods within learning algorithms is essential. Embedded feature selection methods, which perform selection as part

of the model training process, hold promise for improving model performance while simplifying the analysis workflow.

Continued development in this area can lead to more robust predictive models that effectively manage the complexities of big data.

*Addressing Model Compatibility*

The issue of data-model compatibility also requires attention. Models must be compatible with the data features, and this often necessitates careful selection of features based on the chosen model's requirements. This area of research is vital, as it can streamline the feature selection process and improve overall model performance by ensuring that the selected features are suitable for the analytical frameworks in use.

**Conclusion**

As has been demonstrated by the present study, the process of feature selection within big data ecosystems cannot be considered a simple step in data preprocessing; rather, it is a strategic necessity in combating the "curse of dimensionality" that arises due to high-dimensional data.

Increases in the volume, velocity, and variety of data result in more complex models and increased computational costs. However, the elimination of irrelevant or unnecessary features directly optimizes a model's generalizability and prediction accuracy.

As indicated by the extant literature, each of the filter, wrapper, and embedding methods possesses distinct advantages. However, the computational challenges associated with big data are progressively prompting researchers to adopt hybrid approaches. The hybrid nature of these techniques enables a balance to be struck between computational efficiency and model performance. This, in turn, facilitates the development of more robust predictive models, particularly in critical areas such as healthcare, finance, and network security.

Future research is expected to focus on dynamic selection algorithms that can manage feature interactions with greater precision and integrate seamlessly into machine learning processes. Ultimately, an effective feature selection process will continue to play a pivotal role in extracting meaningful patterns from complex data sets and in the operational success of big data analytics.

## REFRENCES


Ali, M. Z., Abdullah, A., Zaki, A. M., Rizk, F. H., Eid, M. M., & El-Kenway, E. M. (2024). Advances and challenges in feature selection methods: a comprehensive review. *J. Artif. Intell. Metaheuristics*, *7*(1), 67-77.

Bohrer, J. D. S., & Dorn, M. (2024). Enhancing classification with hybrid feature selection: A multi-objective genetic algorithm for high-dimensional data. *Expert Systems with Applications*, *255*, 124518.

Cai, J., Luo, J., Wang, S., & Yang, S. (2018). Feature selection in machine learning: A new perspective. *Neurocomputing*, *300*, 70-79.

Fan, J., Han, F., & Liu, H. (2014). Challenges of big data analysis. *National science review*, *1*(2), 293-314.

Guyon, I., & Elisseeff, A. (2003). An introduction to variable and feature selection. *Journal of machine learning research*, *3*(Mar), 1157-1182.

Hemdanou, A. L., Sefian, M. L., Achtoun, Y., & Tahiri, I. (2024). Comparative analysis of feature selection and extraction methods for student performance prediction across different machine learning models. *Computers and Education: Artificial Intelligence*, *7*, 100301.

Khaire, U. M., & Dhanalakshmi, R. (2022). Stability of feature selection algorithm: A review. *Journal of King Saud University-Computer and Information Sciences*, *34*(4), 1060-1073.

Li, J., & Liu, H. (2017). Challenges of feature selection for big data analytics. *IEEE Intelligent Systems*, *32*(2), 9-15.

Pudjihartono, N., Fadason, T., Kempa-Liehr, A. W., & O'Sullivan, J. M. (2022). A review of feature selection methods for machine learning-based disease risk prediction. *Frontiers in bioinformatics*, *2*, 927312.

Pudjihartono, N., Fadason, T., Kempa-Liehr, A. W., & O'Sullivan, J. M. (2022). A review of feature selection methods for machine learning-based disease risk prediction. *Frontiers in bioinformatics*, *2*, 927312.

Rainio, O., Teuho, J. & Klén, R. Evaluation metrics and statistical tests for machine learning. Sci Rep 14, 6086 (2024). https://doi.org/10.1038/s41598-024-56706-x

Subbiah, S. S., & Chinnappan, J. (2021). Opportunities and Challenges of Feature Selection Methods for High Dimensional Data: A Review. *Ingénierie des Systèmes d'Information*, *26*(1).

Tiwari, S. R., & Rana, K. K. (2020). Feature selection in big data: Trends and challenges. *Data Science And Intelligent Applications: Proceedings Of ICDSIA 2020*, 83-98.

Zschaubitz, E., Schröder, H., Glackin, C. C., Vogel, L., Labrenz, M., & Sperlea, T. (2025). A benchmark analysis of feature selection and machine learning methods for environmental metabarcoding datasets. *Computational and Structural Biotechnology Journal*, *27*, 1636-1647.

# CHAPTER 13

# Catalytic Activity of Nickel-Based Systems in Nitrobenzene Hydrogenation

**Dilek Kılınç**[1]

[1] Assoc. Prof. Dr. Harran University, Faculty of Pharmacy, Department of Pharmaceutical Chemistry, ORCID ID:0000-0002-0171-2371

## Introduction

The transformation of nitrobenzene into aniline represents one of the most significant catalytic processes in industrial organic chemistry and the general hydrogenation reaction of nitrobenzene is shown in **Figure 1.** Aniline serves as a vital intermediate for the synthesis of methylene diphenyl diisocyanate, which accounts for over 80% of global aniline consumption. Traditionally, this reduction was performed using stoichiometric reagents, but the advent of catalytic hydrogenation has revolutionized the process by offering higher atom economy and reduced waste (Yan X. et al., 2021:14). Nickel catalysts, particularly in their supported and nanostructured forms, have become indispensable due to their abundance and ability to operate under diverse reaction conditions (Hu Y. et al., 2023:10, Zhou, M. et al., 2022).

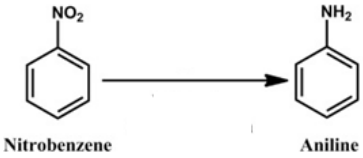


**Figure 1.** The hydrogenation reaction of nitrobenzene

Although noble metal catalysts (Pd, Pt) exhibit high efficiency, nickel-based systems have emerged as the industrial benchmark owing to their superior balance of cost-effectiveness, thermal stability, and inherent catalytic robustness. Recent advances in catalyst design have expanded the scope of nickel-based systems significantly. This comprehensive study provides an in-depth evaluation of nickel catalysts, spanning from conventional Raney nickel to advanced materials such as nanostructured systems, single-atom catalysts, and bimetallic complexes. A detailed analysis of mechanism and alternative reaction pathways is presented, specifically investigating how surface morphology and electronic promoters critically influence both catalytic selectivity and activity. The development of advanced nickel nanoparticles technology, encompassing synthesis methodologies, reaction mechanisms, and diverse applications, has been comprehensively reviewed (Tang, J. et al., 2023) Furthermore, green synthesis approaches for nickel oxide nanoparticles incorporating carbon nanomaterials have opened new avenues for sustainable catalyst preparation (Shoosri T. et al., 2024) The aniline process creation for conversion improvement using process intensification and green chemistry principles has been demonstrated to enhance industrial efficiency (Rohmah, A.N. et al., 2025). These innovations underscore the continued relevance of nickel catalysis in contemporary chemical manufacturing, with ongoing research establishing new paradigms for catalyst design and application.

Understanding the reaction mechanism is crucial for designing highly selective catalysts. The hydrogenation of nitrobenzene can proceed via two primary routes: the direct pathway (Haber mechanism) and the indirect pathway. Recent mechanistic studies have revealed the complexity of these transformations and the critical role of catalyst surface structure.

The direct pathway proceeds through the sequential reduction of nitrobenzene to nitrosobenzene, phenylhydroxylamine, and ultimately, aniline. DFT studies have shown that on Ni surfaces, the direct reduction pathway is energetically more favorable than the indirect route as shown in **Figure 2** (Mahata, A. et al., 2014). Understanding the adsorption dynamics of nitrobenzene on nickel surfaces is crucial for this process; parallel adsorption is generally preferred over vertical orientation, leading to lower activation barriers for the initial N-O bond cleavage (Mahata, A. et al., 2014).

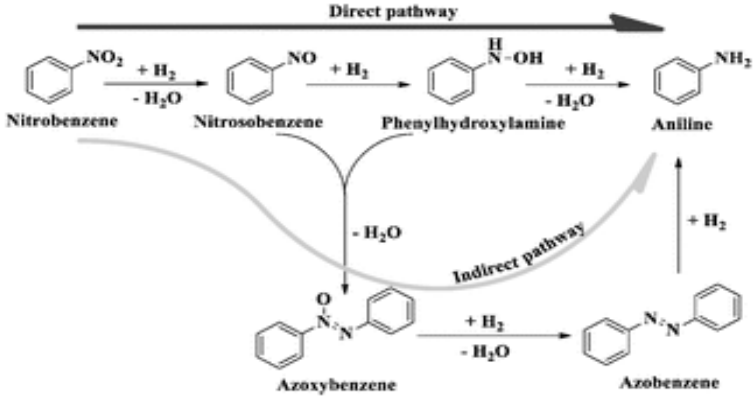


**Figure 2.** Schematic representation of Mechanistic Insights of nitrobenzene hydrogenation

Recent mechanistic investigations have unveiled novel activation pathways that challenge traditional understanding. The Eley–Rideal mechanism, wherein $H_2$ molecules are activated upon adsorption on nitrogen-doped carbon nanotube surfaces with adsorbed nitrobenzene molecules, has been proposed as an alternative pathway for selective hydrogenation (Sobhani, S. et. al., 2025). This discovery expands the mechanistic understanding of how different catalyst supports can modulate reaction pathways and enhance selectivity. Furthermore, to obtain effective hydrogenation of nitro compounds designing single-atom catalysts has demonstrated that isolated metal sites can achieve unprecedented selectivity through unique coordination environments (Cui, X. et al., 2025)

The indirect pathway involves the condensation of nitrosobenzene and phenylhydroxylamine to form azoxybenzene, which is then reduced to azobenzene, hydrazobenzene, and eventually aniline. While this route is often

suppressed on efficient nickel catalysts, it can become significant under specific conditions or with certain promoters. Recent studies on Ni-Niδ+ clusters have demonstrated that partially reduced nickel species can modulate the hydrogenation activity, potentially inhibiting the formation of condensation byproducts (Hou, T. et al., 2017). The hydrogenation performance of $CeO_2$/Ni-Niδ+ system has been shown to enhance selective reduction while minimizing secondary reactions (Hou, T. et al., 2017).

A comprehensive review of hydrogenation of aromatic nitro compounds on nickel and iron-containing catalysts has provided detailed insights into the mechanistic competition between direct and indirect pathways (Kashyap, B. et al., 2025). These findings emphasize that catalyst design must carefully balance multiple factors to achieve high selectivity while maintaining activity. The stabilization of Ni single-atom sites through introducing low-valence Ni clusters or particles has been shown to enhance electrochemical reduction reactions, with implications for catalytic hydrogenation (Wang, C. et al., 2025).

**Advanced Nickel Catalytic Systems**

The evolution of nickel catalysts has moved from bulk metals to highly engineered nanostructures and coordination complexes. Recent developments have demonstrated unprecedented levels of control over catalyst structure and performance.

Metal-organic framework (MOF)-derived catalysts have emerged as a transformative approach for designing selective hydrogenation catalysts. A comprehensive review of MOF-derived catalysts for chemoselective hydrogenation of nitroarenes has highlighted the advantages of this class of materials, including tunable pore structures, well-defined active sites, and enhanced metal dispersion (Yan X. et al., 2021). The pyrolysis of MOF precursors yields nitrogen-doped carbon supports that stabilize nickel nanoparticles and promote selective transformations (Yan X. et al., 2021).

Metal–organic framework-derived ceria-supported Ni–Co bimetallic catalysts have demonstrated exceptional performance in selective hydrogenation of nitroarenes, achieving near-quantitative conversions under mild conditions (Hu Y. et al., 2023).

Additionally, NiM@C catalysts that immobilized with MOF (M= Mo, Co, La) have shown remarkable activity in lignin-derived dimers and monophenols in-situ hydrogenation/ hydrodeoxygenation (Zhou, M. et al., 2022). Under the reaction conditions the application of in-situ restructuring in Ni-based metal-organic frameworks has proven effective for photocatalytic methanation, revealing the structure of MOF-derived catalysts (Gouda A. et al., 2025).

A versatile and durable Ni-based nanocatalyst has been engineered by supporting highly active and air-stable nickel nanoparticles on mesoporous silica

(MCM-41), enabling selective hydrogenation reactions under mild conditions (low temperature and pressure) (Hu Y. et al., 2023). This system exemplifies the advantages of mesoporous supports in achieving high catalytic performance while maintaining operational simplicity. Catalysis derived from flower-like Ni MOF has demonstrated excellent catalytic activity when incorporated into $MgH_2$ systems (Gao, H. et al., 2022).

The development of innovative Ni/Zn metal–organic frameworks for sorbitol generation through catalytic transfer hydrogenation demonstrates the versatility and effectiveness of MOF-based catalysts (Tokoyi, V. et al., 2025). Recent developments in MOF-based catalysts have markedly enhanced the efficiency and sustainability of biodiesel production with Ni-based systems playing a prominent role in achieving high conversion rates (Keshta, B.E. et al., 2025).

The emerging field of single-atom catalysis (SAC) represents a paradigm shift in catalyst design, maximizing atom utilization and achieving unprecedented selectivity. Rational design principles for single-atom catalysts have been established for efficient hydrogenation of nitro compounds, emphasizing the importance of the coordination environment and support material (Cui, X. et al., 2025). Ni single-atoms supported on N-doped carbon, prepared through controlled synthesis methods, have demonstrated highly efficient reduction of nitroarenes using $NaBH_4$ under ambient conditions (Wang, C. et al., 2025).

Nickel-based single-atom catalysts (Ni-SACs) have gained attention as promising noble-metal-free platforms for oxygen evolution/reduction reactions, with implications for catalytic hydrogenation (Liu, M. et al., 2025). The unique electronic properties of isolated nickel atoms enable enhanced activation of both substrate and hydrogen molecules, leading to superior catalytic performance. Recent advances of single-atom catalysts in the selective catalytic reduction of NO by CO have demonstrated the broader applicability of single-atom design principles (Ma, Z. et al., 2022).

The choice of support material significantly influences the dispersion and electronic state of nickel. The comparison of supported Nickel Catalysts is shown in **Table 1.** Silica gel supported nickel catalysts have shown exceptional activity, with selectivity to aniline reaching 99% under mild conditions (90 °C, 1.0 MPa) The particle size effect is prominent; catalysts with Ni particle sizes around 3.7 nm exhibit much higher activity compared to larger particles or commercial Raney nickel (Wang, J. et al., 2010).

Recent studies have explored the utilization of $Al_2O_3$-immobilized Ni (HTC-500) catalysts to the gas phase nitrobenzene hydrogenation, demonstrating the importance of catalyst morphology and crystallite structure in determining performance (McCullagh, C. et al., 2024). Small interface effects in Ni@Si catalysts have been shown to enable synergistic catalysis, leading to enhanced nitrobenzene hydrogenation efficiency (Albeladi, N. et al., 2023). Direct

observation of Ni nanoparticle growth in carbon nanofibers via in situ gas-phase TEM has provided unprecedented insights into catalyst evolution during synthesis (Visser N.L. et al., 2023).

Recent developments in nickel- and silica-supported catalysts for the catalytic hydrogenation of $CO_2$ to methane has revealed fundamental principles applicable to nitrobenzene hydrogenation, including the importance of metal-support interactions and surface morphology (McCullagh, C. et al., 2024). For the selective hydrogenation of pyridine to piperidine, C-immobilized alumina supports have been developed to synergistically optimize nickel catalysts. This approach also shows direct applicability to the reduction of aromatic nitro compounds (Fapojuwo, D.P. et al., 2021, Jiang Y. et al., 2021).

**Table 1.** Supported Nickel Catalysts - Support Material Comparison

| **Support Mat.** | **Ni (%)** | **Particle Size (nm)** | **Conversion (%)** | **Selectivity (%)** | **Temperature (°C)** | **Ref.** |
|---|---|---|---|---|---|---|
| $SiO_2$ | 10-15 | 3.7 | 99 | 99 | 90 | Wang, J. et al., 2010 |
| $Al_2O_3$ HTC-500 | 12-18 | 4-6 | 95-98 | >99 | 300-475 | McCullagh, C. et al., 2024 |
| Ni@Si | 8-12 | 2-4 | 97 | >98 | 120-150 | Albeladi, N. et al., 2023 |
| C-Nano fibers | 5-10 | 5-8 | 92-96 | >95 | 100-200 | Visser N.L. et al., 2023 |
| C-$Al_2O_3$ | 10-14 | 3-5 | 96-99 | >98 | 150-250 | Fapojuwo, D.P. et al., 2021 |
| $TiO_2$ | 8-12 | 4-7 | 90-94 | >92 | 180-280 | Jiang Y. et al., 2021 |

Incorporating a second metal can induce synergistic effects that enhance both activity and stability. Bimetallic PdM (M = Co, Ni) catalysts synthesized on silica microsphere supports have demonstrated interfacially active sites that promote selective hydrogenation of nitroarenes (Fapojuwo, D.P. et al., 2021) as shown in **Table 2**. The synergistic effects between palladium and nickel create electronic modifications that enhance the activation of both the substrate and hydrogen (Jiang Y. et al., 2021).

The hazardous organic dyes reductive degradation and toxic nitroarenes hydrogenation have been effectively achieved using novel magnetic bimetallic AuCu catalysts, which showcases the versatility of such bimetallic systems

(McCullagh, C. et al., 2024). Palladium-copper nanoparticles immobilized on Co-Cr layered double hydroxides have shown catalytic activity in both hydrogenation of nitroarenes and aerobic oxidation of alcohols (Alzarea, L.A. et al., 2023).

High selectivity and for about 100% conversion are provided by three-dimensional network Pd-Ni/γ-$Al_2O_3$ catalysts under mild conditions, leveraging the promotion effect of palladium on nickel activation (Jiang Y. et al., 2021). The design of such bimetallic systems represents a significant advance in achieving both high activity and selectivity simultaneously. Graphene oxide decorated Ni-Pd catalysts have been shown to be effective for transfer hydrogenation of nitroarenes and olefins (Dağalan, Z. et al., 2021).

Bimetallic Copper-Nickel phyllosilicate catalysts have been evaluated to the selective furfural hydrogenation to furfuryl alcohol, demonstrating the applicability of these systems to various carbonyl and aromatic nitro compound reductions (Shoosri T. et al., 2024). The elucidation of structure-activity relationships in Cu-Ni bimetallic catalysts for $CO_2$ hydrogenation has provided insights into how metal composition affects catalytic performance (Feng, Y. et al., 2024).

bimetallic Palladium-Cobalt supported on MIL-53(Al) catalysts have been developed to selective hydrogenation reactions, with performance metrics comparable to or exceeding traditional catalytic systems (Liu, L. et al., 2025). Application and development of bimetallic catalysts in hydrogenation reactions have been comprehensively reviewed, highlighting the importance of metal-metal interactions in determining catalytic properties (Anand, S. et al., 2021).

**Table 2.** Bimetallic Nickel Catalysts Synergistic Effects

| **Bimetallic Sys.** | **Support** | **Metal Ratio** | **Conversion (%)** | **Selectivity (%)** | **Ref.** |
|---|---|---|---|---|---|
| Pd-Ni | Silica microspheres | 1:3 | 98-99 | >99 | Fapojuwo, D.P. et al., 2021 |
| Au-Cu | Magnetic supp. | 1:1 | 96-98 | >97 | Gholinejad, M. et al., 2024 |
| Pd-Cu | Co-Cr LDH | 1:2 | 94-97 | >95 | Alzarea, L.A. et al., 2023 |
| Pd-Ni /γ-$Al_2O_3$ | Alumina (3D) | 1:4 | 99-100 | >99 | Jiang Y. et al., 2021 |
| Ni-Pd | Graphene oxide | 1:1 | 95-98 | >96 | Dağalan, Z. et al., 2021 |

| | | | | | |
|---|---|---|---|---|---|
| Cu-Ni | Phyllosilicate | 1:1 | 92-96 | >92 | Shoosri T. et al., 2024 |
| Cu-Ni | Various supports | Variable | 85-99 | >85 | Feng, Y. et al., 2024 |
| Pd-Co/ MIL-53(Al) | MOF-derived | 1:2 | 96-99 | >97 | Liu, L. et al., 2025 |

Nickel carbide nanoparticles have emerged as a promising alternative to metallic nickel, offering distinct electronic properties and catalytic behavior. High catalytic activity for the selective conversion of nitriles into primary amines is a key feature of the Precisely engineered nanocrystalline nickel carbide (nano-$Ni_3C$) serving as a catalyst (Gholinejad, M. et al., 2024, Yamaguchi S. et al., 2024). The unique electronic structure of nickel carbides, characterized by partially filled d-orbitals and modified electron density, contributes to their enhanced catalytic performance.

Nickel carbide ($Ni_3C$) nanoparticles prepared through controlled synthesis have been evaluated for catalytic hydrogenation of model compounds in colloidal suspension, opening new routes for earth-abundant catalyst development (André, R. F. et al., 2022) (**Table 3**). These findings suggest that metal carbides and other intermetallic compounds may play an increasingly important role in future catalyst design. Nickel nanoparticles embedded in N-doped carbon frameworks have been developed for selective hydrogenation of cinnamaldehyde to cinnamyl alcohol, demonstrating the importance of nitrogen doping in modulating catalyst selectivity (Qiu, Z. et al., 2022).

(NHC-olefin)-nickel (0) nanoparticles have been shown to be efficient and recyclable catalysts for various hydrogenation reactions (Avello, M. G. et al., 2025). The versatility of nickel carbide/$Al_2O_3$ systems is showcased by their effective application in catalyzing the selective furfural and its derivatives hydrogenation (Kawakami, T. et al., 2025) The derivation of nickel carbides from Ni-MOFs to boost CO selectivity in $CO_2$ hydrogenation has opened new pathways for catalyst design (Wang, X. et al., 2025).

Structure-activity relationships of MOF-derived cobalt catalysts in furfural hydrogenation to furfuryl alcohol have provided insights into how catalyst structure influences performance, with implications for nickel-based systems (Gao, Z. et al., 2026).

**Table 3.** Nickel Carbide Catalysts Structural and Performance Data

| Catalyst | Composition | Particle Size (nm) | Conversion (%) | Selectivity (%) | Ref. |
|---|---|---|---|---|---|
| Nano-$Ni_3C$ | Nickel carbide | 5-10 | 97-99 | >98 | Yamaguchi S. et al., 2024 |
| $Ni_3C$ Nanoparticles | Nickel carbide | 3-8 | 94-97 | >95 | André, R. F. et al., 2022 |
| Ni/N-doped C | Ni emb. in N-C | 4-7 | 96-98 | >97 | Qiu, Z. et al., 2022 |
| (NHC-olefin)-Ni(0) | Organometallic Ni | 2-6 | 95-99 | >96 | Avello, M. G. et al., 2025 |
| $Ni_3C$-$Al_2O_3$ | Carbide on $Al_2O_3$ | 6-12 | 93-96 | >94 | Kawakami, T. et al., 2025 |
| Ni-MOF-carbide | MOF- Ni carbide | 8-15 | 92-95 | >91 | Wang, X. et al., 2025 |
| MOF- Co catalyst | Cobalt analog | 5-10 | 91-94 | >90 | Gao, Z. et al., 2026 |

Beyond traditional hydrogen-based hydrogenation, alternative methods have emerged that offer distinct advantages in terms of sustainability and operational simplicity.

Transfer hydrogenation reactions, which utilize hydrogen donors instead of molecular hydrogen, have emerged as sustainable alternatives for reducing nitroaromatics. Selective transfer hydrogenation coupling of nitroaromatics with alcohols catalyzed by non-precious metal catalysts has demonstrated the feasibility of this approach (Zhang T. et al, 2022) (**Table 4**). Facile transfer hydrogenation of N-heteroarenes and aromatic nitro compounds catalyzed by Pd@$Fe_3O_4$ nanoparticles has achieved >99% conversion of quinoline to N-ring hydrogenated products (Alghamdi H.S. et al., 2024).

Nickel-catalyzed hydrogenation and dehydrogenation reactions have been comprehensively reviewed, covering three decades of research and demonstrating the versatility of nickel catalysts across diverse transformations (Paul, R. et al., 2025). Efficient and sustainable transfer hydrogenation and N-formylation of nitroarenes in one-pot transformations have been achieved, combining substrate reduction with value-added product formation (Rubab, A. et al., 2025).

Nickel boride supported on graphitic carbon nitride has been developed as a highly active catalyst for hydrogenation of nitroarenes to aromatic amines (Kashyap, B. et al., 2025). The selective transfer hydrogenation and N-formylation of nitroarenes by facilely-prepared N, S co-doped carbon

encapsulated cobalt nanoparticles catalysts has demonstrated the effectiveness of heteroatom-doped carbon supports (Guo, W. et al., 2025).

**Table 4.** Transfer Hydrogenation Methods - Comparative Performance

| **Method** | **$H_2$ Donor** | **Catalyst** | **Conversion (%)** | **Selectivity (%)** | **Sustainability Adv.** | **Ref.** |
|---|---|---|---|---|---|---|
| Transfer Hydrogenation | Alcohols | Non-precious metal | 95-98 | >97 | Avoids $H_2$ gas | Zhang T. et al, 2022 |
| Transfer Hydrogenation | Formic acid | Pd@$Fe_3O_4$ | 99+ | >99 | Magnetic recovery | Alghamdi H.S. et al., 2024 |
| Ni-catalyzed | $H_2$ or donors | Ni-based | 90-99 | >90 | Versatile transformations | Paul, R. et al., 2025 |
| One-pot TH + N-formylation | Formic acid | Ni-based | 94-98 | >95 | Value-added synthesis | Rubab, A. et al., 2025 |
| Ni boride/g-$C_3N_4$ | $H_2$ or donors | Ni boride | 96-99 | >98 | Graphitic support stability | Kashyap, B. et al., 2025 |
| N, S co-doped C | Formic acid | Co-based | 93-97 | >94 | Heteroatom dop. | Guo, W. et al., 2025 |

Recent catalyst advancements in nitroaromatics selective hydrogenation have encompassed thermal, electrocatalytic, and photocatalytic methods (Liu, M. et al., 2025). Photocatalytic and Electrocatalytic Methods-Performance Summarized in **Table 5**. High conversion of nitrobenzene and high selectivity towards aniline can be achieved at room temperature and low hydrogen pressure by employing photocatalysis. MIL-101-DIST/g-$C_3N_4$/Ni has been developed as a new nano-photocatalyst for selective hydrogenation of nitrobenzene to aniline (Sobhani, S. et al. 2025).

Recent developments in catalysts enabling the selective photocatalytic conversion of nitrobenzene to aniline have demonstrated that semiconductor photocatalysts can achieve high conversion rates under mild conditions. Enhanced electron transfer in Fe–N–C catalysts have been shown to enable highly efficient reduction of nitrobenzene, with Fe–$N_4$ coordination enhancing catalytic performance (Wei, B. et al., 2025).

Advancements in catalytic strategies for the reduction of nitroaromatics and related derivatives have highlighted multiple methodologies beyond traditional hydrogenation, including metal reduction and hydrazine hydrate reduction (Paul, R. et al., 2025). Selective electrocatalytic nitrobenzene-to-aniline reduction on nickel-cobalt layered double hydroxide has achieved >99% conversion with 98.3% selectivity (McCullagh, C. et al., 2024).

**Table 5.** Comparison of Photocatalytic and Electrocatalytic Methods - Performance

| Method | Catalyst System | Light Source | Conversion (%) | Selectivity (%) | Reac. Conditions | Reference |
|---|---|---|---|---|---|---|
| Photocatalysis | Thermal + Photo | Visible light | 90-99 | >95 | Room temperature, low P | Liu, M. et al., 2025 |
| Photocatalysis | MIL-101-DIST/g-$C_3N_4$/Ni | Visible light | 95-99 | >98 | Mild conditions | Sobhani, S. et al. 2025 |
| Photocatalysis | Semiconductor catalysts | UV/Visible | 92-98 | >94 | Room temperature | Wei, B. et al., 2025 |
| Electrocatalysis | Fe–N–C | Electrochemical | 96-99 | >97 | Enhanced electron transfer | Wei, B. et al., 2025 |
| Electrocatalysis | Ni-Co LDH | Electrochemical | 99+ | 98.3 | Layered structure adv. | McCullagh, C. et al., 2024 |
| Chem. eduction | Various methods | N/A (chem.) | 85-99 | >85 | Multiple reduction agents | Guo, W. et al., 2025 |

## Industrial Applications and Techno-Economic Analysis

Nickel catalysts are the workhorse of industrial aniline production, utilized in both liquid-phase and gas-phase processes. Understanding the industrial context is essential for appreciating the practical significance of recent catalyst developments.

Industrial leaders like BASF and Bayer utilize different reactor configurations to manage the highly exothermic nature of nitrobenzene hydrogenation. BASF typically employs fluidized-bed reactors with supported nickel or copper catalysts, allowing for efficient heat removal and high steam recovery. In contrast, the Bayer process often utilizes fixed-bed reactors with nickel sulfide (NiS) catalysts, which are activated with copper or chromium to maintain high selectivity (>99%) at temperatures between 300°C and 475°C (McCullagh, C. et al., 2024, Borthakur, P. P. et al., 2025).

Recent industrial investigations have focused on optimizing catalyst morphology and crystallite structure for enhanced performance. Using $Al_2O_3$ supported Ni catalysts (HTC-500) in gas phase nitrobenzene hydrogenation has been systematically studied, revealing the critical importance of catalyst preparation methods in determining industrial viability (McCullagh, C. et al., 2024). Efficient nitroarene reduction through the novel strategy for nickel immobilization on $ZnFe_2O_4$@EDTA-based nanocomposites has demonstrated novel approaches to catalyst design (Shafik, MS. Et al., 2025).

A breakthrough in selective nitroarene hydrogenation has been achieved through the development of nested NiPd nanocatalysts, which are fabricated using reactive laser ablation in liquids offering new synthesis methodologies for industrial-scale catalyst preparation (Havelka, O. et al., 2025).

The primary driver for using nickel over noble metals is cost. Nickel is approximately 100 times cheaper than palladium or platinum per unit mass. When combined with high aniline-to-catalyst ratios (up to 800:1) and effective energy recovery systems, nickel-based processes offer superior economic viability for large-scale production (McCullagh, C. et al., 2024). Recent advances in catalyst design have further improved the economic profile by reducing catalyst loading requirements and extending catalyst lifetime.

Highly efficient catalytic reduction of nitrobenzene using bimetallic nanoparticles has been demonstrated, offering alternative pathways for selective synthesis (Tang, J. et al., 2023). These developments expand the industrial toolkit for aniline production and enable process optimization based on feedstock availability and economic considerations. The critical contribution of industrial catalysts to accelerating renewable energy adoption has been highlighted, with nickel-based systems playing a crucial role in sustainable chemical manufacturing (Borthakur, P. P. et al., 2025). Techno-Economic Comparison of Ni and Noble Metals is demonstrated in **Table 6**.

**Table 6.** Techno-Economic Comparison of Ni and Noble Metals

| **Parameter** | **Nickel** | **Palladium** | **Platinum** | **Ref.** |
|---|---|---|---|---|
| **Metal Cost ($/kg)** | 8-12 | 800-1200 | 1000-1500 | Borthakur, P. P. et al., 2025 |
| **Cost Ratio (Ni:Pd)** | 1 | ~100 | ~120 | McCullagh, C. et al., 2024 |
| **Aniline/Catalyst Ratio** | 800:1 | 1000:1 | 1200:1 | McCullagh, C. et al., 2024 |
| **Catalyst Lifetime (months)** | 12-24 | 24-36 | 24-36 | McCullagh, C. et al., 2024 |
| **Energy Recovery Potential** | High (steam) | Medium | Medium | Borthakur, P. P. et al., 2025 |
| **Industrial Adoption** | >80% of capacity | <15% | <5% | Borthakur, P. P. et al., 2025 |

## Green Chemistry and Sustainability

The transition towards "Green Chemistry" necessitates the evaluation of catalysts based on their environmental footprint and recyclability. Recent developments have demonstrated that nickel catalysts can be designed with sustainability as a primary objective. In **Table 7**. it is emphasized that the green chemistry metrics for nickel catalysts

Nickel catalysts contribute to a lower overall carbon footprint compared to noble metals due to the lower energy intensity of nickel mining and refining. Furthermore, the high selectivity of modern nickel systems ensures an atom economy close to the theoretical maximum, minimizing waste generation (low E-factor) (Wang, J. et al., 2010). Recent advances in catalytic methods have demonstrated that thermal, electrocatalytic, and photocatalytic approaches can all be optimized for sustainable aniline production (Liu, M. et al., 2025).

The sustainability of producing amines from renewable feedstocks has been quantified and detailed using the CHEM21 green metrics toolkit. This analysis demonstrates that nickel-based catalyst systems can achieve high sustainability metrics, highlighting their potential for 'green' chemistry. Green chemistry innovation through systematic review on sustainable catalysis has illustrated how nickel catalysts embody circular economy principles (Cao, X. et al., 2023).

Under the mild conditions reusable and stable Nickel-based catalysts that supported on silica have been developed for general and selective nitriles hydrogenation to primary amines, with emphasis on catalyst recovery and reuse (Ma, Z. et al., 2022). Spent nickel catalysts can be recycled with high efficiency. Up to 98% of nickel can be recovered from spent hydrogenation catalysts via hydrometallurgical processes, allowing the metal to be reused in fresh catalyst preparation and closing the material loop (Fapojuwo, D.P. et al., 2021).

Unsupported and supported nickel nanoparticles have been synthesized and applied in catalysis, with particular attention to recyclability and reuse (Havelka, O. et al., 2025, Cao, X. et al., 2023). The advancement and contributions of nanoparticle technology in Thailand from 2008 to 2024 have highlighted the growing importance of sustainable catalyst development (Liu, L. et al., 2025).

**Table 7.** Green Chemistry Metrics for Nickel Catalysts

| Metric | Ni Cat. | Pd Cat. | Pt. Cat. | Reference |
|---|---|---|---|---|
| **E-Factor (kg waste/kg product)** | 0.5-1.5 | 0.3-0.8 | 0.3-0.8 | Fapojuwo, D.P. et al., 2021 |
| **Atom Economy (%)** | 95-99 | 96-99 | 96-99 | Fapojuwo, D.P. et al., 2021 |
| **Metal Recovery Rate (%)** | 98 | 95-97 | 95-97 | Fapojuwo, D.P. et al., 2021 |
| **C Footprint (kg $CO_2$/kg Ni)** | 2.5-3.5 | 8-12 | 10-15 | Borthakur, P. P. et al., 2025 |
| **Catalyst Recyclability** | Excellent (>5 cycles) | Good (>3 cycles) | Good (>3 cycles) | Havelka, O. et al., 2025 |
| **Mining Energy Intensity** | Low | Medium | High | Borthakur, P. P. et al., 2025 |
| **Abundance inEarth's Crust(ppm)** | 80 | 0.015 | 0.005 | Ma, Z. et al., 2022 |

## CONCLUSION

Nickel-based catalysts remain at the forefront of nitrobenzene hydrogenation due to their unique balance of activity, selectivity, and cost. The recent explosion of research in this field, particularly in MOF-derived catalysts, single-atom systems, and bimetallic architectures, demonstrates the continued vitality of nickel catalysis. The comprehensive review of recent sources reveals several emerging trends and future directions.

The development of single-atom nickel catalysts has demonstrated unprecedented selectivity and atom utilization efficiency. MOF-derived catalysts have emerged as a versatile platform for designing highly active and selective systems. Bimetallic systems have shown remarkable synergistic effects that enhance both activity and stability. Transfer hydrogenation and photocatalytic methods have provided sustainable alternatives to traditional hydrogen-based processes.

As the chemical industry moves towards carbon neutrality and circular economy principles, the role of efficient, recyclable, and earth-abundant nickel catalysts will only become more critical. The convergence of catalyst design principles, mechanistic understanding, and industrial implementation will drive the next generation of sustainable aniline production technologies. In this study represent the cutting edge of nickel catalysis research and provide a foundation for continued innovation in this vital field.

## REFERENCES


Albeladi, N., Alsulami, Q. A., and Narasimharao, K. (2023). Recent progress in nickel and silica containing catalysts for $CO_2$ hydrogenation to $CH_4$. *Catalysts,* 13(7), 1104.

Alghamdi, H. S., Ajeebi, A. M., Aziz, M. A., Alzahrani, A. S., and Shaikh, M. N. (2024). Facile transfer hydrogenation of N-heteroarenes and nitroarenes using magnetically recoverable Pd@SPIONs catalyst. *ACS Omega*, 9(10), 11377-11387.

Alzarea, L. A., Alhumaimess, M. S., Alsohaimi, I. H., Hassan, H. M. A., El-Aassar, M. R., Essawy, A. A., and Kalil, H. (2023). Efficient dual-function catalyst: Palladium–copper nanoparticles immobilized on Co-Cr LDH for seamless aerobic oxidation of benzyl alcohol and nitrobenzene reduction. Nanomaterials, 13(13), 1956.

Anand, S., Pinheiro, D., and Sunaja Devi, K. R. (2021). Recent advances in hydrogenation reactions using bimetallic nanocatalysts: A review. Asian *Journal of Organic Chemistry,* 10(12), 3068-3100.

André, R. F., Meyniel, L., and Carenco, S. (2022). Nickel carbide ($Ni_3C$) nanoparticles for catalytic hydrogenation of model compounds in solvent. *Catalysis Science & Technology,* 12, 4572-4583.

Avello, M. G., Singh, G., Truong-Phuoc, L., Vidal, L., Papaefthimiou, V., Chessé, M., Gruber, N., Chetcuti, M. J., Vanka, K., Ritleng, V., Pham-Huu, C., and Michon, C. (2025). (NHC-olefin)-nickel (0) nanoparticles: An efficient and selective catalyst for hydrogenation reactions at low temperature and pressure. *Journal of Catalysis,* 453, 116487.

Borthakur, P. P., and Borthakur, B. (2025). The role of industrial catalysts in accelerating the renewable energy transition. *Chemistry Proceedings,* 17(1), 6.

Cao, X., Jang, B. W.-L., Hu, J., Wang, L., and Zhang, S. (2023). Synthetic strategies of supported Pd-based bimetallic catalysts for selective semi-hydrogenation of acetylene: A review and perspectives. *Molecules,* 28(6), 2572.

Cui, X., Liu, K., Han, Y., and Wang, L. (2025). Rational design of single-atom catalysts for efficient hydrogenation of nitro compounds. *Chemical Synthesis,* 5, 79.

Dağalan, Z., Behboudikhiavi, S., Turgut, M., Sevim, M., Kasapoğlu, A. E., Nişancı, B., and Metin, Ö. (2021). Nickel−palladium alloy nanoparticles supported on reduced graphene oxide decorated with metallic aluminum nanoparticles (Al-rGO/NiPd): A multifunctional catalyst for the transfer hydrogenation of nitroarenes and olefins using water as a hydrogen source. *Inorganic Chemistry Frontiers*, 8, 2200-2212.

Feng, Y., Shen, L., Zhang, W., Yuan, X., Zhu, M., and Xu, J. (2024). Elucidating the structure-activity relationship of the bimetallic Ni-Cu catalysts for $CO_2$ hydrogenation. *Journal of $CO_2$ Utilization,* 80, 102683.

Fapojuwo, D. P., Oseghale, C. O., Akinnawo, C. A., and Meijboom, R. (2021). Bimetallic PdM (M = Co, Ni) catalyzed hydrogenation of nitrobenzene at the water/oil interface in a Pickering emulsion. C*olloids and Surfaces A: Physicochemical and Engineering Aspects,* 619, 126513.

Gao, H., Shi, R., Shao, Y., Liu, Y., Zhu, Y., Zhang, J., and Li, L. (2022). Catalysis derived from flower-like Ni MOF towards the hydrogen storage performance of magnesium hydride. *International Journal of Hydrogen Energy*, 47(15), 9346–9356.

Gao, Z., Wang, F., Feng, J., Zhang, H., and Wang, F. (2026). Structure-activity relationship of MOF-derived cobalt catalyst in selective hydrogenation of furfural to furfuryl alcohol. *Fuel,* 410, 137882.

Gholinejad, M., Bashirimousavi, S., and Sansano, J. M. (2024). Novel magnetic bimetallic AuCu catalyst for reduction of nitroarenes and degradation of organic dyes. *Scientific Reports*, 14, 5852.

Gouda, A., Hannouche, K., Mohan, A., Mao, C., Nikbin, E., Carrière, A., Ye, J., Howe, J. Y., Sain, M., Hmadeh, M., and Ozin, G. A. (2025). In-situ restructuring of Ni-based metal organic frameworks for photocatalytic $CO_2$ hydrogenation. *Nature Communications*, 16(1), 695.

Guo, W., Zheng, W., Xiang, Y., and Zhang, Y. (2025). Advances in the catalysis of reduction of nitroaromatics and its mechanism: A tutorial review. *RSC Sustainability*, 3, 243–254.

Havelka, O., Thomas, A., Rodenes, M., Cvek, M., Łukowiec, D., Sorribes, I., and Torres-Mendieta, R. (2025). Nested NiPd nanocatalysts fabricated by reactive laser ablation in liquids: A breakthrough in selective nitroarene reduction to anilines. *Inorganic Chemistry Frontiers*, 12, 8407–8423.

Hou, T., Wang, Y., Zhang, J., Li, M., Lu, J., Heggen, C., Sievers, F., and Wang, F. (2017). Peculiar hydrogenation reactivity of Ni–Ni^δ+ clusters stabilized by ceria in reducing. *Journal of Catalysis,* 353, 107–115.

Hu, Y., Liu, M., Bartling, S., Lund, H., Atia, H., Dyson, P. J., and Ramirez, A. (2023). A general and robust Ni-based nanocatalyst for selective hydrogenation reactions at low temperature and pressure. *Science Advances,* 9(45), 8225.

Jiang, Y., Li, Q., Li, X., Wang, X., Dong, S., Li, J., Hou, L., Jiao, T., Wang, Y., and Gao, F. (2021). Three-dimensional network Pd-Ni/γ-$Al_2O_3$ catalysts for highly active catalytic hydrogenation of nitrobenzene to aniline under mild conditions. *ACS Omega*, 6(14), 9780–9790.

Kashyap, B., Kumar, S., Sharma, D., and Krishnan, V. (2025). Nickel boride supported on graphitic carbon nitride as robust and efficient catalyst for transfer hydrogenation of nitroarenes. *ChemNanoMat,* 11(6), e202500117.

Kawakami, T., Yamaguchi, S., Suganuma, S., Nakajima, K., Mitsudome, T., and Mizugaki, T. (2025). Mild and selective hydrogenation of furfural and its derivatives to tetrahydrofurfuryl compounds catalyzed by aluminum oxide-supported nickel carbide nanoparticles. *ACS Sustainable Chemistry and Engineering*, 13(21), 7994–8002.

Keshta, B. E., Abdalla, S., Tesnim, D., Abou El-Reash, Y. G., Al-Farraj, E. S., Shaban, M. M., El-Harairy, A., El-Saeed, H. M., Shaban, E. A., Abou-Elyazed, A. S., Goda, M. N., Atwa, E. M., and Keshta, A. E. (2025). MOF-based catalysts for sustainable biodiesel production: Classification, performance, and advances from 2020 to 2025. *RSC Advances,* 15, 48692–48726.

Liu, L., Zang, M., Li, L., Zhang, Y., Wang, L., Zhou, X., Xin, C., and Tai, T. (2025). MIL-53(Al)-derived bimetallic Pd–Co catalysts for the selective hydrogenation of 1,3-butadiene at low temperature. *Scientific Report*s, 15, 448.

Liu, M., Sun, X., Xu, K., Wei, Z., and Xie, K. (2025). Recent advances in catalysts for selective hydrogenation of nitro compounds. *International Journal of Hydrogen Energy*, 128, 22-46.

Ma, Z., Chandrashekhar, V. G., Zhou, B., Alenad, A. M., Rockstroh, N., Bartling, S., Beller, M., and Jagadeesh, R. V. (2022). Stable and reusable Ni-based nanoparticles for general and selective hydrogenation of nitriles to primary amines. *Chemical Science*, 13, 10914-10922.

Mahata, A., Rai, R. K., Singh, S. K., and Pathak, B. (2014). Direct vs. indirect pathway for nitrobenzene reduction reaction on a Ni catalyst surface: A density functional study. *Physical Chemistry Chemical Physics*, 16, 26365-26374.

McCullagh, C., Davidson, A. L., Ballas, C. E., How, C., MacLaren, D. A., Boulho, C., and Brennan, C. (2024). The application of an alumina-supported Ni catalyst for the hydrogenation of nitrobenzene to aniline. *Journal of Catalysis,* 442, 114933.

Paul, R., Ahamed, S. S., and Ghosh, T. (2025). Nickel-catalyzed hydrogenation and dehydrogenation processes: A useful tool in organic synthesis. *Asian Journal of Organic Chemistry,* 14(9), e00069.

Qiu, Z., He, X., Ma, S., Li, Z., Xiong, Y., and Cao, Y. (2022). Ni nanoparticles embedded in nitrogen doped carbon derived from metal–organic frameworks for the efficient hydrogenation of vanillin to vanillyl alcohol. *New Journal of Chemistry*, 46, 10347–10356.

Rohmah, A. N., Palupi, A. R., Manullang, A. N. H. M., and Erawati, H. D. B. (2025). Aniline process creation for conversion improvement using hydrogenation process. *Journal of Chemical Engineering Research Progress,* 2(1), 132–141.

Rubab, A., Wahab, M. A., Abdala, A., Sharif, M., Ahmed, W., and Sohail, M. (2025). Efficient and sustainable transfer hydrogenation and N-formylation of nitroarenes using a facilely synthesized $Co_4N$/NC nanocatalyst. *Journal of Environmental Chemical Engineering,* 13(5), 118993.

Shafik, M. S., PadmaPriya, G., Aldulaimi, A. T., Anand, O. S. W., Maharana, L., Sharma, R., and Singh, A. (2025). Efficient nitroarene reduction: Innovative nickel immobilization on $ZnFe_2O_4$@EDTA nanocomposite *Monatshefte für Chemie,* In press. https://doi.org/10.1007/s00706-025-03419-0.

Shoosri, T., Chotiwilaiwan, P., Rattanapornchaiwat, T., Teerawatananond, T., Miyake, T., Panpranot, J., and Weerachawanasak, P. (2024). Bimetallic copper- and nickel-rich Cu-Ni phyllosilicate catalysts for the liquid phase selective hydrogenation of furfural to furfuryl alcohol. *RSC Advances*, 14(51), 38232–38244.

Sobhani, S., Mohamadi, B., and Sansano, J. M. (2025). MIL-101-DIST/g-$C_3N_4$/Ni a new nano-photocatalyst for nitrobenzene photo-reduction via in-situ hydrogen generation from water splitting. *Scientific Reports*, 15, 38808.

Tang, J., Zhang, S., Chen, X., Zhang, L., Du, L., and Zhao, Q. (2023). Highly efficient catalytic reduction of nitrobenzene using Cu@C based on a novel Cu–MOF precursor. *Catalysts*, 13(6), 956.

Tokoyi, V., and Deenadayalu, N. (2025). Novel Ni/Zn MOFs for sorbitol production via catalytic transfer hydrogenation. *Molecules*, 30(23), 4565.

Visser, N. L., Turner, S. J., Stewart, J. A., Vandegehuchte, B. D., van der Hoeven, J. E. S., and Jongh, P. E. (2023). Direct observation of Ni nanoparticle growth in carbon-supported nickel under carbon dioxide hydrogenation atmosphere. *ACS Nano*, 17(15), 14963–14973.

Wang, C., Chen, B., Ren, H., Wang, X., Li, W., Hu, H., Chen, X., Liu, Y., Guan, Q., and Li, W. (2025). Stabilizing Ni single-atom sites through introducing low-valence Ni species for durably efficient electrochemical $CO_2$ reduction. *Applied Catalysis B: Environmental*, 368, 125151.

Wang, J., Yuan, Z., Nie, R., Hou, Z., and Zheng, X. (2010). Hydrogenation of nitrobenzene to aniline over silica gel supported nickel catalysts. *Industrial & Engineering Chemistry Research*, 49(10), 4664–4669.

Wang, X., Xie, G., Cui, C., Man, Y., and Wang, Z. (2025). Deriving nickel carbides from Ni-MOFs to boost CO selectivity in $CO_2$ hydrogenation. *Fuel*, 399, 135661.

Wei, B., Liu, D., Peng, R., Zhou, Y., Li, Q., and Zhao, H. (2025). Enhanced electron transfer in Fe–N–C catalysts for nitrobenzene reduction: From electrodes to functional materials. *Frontiers of Environmental Science & Engineering*, 19, 158.

Yamaguchi, S., Kiyohira, D., Tada, K., Kawakami, T., Miura, A., Mitsudome, T., and Mizugaki, T. (2024). Nickel carbide nanoparticle catalyst for selective hydrogenation of nitriles to primary amines. *Chemistry*, 30(13), e202303573.

Yan, X., Chen, L., Song, H., Gao, Z., Wei, H., Ren, W., and Zhang, Y. (2021). Metal-organic framework (MOF)-derived catalysts for chemoselective hydrogenation of nitroarenes. *New Journal of Chemistry,* 45(28), 12345–12358.

Zhang, T., Xie, Z., Jiang, L., Zhao, W., Cao, S., Wang, B., Si, R., Zhang, R., Liu, Y., and Zhao, Z. (2022). Selective transfer hydrogenation coupling of nitroaromatics to azoxy/azo compounds by electron-enriched single Ni-$N_4$ sites on mesoporous N-doped carbon. *Chemical Engineering Journal,* 443, 136416.

Zhou, M., Xue, Y., Ge, F., Li, J., Xia, H., Xu, J., Zhao, J., Chen, C., and Jiang, J. (2022). MOF-derived NiM@C catalysts (M = Co, Mo, La) for in-situ hydrogenation/hydrodeoxygenation of lignin-derived monophenols and dimers. *Fuel,* 329, 125446.

# CHAPTER 14

# The Role of Palladium Complex Catalysts in the Hydrogenation of Cyclohexene

**Dilek Kılınç**[1]

[1] Assoc. Prof. Dr. Harran University, Faculty of Pharmacy, Department of Pharmaceutical Chemistry, ORCID ID:0000-0002-0171-2371

## Introduction

The catalytic hydrogenation of unsaturated organic compounds stands as one of the most fundamental and industrially significant transformations in modern chemistry, playing a critical role in the synthesis of fine chemicals, pharmaceuticals, and petrochemical intermediates (Rylander, P.Y., 1985). This process, which involves the addition of molecular hydrogen across a multiple bond, is essential for converting readily available feedstocks into high-value saturated products. Among the various substrates, cyclohexene has long been established as a crucial benchmark molecule for evaluating the activity, selectivity, and mechanistic pathways of hydrogenation catalysts (Cazaña, F., 2015). Its simple structure, featuring an isolated carbon-carbon double bond within a six-membered ring, provides a clean system for studying the intrinsic catalytic performance without the complications of competing functional groups. Palladium (Pd) is a noble metal renow-

ned for its exceptional catalytic properties, particularly in hydro genation and cross-coupling reactions (Crabtree, R.H., 2019). Pd -based catalysts are highly effective for the hydrogenation of olefins, often operating under mild conditions. driven by the dual goals of enhancing catalytic efficiency and improving catalyst recyclability and stability

This study presents an exhaustive review of the application of palladium complexes as catalysts for the cyclohexene hydrogenation, the reaction that serves as a critical benchmark across academic and industrial catalysis. The discussion systematically explores the fundamental principles governing catalytic hydrogenation, providing a detailed comparison of homogeneous, heterogeneous, and immobilized Pd systems (Baskar, G., 2017). The study meticulously analyzes the pivotal role of ligand design in modulating the electronic and steric properties of the Pd center, thereby optimizing catalytic activity and selectivity (Sprengers, J.W., 2005). Furthermore, a comprehensive comparative analysis is provided, contrasting Pd performance with that of other prominent transition metals, specifically Rhodium (Rh) and Ruthenium (Ru), in this reaction (Hamdy, M.S. 2020). Detailed performance data are presented in multiple tables to delineate the current state-of-the-art in catalytic efficiency (Patel, A., 2021). Finally, the study addresses persistent challenges, such as catalyst deactivation and leaching, and outlines future research pathways, underscoring the rapid advancement of single-atom catalysis (Wang, L., Li, J., 2022).

## The Significance of Alkene Hydrogenation in Chemical Synthesis

Catalytic hydrogenation, defined as the addition of molecular hydrogen ($H_2$) across a carbon-carbon double bond, represents one of the most fundamental and widely utilized transformations in modern chemical synthesis (Rylander, P.Y., 1985). This reaction is indispensable for the large-scale production of numerous bulk chemicals, the synthesis of pharmaceutical intermediates, and the

manufacturing of various fine chemicals (Crabtree, R.H., 2019). The conversion of unsaturated hydrocarbons to their saturated counterparts is inherently an exothermic process, confirming its thermodynamic favorability (Somorjai, G.A., Li, Y., 2010). However, the reaction is kinetically constrained by the exceptionally high bond dissociation energy of the H-H bond, which necessitates the use of a catalyst to lower the activation energy barrier (Ea) (Halpern, J., 1985). Transition metal catalysts, particularly those from Group 10, are uniquely suited for this role due to their ability to effectively activate both the H-H and C=C bonds (Zhao, X., 2022). Beyond simple saturation, catalytic hydrogenation is frequently employed in complex synthetic routes to achieve high levels of chemo-, regio-, and enantioselectivity, underscoring its versatility and importance (Chen, B., 2005).

## Cyclohexene as the Benchmark Substrate

The hydrogenation of cyclohexene to cyclohexane (**Figure. 1**) is universally recognized as a classic benchmark reaction for assessing the activity and stability of novel hydrogenation catalysts (Jo, Y.D.,1996).

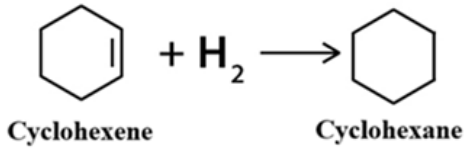


**Figure1.** Hydrogenation reaction of cyclohexene to cyclohexane

As a readily available and simple cyclic alkene, cyclohexene allows researchers to effectively isolate the intrinsic catalytic performance from potential complications that may arise from functional group tolerance or competing side reactions in more complex molecules (Satterfield, C.N., 1991). Studying this reaction under varying conditions provides a robust and standardized platform for the direct comparison of diverse catalytic approaches, ranging from soluble molecular complexes to supported metallic nanoparticles (Cagnola, E.A., 2004). The results obtained from cyclohexene hydrogenation studies are often used to predict the potential utility of a catalyst in broader industrial applications (Heldal, J.A., 1984).

Palladium-based catalysts are broadly classified into two main categories: homogeneous systems, which utilize soluble coordination complexes, and heterogeneous systems, where Pd metal is dispersed onto a solid support material (Baskar, G., 2017). The primary advantage offered by Pd complexes, which is the central focus of this chapter, is the exceptional capacity for ligand tunability (Sprengers, J.W., 2005). This tunability permits the precise manipulation of the electronic and steric environment surrounding the central Pd metal atom (Crabtree, R.H., 2019). Such control is absolutely paramount for the optimization

of catalytic performance, including activity, selectivity, and stability Furthermore, Pd complexes often serve as essential precursors for the generation of both truly homogeneous catalysts and advanced heterogeneous systems, such as immobilized complexes and the highly efficient single-atom catalysts (SACs) (Wang, Y., 2022).

The use of palladium as a hydrogenation catalyst dates back to the early 20th century, with the pioneering work of Paul Sabatier and Jean-Baptiste Senderens (Elnaz, M., 2024). Initially, the focus was almost exclusively on heterogeneous Pd systems, such as Pd/C (palladium on carbon), which quickly became the workhorse of industrial hydrogenation (Satterfield, C.N., 1991). The development of homogeneous Pd complexes for hydrogenation, however, lagged behind that of Rh and Ru (Chen, B., 2005). It was not until the latter half of the 20th century that the potential of molecular Pd complexes, particularly in cross-coupling reactions, spurred intensive research into their application in hydrogenation (Beller, M., 2004). The cyclohexene model reaction played a crucial role in this historical development, providing a consistent metric for comparing the performance of these emerging homogeneous Pd systems against the established heterogeneous catalysts (Jo, Y.D., 1996).

## Fundamentals of Catalytic Hydrogenation

The hydrogenation of alkenes is characterized by the negative value ($\Delta G<0$), confirming its thermodynamic spontaneity (Somorjai, G.A., 2010). Despite this favorable thermodynamic driving force, the reaction rate is governed by kinetic limitations, primarily the energy required to break the strong H-H bond (Halpern, J., 1981). The catalyst's fundamental role is to provide an alternative reaction pathway with a significantly lower activation energy (Ea) thereby enabling molecular hydrogen activation and the subsequent delivery of hydrogen atoms to the unsaturated substrate. (Beller, M., 2004). Detailed kinetic studies are therefore indispensable for identifying the rate-determining step of the catalytic cycle and for establishing the optimal reaction conditions necessary for maximum efficiency (Cazaña, F., 2015). The performance and efficiency of any catalyst must be rigorously quantified using standardized metrics (Chen, B., 2005).

The homogeneous and heterogeneous catalysis involves a fundamental trade-off between catalytic precision and practical separation (Baskar, G., 2017) as seen in **Table 1.** Homogeneous catalysts, being soluble molecular complexes, offer highly defined active sites, which generally leads to superior selectivity and the potential for very high intrinsic activity (Halpern, J., 1981). Conversely, heterogeneous catalysts, such as supported Pd nanoparticles can be readily separated from the reaction mixture. simple filtration, making them the preferred choice for large-scale industrial processes due to their recyclability and robustness (Satterfield, C.N., 1991). The development of immobilized Pd complexes represents a strategic effort to bridge this gap, aiming to combine the

high selectivity of molecular systems with the facile recyclability of solid-supported materials (Cagnola, E.A., 2004).

**Table 1:** Comparison of the Heterogeneous and Homogeneous Pd Catalysis systems

| Feature | Homogeneous Catalysis | Heterogeneous Catalysis | Ref. |
|---|---|---|---|
| **Active Site Definition** | Well-defined, single metal center | Ill-defined, surface atoms/ensembles | Crabtree, 2019, Zhang, 2018 |
| **Selectivity Control** | Generally high, ligand-controlled | Often lower, surface effects dominate | Somorjai, 2010 |
| **Catalyst Separation** | Difficult, requires specialized techniques | Easy (Filtration, decantation) | Sheldon, 2000, Satterfield, 1991 |
| **Stability** | Often sensitive to air/moisture | Generally robust, high thermal stability | Cazin, 2008, Heldal, 1984 |

While the homogeneous and heterogeneous catalytic cycles are often treated separately, the underlying chemical principles of $H_2$ activation and subsequent transfer to the alkene are fundamentally related (Baskar, G., 2017). The Horiuti-Polanyi mechanism**,** originally developed for heterogeneous catalysis, provides a conceptual framework that can be adapted to understand the elementary steps in both systems (Somorjai, G.A., 2010). The organometallic cycle can be viewed as the molecular analogue of the Horiuti-Polanyi mechanism, where the Pd center acts as the "surface" (Sheldon & Wallau, 2000). The oxidative addition of $H_2$ is analogous to the dissociative adsorption of $H_2$, and the migratory insertion is the molecular equivalent of the first hydrogen transfer. This unified perspective is particularly useful when considering immobilized Pd complexes, which blur the line between the two catalytic regimes (Cagnola, E.A., 2004). The reaction conditions, particularly the solvent and temperature, can dramatically influence whether the Pd catalyst operates in a truly homogeneous or a heterogeneous regime.

In some cases, a seemingly homogeneous Pd complex can act as a precursor for the *in-situ* formation of Pd nanoparticles, which then serve as the true active catalyst. This phenomenon is often observed when the solvent is non-coordinating or when the ligands are easily dissociated (Wessel, N., 2024). The use of highly coordinating solvents or ligands, such as NHCs, is a deliberate strategy to maintain the molecular integrity of the Pd complex and ensure a truly homogeneous catalytic cycle (Hoyos, M., 2014).

High temperatures and pressures, while often increasing the reaction rate, can also accelerate the deactivation pathways, particularly the aggregation of Pd complexes into nanoparticles. Therefore, the choice of reaction conditions

critically influences the identity of the active species. For industrial applications, the trend is to develop catalysts that can maintain high activity and stability under the mildest possible conditions, minimizing energy consumption and side reactions (Patel, A., 2021).

The active site is the specific location on the catalyst where the chemical transformation occurs (Somorjai, G.A., 2010). In homogeneous Pd complexes, the active site is the central Pd atom, whose reactivity is precisely controlled by the surrounding ligands (Crabtree, R.H., 2019). In heterogeneous Pd nanoparticles, the active sites are the surface atoms, particularly those at the edges and corners, which possess lower coordination numbers and higher reactivity (Zhang, J., 2022). The active site concept is essential for interpreting the inherent activity of a catalyst. The development of Pd SACs represents the ultimate realization of a well-defined active site in heterogeneous catalysis, where every Pd atom is an isolated, potentially active center. The ability to accurately characterize and manipulate the active site is the core challenge in modern catalyst design (Beller, M., 2004).

## Homogeneous Palladium Complexes in Cyclohexene Hydrogenation

The mechanism for the homogeneous Pd-catalyzed hydrogena- tion of cyclohexene is typically understood through the frame- work of a catalytic cycle involving a sequence of fundamental organometallic steps (Halpern, J., 1981). This cycle is generally initiated by the activation of the Pd precursor to form the true active species, often a low-valent Pd (0) or Pd (II) complex (Beller, M., 2004).

The ligand environment surrounding the central Pd atom is arguably the most critical factor determining the performance of a homogeneous catalyst. Ligands exert control by dictating the electronic density at the metal center and by imposing steric constraints on the coordination sphere (Hoyos, M., 2014). This precise control allows for the fine-tuning of the rates of the elementary steps, thereby optimizing the overall catalytic turnover (Wang, Y., 2024).

Classical phosphine ligands, such as triphenylphosphine ($PPh_3$) have been extensively used in Pd catalysis due to their tunable electronic properties (Chen, B., 2005). However, a major challenge associated with monodentate phosphines is their tendency to dissociate from the Pd center under reaction conditions. This dissociation can lead to the aggregation of the free Pd metal into catalytically inactive Pd black (nanoparticles), a primary deactivation pathway. To counteract this, bidentate phosphines, which form more stable chelate rings with the Pd center, are frequently employed to enhance the catalyst's robustness and stability (Ojwach, S., 2016).

N-Heterocyclic Carbene (NHC) ligands have emerged as superior alternatives to phosphines in many Pd-catalyzed reactions (Hoyos, M., 2014). NHCs are

characterized by their exceptionally strong sigma-donating ability, which effectively stabilizes the Pd center in lower oxidation states (Sprengers, J.W., 2005). This enhanced stabilization significantly reduces the propensity for ligand dissociation and subsequent Pd black formation, thereby minimizing catalyst deactivation and leaching (Wessel, N., 2024). Furthermore, the steric bulk of NHC ligands can be easily modified by varying the substituents on the nitrogen atoms, providing a powerful tool for optimizing the catalyst's selectivity and activity (Hoyos, M., 2014).

Pincer ligands, characterized by a tridentate coordination mode that "pincers" the metal center, represent a highly effective strategy for creating exceptionally stable and robust homogeneous Pd catalysts (Sprengers, J.W., 2005). ligands, typically featuring a central N or C donor atom flanked by two phosphine or NHC arms, enforce a rigid geometry around the Pd atom (Crabtree, R.H., 2019). This rigidity is crucial as it prevents the ligand from dissociating, which is the primary cause of catalyst deactivation through Pd black formation. The high stability conferred by pincer ligands allows the catalysts to operate at higher temperatures and pressures, significantly increasing the overall TON.

For cyclohexene hydrogenation, pincer Pd complexes have demonstrated remarkable longevity. The PNP pincer system, for example, achieves a TON of 5000, which is substantially higher than many traditional phosphine-based systems (Olaoye, O.E., 2025). The rigid structure ensures that the Pd center remains in its molecular form throughout the catalytic cycle, minimizing the risk of leaching and aggregation. Additionally, the electronic behavior of pincer ligands can be modulated by tailored substituent modifications on the flanking arms, providing a powerful tool for optimizing the catalyst's selectivity and activity (Crabtree, R.H., 2019).

The performance of homogeneous Pd complexes in cyclohexene hydrogenation varies widely depending on the specific ligand system and reaction conditions employed (Wang, Y., 2024). **Table 2** provides a comparative overview of selected homogeneous Pd systems, illustrating the range of achievable catalytic activities.

**Table 2**: Activity of selected homogeneous Pd complexes in cyclohexene hydrogenation

| **Catalyst** | **Ligand System** | **Temp (°C)** | **TOF ($h^{-1}$)** | **TON** | **Ref.** |
|---|---|---|---|---|---|
| $Pd(OAc)_2$ | NHC | 25 | 1031 | 2090 | Hoyos, M., 2014 |
| $PdCl_2$ | PNP:(N, N'-bis diphenylphosphine) | 80 | 150 | 5000 | Olaoye, O.E., 2025 |
| $Pd(OAc)_2$ | Schiff Base | 60 | 85 | 2500 | Ojwach S., 2016 |
| $PdCl_2$ | Pyridyl-imine | 25 | 220 | 8000 | Ojwach S., 2016 |
| $Pd(acac)_2$ | $P(OPh)_3$ | 50 | 250 | N/A | Chen, B., 2005 |

The NHC-based system reported by Hoyos, M., et al., 2024 and demonstrates a remarkably high TOF of 1031 $h^{-1}$ under ambient temperature and pressure, highlighting the effectiveness of strong sigma-donating ligands in accelerating the catalytic cycle. Conversely, the PNP system, while having a lower TOF, achieves a high TON of 5000, indicating superior long-term stability under the slightly elevated temperature and pressure conditions (Olaoye, O.E., 2025). The ability to achieve high TONs is particularly important for the economic viability of homogeneous processes (Baskar, G., 2017).

The choice of solvent is not a passive parameter; it profoundly influences the kinetics, mechanism, and stability of homogeneous Pd complexes in cyclohexene hydrogenation (Jo, y.d., 1996). The solvent can affect the solubility of the reactants and products, the coordination sphere of the Pd complex, and the rate of the elementary steps (Halpern, J., 1981). In non-polar solvents like toluene or benzene, the Pd complex often exists in a less-solvated state, which can enhance the rate of substrate coordination by providing more open coordination sites (Chen, B., 2005). However, these solvents can also promote the aggregation of the Pd complex, leading to deactivation. Polar aprotic solvents, such as DMF or

$CH_2CI_2$ offer better stabilization of the charged intermediates in the catalytic cycle, which can be beneficial for overall activity (Wessel, N., 2024). The $PdCl_2$ complex with a pyridyl-imine ligand, for instance, showed high stability and a TON of 8000 in $CH_2CI_2$ suggesting that the solvent effectively stabilizes the active species (Ojwach, S., 2016).

The development of catalysts that operate efficiently in water is a major goal in green chemistry (Patel, A., 2021). Water is an environmentally benign and cost-effective solvent, but it poses a challenge for many organometallic Pd complexes due to their poor solubility and sensitivity to hydrolysis (Baskar, G., 2017). To overcome this, researchers have designed water-soluble Pd complexes, often by incorporating hydrophilic groups (e.g., sulfonates) into the ligands (Wang, Y., 2024). More recently, the use of supported Pd nanoparticles in water has demonstrated exceptional performance, with the PdPW11\ $ZrO_2$ system achieving a TOF of 14,005 $h^{-1}$ in an aqueous medium. This high activity is attributed to the unique stabilization provided by the polyoxometalate in the aqueous environment, which prevents aggregation and maintains the high surface area of the Pd nanoparticles (Patel, A., 2021).

The study of homogeneous Pd complexes has provided crucial mechanistic insights that are often difficult to obtain in heterogeneous systems (Halpern, J., 1981). The key mechanistic question revolves around the nature of the active species: is it the molecular Pd complex, or is it a Pd nanoparticle formed *in situ*. The Mercury Test is a standard diagnostic tool used to address this question. If the addition of elemental mercury, which poisons metallic Pd nanoparticles, halts the reaction, it suggests that the true active species is heterogeneous Pd black (Zhao, X., 2022). Conversely, if the reaction continues, the active species is likely the molecular Pd complex. However, the reliability of the mercury test has been debated, as some molecular complexes can be resistant to mercury poisoning, and some nanoparticles can be too small to be affected. Therefore, modern studies often rely on a combination of techniques, including kinetic analysis, NMR spectroscopy, and TEM imaging, to definitively characterize the active species. The use of benchtop NMR has been shown to be particularly effective in monitoring the stability of Pd complexes and detecting the formation of Pd black *in situ* (Wessel, N., 2024).

While cyclohexene is an achiral substrate by itself, the principles derived from Pd-catalyzed hydrogenation are directly applicable to the highly important field of asymmetric hydrogenation (Wang, Y., 2024). Asymmetric hydrogenation is a cornerstone of modern organic synthesis, particularly in the pharmaceutical industry, where the production of single-enantiomer drugs is mandatory (Chen, B., 2005).

The success of asymmetric hydrogenation hinges entirely on the design of chiral ligands**.** These ligands, when coordinated to the Pd center, create a chiral

environment that forces the prochiral substrate to bind in a specific orientation (Crabtree, R.H., 2019). The subsequent migratory insertion and reductive elimination steps then proceed with a high degree of stereo control, leading to the formation of a single enantiomer of the product (Wang, Y., 2024).

Palladium complexes, often utilizing chiral phosphine ligands such as BINAP or DuPhos, have been successfully used for enantioselective hydrogenation of various functionalized alkenes, including alpha\beta-unsaturated esters and enamides (Chen, B., 2005). The mechanism remains fundamentally the same as that for cyclohexene, but the ligand's chirality introduces a critical differentiation in the transition state energies (Halpern, J., 1981). The difference in activation energy between the two possible diastereomeric transition states determines the enantiomeric excess of the final product (Crabtree, R.H., 2019).

In many Pd-catalyzed asymmetric hydrogenations, the active species is believed to be a Pd(II) dihydride complex, which is formed after the oxidative addition of $H_2$ to a Pd(0) precursor (Beller, M., 2004). However, the precise oxidation state and coordination geometry of the active species are highly dependent on the specific chiral ligand employed (Sprengers, J.W.2005). The ability of Pd to cycle between Pd (0) and Pd (II) makes it a versatile metal for this transformation, although Rh and Ru often dominate the field due to their typically higher ee values (Chen, B., 2005). Nevertheless, the principles of ligand tuning established in the cyclohexene model reaction are directly translated to the design of high-performance chiral Pd.

### Heterogeneous and Immobilized Palladium Systems

Heterogeneous catalysts, particularly supported palladium nanoparticles (Pd NPs), remain the undisputed industrial standard for large-scale hydrogenation processes due to their superior robustness, thermal stability, and ease of separation and recyclability (Satterfield, C.N., 1991). The activity and selectivity of these supported Pd NPs are critically is influenced by a range of factors, such as size and morphology of the nanoparticles, the nature of the support material, and the strength of the metal-support interaction (Zhang, J., 2022).

The support material is not merely an inert scaffold; it actively influences the electronic state of the Pd nanoparticles through a phenomenon known as the Strong Metal-Support Interaction (Somorjai, G.A., 2010). For instance, the use of reducible oxide supports, such as $CeO_2$ or$TiO_2$, can lead to electron transfer from the support to the Pd nanoparticles, altering the binding energy of the reactants and thereby modifying the catalytic activity (Wang, Y. 2024). Carbon-based supports, such as activated carbon (Pd/C) or biomorphic carbon, offer high surface area and excellent conductivity, making them highly effective for liquid-phase reactions like cyclohexene hydrogenation (Satterfield, 1991, Cazaña, F., 2015).

Recent advancements in materials science have led to the development of highly stabilized Pd nanoparticles that exhibit exceptional performance metrics, even under mild conditions. The system developed by Patel A., 2021, utilizing Pd nanoparticles stabilized by a polyoxometalate (PW11) and supported on $ZrO_2$, demonstrated a record-breaking TOF of 14,005 $h^{-1}$ and a TON of 28,010 for cyclohexene hydrogenation in water at 25 °C and 1 bar $H_2$ (Patel, A., 2021). This achievement underscores the potential of stabilizing Pd NPs with external ligands or capping agents to prevent aggregation and enhance catalytic longevity (Zhang, J., 2022).

The strategy of immobilizing homogeneous Pd complexes onto solid supports (e.g. polymers, silica, zeolites) is a deliberate attempt to combine the high selectivity and well-defined active sites of molecular catalysts with the practical recyclability of heterogeneous systems (Cagnola, E.A., 2004). The ligand is chemically tethered to the support, which prevents leaching and aggregation while maintaining the molecular structure of the active site (Baskar, G., 2017). The most advanced form of immobilization and a rapidly growing area of research is the development of Single-Atom Catalysts (SACs) (Wang, Y., 2024). SACs are characterized by the isolation and anchoring of individual Pd atoms onto a support material, maximizing the atom utilization efficiency (Wang, Y., 2024). For cyclohexene hydrogenation, Pd SACs anchored on supports like $CeO_2$ have been investigated, often showing unique catalytic properties distinct from those of Pd nanoparticles (Atran, A.A., 2024). The high coordination unsaturation of the single Pd atom can lead to enhanced intrinsic activity, although stability under harsh reaction conditions remains a significant challenge. SACs often exhibit unique selectivity profiles that are not observed in nanoparticle catalysts. For cyclohexene hydrogenation, the isolated Pd atom may follow a different reaction pathway (Atran, A.A., 2024). While nanoparticles rely on the ensemble effect for the dissociative adsorption of $H_2$, the single Pd atom must activate $H_2$ via a non-dissociative or heterolytic pathway. This difference in the $H_2$ activation mechanism can be exploited to achieve high chemoselectivity in the hydrogenation of molecules containing multiple reducible functional groups (Wang, Y., 2024).

Despite their high atom efficiency, Pd SACs face significant stability challenges. Under the reducing atmosphere of hydrogenation, the isolated Pd atoms are prone to migration and aggregation, leading to the formation of inactive Pd clusters or nanoparticles (Atran, A.A., 2024). The design of robust anchoring sites that can withstand high temperatures and pressures is a critical area of ongoing research to make Pd SACs viable for industrial applications **Table 3** offers a detailed evaluation of performance indicators across a range of heterogeneous and immobilized Pd catalysts, highlighting the significant progress made in achieving high activity and stability (Patel, A., 2021, Cazaña, F., 2015).

**Table 3**: Comparative performance of selected heterogeneous and immobilized Pd catalysts in cyclohexene hydrogenation

| Catalyst | Pd/ Support | Pd Loading | Temp (°C) | TOF ($h^{-1}$) | TON | Ref. |
|---|---|---|---|---|---|---|
| Supported NP | Pd-PW11/$ZrO_2$ | 0.0034 mol% | 25 | **14005** | **28010** | Patel A., 2021 |
| Supported NP | Pd\Al-C | 1.0 wt% | 30 | 500 | N/A | Cazaña F., 2015 |
| Single-Atom Catalyst | Pd-SA/ $CeO_2$ | 5 wt% | 120 | N/A | N/A | Atran A.A., 2024 |
| Immobilized Complex | Pd (II)-Tridecylamine/ $SiO_2$ | N/A | 60 | 120 | N/A | Cagnola E.A. 2004 |
| Supported NP | Pd/C | 5 wt% | 50 | 500 | >5000 | Satterfield, C. N.,1991 |

In heterogeneous Pd catalysis, the size and morphology of the Pd nanoparticles are critical parameters that directly influence the catalytic performance (Zhang, J., 2022). The surface of a Pd nanoparticle is not uniform; it consists of different types of sites, including corner atoms, edge atoms, and terrace atoms, each possessing distinct coordination numbers and electronic properties (Somorjai, G.A., 2010). Generally, smaller Pd nanoparticles exhibit higher catalytic activity for hydrogenation reactions due to the increased proportion of low-coordination number atoms (corners and edges) (Zhang, J., 2022). These low-coordination sites are often more active for the dissociative adsorption of $H_2$ and the subsequent activation of the C=C bond (Somorjai, G.A., 2010). However, this relationship is not always linear. Below a certain critical size (often around 1-2 nm), the electronic structure of the Pd nanoparticle can change significantly, leading to a decrease in activity. The optimal size for maximum TOF is therefore a complex balance between maximizing the population of active sites and maintaining the bulk-like electronic structure necessary for efficient catalysis (Wang, Y., 2024).

The morphology of the Pd nanoparticle, which refers to its overall shape and the exposed crystal facets, also plays a crucial role (Somorjai, G.A., 2010). For

face-centered cubic (fcc) metals like Pd, the most common facets are (111), (100), and (110) (Zhang, J., 2022). The Pd (111) facet, which is the most densely packed, is often found to be less active for hydrogenation than the more open Pd (100) or Pd (110) facets (Somorjai, G.A., 2010). By controlling the synthesis conditions, researchers can selectively expose specific facets, thereby tuning the catalytic properties. For instance, Pd nanocubes (which expose the (100) facet) have been shown to exhibit different selectivity profiles compared to Pd octahedra (which expose the (111) facet) (Wang, Y., 2024).

The performance of Pd catalysts can be further enhanced through the addition of a second metallic element (bimetallic systems) or by the use of non-metallic promoters (Wang, Y., 2024). The inclusion of a second metallic species, exemplified by Au,Ag, or a non-noble metal like Cu, to Pd nanoparticles can lead to synergistic effects that improve activity, selectivity, and stability (Zhang, J., 2022).

Non-metallic promoters, such as P or N doping in carbon supports, can also significantly impact the catalytic performance of Pd. The introduction of these heteroatoms can create defects in the support material, which act as anchoring sites for the Pd nanoparticles, preventing sintering and enhancing stability (Zhang, J., 2022). Furthermore, the electronic interaction between the Pd and the doped support can be optimized to improve the intrinsic activity of the Pd sites (Wang, Y., 2024).

Catalyst deactivation is a major economic and environmental challenge in both homogeneous and heterogeneous Pd catalysis. In homogeneous and immobilized systems, the primary deactivation pathway is leaching**,** which is the dissociation of the Pd metal center from its stabilizing ligands or support. The leached Pd can then aggregate to form Pd nanoparticles (often referred to as Pd black), which may or may not be the "true" active catalyst (Zhao, X., 2022). The mercury test is a classic diagnostic tool used to distinguish between homogeneous and heterogeneous catalysis, where the addition of elemental mercury is expected to poison only the metallic nanoparticles, thus halting the reaction if the nanoparticles are the true active species. The design of highly stable, non-dissociating ligands, such as NHC ligands, is the most effective strategy to mitigate leaching in molecular systems (Hoyos, M., 2014). For heterogeneous Pd catalysts, the main deactivation mechanisms are sintering and poisoning (Zhang, J., 2022). Sintering involves the thermal migration and coalescence of small Pd nanoparticles into larger, less active particles, which reduces the total active surface area (Satterfield, C.N., 1991). Poisoning occurs when impurities present in the reaction mixture, such as sulfur-containing compounds or strongly coordinating solvents, irreversibly adsorb onto the active Pd sites, blocking the catalytic cycle (Heldal, J.A., 1984). Strategies to combat sintering include the use

of strong metal-support interactions and the application of stabilizing capping agents (Patel, A., 2021).

The activation of molecular hydrogen is a prerequisite for both homogeneous and heterogeneous hydrogenation (Halpern, J., 1981). The efficiency of this step often dictates the overall TOF of the catalyst. In homogeneous Pd complexes, $H_2$ activation occurs via the oxidative addition step, which proceeds via H-H bond dissociation, followed by the concurrent formation of two Pd-H bonds. (Beller, M., 2004). This step is highly sensitive to the electronic environment of the Pd center (Crabtree, R.H., 2019). Electron-rich Pd centers, typically stabilized by strong sigma-donating ligands like NHCs, facilitate the oxidative addition by readily transferring electron density to the $H_2$ molecule. This is a key reason why NHC-based Pd catalysts often exhibit high TOF values (Wessel, N., 2024). In heterogeneous Pd systems, $H_2$ activation involves the dissociative chemisorption of the molecule onto the Pd surface, forming two adsorbed hydrogen *atoms (H*ads) (Somorjai, G.A., 2010). This process is extremely rapid on clean Pd surfaces, but its rate can be limited by mass transport phenomena, particularly in liquid-phase reactions (Satterfield, C.N., 1991). The transport of $H_2$ from the gas phase, through the liquid film, and onto the catalyst surface can become the rate-limiting step under high agitation or high catalyst loading conditions (Cazaña, F., 2015). The activation energy (Ea) values ranging from 23.8 kJ/mol to 38.5 kJ/mol, are characteristic of chemically controlled reactions, suggesting that the chemical steps on the surface, rather than mass transport, are generally rate-limiting under the reported experimental conditions (Heldal, J.A. 1984, Jo, Y.D., 1996).

The adsorption of cyclohexene onto the Pd active site is the second crucial step in the catalytic cycle. In homogeneous systems, cyclohexene coordinates to the Pd center via its pi-bond (Crabtree, R.H., 2019). In heterogeneous systems, the strength of the cyclohexene adsorption is a major factor determining the reaction order. Strong adsorption leads to surface saturation and zero-order kinetics in relation to the alkene, as the active sites are constantly occupied by the substrate (Cazaña, F., 2015). Conversely, weak adsorption leads to a fractional or first-order dependence on the alkene concentration (Jo, Y.D.,1996). The ability of the catalyst to balance the adsorption strength-strong enough to activate C=C bond but weak enough to allow for rapid product desorption is key to achieving high TOF (Teschner, D., 2008).

### Comparative Analysis with Other Transition Metal Catalysts

The preeminence of palladium in alkene hydrogenation is often challenged or complemented by other Group 8-10 transition metals, most notably Rhodium (Rh) and Ruthenium (Ru) (Cagnola, E.A., 2004). A comprehensive evaluation of Pd's role necessitates a detailed comparative analysis, focusing on intrinsic

activity (TOF), stability, cost-effectiveness, and application scope (Teschner, D., 2008).

### Rhodium (Rh) Complexes

Rhodium complexes, particularly the seminal Wilkinson's catalyst ($RhCl(PPh_3)_3$), established the foundation for modern homogeneous hydrogenation (Hussey, A.S., 1970). Rhodium generally exhibits exceptional activity, often achieving TOF values that are comparable to or even surpass those of the most active Pd systems, especially under mild reaction conditions (Hamdy, M.S., 2020). The catalytic cycle for Rh is well-understood, typically proceeding through a Rh(I)/Rh (III) mechanism, which is highly efficient for the activation of $H_2$ (Halpern, J., 1981).

However, the primary limitations of Rh are its significantly higher cost compared to Pd and the persistent challenge of maintaining high TONs due to catalyst deactivation and leaching. Despite these drawbacks, recent innovations in supported Rh nanoparticles have yielded some of the highest reported TOF values for cyclohexene hydrogenation, reaching up to 17,784 $h^{-1}$under ambient conditions. This demonstrates that while Rh is costly, its potential for raw catalytic power in this model reaction is arguably the highest among the noble metals (Hamdy, M.S., 2020).

### Ruthenium (Ru) Complexes

Ruthenium complexes are frequently positioned as a more cost-effective and robust alternative to both Pd and Rh, making them highly attractive for large-scale industrial applications (Cui, X., 2016). While homogeneous Ru complexes often display lower intrinsic activity (TOF) for simple alkene hydrogenation compared to their Pd and Rh counterparts, they possess superior stability, allowing them to operate effectively under more demanding conditions, such as high temperatures and pressures (Bugarin, A., 2024).

A key advantage of Ru is its versatility, particularly its excellence in transfer hydrogenation reactions and its high effectiveness in the selective hydrogenation of aromatic rings, a reaction where Pd and Rh can be less selective (Cui, X., 2016). For cyclohexene hydrogenation, homogeneous Ru complexes typically show moderate activity, with TOF values around 100 $h^{-1}$. The strength of Ru lies not in achieving peak TOF but in providing a stable, lower-cost catalyst that can withstand the rigors of continuous industrial operation. **Table 4** enables a direct assessment of the performance metrics associated with representative Pd, Rh, and Ru catalysts in the benchmark cyclohexene hydrogenation reaction, illustrating the distinct advantages of each metal (Patel, A., 2021; Hamdy, M.S., al., 2020; Bugarin, A., 2024).

**Table 4**: Comparative performance of Pd, Rh, and Ru catalysts in cyclohexene hydrogenation.

| Metal | Catalyst Type | Ligand/ Support | TOF ($h^{-1}$) | TON | Ref. |
|---|---|---|---|---|---|
| **Pd** | Supported NP | Pd-PW11/ZrO$_2$ | 14005 | 28010 | Patel. A., 2021 |
| **Rh** | Supported NP | Rh/SiO$_2$ | 17784 | N/A | Hamdy, M.S., 2020 |
| **Ru** | Homogeneous | Ru (III) complex (Imidazol) | 100 | N/A | Bugarin, A., 2024 |

The choice of metal is fundamentally dictated by the specific application requirements. Rhodium catalysts, particularly in nanoparticle form, offer the highest intrinsic activity (TOF) but are limited by cost and stability challenges (Hamdy, M.S., 2020). Ruthenium provides a robust, cost-effective solution, favored for its stability under harsh conditions, though it typically exhibits lower TOF for simple alkene hydrogenation (Cui, X., 2016). Palladium, however, emerges as the most versatile and balanced choice (Sprengers, J.W., 2005). Pd systems, especially the advanced supported nanoparticles, offer a superior combination of high activity, excellent ligand tunability for selectivity control, and a favorable cost to performance ratio compared to Rh (Patel, A., 2021).

## Conclusion

The extensive study of Pd complexes in the hydrogenation of cyclohexene has driven significant advancements in catalytic science. The reaction remains a crucial model for probing fundamental catalytic principles, leading to the evolution from classical homogeneous systems to highly efficient immobilized and single-atom catalysts (Wang, Y., 2024). The ability to precisely control the electronic and steric environment of Pd center through sophisticated ligand design has been the most powerful tool for optimizing homogeneous systems (Sprengers, J.W., 2005). Concurrently, breakthroughs in materials science have facilitated the creation of heterogeneous catalysts with unprecedented activity and stability, exemplified by the high TOF values achieved by stabilized Pd nanoparticles (Patel, A., 2021).

The ultimate goal is to achieve a catalyst that exhibits both high intrinsic activity (TOF) and exceptional long-term stability (TON), a combination that is essential for the economic viability of industrial hydrogenation processes (Baskar, G., 2017). The continued use of cyclohexene hydrogenation as a model reaction will be instrumental in validating these next-generation Pd catalysts. The continued, rigorous investigation into Pd complexes for cyclohexene hydrogenation will undoubtedly serve as a catalyst for the development of more sustainable, efficient, and selective catalytic technologies across the chemical industry (Rylander, P.N., 1985).

## References


Atran, A. A., & Hamdy, M. S. (2024). Hydrogenation of cyclohexene over single-atom Pt or Pd incorporated porous ceria nanoparticles under solvent-free conditions. *RSC Advances, 14*(15), 10644-10652.

Baskar, G., Aiswarya, R., Soumiya, S., Mohanapriya, N., & Nivetha, S. R. (2017). Recent advances in heterogeneous catalysts for biodiesel production. *Journal of Energy and Environmental Sustainability, 4*, 1-5.

Beller, M., Seayad, J., Tillack, A., & Grote, D. (2004). Catalytic Markovnikov and anti-Markovnikov functionalization of alkenes and alkynes: Recent developments and trends. *Angewandte Chemie International Edition, 43*(26), 3368–3398.

Bugarin, A., Patil, S. A., Tran, R. Q., & Marichev, K. O. (2024). Metal complexes of backbone-halogenated imidazol-2-ylidenes. *Inorganica Chimica Acta, 572*, 122263.

Cagnola, E. A., Quiroga, M. E., Liprandi, D. A., & L'Argentière, P. C. (2004). Immobilized Rh, Ru, Pd and Ni complexes as catalysts in the hydrogenation of cyclohexene. *Applied Catalysis A: General, 274*, 205-212.

Cazaña, F., Jimaré, M. T., Romeo, E., Sebastián, V., Irusta, S., Latorre, N., Royo, C., & Monzón, A. (2015). Kinetics of liquid phase cyclohexene hydrogenation on Pd–Al/biomorphic carbon catalysts. *Catalysis Today, 249*, 127-136.

Chen, B., Dingerdissen, U., Krauter, J. G. E., Lansink Rotgerink, H. G. J., Mobus, K., Ostgard, D. J., Panster, P., Riermeier, T. H., Seebald, S., Tacke, T., & Trauthwein, H. (2005). New developments in hydrogenation catalysis particularly for fine chemicals. *Applied Catalysis A: General, 280*(1), 17-46.

Crabtree, R. H. (2019). *The organometallic chemistry of the transition metals* (7th ed.). Wiley.

Cui, X., Surkus, A. E., Junge, K., Topf, C., Radnik, J., Kreyenschulte, C., & Beller, M. (2016). Highly selective hydrogenation of arenes using nanostructured ruthenium catalysts modified with a carbon–nitrogen matrix. *Nature Communications, 7*, 11326.

Elnaz, M., Somayeh, J., Prshang, A., Farhad, G. F., Esmaeil, & F. G. (2024). Surface Chemistry and Catalysis: Understanding Interfaces for Enhanced Reactivity. *Iran. J. Chem. Chem. Eng.* 43(5),1-14.

Gorunova, O. N., Novitskiy, I. M., Grishin, Y. K., Gloriozov, I. P., Roznyatovsky, V. A., Khrustalev, V. N., Kochetkov, K. A., & Dunina, V. V. (2018). When applying the mercury poisoning test to palladacycle-catalyzed reactions, one should not consider the common misconception of mercury (0) selectivity. *Organometallics, 37*, 2842-2858.

Halpern, J. (1981). Mechanistic aspects of homogeneous catalytic hydrogenation and related reactions. *Inorganica Chimica Acta, 50*, 11-19.

Hamdy, M. S., Alhanash, A. M., Benaissa, M., Alsalme, A., Alharthi, F. A., & Al-Zaqri, N. (2020). Rhodium nanoparticles incorporated mesoporous silica as an active catalyst for cyclohexene hydrogenation under ambient conditions. *Catalysts, 10*(8), 925.

Heldal, J. A., & Frankel, E. N. (1984). Comparison of homogeneous and heterogeneous palladium hydrogenation catalysts. *Journal of the American Oil Chemists' Society, 61*, 756-761.

Horváth, A. (2002). *Supported palladium nanoparticles prepared by colloidal synthesis: Characterization and catalytic activity* (Doctoral dissertation). University of Szeged, Szeged, Hungary.

Hoyos, M., Guest, D., & Navarro, O. (2014). (N-heterocyclic carbene)-palladium complexes in catalysis. In *N-heterocyclic carbenes* (Chap. 4). Wiley-VCH. https://doi.org/10.1002/9783527671229.ch04

Hussey, A. S., & Takeuchi, Y. (1970). Hydrogenation of cycloalkenes using homogeneous rhodium complexes as catalysts. *The Journal of Organic Chemistry, 35*(3), 643-647.

Jayamurugan, G., Umesh, C. P., & Jayaraman, N. (2009). Preparation and catalytic studies of palladium nanoparticles stabilized by dendritic phosphine ligand-functionalized silica. *Journal of Molecular Catalysis A: Chemical, 307*, 142-148.

Jo, Y. D., Park, K. S., Ahn, J. H., & Ihm, S. K. (1996). Mechanistic study of hydrogenation of cyclohexene catalyzed by polymer-supported palladium (II) complex in various solvents. *Reactive and Functional Polymers, 29*(2), 91-99.

Ma, C., Wang, X., Soós, T., Zhang, J., & Yang, J. (2025). Ligand-controlled regiodivergent and enantioselective hydrophosphorylation of styrenes by palladium. *Nature Communications, 16*, 5436.

Ojwach, S., Ogwenoa, A. O., & Akermana, M. P. (2016). (Pyridyl) benzoazole palladium (II) complexes as homogeneous catalysts in hydrogenation of alkenes and alkynes. *Catalysis Science & Technology, 6*, 5069-5078.

Olaoye, O. E. (2025). *Exploring cobalt, nickel, and palladium complexes for the catalytic hydrogenation of alkenes*. IntechOpen. https://doi.org/10.5772/intechopen.100945

Patel, A., & Patel, A. (2021). Synthesis and characterization of supported stabilized palladium nanoparticles for selective hydrogenation in water at low temperature. *RSC Advances, 11*(14), 8218-8227.

Rylander, P. N. (1985). *Hydrogenation methods*. Academic Press.

Satterfield, C. N. (1991). *Heterogeneous catalysis in industrial practice* (2nd ed.). Krieger Publishing Company.

Somorjai, G. A., & Li, Y. (2010). *Introduction to surface chemistry and catalysis* (2nd ed.). Wiley.

Sprengers, J. W., Wassenaar, J., Clement, N. D., Cavell, K. J., & Elsevier, C. J. (2005). Palladium (N-Heterocyclic Carbene) Hydrogenation Catalysts. *Angewandte Chemie,* 117(13), 2062-2065.

Teschner, D., Révay, Z., Borsodi, J., Hävecker, M., Gericke, A. K., Schlögl, R., Milroy, D., Jackson, S. D., Torres, & D., Sautet, P. (2008). Understanding Palladium Hydrogenation Catalysts: When the Nature of the Reactive Molecule Controls the Nature of the Catalyst Active Phase. *Angewandte Chemie International Edition*. 47(48), 9274-9278.

Wang, Y., Feng, J., Li, E. Q., Jia, Z., & Loh, T. P. (2024). Recent advances in ligand-enabled palladium-catalyzed divergent synthesis. *Organic & Biomolecular Chemistry, 22*, 37-54.

Wasim, E., Din, N., Le, D., Zhou, X., Sterbinsky, G. E., Pape, M. S., Rahman, T. S., & Tait, S. L. (2022). Ligand-coordination effects on the selective hydrogenation of acetylene in single-site Pd–ligand supported catalysts. *Journal of Catalysis, 413*, 81-92.

Wessel, N., Medhekar, R. S., Sonnenberg, M., Stieber, H., Leitner, W., & Vorholt, A. J. (2024). Catalyst in sight: The use of benchtop NMR spectrometers to maintain the activity of Pd–$PPh_3$ catalysts. *ACS Catalysis, 14*(14), 10679-10688.

Westa, M. J., & Watson, A. J. B. (2019). Ni vs. Pd in Suzuki–Miyaura $sp^2$–$sp^2$ cross-coupling: A head-to-head study in a comparable precatalyst/ligand system. *Organic & Biomolecular Chemistry, 17*, 5055-5059.

Yao, H. C., & Emmett, P. H. (1959). Kinetics of catalytic liquid phase hydrogenation. I. The hydrogenation of aromatic nitrocompounds over colloidal rhodium and palladium. *Journal of the American Chemical Society, 81*, 4125-4132.

Zhao, X., Zhu, X., Wang, K., Lv, J., Chen, S., Yao, G., Lang, J., Lv, F., Pu, Y., Yang, R., Zhang, B., Jiang, Z., & Wan, Y. (2022). Palladium catalyzed radical relay for the oxidative cross-coupling of quinolines. *Nat Commun.* 13(1), 4180.

Zhang, J., Zhang, H., Wu, Y., Liu, C., Huang, Y., Zhou, W., & Zhang, B. (2022). Single-atom catalysts for thermal- and electro-catalytic hydrogenation reactions. *Journal of Materials Chemistry A, 10*, 5743-5757.